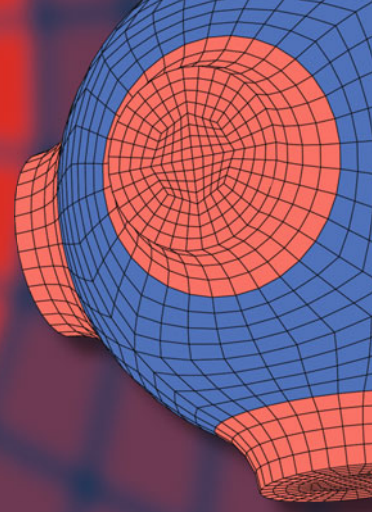


Advanced Structured Materials

Muhamad Husaini Abu Bakar
Tajul Adli bin Abdul Razak
Andreas Öchsner *Editors*



Progress in Engineering Technology V

 Springer


Advanced Structured Materials

Volume 183

Series Editors

Andreas Öchsner, Faculty of Mechanical Engineering, Esslingen University of Applied Sciences, Esslingen, Germany

Lucas F. M. da Silva, Department of Mechanical Engineering, Faculty of Engineering, University of Porto, Porto, Portugal

Holm Altenbach , Faculty of Mechanical Engineering, Otto von Guericke University Magdeburg, Magdeburg, Sachsen-Anhalt, Germany

Common engineering materials are reaching their limits in many applications, and new developments are required to meet the increasing demands on engineering materials. The performance of materials can be improved by combining different materials to achieve better properties than with a single constituent, or by shaping the material or constituents into a specific structure. The interaction between material and structure can occur at different length scales, such as the micro, meso, or macro scale, and offers potential applications in very different fields.

This book series addresses the fundamental relationships between materials and their structure on overall properties (e.g., mechanical, thermal, chemical, electrical, or magnetic properties, etc.). Experimental data and procedures are presented, as well as methods for modeling structures and materials using numerical and analytical approaches. In addition, the series shows how these materials engineering and design processes are implemented and how new technologies can be used to optimize materials and processes.

Advanced Structured Materials is indexed in Google Scholar and Scopus.

Muhamad Husaini Abu Bakar ·
Tajul Adli bin Abdul Razak · Andreas Öchsner
Editors

Progress in Engineering Technology V

 Springer

Editors

Muhamad Husaini Abu Bakar
Malaysian Spanish Institute
Universiti Kuala Lumpur
Kulim, Kedah, Malaysia

Tajul Adli bin Abdul Razak
Malaysian Spanish Institute
Universiti Kuala Lumpur
Kulim, Kedah, Malaysia

Andreas Öchsner
Faculty of Mechanical Engineering
Esslingen University Applied Sciences
Esslingen am Neckar, Baden-Württemberg
Germany

ISSN 1869-8433

ISSN 1869-8441 (electronic)

Advanced Structured Materials

ISBN 978-3-031-29347-4

ISBN 978-3-031-29348-1 (eBook)

<https://doi.org/10.1007/978-3-031-29348-1>

© The Editor(s) (if applicable) and The Author(s), under exclusive license to Springer Nature Switzerland AG 2023

This work is subject to copyright. All rights are solely and exclusively licensed by the Publisher, whether the whole or part of the material is concerned, specifically the rights of translation, reprinting, reuse of illustrations, recitation, broadcasting, reproduction on microfilms or in any other physical way, and transmission or information storage and retrieval, electronic adaptation, computer software, or by similar or dissimilar methodology now known or hereafter developed.

The use of general descriptive names, registered names, trademarks, service marks, etc. in this publication does not imply, even in the absence of a specific statement, that such names are exempt from the relevant protective laws and regulations and therefore free for general use.

The publisher, the authors, and the editors are safe to assume that the advice and information in this book are believed to be true and accurate at the date of publication. Neither the publisher nor the authors or the editors give a warranty, expressed or implied, with respect to the material contained herein or for any errors or omissions that may have been made. The publisher remains neutral with regard to jurisdictional claims in published maps and institutional affiliations.

This Springer imprint is published by the registered company Springer Nature Switzerland AG
The registered company address is: Gewerbestrasse 11, 6330 Cham, Switzerland

Contents

| | | |
|----------|--|----------|
| 1 | Polypropylene Composites Reinforced by Natural and Recycled Fibers for Bumper Application: Effects of Fiber Loading on the Tensile Properties | 1 |
| | Siti Rohana Binti Ahmad, Muhammad Izzuddin Aqil Bin Abdul Aziz, and Muhammad Rasidi Bin Alzahari | |
| 1.1 | Introduction | 1 |
| 1.2 | Experimental Investigations | 2 |
| 1.2.1 | Materials | 2 |
| 1.2.2 | Preparation of Sansevieria Leaf Fiber | 2 |
| 1.2.3 | Preparation of Beverage Box Fiber | 3 |
| 1.2.4 | Mixing Process | 3 |
| 1.2.5 | Hot-Press Process | 4 |
| 1.2.6 | Tensile Test | 4 |
| 1.3 | Result and Discussion | 4 |
| 1.4 | Conclusion | 6 |
| | References | 7 |
| 2 | A Comparison Analysis on Mechanical Properties Between Laminated Woven Bamboo and Epoxy Composite Versus Laminated Strip Bamboo and Polyester Composite | 9 |
| | Kannan Rassiah, Aidy Ali, and Megat Mohamad Hamdan Megat Ahmad | |
| 2.1 | Introduction | 10 |
| 2.2 | Materials | 10 |
| 2.2.1 | Epoxy | 10 |
| 2.2.2 | Polyester | 11 |
| 2.2.3 | Bamboo | 11 |
| 2.3 | Experiment | 11 |
| 2.3.1 | Mechanical Testing | 11 |
| 2.4 | Results and Discussion | 12 |

- 2.4.1 Tensile Analysis 13
- 2.4.2 Flexural Analysis 14
- 2.4.3 Hardness Analysis 15
- 2.4.4 Scanning Electron Microscope 16
- 2.5 Conclusion 17
- References 17
- 3 Investigation of the Effect of Surface Roughness and Dimensional Accuracy on the Layer Thickness of PLA Parts Produced by the FDM Process 19**
 Maria F. Jasim, Abdullah F. Huayier, and Tahseen F. Abbas
- 3.1 Introduction 19
- 3.2 Related Research 21
 - 3.2.1 Surface Roughness 21
 - 3.2.2 Dimensional Accuracy 22
- 3.3 Experimental Details 23
 - 3.3.1 Specimen Design and Material 23
 - 3.3.2 Process Parameter 24
- 3.4 Testing 25
 - 3.4.1 Surface Roughness Test 25
 - 3.4.2 Dimensional Accuracy Test 25
- 3.5 Results and Discussion 26
- 3.6 Conclusion 28
- References 28
- 4 Low Pressure, Solvent-Assisted Thermal Bonding of PMMA–PMMA Substrates for Microfluidics Device Fabrication 31**
 Farah A. Mat Nawang, Azmi M. Yusof, Sheikh F. S. M. Nasir, Rizal M. Noor, and Intan S. Zaine
- 4.1 Introduction 32
- 4.2 Materials and Method 32
 - 4.2.1 Sample Preparation 32
 - 4.2.2 Bonding Procedure 33
 - 4.2.3 Bonding Strength Test 33
 - 4.2.4 Fabrication of Microfluidics Device 34
- 4.3 Results and Discussion 34
 - 4.3.1 Bonding Result 34
 - 4.3.2 Sealing of a Microfluidics Device 34
- 4.4 Conclusion 36
- References 36
- 5 Temperature Distribution Analysis of an Insulated Turbocharger Manifold 39**
 Khairul Shahril, Shahril Nizam, Muhammad Najib, and Ishak Azid
- 5.1 Introduction 40

- 5.2 Literature 40
 - 5.2.1 Heat Transfer in Exhaust System 40
 - 5.2.2 The Exhaust Manifold of the Turbocharger 41
 - 5.2.3 Development of Thermal Barrier Coating 41
- 5.3 Methodology 41
- 5.4 Result and Discussion 43
 - 5.4.1 Temperature Distribution Analysis 43
- 5.5 Conclusion 46
- References 46

- 6 Experimental Analysis of Carburetor System on Turbocharger Performance 49**
Khairul Shahril, Mohd Nurhidayat Zafelem, Shahril Nizam Soid, Muhammad Najib Abdul Hamid, and Ishak Abduls Azid
 - 6.1 Introduction 49
 - 6.2 Literature Review 50
 - 6.2.1 Carburetor 50
 - 6.3 Methodology 52
 - 6.3.1 Methodology Process 52
 - 6.3.2 Parameter Study 52
 - 6.4 Results and Discussion 53
 - 6.4.1 Fuel Consumption 53
 - 6.4.2 Velocity 54
 - 6.4.3 Flow Rate 54
 - 6.5 Conclusion 55
 - References 56

- 7 Effect of Fuel Injection Pressure to Engine Performance Characteristics of Palm Oil Diesel Blends in a Small Diesel Engine 57**
Muhammad Haziq Bin Azizan, Shahril Nizam Mohamed Soid, Muhammad Najib Abdul Hamid, Mohd Suyerdi Omar, and Tajul Adli bin Abdul Razak
 - 7.1 Introduction 58
 - 7.2 Palm Oil Diesel Blends-Fueled Engine 58
 - 7.3 Methodology 59
 - 7.4 Results and Discussion 61
 - 7.5 Conclusion 61
 - References 64

- 8 Development of an Optical Measurement Test Rig for Fuel Spray Characteristics Study of a Diesel Direct Injection System—An Experimental Approach 67**
Megat Mohd Amzari Megat Mohd Aris, Shahril Nizam Mohamed Soid, and Ishak Abdul Azid
 - 8.1 Introduction 68

- 8.2 Methodology 69
- 8.3 Results and Discussion 71
- 8.4 Conclusion 72
- References 73
- 9 Effect of Rectangular Fins on the Heat Transfer Performance of an Automotive Radiator 75**
 - Faiza M. Nasir
 - 9.1 Introduction 75
 - 9.2 Simulation Setup 76
 - 9.2.1 Simulation Models 76
 - 9.2.2 Boundary Conditions 77
 - 9.2.3 Data Analysis 78
 - 9.3 Results and Discussion 78
 - 9.3.1 Effect of Fins 78
 - 9.3.2 Effect of Convection Heat Transfer Coefficient 79
 - 9.3.3 Effect of Coolants' Flow Rate 82
 - 9.4 Conclusion 83
 - References 84
- 10 Effect of Geometrical Dimension of Fins on the Cooling Performance of an Air-Cooled Engine Cylinder Block 85**
 - Faiza M. Nasir
 - 10.1 Introduction 85
 - 10.2 Simulation Study 87
 - 10.2.1 Simulation Base Model 87
 - 10.2.2 Assumptions and Boundary Conditions 88
 - 10.2.3 Independent Variables 88
 - 10.2.4 Response Variables 88
 - 10.3 Results and Discussion 89
 - 10.3.1 Temperature Distribution of the Fin 89
 - 10.3.2 The Effect of Fin Thickness 89
 - 10.3.3 The Effect of Fin's Length 90
 - 10.3.4 The Effect of Number of Fins 91
 - 10.4 Conclusion 93
 - References 94
- 11 Analysis of Hydraulic Arm Using Hydraulic Jack for Motorcycle Hydraulic Lift 95**
 - Khairul Shahril, Muhammad Afif Asnawi, Mior Firdaus Mior Abdul Majid, S. Nurashikin, and Ahmad Kamal
 - 11.1 Introduction 95
 - 11.2 Classification Based on Type of Energy Used 96
 - 11.2.1 Hydraulic Lift 96
 - 11.2.2 Pneumatic Lifts 97
 - 11.2.3 Mechanical Lifts 97

| | | |
|-----------|--|------------|
| 11.2.4 | Application of Hydraulic Lift | 97 |
| 11.3 | Problem Statement | 97 |
| 11.4 | Literature | 98 |
| 11.4.1 | Material Selection | 99 |
| 11.5 | Methodology | 99 |
| 11.5.1 | Analytical Analysis | 100 |
| 11.5.2 | Simulation Setup | 100 |
| 11.6 | Result and Discussion | 101 |
| 11.6.1 | Hydraulic Arm | 101 |
| 11.6.2 | Analysis of the Result | 101 |
| 11.7 | Conclusion | 103 |
| | References | 103 |
| 12 | FMEA Approach to Extend the Engine Oil Drain Interval of a 100-t Truck: A Case Study | 105 |
| | Surya Atmadyaya, Mohamad Sazali Said, Azmi Hassan, Fauzan Rahman, Iwan Susanto, Tumianto, and Yusri Yamin | |
| 12.1 | Introduction | 106 |
| 12.2 | Case Study | 106 |
| 12.2.1 | Methodology | 106 |
| 12.3 | Result and Discussion | 115 |
| 12.4 | Conclusions | 115 |
| | References | 117 |
| 13 | Design and Fabrication of a Dip Immersion Probe for Melting and Pouring Practice in Casting Technology | 119 |
| | Yap Tek Hong, Nadzri Che Kamis, and Choong Chee Guan | |
| 13.1 | Introduction | 120 |
| 13.2 | Literature Review | 121 |
| 13.3 | Methodology | 123 |
| 13.3.1 | Specification of DIP Immersion Probe for a Measurement Probe of Casting Process | 123 |
| 13.3.2 | Conceptual, Design, and Fabrication of the Dip Immersion Probe | 123 |
| 13.3.3 | Pouring Temperature Measurement | 124 |
| 13.4 | Results and Discussion | 124 |
| 13.5 | Conclusion | 126 |
| | References | 127 |
| 14 | Heat Transfer Coefficient for Synthetic Jet Cooling at Various Distance | 129 |
| | Sh Mohd Firdaus, Nawal Radiah, Ahmad Faiz, Rohidatun Mahmud, Mohd Zulkifli Abdullah, Muhammad Khalil Abdullah, and Khairul Anuar Abd Wahid | |
| 14.1 | Introduction | 130 |
| 14.2 | Methodology | 130 |

| | | |
|-----------|---|------------|
| 14.3 | Results and Discussions | 131 |
| 14.3.1 | Heater Characteristic | 131 |
| 14.3.2 | Fluid Velocity at Various Distance | 131 |
| 14.3.3 | HTC Value at Various Distance | 132 |
| 14.4 | Conclusions | 134 |
| | References | 135 |
| 15 | Thermoelectric Conversion of Engine Cylinder Heat into Electric Energy | 137 |
| | Mohamad Shukri bin Mohd Zain, Ahmad Kamal bin Ismail, Khairul Shahril bin Shaffee, Khairul Akmal bin Shamsuddin, Tajul Adli bin Abdul Razak, and Sharzali bin Che Mat | |
| 15.1 | Introduction | 138 |
| 15.2 | Literature Review | 138 |
| 15.2.1 | Heat Energy | 138 |
| 15.2.2 | Thermoelectric Generator | 139 |
| 15.3 | Methodology/Experimental Setup | 140 |
| 15.3.1 | Experimental Setup | 140 |
| 15.4 | Result and Discussion | 143 |
| 15.5 | Conclusion | 144 |
| | References | 145 |
| 16 | Ergonomic Analysis of Hand Machine Vibration Based on ISO Standard 5439 (2001) | 147 |
| | Mohd Fahmi bin Mohd Husni, Tajul Adli bin Abdul Razak, Nadya binti Abdullah, Mohd Riduan bin Ibrahim, and Shahril Nizam Mohamed Soid | |
| 16.1 | Introduction | 148 |
| 16.2 | ISO 5349 | 148 |
| 16.3 | Experimental Setup | 149 |
| 16.4 | Data Collection | 150 |
| 16.5 | Result | 151 |
| 16.6 | Discussion | 153 |
| 16.7 | Conclusion | 153 |
| | References | 153 |
| 17 | Non-symmetrical Force–Deflection Behavior of a NiTi Archwire in Orthodontic Leveling Treatment | 155 |
| | Mohd Nizam Ahmad, Abdus Samad Mahmud, Muhammad Hazwan Yusof, and Mohd Suyerdi Omar | |
| 17.1 | Introduction | 156 |
| 17.2 | Literature | 156 |
| 17.3 | Methodology | 157 |
| 17.4 | Result and Discussion | 158 |
| 17.4.1 | Non-Symmetrical Three-Bracket Bending | 158 |
| 17.4.2 | Influence on Clinical Perspectives | 160 |

| | | |
|-----------|---|------------|
| 17.5 | Conclusions | 161 |
| | References | 162 |
| 18 | Evaluation of Bending Deformation Behavior of a NiTi Archwire at Various Orthodontic Bracket Conditions | 163 |
| | Mohd Nizam Ahmad, Abdus Samad Mahmud, and Mohd Suyerdi Omar | |
| 18.1 | Introduction | 164 |
| 18.2 | Literature | 164 |
| 18.3 | Methodology | 165 |
| 18.4 | Result and Discussion | 167 |
| 18.5 | Conclusions | 170 |
| | References | 170 |
| 19 | Application of Dampening Accessories for Reduction of Hand-Arm Vibration Exposure | 173 |
| | Mohd Fahmi bin Mohd Husni, Tajul Adli bin Abdul Razak, Ahmad Khusairy Hakiim bin Abdul Azim, Mohd Nizam Ahmad, and Muhammad Najib Abdul Hamid | |
| 19.1 | Introduction | 174 |
| 19.2 | ISO 5349 | 174 |
| 19.3 | Experimental Setup | 175 |
| 19.4 | Data Collection | 176 |
| 19.5 | Result | 177 |
| 19.6 | Discussion | 178 |
| 19.7 | Conclusion | 181 |
| | References | 181 |
| 20 | The Analysis of Automatic Transmission Stands (U-Shaped Holder) for Repair, Maintenance and Educational Purposes Using a Simulation Method | 183 |
| | Siti Rohana Binti Ahmad, Nur Nadhirah Binti Abdul Razak, and Muhammad Zunnurbin Bin Ghazali | |
| 20.1 | Introduction | 184 |
| 20.2 | Literature | 185 |
| 20.2.1 | Automatic Transmission | 185 |
| 20.2.2 | Maintenance of Automatic Transmission | 186 |
| 20.2.3 | Automatic Transmission Stand/Holder | 187 |
| 20.2.4 | Comparison Between Previous Product and Automatic Transmission Stands (U-shaped Holder) Structure | 188 |
| 20.3 | Methodology | 189 |
| 20.3.1 | Design and Morphological Chart for Automatic Transmission Stands (U-Shaped Holder) Structure | 189 |
| 20.3.2 | Specification | 189 |
| 20.3.3 | Detailed Drawing | 190 |

- 20.3.4 Simulation Method 192
- 20.4 Results and Discussion 192
- 20.5 Conclusions 194
- References 195
- 21 Design Improvement and Fabrication of a Jig for Holding
a Workpiece in a Coordinate Measuring Machine 197**
Siti Shareeda Mohd Nasir, Norasikin Hussin,
Nor Azirah Mohd Fohimi, Dzullijah Ibrahim,
and Rohidatun Mahmud Wahab
 - 21.1 Introduction 198
 - 21.2 Problem Statement 198
 - 21.3 Methodology 199
 - 21.4 Results and Discussion 202
 - 21.5 Conclusion 204
 - References 205
- 22 Design of a Measurement Method for Surface Roughness
Using a Vision System 207**
Mohd Fauzi Abu Hassan, Muhammad Azhan Abdull Lazit,
Mohd Faizal Abu Talib, Zakiah Ahmad,
and Mohd Fadzil Abu Hassan
 - 22.1 Introduction 208
 - 22.2 Literature 208
 - 22.3 Methodology 209
 - 22.3.1 Data Collection and Experimental Setup 209
 - 22.3.2 Preprocessing 210
 - 22.3.3 Features' Extraction 212
 - 22.3.4 Regression 212
 - 22.3.5 Implementation 212
 - 22.4 Result and Discussion 213
 - 22.5 Conclusions 215
 - References 217

Chapter 1

Polypropylene Composites Reinforced by Natural and Recycled Fibers for Bumper Application: Effects of Fiber Loading on the Tensile Properties



Siti Rohana Binti Ahmad, Muhammad Izzuddin Aqil Bin Abdul Aziz, and Muhammad Rasidi Bin Alzahari

Abstract In this research, the effect of fiber loading on the tensile properties and water absorption of polypropylene-filled beverage box fiber was investigated for bumper fascia application. The additional beverage box as filler is to reduce the plastic usage and to overcome the limitation of pure PP. The polypropylene (PP) and beverage box fiber (BB) were mixed at 0, 10, 20, 30, and 40 wt% fiber loadings in the HAAKE PolyLab QC mixer machine at 180 °C and at rotor speeds of 50 rpm for 20 min. Then, the dumbbell shape was obtained from a hot-press machine (GT 7014) before going through the tensile test. The tensile strength and the elongation at break of the PP/BB composite decreased by 26% and 54%, respectively. However, the Young's modulus of the composites increased (13%), as well as the BB fiber loading.

Keywords Beverage box fiber · Polypropylene · Bumper fascia application

1.1 Introduction

Emissions of gases and vehicle fuel economy are two important challenges in the automobile industry today. The manufacturer being obliged to lessen car components is the most effective way to address these problems. The bumper is one of the components that adds to the vehicle's weight (Agarwal et al. 2020). Therefore, the use of composite materials is required without jeopardizing safety (Patel et al. 2018).

Polypropylene (PP) composites are well known as a thermoplastic material which is widely used in automotive application. PP is commonly used as side cladding, bumper fascia instrumental panel and door trims (Shahril et al. 2016; Patel et al. 2018). In crash protection components, the bumper fascia becomes one of the significant

S. R. B. Ahmad (✉) · M. I. A. B. A. Aziz · M. R. B. Alzahari
Mechanical Section, Universiti Kuala Lumpur Malaysian Spanish Institute, Kulim Hi-Tech Park,
09000 Kulim, Kedah, Malaysia
e-mail: sitirohana@unikl.edu.my

parts. It acts as cover for the front car which provides the esthetic value to the image of the specific car's model. Moreover, the bumper fascia is also manufactured to be the part which is able to absorb the energy while collision.

Several classes of PP compounds have been developed, each with its own set of performance characteristics, by combining PP with a variety of different materials to meet the performance requirements of the intended components. Some of the researchers combined the PP with natural fiber such as coconut fiber (Shahril et al. 2016; Sabri et al. 2013a, b; Ayrlmis et al. 2011), kenaf fiber (Hamidon et al. 2019) and blue agave (Langhorst et al. 2018). Furthermore, others blended the PP with glass fiber (Hufenbach et al. 2011) and cellulose-inorganic hybrid (Reale Batista et al. 2020). However, sometimes, the processing method and the filler itself are quite expensive. Therefore, the presence of recycle product-filled PP composites slightly provides more relatively low-cost materials, lightweight and is more environmental-friendly by reducing the plastic content. Furthermore, the PP filled by recycle product is expected to enhance the energy absorption during accidents.

In this paper, the effect of fiber loading on the tensile test of polypropylene/sansevieria leaf and polypropylene/beverage box fiber composites was investigated for bumper fascia application.

1.2 Experimental Investigations

1.2.1 Materials

Materials used in the experiment consist of polypropylene as the matrix phase and beverage box fiber or sansevieria leaf as filler material. Polypropylene Malaysia Sdn. Bhd. provides polypropylene in the form of pellets with the grade S12232 G112. Sansevieria leaf (Fig. 1.1a–c) and beverage box (Fig. 1.1d–f) fibers were prepared using several steps as mentioned in Sects. 1.2.2 and 1.2.3, respectively. Five samples were needed for each different composition before tensile testing. Table 1.1 shows the formulation of the PP/BB and PP/SL fiber samples.

1.2.2 Preparation of Sansevieria Leaf Fiber

Firstly, the leaves were cleaned using water to eliminate any dirt or soil. The leaves were then placed on the tray for the drying process. The leaves were cut into small pieces. It was then continuously chopped in a grinder to get a fine fiber. The fibers were sifted via a sieve to obtain an average size of between 6 and 10 mm for individual SL fibers.

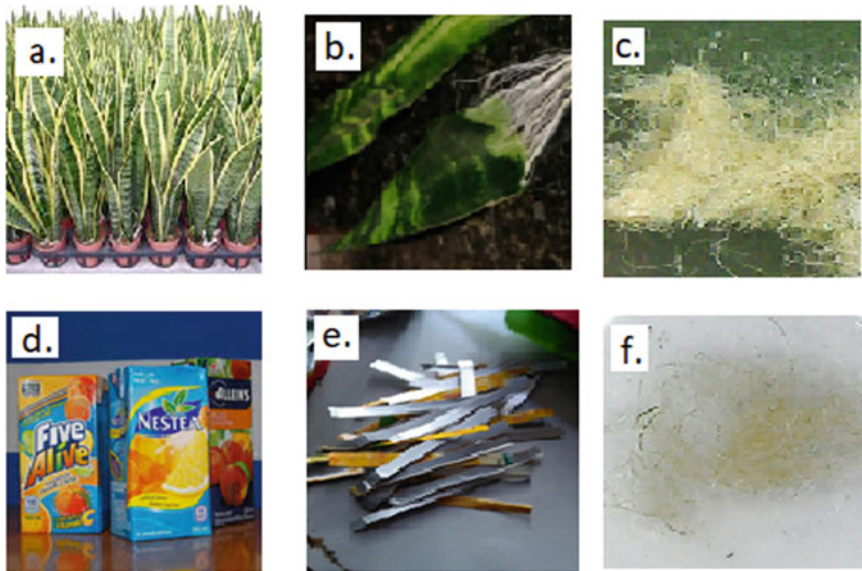


Fig. 1.1 Preparation of sansevieria leaf (a, b, c) and beverage box (d, e, f) fibers

Table 1.1 Material composition of the PP/BB and PP/SL fiber composites at different fiber loadings

| Materials | PP/SL composites (wt%) | PP/BB composites (wt%) |
|-----------------------------|------------------------|------------------------|
| Polypropylene (PP) | 100 | 100 |
| Sansevieria leaf (SL) fiber | 10, 20, 30, 40 | – |
| Beverage box (BB) fiber | – | 10, 20, 30, 40 |

1.2.3 Preparation of Beverage Box Fiber

The shredded liquid packaging box fiber is first washed and dried for the cleaning process. Then, it is cut into small sections of about 100 mm using scissors, and then they are refined by using a paper cutter to obtain finer and shorter fiber. The shred box fiber is strained repetitively to obtain discrete fibers. The fiber was filtered using a sieve in the range of 6–10 mm in size of BB fibers.

1.2.4 Mixing Process

The composites were mixed for 20 min at a temperature of 180 °C and a rotor speed of 50 rpm in a HAAKE PolyLab QC mixer machine. The polypropylene was initially released into the mixer chamber, where it melted entirely after 15 min. The fibers were then discharged into the mixing chamber (beverage box or sansevieria leaf).

Mixing will continue for another 5 min until everything is completely mixed. Each composition's mixing took 20 min to finish. As indicated in Table 1.1, the composites are made with varying fiber loadings of 0, 10, 20, 30, and 40 wt%.

1.2.5 Hot-Press Process

The composite mixtures are then compressed in a hot-press machine (GT 7014) to obtain a 1-mm composite sheet utilizing the ASTM D638 standard for dumbbell shape type IV. Preheating at 180 °C for 7 min, compressing for 3 min at the same temperature and chilling under pressure for 3 min are all part of the hot-press operations. Each composite mixture is compressed twice to get at least five examples of each composition. Therefore, there are a total of 25 samples.

1.2.6 Tensile Test

A dumbbell-shaped (type IV) specimen is required for reinforced composite testing according to ASTM (D638). The tests were conducted at a standard laboratory setting with a temperature of 23 ± 2 °C and a relative humidity of $50 \pm 5\%$. In line with ASTM D618 Procedure A, the plastic must be in this condition for at least 40 h before the test. A Galdabini model Quasar 100 tensile testing machine was used with a crosshead speed of 10 mm/minutes. The specimens were held vertically in the testing machine's grips. The grips were adjusted evenly and securely, with the gauge length remaining at 50 mm to prevent any slippage. Five specimens of each composition are used in the test. The test results for tensile strength, Young's modulus and elongation at break were analyzed.

1.3 Result and Discussion

Table 1.2 indicates the tensile properties for PP/SL and PP/BB fiber composites. Three tensile properties were analyzed: tensile strength, Young's modulus and elongation at break. The tensile strength used here is the ultimate tensile strength.

Figure 1.2 indicates that increasing fiber content reduced the tensile strength of the composites from 27 to 19.8 MPa for PP/BB composites. However, after 20 wt% of fiber in PP/SL composites, the trends dropped to 12 MPa. It happened due to the poor interfacial area between fiber and matrix when fiber content increased (Sabri et al. 2013a, b; Shahril et al. 2016). Moreover, the composites had weak bonding between the hydrophilic fiber and the hydrophobic matrix polymer. As a result, the recycled fibers have a greater tensile strength compared to natural fibers.

Table 1.2 Tensile properties of polypropylene/beverage box and polypropylene/sansevieria leaf fiber composites at different loading

| Composites | Tensile strength (MPa) | Young's modulus (MPa) | Elongation at break (%) |
|---------------|------------------------|-----------------------|-------------------------|
| PP pure:100/0 | 27.49 ± 1.07 | 2182.95 ± 54.71 | 2.82 ± 0.33 |
| PP/SL:100/10 | 21.13 ± 1.97 | 2395.06 ± 168.63 | 1.30 ± 0.33 |
| PP/SL:100/20 | 19.85 ± 1.19 | 2455.61 ± 189.93 | 1.25 ± 0.15 |
| PP/SL:100/30 | 14.09 ± 0.54 | 2654.03 ± 222.03 | 0.99 ± 0.11 |
| PP/SL:100/40 | 12.83 ± 0.34 | 2770.39 ± 262.4 | 0.67 ± 0.09 |
| PP/BB:100/10 | 21.85 ± 1.91 | 2345.06 ± 70.06 | 1.65 ± 0.16 |
| PP/BB:100/20 | 20.38 ± 0.71 | 2430.84 ± 118.31 | 1.56 ± 0.38 |
| PP/BB:100/30 | 20.14 ± 0.68 | 2520.19 ± 101.60 | 1.31 ± 0.26 |
| PP/BB:100/40 | 19.8 ± 0.54 | 2535.22 ± 103.51 | 1.27 ± 0.18 |

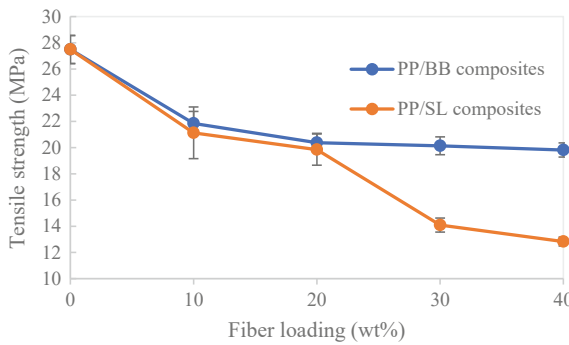


Fig. 1.2 Tensile strength of polypropylene/beverage box and polypropylene/sansevieria leaf fiber composites

The Young’s modulus for polypropylene filled by beverage box and sansevieria leaf fiber is shown in Fig. 1.3. The graph reveals that the pattern of the Young’s Modulus is slightly increased from 0 to 40 wt% fiber loading. The composites are becoming stiffer as the fiber loading is increased (Shahril et al. 2016; Salmah et al. 2014). The maximum and minimum values of the Young’s modulus of the PP/BB fiber composites are 2533 MPa and 2345 MPa, respectively. For PP/SL fiber, the Young’s modulus is between 2395 and 2770 MPa. If the tensile strength trend decreased slightly, the trend of Young’s modulus of PP/SL composites also suddenly changed after 20 wt% of fiber loading. This means that after 20 wt%, the presence of SL fiber makes the composites more brittle compared to BB fiber. The maximum Young’s modulus of PP/SL fiber is about 10% higher than PP/BB fiber.

The pattern of elongation at break is continuously decreased from 0 to 40 wt% filler loading as shown in Fig. 1.4. When the percentage of filler loading was increased, the ductility of the composites greatly decreased (Sabri et al. 2013a, b). This is because the fillers had hardened the composites and reduced their ductility. The value of

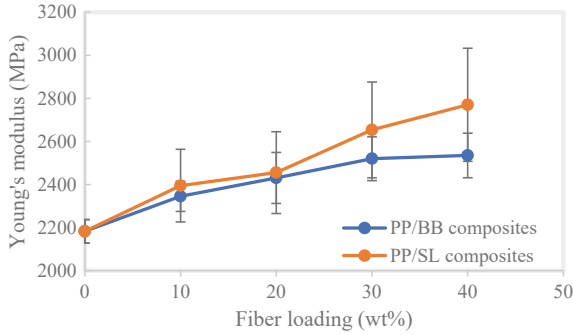


Fig. 1.3 Young's modulus of polypropylene/beverage box polypropylene/sansevieria leaf fiber composites

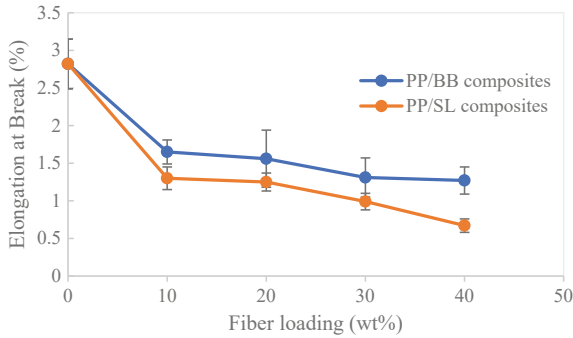


Fig. 1.4 Elongation at break of polypropylene/beverage box and polypropylene/sansevieria leaf fiber composites

elongation value is in the range of 2.82 to 1.27% and 2.82% to 0.67% for PP/BB and PP/SL composites, respectively. The presence of fiber indicates that the composites are easy to fracture.

1.4 Conclusion

In conclusion, the tensile strength decreased by 53% and 28% for PP/SL and PP/BB fiber composites compared to PP composites without fiber, respectively. The addition of fiber reduced the ability of the composite to withstand the force due to irregular size and arrangement of fiber in the composites. However, the Young's modulus of the composites increased about 16% and 27% as well as increasing the beverage box and sansevieria leaf fiber loading, respectively. The presence of SL fiber in PP shows that the composites became stiffer compared to the BB fiber. Similar to the

tensile strength, the elongation at break also decreased. The elongation at break for PP/BB fiber composites is 55%. Besides, the PP/SL fiber composites reveal the 76% of reduction compared to the PP composites without fiber. The composites come to be easy to break due to the addition of fibers. Therefore, the PP/BB and PP/SL fiber composites were successfully prepared, and their tensile stress was investigated. By using these properties, the data can be used for bumper fascia simulation research in the scope of future projects.

References

- Agarwal J, Sahoo S, Mohanty S, Nayak SK (2020) Progress of novel techniques for lightweight automobile applications through innovative eco-friendly composite materials: a review. *J Thermoplast Compos* 33(7):978–1013
- Ayrlimis N, Jarusombuti S, Fueangvivat V et al (2011) Coir fiber reinforced polypropylene composite panel for automotive interior applications. *Fibers Polym.* 12(7):919–926
- Hamidon MH, Sultan MT, Ariffin AH et al (2019) Effects of fibre treatment on mechanical properties of kenaf fibre reinforced composites: a review. *J Mater Sci Technol* 8(3):3327–3337
- Hufebach W, Böhm R, Thieme M et al (2011) Polypropylene/glass fibre 3D-textile reinforced composites for automotive applications. *Mater Des* 32(3):1468–1476
- Langhorst AE, Burkholder J, Long J et al (2018) Blue-agave fiber-reinforced polypropylene composites for automotive applications. *BioResources* 13(1):820–835
- Patel M, Pardhi B, Chopara S, Pal M (2018) Lightweight composite materials for automotive-a review. *Int J Eng Technol.* 5(11):41–47
- Reale Batista MD et al (2020) Hybrid cellulose-inorganic reinforcement polypropylene composites: lightweight materials for automotive applications. *Polym Compos* 41(3):1074–1089
- Sabri M, Mukhtar A, Shahril K et al (2013a) Effect of compatibilizer on mechanical properties and water absorption behaviour of coconut fiber filled polypropylene composite. *Adv Mat Res* 795:313–317
- Sabri M, Hafiz F, Shahril K et al (2013b) Effects of silane coupling agent on mechanical properties and swelling behaviour of coconut fiber filled polypropylene composite. *Adv Mat Res* 626:657–661
- Salmah H, Rohana AS, Kamarudin H (2014) Effect maleic anhydride polypropylene on properties of calcium carbonate filled polypropylene/ethylene propylene diene terpolymer composites. *Key Eng Mat* 594:770–774
- Shahril K, Nizam A, Sabri M et al (2016) Effect of chemical modifier on the properties of polypropylene (PP)/Coconut fiber (CF) in automotive application. *Int J Mater Metall Eng* 9(7):940–943

Chapter 2

A Comparison Analysis on Mechanical Properties Between Laminated Woven Bamboo and Epoxy Composite Versus Laminated Strip Bamboo and Polyester Composite



Kannan Rassiah, Aidy Ali, and Megat Mohamad Hamdan Megat Ahmad

Abstract Natural fibers are presently considered in many fiber-based composites. Unique in every of their prospective, particularly which is said to mechanical reinforcement, are often found in bamboo fibers. Therefore, to investigate the most effective properties of bamboo fibers, this study is targeted on what manner the mechanical characteristic of strip and woven bamboo, produced by convincing thermoset, is influenced. During this study, by applying the hand lay-up technique, woven bamboo with 2 layers and strip bamboo fiber with 1.5–2.5 mm thicknesses compositions were prepared in a 3 mm thick mold, respectively. The outcomes revealed that the properties of the woven bamboo-induced epoxy are improved as compared to the strip bamboo-induced polyester. The mechanical behavior of the woven bamboo composite like tensile modulus, hardness, flexural strength, and tensile strength improved by 11.4–45.1% compared to the strip bamboo composite. However, the opposite trend was found for the flexural modulus (13.5%). These findings propose that woven bamboo-supported epoxy has outstanding mechanical properties and is a practical alternative to classical composites.

Keywords Woven bamboo · Strip bamboo · Laminated composite · Mechanical properties

K. Rassiah (✉)

Department of Mechanical Engineering, Politeknik Melaka (PMK), No 2 Jalan PPM 10, Plaza Pandan Malim, 75250 Melaka, Malaysia
e-mail: kannan@polimelaka.edu.my

A. Ali · M. M. H. M. Ahmad

Department of Mechanical Engineering, Faculty of Engineering, Universiti Pertahanan Nasional Malaysia (UPNM), Kem Sg. Besi, 57000 Kuala Lumpur, Malaysia
e-mail: aidy@upnm.edu.my

M. M. H. M. Ahmad

e-mail: megat@upnm.edu.my

2.1 Introduction

Natural fibers are interesting for scholars due to their benefits to produce over straight reinforcement materials, like biomass productivity, easy and readily to grow, biodegradability, wide availability, abundance, high specific strength, and low cost (Yusuf et al. 2018; Huang et al. 2019, and Mamandhar et al. 2019). As most unoriginal composites are non-recyclable and non-renewable, the pollution problem has become a problem when unoriginal composites are used. Observing on this cause, especially bamboo, many works are dedicated to use this natural filler in composites within the past and up-to-date years.

First, bamboo is an enclosed fiber that covers the complete palm. Second, bamboo culm is one among the foremost significant natural fillers and a possible applicant in latest composites thanks to its high-strength characteristics and modulus properties (Yang et al. 2020 and Ridzqo et al. 2020). The practice of bamboo fiber as a strengthening component for polymer materials is indeed beneficial thanks to several aspects, as an example, abundant, sustainable, good specific strength, and high holocellulose, similarly as environmental-friendly (Sulastiningsih et al. 2018 and Javadian et al. 2020). Through its costs in mechanical properties and naturally approachable renewable resources, the application of bamboo composites is becoming progressively extensive as alternate materials in several sorts of use. Together with the natural fibers, above-mentioned are the composites manufactured from polymeric materials, which are being employed in many areas, such as aeronautics, furnishing, and construction (Zhang et al. 2018, Javadian et al. 2020, and Widiastuti et al. 2018).

As a result, this paper will target the exploration of woven bamboo and epoxy composite vs. strip bamboo and polyester composite with regards to their mechanical properties. Finally, the most effective sort of bamboo as reinforcement is evaluated.

2.2 Materials

The materials employed in this research are epoxy and polyester as the matrix and bamboo fiber in the form of woven fabric and strips.

2.2.1 Epoxy

The resin EpoxAmite100 and the SLOW Hardener 103 revealing a mixed viscosity at 650 CPS, specific volume at 25.2, specific gravity of 1.10 at 23 °C, cure time by 20–24 h, and pot life 55 min were used for the woven bamboo reinforcement.

2.2.2 Polyester

The unsaturated polyester (UP) Reversol P 9509 with a specific gravity of 1.12 at 25 °C, a volumetric shrinkage of 8%, a viscosity of 450–600 CPS, and an acid value with 29–34 mg KOH/g for the solid resin was used for the strip bamboo reinforcement.

2.2.3 Bamboo

Bamboo is obtained within the area of Kampung Bukit Larang, Melaka, Malaysia. Above the third culm from the bottom, the bamboo is cut. Then, the bamboo is cut in between the segments. The fiber between the inner and outer parts of the bamboo is taken and cut to a length and width of 100 mm × 12 mm × 3 mm for the strips while 300 mm × 5 mm × 0.5 mm for the woven fabric, respectively (Rassiah et al. 2018 and Rassiah et al. 2014).

2.3 Experiment

The formulation for epoxy, polyester, and bamboo is separated into two composites as shown in Table 2.1. Besides that, the laminated composite is shown in Fig. 2.1 (Rassiah et al. 2018 and Rassiah et al. 2014).

2.3.1 Mechanical Testing

The two types of laminated woven and strip bamboo fibers are cut and prepared for tensile, flexural, and hardness testing according to ASTM D-3039, ASTM D-790, and ASTM D-2240, respectively (Rassiah et al. 2014, 2018). To investigate the

Table 2.1 Composite of epoxy, polyester, and bamboo

| Sample series | Epoxy/woven bamboo with 2 layers | Polyester/strip bamboo thickness (mm) |
|---------------|----------------------------------|---------------------------------------|
| S1 | Woven 1 | Strip 1.5 |
| S2 | Woven 2 | Strip 1.5 |
| S3 | Woven 3 | Strip 1.5 |
| S4 | Woven 4 | Strip 2.0 |
| S5 | Woven 5 | Strip 2.0 |
| S6 | Woven 6 | Strip 2.0 |
| S7 | Woven 7 | Strip 2.5 |
| S8 | Woven 8 | Strip 2.5 |
| S9 | Woven 9 | Strip 2.5 |



Fig. 2.1 Laminates of woven and strip bamboo

fracture surface, the scanning electron microscope (SEM) observation is done using a Philips XL 30 ESEM operating at 20–30 kV after the entire mechanical testing related to the epoxy, polyester, and bamboo composite was carried out.

2.4 Results and Discussion

Table 2.2 illustrates the individual sample results depicting the laminated woven and strip composites with respect to 1.5–2.5 mm thickness of strip and 2-layer woven bamboo. The table also shows that the strip and woven illustrate the various durability values on the mechanical properties of the composites.

Table 2.2 Mechanical properties of laminated woven and strip bamboo composite

| Bamboo composite | Strip | Woven | Strip | Woven | Strip | Woven | Strip | Woven | Strip | Woven |
|------------------|------------------|-------|-----------------|-------|-------------------|-------|------------------|-------|----------|-------|
| | Tensile strength | | Tensile modulus | | Flexural strength | | Flexural modulus | | Hardness | |
| Series | TS (MPa) | | TM (GPa) | | FS (MPa) | | FM (GPa) | | Shore | |
| S1 | 35.3 | 82.9 | 2.8 | 3.4 | 52.7 | 106.3 | 4.6 | 3.3 | 49.7 | 71 |
| S2 | 34.9 | 65.7 | 2.5 | 3.8 | 54.6 | 118.8 | 4.1 | 3.7 | 49.4 | 70 |
| S3 | 37.5 | 69.5 | 2.7 | 4.3 | 48.9 | 112.5 | 4.2 | 3.9 | 47.0 | 68 |
| S4 | 38.6 | 75.4 | 2.8 | 3.9 | 65.1 | 120.3 | 4.5 | 4.1 | 52.1 | 69 |
| S5 | 40.5 | 81.2 | 3.3 | 3.7 | 62.0 | 118.8 | 4.7 | 4.5 | 50.0 | 64 |
| S6 | 39.9 | 65.6 | 3.1 | 4.0 | 68.7 | 109.4 | 4.1 | 3.9 | 51.5 | 65 |
| S7 | 48.8 | 53.3 | 3.9 | 4.4 | 78.8 | 106.3 | 5.2 | 4.2 | 56.8 | 62 |
| S8 | 47.0 | 69.0 | 3.8 | 4.2 | 85.6 | 107.8 | 5.1 | 4.2 | 57.1 | 66 |
| S9 | 45.9 | 88.9 | 3.7 | 3.9 | 82.1 | 93.8 | 5.2 | 3.2 | 58.7 | 70 |

Fig. 2.2 Chart of tensile strength against bamboo series composite

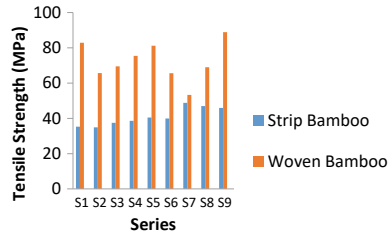
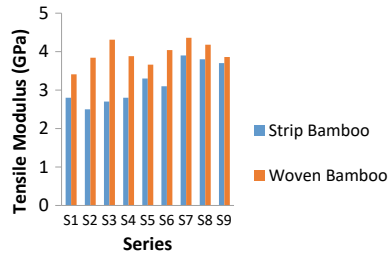


Fig. 2.3 Chart of tensile modulus against bamboo series composite



2.4.1 Tensile Analysis

Table 2.2 shows the specific sample results representing the laminated woven and strip thermoset composites with relation to 1.5–2.5 mm thickness of strip and 2-layer woven bamboo. The table also illustrates that the best durability values, i.e., 88.9 and 48.8 MPa, were found for the woven and strip, respectively. Those values had been the very best when compared with the woven and strip laminated thermoset composites.

In the meantime, the best tensile modulus values, i.e., 4.4 GPa for the woven and 3.9 GPa for the strip configuration, were also observed for the woven layer instead of the strip. Additionally, the strength and therefore the tensile modulus of the all series laminated bamboo and strip composite layers are presented in Figs. 2.2 and 2.3. During this instance, the tensile strength documented for the laminated bamboo woven composite with 2 layers had been within the range of 53.3 and 88.9 MPa, whereas the values for the strip laminate had been 34.9–48.8 MPa, respectively. In addition, Fig. 2.2 illustrates that the strip bamboo layers reduced the tensile strength. In place of such, the very best tensile strength, which was 48.8 MPa, was obtained for the strip laminated composite. Nonetheless, tensile strength was recorded at 53.3 MPa for the woven series, which depicted a change by about 9.2% in tensile strength. In fact, the adding of strip layers of bamboo in the polyester exhibited a decrease within the tensile strength of the composite up to 82.1%, as compared to the woven layers.

The experimental results presented in Fig. 2.3 clearly show a declining trend in tensile modulus because of the layer of bamboo strip. The figure illustrates the tensile modulus with the addition of 1.5–2.5 mm bamboo strip layers. In fact, the best tensile modulus of 4.4 GPa was achieved for the woven bamboo laminated composite

series. On the opposite hand, tensile modulus, which was 2.5 GPa, was logged from the strip series, which pointed toward a change by about 76% tensile modulus. The addition of strip bamboo layers from 1.5 to 2.5 mm reduced the tensile modulus to almost 12.8%. Consequently, both adhesion and compatibility phases between 1.5 and 2.5 mm strip bamboo layers and polyester matrix had been proven to lower the strength of the composites.

2.4.2 Flexural Analysis

Table 2.2 displays the separate sample results of the laminated thermoset with 1.5–2.5 mm strips and woven bamboo layers. The table displays that the best flexural strength, i.e., 120.3 MPa, has been obtained for the woven series. These values are the best as compared to strip layer laminated composites. Meanwhile, the very best flexural modulus values, i.e., 5.2 GPa, have been noted for the strip layers, rather than the woven layers.

Other than that, Figs. 2.4 and 2.5 represent the results achieved for flexural strength and flexural modulus of the laminated woven and strip composite with various bamboo layers. The results specified that the woven bamboo layer laminated composite shows the best flexural strength, while the strip bamboo layer laminated composite demonstrated less flexural strength. Figure 2.4 also obviously shows that the layer laminated woven composite demonstrated more strength and rigidity, as compared to samples with strip layers. Additionally, it can be noted that series 4 influenced the best flexural strength compared to other laminated composites. As confirmed, the flexural properties were reduced because the strip bamboo layers were added. As such, the best flexural strength value, i.e., 120.3 MPa, was observed for the laminated woven series. In the meantime, the best flexural strength, i.e., 85.6 MPa, was achieved for the strip series, which emphasized a change by about 40.5% in flexural strength. Moreover, the adding of strip layers of bamboo reduced the flexural strength of the composite by a maximum amount of 146.0%, compared to the one of the woven layers. Furthermore, the lowest flexural strength for the laminated woven composite was found to be 93.8 MPa, whereas the lowest flexural strength for the laminated strip composite was 48.9 MPa, which is 91.8% of the series 9 laminated woven composite.

Fig. 2.4 Chart of flexural strength against bamboo series composite

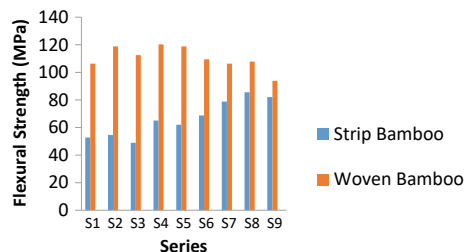
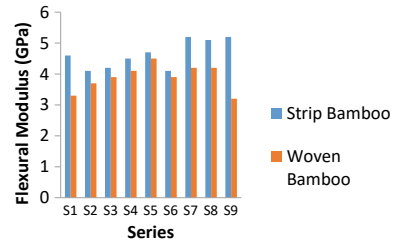


Fig. 2.5 Chart of flexural modulus against bamboo series composite



On the opposite, the outcomes for flexural modulus, as represented in Fig. 2.5, directed that the strip layer displayed the very best stiffness during bending from 4.1 to 5.2 GPa. The chart also portrayed that the flexural modulus for the strip bamboo layer increased. In fact, the best flexural modulus value, i.e., 5.2 GPa, was observed for the strip laminated composite. On the contrary, the lowest value for the flexural modulus, i.e., 3.2 GPa, demonstrated a change by about 62.5% in flexural modulus. Furthermore, increasing the strip thickness from 1.5 to 2.5 mm increased the flexural modulus by around 26.8%. Moreover, the flexural modulus for the laminated strip bamboo composite also enlarged with the increase in bamboo thickness.

2.4.3 Hardness Analysis

The values of surface hardness for the laminated woven and strip bamboo exhibit the fundamental properties of the fabric. Table 2.2 presents the results gained from the specific hardness sample for strip and woven laminated thermoset composites with reference to 1.5–2.5 mm thickness of strip and woven bamboo with two layers. The outcomes portrayed that the best hardness strength, which was 71, has been found at the series of laminated woven bamboo. In fact, the woven bamboo with two layers gave the best value, compared to the strip layer laminated composites.

Figure 2.6 portrays the hardness value for every laminated bamboo composite with relevance to the strip and woven series. It can be seen that the hardness of the woven bamboo enhanced radically when compared to the strip bamboo. The figure also presents that the best hardness value was 71.0 for the layer 2 series laminated woven bamboo composite, whereas the strip bamboo laminated series showed the lowest value of 47.0. Aside from that, the adding of two layers of woven bamboo improved the hardness of the composite up to 51.1%, in comparison with the strip layers. Therefore, the increment of two bamboo layers from series 1 to series 9 caused a rise by 31.9% for hardness.

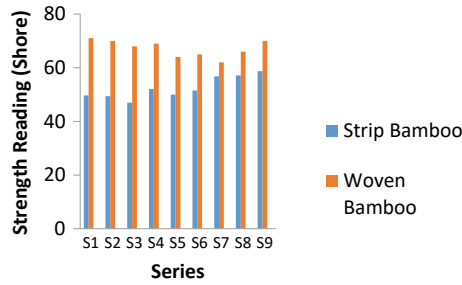


Fig. 2.6 Chart of strength reading against bamboo series composite

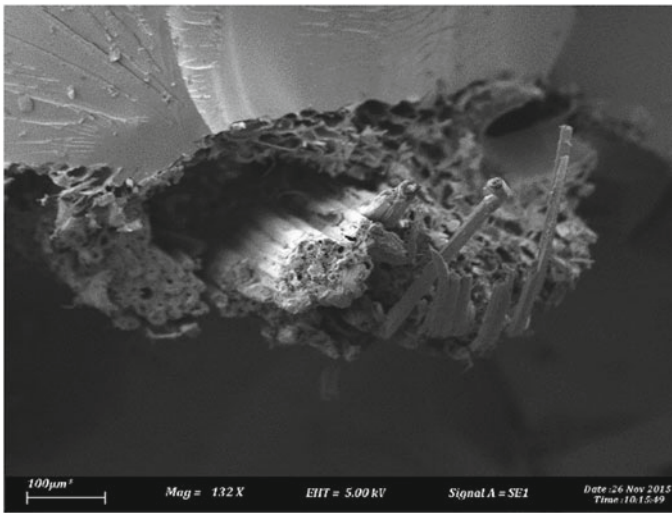


Fig. 2.7 Failure modes of laminated woven bamboo

2.4.4 Scanning Electron Microscope

The examination toward surface morphology of the fractured samples was carried out by using a scanning electron microscope after the tensile testing. The morphology is used to recognize the bonds between the thermoset and bamboo fiber structures, in addition to modifications on the material after being tested with a strong tensile strength. Figures 2.7 and 2.8 show the change from other laminated composite due to the bamboo structure. From the images shown, interfacial bond strength, existence of voids, matrix as well as fiber are critically exaggerated.



Fig. 2.8 Failure modes of laminated strip bamboo

2.5 Conclusion

A number of the mechanical properties of the epoxy/woven bamboo and therefore the polyester/strip bamboo fiber composites were investigated. The hardness, tensile, and flexural properties of woven bamboo reinforced composites are perceived where they are enhanced by the combination of epoxy presenting a positive composite effect. At the optimum stacking of both woven bamboos, the strength appeared to be increasing. Thus, woven bamboo composites caused improved mechanical properties. The investigation also shows that increasing the strip bamboo thickness within the polyester thermoset increases the related mechanical attributes of the laminated composites.

Acknowledgements The authors acknowledge the Research Grant UPNM/2020/GPJT/TK/2 and Universiti Pertahanan Nasional Malaysia (UPNM) for supporting the research work, as well as The Mechanical Engineering Department at Politeknik Melaka (PMK) and the coordinator of composite engineering laboratory (UTeM) for the permission to use all equipment obtainable.

References

- Huang Y, Ji Y, Yu W (2019) Development of bamboo scrimber: a literature review. *J Wood Sci* 65:25
- Javadian A, Smith IFC, Hebel DE (2020) Application of sustainable bamboo-based composite reinforcement in structural-concrete beams: design and evaluation. *Materials* 13(3). <https://doi.org/10.3390/ma13030696>

- Mamandhar R, Kim JH, Kim JT (2019) Environmental, social and economic sustainability of bamboo and bamboo-based construction materials in buildings. *J Asian Arch Build Eng* 18:4959
- Rassiah K, Ahmad MMHM, Ali A (2014) Mechanical properties of laminated bamboo strips from *Gigantochloa scortechinii*/polyester composites. *Mater Des* 57:551–559
- Rassiah K, Megat Ahmad MMH, Ali A (2018) Mechanical properties of layered laminated woven bamboo *Gigantochloa Scortechinii*/epoxy composites. *J Polym Environ* 26:1328–1342
- Ridzqo IF, Susanto D, Panjaitan TH, Putra N (2020) Sustainable material: development experiment of bamboo composite through biologically binding mechanism. *IOP Conf Ser Mater Sci Eng* 713:012010
- Sulastiningsih IM, Damayanti R, Supriadi A, Supriadi A (2018) Some Properties of Bamboo Composite Lumber Made of *Gigantochloa Pseudoarundinacea*. *J Agric Sci Technol* 8:122–130
- Widiastuti I, Solikhun M, Cahyo DN, Pratiwi YR, Juwanton H (2018) Treatment of bamboo fibres in improving mechanical performance of polymer composites—a review. *AIP Conf Proc* 030046(2013):1–7. <https://doi.org/10.1063/1.5042966>
- Yang F, Long H, Xie B et al (2020) Mechanical and biodegradation properties of bamboo fiber-reinforced starch/polypropylene biodegradable composites. *J Appl Polym Sci* 137:48694
- Yusuf S, Syamani FA, Fatriasari W (2018) Review on bamboo utilization as biocomposites, pulp and bioenergy. *E Environ Sci* 141:012039
- Zhang K, Wang F, Liang W, Wang Z, Duan Z, Yang B (2018) Thermal and mechanical properties of bamboo fiber reinforced epoxy composites. *Polymers* 10(6):608

Chapter 3

Investigation of the Effect of Surface Roughness and Dimensional Accuracy on the Layer Thickness of PLA Parts Produced by the FDM Process



Maria F. Jasim, Abdullah F. Huayier, and Tahseen F. Abbas

Abstract Fused deposition modeling (FDM) machines are becoming increasingly popular for producing functioning components. One of the drawbacks of used filament fabrication 3D printers is that the printed part's surface roughness is excessively rough due to the layer-by-layer deposition of the material. Therefore, it is necessary to verify that the components have a high-quality surface finish and precise dimensions. The purpose of this study is to identify the optimal layer thickness that may be used to manufacture components with both high surface quality and accuracy of dimension. Six different layer thicknesses of FDM were used to manufacture the test parts (0.1, 0.15, 0.2, 0.25, 0.3, and 0.35 mm). The optimum layer thickness levels for dimensional accuracy were discovered to be the same as that of surface roughness. The results of the experiment were confirmed by fabricating parts with the optimal layer thickness that had been determined. Reduced printing layers increased the specimens' surface smoothness. The smaller layer thickness was shown to be required for greater overall dimensional accuracy, according to the findings.

Keywords Fused deposition modeling (FDM) · Polylactide (PLA) · Layer thickness · Surface roughness · Dimensional accuracy

3.1 Introduction

In a manufacturing process known as additive manufacturing (AM), successive layers are bonded together to form the desired structure. Because of recent developments in process control, additive manufacturing is now a matching technology for the rapid,

M. F. Jasim (✉) · A. F. Huayier · T. F. Abbas
Production Engineering and Metallurgy Department, University of Technology, Baghdad, Iraq
e-mail: pme.19.10@grad.uotechnology.edu.iq

A. F. Huayier
e-mail: 70041@uotechnology.edu.iq

T. F. Abbas
e-mail: Tahseen.f.abbas@uotechnology.edu.iq



Fig. 3.1 Process flow of FDM

efficient, and cost-effective production of custom and complex parts, particularly in small quantities (Bakır et al. 2021). FDM is one of the most common AM methods for the manufacturing of plastic components because of the low equipment cost and easy operation (Boparai et al. 2016; Mohamed et al. 2015). Many factors influence the product quality and material quality, and it can be difficult to understand how these aspects interact (Casavola et al. 2016). A wide range of printing variables, including the building orientation and thickness of the layer, raster angle, width of the raster, air gap, as well as the density of infill and infill shape, and feed rate, has a significant impact on the quality and performance of FDM-produced components (Kristiawan et al. 2021). FDM's primary goal is to build three-dimensional objects using extruded thermoplastic filament, such as ABS or PLA, with temperatures of melting low enough to be used in non-specialist conditions (Chacón et al. 2017).

As shown in Fig. 3.1, a CAD 3D model of the finished product is exported in STL format before being sent to a 3D printer for fabrication using the FDM technology. An Ultimaker "Cura" slicer software, for example, prepares CAD 3D models into STL format for 3D printing and generates G-code with all the printing settings (Pandžić et al. 2021).

Layers of materials are fused in a pattern to form objects in the FDM. The filament is heated in the printer's nozzle until it melts, then extruded in a pattern over or adjacent to previous extrusions to build objects layer-by-layer (Milde et al. 2021). The nozzle should be heated to the proper temperature before use. The extrusion head feeds the filament into the nozzle where it is melted (Doshi et al. 2022). It is possible to move the extrusion head in direction of the X, Y, and Z-axes. The melted material is extruded from the extrusion head in very fine strands. The material is placed layer-by-layer on the platform, which cools and solidifies as it proceeds (Dave and Patel 2021). In certain machines, the build platform (or extrusion head) moves down, and a new layer is deposited when one layer is completed. This procedure is repeated until the component is complete (Dev and Srivastava 2021) as shown in Fig. 3.2.

The current study focuses on layer thickness on the physical properties (surface roughness and dimensional accuracy) of samples made from PLA with different layer thicknesses, which are (0.1, 0.15, 0.2, 0.25, 0.3, and 0.35 mm).

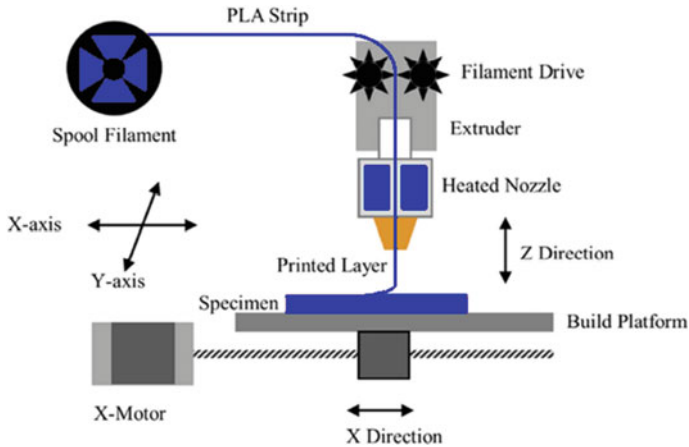


Fig. 3.2 Schematic diagram of FDM printing machine

3.2 Related Research

Many researchers have sought to enhance product quality by optimizing process parameters to achieve the best results for the physical external surface roughness and dimensional accuracy (Vaes and Van Puyvelde 2021).

For this purpose, many advanced statistical methods are used by DOE to improve the parameters of the process to achieve the best possible output by designing variable values and testing their impact on the process outputs to maximize or minimize the values of the process outputs according to the nature of the outputs (Hikmat et al. 2021).

3.2.1 Surface Roughness

Hafsa et al. (2013) used 3D printers with various layer thicknesses to test the dimensional accuracy and surface roughness of ABS and PLA precision casting models. The ABS model developed by lowering the layer thickness has a superior surface roughness than other models, according to the results. It has also been shown that PLA models produce a larger cast model, and the surface roughness improves as the layer thickness increases, making them ideal for casting.

Akande (2015) 3D Touch FDM machine with polylactide (PLA) material was used to create cuboid-shaped specimens and analyzed the impact of the thickness of the layer, fill density, and printing speed on the roughness of the surface. It was found that reducing each parameter to the lowest possible value resulted in the best surface finishing.

Kovan et al. (2017) noted that surface roughness affects the strength of adhesive bond connections between printed objects. It has been shown that the layers' thickness and the printing direction in printed parts have a substantial impact on the adhesion strength. In the case of low layer thicknesses, the layer created on the side edge has the biggest strength of adhesive, whereas in the case of the high layer thickness, the horizontal layer has the biggest strength of adhesive.

Pérez et al. (2018) utilized a cylindrical-shaped PLA specimen instead of a cuboid-shaped PLA part for this experiment. The layer thickness, printing speed, the extrusion temperature, and the shell thickness were some of the variables studied in this study. In this experiment, the low layer thickness was chosen because it would give the best surface finish. Extrusion temperature and print speed had little effect.

Ramli et al. (2018) investigated the surface roughness and dimensional accuracy of open-source 3D printers, Mendel Max and Kossel Mini, were studied. PLA and ABS materials were used to create spherical, cubical, and cylindrical objects on both machines, with varying layer thicknesses and filling ratios. Because of this, it has been discovered that PLA has a greater surface quality than ABS when comparing the models produced by the two machines. When the infill ratio was 20% and the layer thickness was 0.178 mm, surface qualities were found to be better.

Altan et al. (2018) researched the impact of printing parameters on the surface roughness and tensile strength. PLA samples are produced at various layer thicknesses, printing temperatures, and printing speeds. Layer thickness and print speed have been determined to be the most important parameters in determining the surface roughness of a product. The smaller the layer thickness, the lower the surface roughness.

3.2.2 Dimensional Accuracy

Nancharaiah et al. (2010) investigated the impact of the layer thickness, the raster width, the raster orientation, and the air gap on the dimensional accuracy. ANOVA was used to find important factors and their connections to assure dimensional accuracy. The Prodigy plus FDM machine was used to make ABS components for a variety of parameter combinations. In their experiment, ANOVA found that the raster width and the relationship between the raster width and the raster orientation were important determinants for the dimensional accuracy. Except for that, they found a link between layer thickness and dimensional accuracy. Based on the S/N ratio, they recommend that the layer thickness should be reduced to improve the dimensional accuracy.

Nidagundi et al. (2015) used a Julia 3D printing machine to study how the layer thickness, the raster orientation, and building orientation affect the precision of the ABS pieces. It was determined that an orthogonal array (L9) and a high S/N ratio provided the optimum parameter values. Low layer thickness, 0° orientation, and building orientation were shown to be the optimum characteristics for reducing dimensional deviations, with the most critical variable being the layer thickness.

Wu (2018) recommended that adopting a layer thickness of a minimum would result in high dimensional accuracy.

Alafaghani and Qattawi (2018) analyzed the dimensional correctness and tensile strength of PLA components. Minimum slice height and extrusion temperature values, as well as a hexagonal infill pattern with a minimum infill density, are all necessary for good dimensional accuracy, according to this research.

Mohamed et al. (2018) determined that FDM is capable of producing precise components after measuring the consistency of dimensions of parts produced by FDM using gauge repeatability and reproducibility.

Beniak et al. (2019) conducted investigations on the relevant layer thickness and extrusion temperature for dimensional accuracy. The layer thickness and extrusion temperature were compared and found to have a significant impact on the dimensional accuracy, and a low extrusion temperature was once again recommended.

3.3 Experimental Details

This section explains in detail the many factors, such as the material, selected process parameters, specimen manufacturing, and testing conditions used for printed parts testing.

3.3.1 Specimen Design and Material

The same 3D printer produced all specimens using the same PLA filament. The diameter of the used filament is 1.75 mm. Due to the potential for jamming a printer nozzle, PLA was chosen as a filament material since there is no need for the hotbed to print. Because of this, high-quality prototypes and functional components take less energy and temperature to process. The SolidWorks software is used to generate a 3D design model. After finishing the design with all dimensions (50 mm × 30 mm × 20 mm) in a standard form, the file was converted into STL format, which was then exported to the Cura software for establishing the required printing parameters. Cura's slicer provides 13 different infill patterns for the user to choose from. For this test, on all specimens, the "grid" pattern was used with six different thicknesses: 0.1, 0.15, 0.2, 0.25, 0.3, and 0.35 mm. Figure 3.3 illustrates the specimen design and infill pattern of the printed parts.

Samples created in SolidWorks and Cura need to be printed on a (FDM) 3D printer (Ender 5). The methodology for preparing the 3D printing specimens is illustrated in Fig. 3.4.

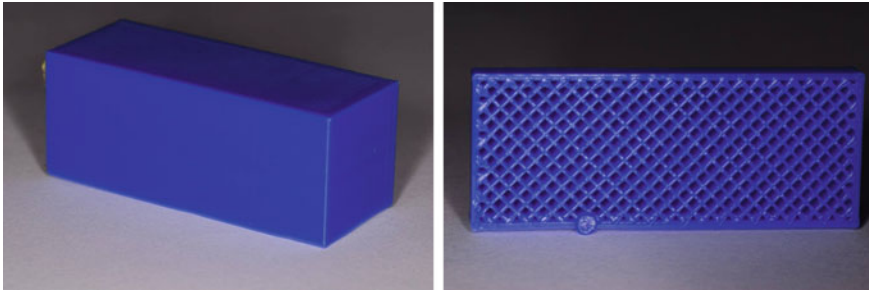


Fig. 3.3 Specimen design and grid pattern of the printed part

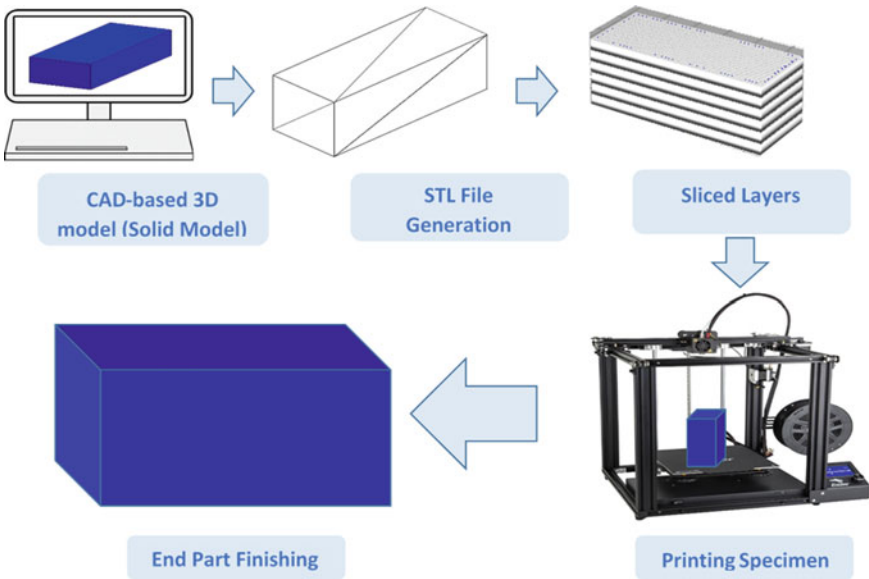


Fig. 3.4 Preparing 3D printing specimen

3.3.2 Process Parameter

Research shows that the thickness of the layers affects both surface polish and dimensional accuracy; they are thus considered in these experiments at six levels.

The layer thickness, or layer height, the height of the deposited layers is measured along the Z-axis, which is often the vertical axis of a FDM machine. In the majority of situations, it is smaller than the extruder nozzle’s diameter, and it changes based on the nozzle’s diameter. Figure 3.5 illustrates the layer thickness.

It is necessary to meet the parameters listed below. Table 3.1 shows the parameters used in the Cura 3D printing software to generate the G-code for 3D printing.

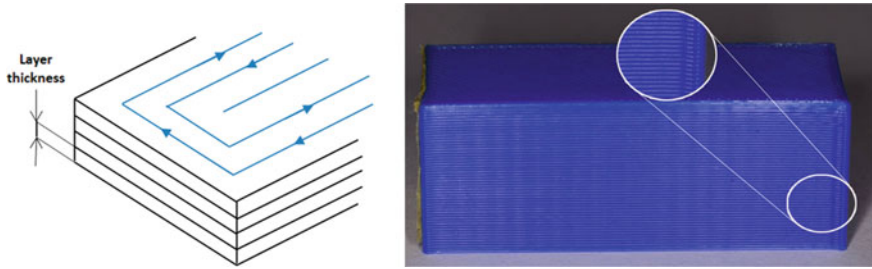


Fig. 3.5 Layer thickness

Table 3.1 Fixing parameters

| Parameter | Value | Unit |
|----------------------|-------|--------|
| Printing speed | 60 | mm/sec |
| Filling density | 50 | % |
| Bed temperature | 60 | °C |
| Printing temperature | 200 | °C |
| Shell wall thickness | 0.8 | mm |
| Orientation angle | 0 | ° |

3.4 Testing

3.4.1 Surface Roughness Test

The surface roughness test was carried out with the profilometer device (surface quality), and a surface analyzer (a sharp diamond stylus) is included, with a maximum distance that may be moved being 11 mm. The surface roughness (R_a) of printed block samples was measured at the side of the 3D printed block to investigate the effect of the thickness of the layer.

The surface is characterized by the profile of the surface imperfections and recesses, which are created on a scale. At the same time, each specimen was tested four times in different places on the same specimen, with the average value obtained from the four tests. Figure 3.6 shows the machine used in this test.

3.4.2 Dimensional Accuracy Test

The dimensions were measured with a digital Vernier caliper with the smallest count of 0.01 mm, which measured the length, width, and thickness of the part. Equation (3.1) is used to determine the accuracy of the length (L). In the same way, the width (W) and thickness (T) of the object are also determined.

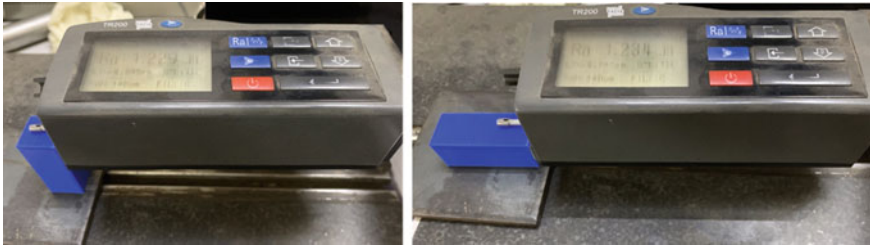


Fig. 3.6 Roughness test device

$$L = \frac{\text{length of CAD model} - \text{length of fabricated specimen}}{\text{length of CAD model}} \tag{3.1}$$

The deviation is defined as the difference between the nominal measurements and the dimensions that were measured. All of the molded specimens were measured and compared to the CAD model to see how the layer thickness affected the dimensional accuracy.

3.5 Results and Discussion

Table 3.2 shows that the thickness of the layer is the most important factor in determining the surface roughness and dimensional accuracy. Surface roughness ranges from 1.779 to 3.979 μm for specimens. The dimensional accuracy of manufactured specimens is determined to be in the range of 50.01–50.08 mm in the length direction, 30.02–30.08 mm in the width direction, and 20.01–20.26 mm in the thickness direction.

Our method of calculating each sample’s single-width value included averaging three measurements of width (W_1 , W_2 , and W_3), as shown in Table 3.2. The overall thickness measures of OT_1 , OT_2 , and OT_3 were all measured in the same way. The results of these measures are presented in Table 3.2. These measurements were

Table 3.2 Result of surface roughness for different levels of layer thickness

| Levels | Layer thickness (mm) | Surface roughness (μm) | Overall length | Overall width | Thickness |
|--------|----------------------|-------------------------------------|----------------|---------------|-----------|
| 1 | 0.1 | 1.779 | 50.01 | 30.02 | 20.01 |
| 2 | 0.15 | 2.798 | 50.02 | 30.03 | 20.02 |
| 3 | 0.2 | 3.308 | 50.04 | 30.02 | 20.07 |
| 4 | 0.25 | 3.574 | 50.08 | 30.04 | 20.10 |
| 5 | 0.3 | 3.944 | 50.96 | 30.05 | 20.14 |
| 6 | 0.35 | 3.979 | 50.98 | 30.06 | 20.26 |

compared to the design parameters, i.e., $OL = 50$ mm for overall length, $OW = 30$ mm for overall width, and $T = 20$ mm for thickness.

The CAD model was used to compare the dimensions of the produced specimens. It is important to note right away that the majority of the errors have positive values, which suggests that the printer prefers to produce larger parts than intended. The results indicated that to achieve higher dimensional accuracy, the thickness of the layers was reduced. Furthermore, as compared to the CAD model, the present FDM manufacturing technique often produces parts with bigger dimensions.

It has been shown that the accuracy of the dimension of FDM components is dependent on the dimensions (i.e., length, width, and thickness). In FDM components, layer thicknesses have been discovered to be important influencers of the accuracy of dimension in the length direction. Accuracy increases first with increasing layer thickness and then decreases with decreasing layer thickness. This is the same in width and thickness as shown in Fig. 3.7.

Figure 3.8 depicts the surface effect plots for the surface roughness. It is observed that the layer thickness influences the surface roughness of the parts. The surface roughness is essentially unaffected by a layer thickness of 0.1 mm. In addition, the lowest surface roughness value is at a layer thickness of 0.1 mm. The highest surface roughness values are at both 0.35 mm and 0.3 mm layer thicknesses. The higher the value of layer thickness, the higher the value of surface roughness. This is due to the smaller layer thickness; a smooth surface of the block was developed.

Because of the stair-stepping effect caused by stacking layers, the produced FDM part differs geometrically from the original CAD model. While using a FDM nozzle to deposit layers of material, the layer thickness is the measure of the thickness of each layer of material that is deposited. The forming accuracy of the printed specimen reduces as the layer thickness increases, the surface roughness increases, and the outer profile becomes more susceptible to the step effect. However, a reduction in the layer thickness improves the printed sample's accuracy, smoothness, printing time, and efficiency in a reverse way. For FDM parts made of PLA, the layer thickness levels

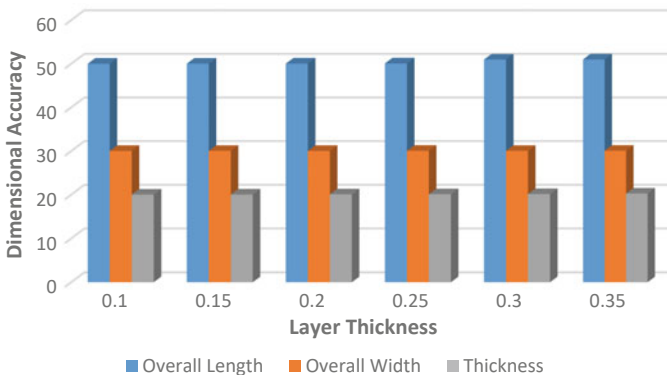


Fig. 3.7 Dimensional accuracy versus layer thickness

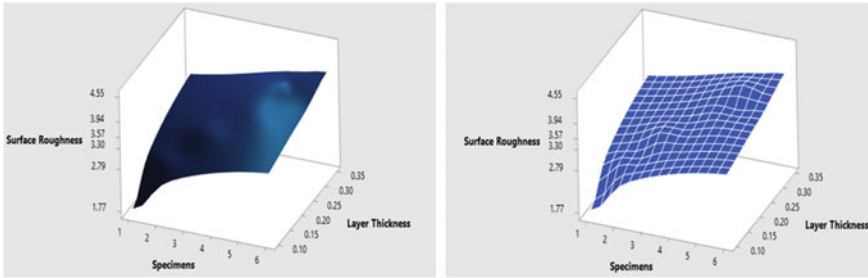


Fig. 3.8 Surface roughness vs. layer thickness

in the range of 0.1–0.2 mm are more likely to be optimum for surface roughness and accuracy of dimensions than other levels.

3.6 Conclusion

The effect of the layer thickness of the 3D printed block was studied, and it showed that variations of layer thickness affected the surface roughness and dimensional accuracy. It was also found that the range of roughness for all 3D printed materials in the study is between 1.779 and 3.979 μm . The desired function was then utilized to establish the optimal layer thickness for the reduction of both inaccuracy dimension and roughness of the surface in the final product. The findings of the experiments tend to indicate that it is feasible to make components with the best possible surface roughness and dimensional accuracy at the same time. A CAD model was used to make sure that the specimens had the same dimensions as the CAD model. To achieve improved dimensional accuracy in FDM products, we discovered that a smaller layer thickness is important. Reduced layer thickness means longer production times and a higher total cost because of the longer time it takes to print each layer. Based on test results and printing time, we have concluded that it was determined that layer thicknesses of 0.1 and 0.2 mm were the most optimal for the roughness of the surface and accuracy of the dimension of 3D printed PLA specimens.

References

- Alafaghani A, Qattawi A (2018) Investigating the effect of fused deposition modeling processing parameters using Taguchi design of experiment method. *J Manuf Process* 36:164–174
- Altan M, Eryildiz M, Gumus B, Kahraman Y (2018) Effects of process parameters on the quality of PLA products fabricated by fused deposition modeling (FDM): surface roughness and tensile strength. *Mater Test* 60(5):471–477

- Bakır AA, Atik R, Özeriç S (2021) Effect of fused deposition modeling process parameters on the mechanical properties of recycled polyethylene terephthalate parts. *J Appl Polym Sci* 138(3):49709
- Beniak J, Križan P, Šooš Ľ, Matúš M (2019) Research on shape and dimensional accuracy of FDM produced parts. *IOP Conf Ser: Mater Sci Eng* 501:12030
- Boparai KS, Singh R, Singh H (2016) Development of rapid tooling using fused deposition modeling: a review. *Rapid Prototyp J* 22:281–299
- Casavola C, Cazzato A, Moramarco V, Pappalettere C (2016) Orthotropic mechanical properties of fused deposition modelling parts described by classical laminate theory. *Mater Des* 90:453–458
- Chacón JM, Caminero MA, García-Plaza E, Núñez PJ (2017) Additive manufacturing of PLA structures using fused deposition modelling: effect of process parameters on mechanical properties and their optimal selection. *Mater Des* 124:143–157
- Dave HK, Patel ST (2021) Introduction to fused deposition modeling based 3D printing process. In: *Fused deposition modeling based 3D printing*, pp 1–21
- Dev S, Srivastava R (2021) Optimization of fused deposition modeling (FDM) process parameters for flexural strength. *Mater Today: Proc* 44:3012–3016
- Doshi M, Mahale A, Kumar Singh S, Deshmukh S (2022) Printing parameters and materials affecting mechanical properties of FDM-3D printed parts: perspective and prospects. *Mater Today: Proc* 50:2269–2275
- Hafsa M, Ibrahim M, Wahab MS, Zahid M (2013) Evaluation of FDM pattern with ABS and PLA material. *Appl Mech Mater* 465–466:55–59
- Hikmat M, Rostam S, Ahmed YM (2021) Investigation of tensile property-based Taguchi method of PLA parts fabricated by FDM 3D printing technology. *Results Eng* 11:100264
- Kovan V, Altan G, Topal ES (2017) Effect of layer thickness and print orientation on strength of 3D printed and adhesively bonded single lap joints. *J Mech Sci Technol* 31(5):2197–2201
- Kristiawan RB, Imaduddin F, Ariawan D, Arifin Z (2021) A review on the fused deposition modeling (FDM) 3D printing: filament processing, materials, and printing parameters. *Open Eng* 11(1):639–649
- Milde J, Jurina F, Peterka J, Dobrovský P, Hrbál J, Martinovič J (2021) Influence of part orientation on the surface roughness in the process of fused deposition modeling. *Key Eng Mater* 896:29–37
- Mohamed OA, Masood SH, Bhowmik JL (2015) Optimization of fused deposition modeling process parameters: a review of current research and future prospects. *Adv Manuf* 3(1):42–53
- Mohamed OA, Masood SH, Bhowmik JL (2018) Investigation of dimensional variation in parts manufactured by fused deposition modeling using gauge repeatability and reproducibility. *IOP Conf Ser: Mater Sci Eng* 310:12090
- Nancharaiah T, Raju DR, Raju VR (2010) An experimental investigation on surface quality and dimensional accuracy of FDM components
- Nidagundi VB, Keshavamurthy R, Prakash CPS (2015) Studies on parametric optimization for fused deposition modelling process. *Mater Today: Proc* 2:1691–1699
- Pandžić A, Hodžić D, Kadrić E (2021) Experimental investigation on influence of infill density on tensile mechanical properties of different FDM 3D printed materials. *Parameters* 3:4
- Pérez M, Medina-Sánchez G, García-Collado A, Gupta M, Carou D (2018) Surface quality enhancement of fused deposition modeling (FDM) printed samples based on the selection of critical printing parameters. *Materials* 11:8
- Ramli F, Nazan M, Alkahari MR, Sudin MN, Mat S, Khalil SN (2018) Dimensional accuracy and surface roughness of part features manufactured by open source 3D printer. *J Eng Appl Sci* 13
- Akande SO (2015) Dimensional accuracy and surface finish optimization of fused deposition modelling parts using desirability function analysis. *Int J Eng Res Appl* 4(4):196–202
- Vaes D, Van Puyvelde P (2021) Semi-crystalline feedstock for filament-based 3D printing of polymers. *Prog Polym Sci* 118:101411
- Wu J (2018) Study on optimization of 3D printing parameters. *IOP Conf Ser: Mater Sci Eng* 392:62050

Chapter 4

Low Pressure, Solvent-Assisted Thermal Bonding of PMMA–PMMA Substrates for Microfluidics Device Fabrication



Farah A. Mat Nawang, Azmi M. Yusof, Sheikh F. S. M. Nasir, Rizal M. Noor, and Intan S. Zaine

Abstract Sealing of microfluidics devices during microfabrication is crucial specially to ensure that the microchannel is watertight and leak-free. This work evaluates direct thermal bonding of PMMA–PMMA material by treating the surface area with organic solvents. Ethanol and isopropanol were used to cover the bonded area before curing the PMMA samples in an oven, and a low clamping pressure was applied to the sample by using an office paper clip. Three curing parameter settings were evaluated at 95 °C for 15 min, 90 °C for 20 min, and 85 °C for 15 min. Results show that 100% bonded area was obtained when the sample was treated with ethanol and cured at a temperature of 85 °C for 15 min. Bond strength of 13 MPa was obtained using this parameter setting. To demonstrate the application in microfluidic device fabrication, two PMMA substrates were micromachined to form a serpentine microchannel using 0.2 mm end mill bit through CNC machining. The PMMA substrates were successfully bonded after treating the surface with ethanol and cured in an oven at a temperature of 85 °C for 15 min. Excellent microchannel sealing was achieved with leak proof and capable to deliver fluid at 0.3 ml/min.

Keywords Microfluidics · Thermal bonding · Solvent bonding

F. A. M. Nawang · A. M. Yusof (✉) · S. F. S. M. Nasir · R. M. Noor
Center for Mechanical Engineering Studies, Universiti Teknologi MARA, Cawangan Pulau Pinang, Kampus Permatang Pauh, 135000 Permatang Pauh, Pulau Pinang, Malaysia
e-mail: azmi349@uitm.edu.my

F. A. M. Nawang
e-mail: 2021330403@isiswa.uitm.edu.my

S. F. S. M. Nasir
e-mail: sh.firdaus@uitm.edu.my

I. S. Zaine
Department of Applied Sciences, Universiti Teknologi MARA, Cawangan Pulau Pinang, Kampus Permatang Pauh, 135000 Permatang Pauh, Pulau Pinang, Malaysia
e-mail: intan.zaine@uitm.edu.my

4.1 Introduction

Polymethyl methacrylate (PMMA), generally known as acrylic, is a transparent thermoplastic polymer that has been extensively employed for microfluidics device fabrication, mostly because it is optically transparent and offers low-cost fabrication processing steps (Faghieh and Sharp 2019). One of the challenges in microfluidics devices fabrication using PMMA has been to form a good sealing with a leak-free device. Depending on the type of paired material with PMMA, a direct bonding can be achieved through adhesive bonding (Song and Park 2017), thermal fusion, ultrasonic welding, and solvent bonding (Trinh et al. 2020).

Untreated PMMA surfaces are difficult to bond below their glass transition temperature. Generally, homogenous PMMA–PMMA thermal bonding requires surface modification with a combination of microwave (Toossi et al. 2015), UV (Trinh et al. 2020), plasma, organic solvents, or high clamping pressure (Chiang et al. 2021). A study from Giri and Tsao (2022) shows that solvent-assisted thermal bonding produces moderate to high bonding strength compared to thermal bonding without solvent which results in low to moderate bonding strength. There are a few previous studies that used solvent to assist the thermal bonding of PMMA. Ethanol (Wan et al., 2017), isopropanol (Faghieh and Sharp 2019), acetic acid (Trinh et al. 2021), water (Tsao et al. n.d.), and acetone (Wan et al. 2017; Faghieh and Sharp 2019) are the solvent that were used in previous studies.

This work evaluates the surface treatment of PMMA with isopropanol and ethanol to assist thermal bonding of two PMMAs after considering high optical transmissivity after bonding result. A low clamping pressure using paper clips was applied during thermal bonding. Results show that a good hermetic bonding with watertight sealing of microfluidics device can be achieved when the PMMA surface was treated with ethanol during thermal bonding.

4.2 Materials and Method

4.2.1 *Sample Preparation*

The PMMA samples were prepared according to ASTM D3163 as shown in Fig. 4.1a. A transparent PMMA sheet of 3 mm thickness was laser cut into 100 mm × 25 mm sized as shown in Fig. 4.1c. The PMMA samples were then sonically cleaned in isopropanol bath for 10 min followed by DI water bath for 10 min to remove foreign matter and debris. The samples were allowed to dry in the oven at 50 °C for 60 min (annealing). The annealing procedure was performed before thermal bonding in order to minimize the tendency of the sample to crack due to stress concentration on the sample during the laser-cutting process (Faghieh and Sharp 2019).

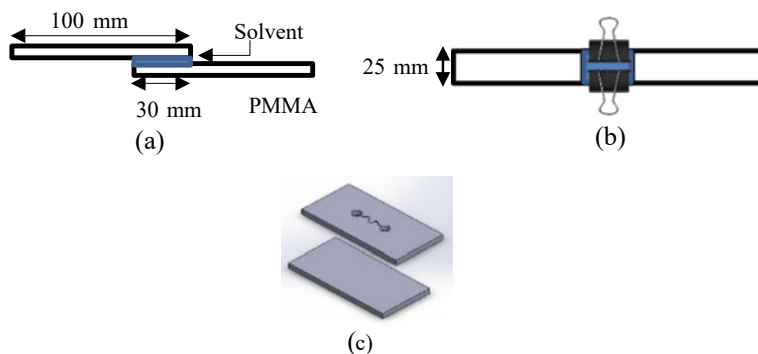


Fig. 4.1 a PMMA sample preparation, b PMMA samples were securely clamped using office paper clip, and c illustration of microfluidic device before bonding

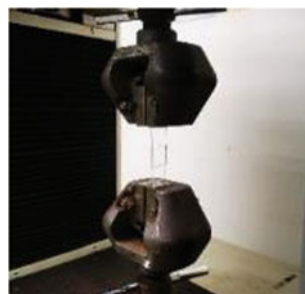
4.2.2 Bonding Procedure

Two types of organic solvents were evaluated, isopropanol (R&S Chemicals) and ethanol (R&S Chemicals). Prior to curing in the oven, 100 μL of solvent was pipetted evenly onto the PMMA surface (bonding area), and both PMMA were securely clamped using an office paper clip as shown in Fig. 4.1b. The PMMA samples were later placed in a convection oven and cured at different temperatures and time settings: 95 $^{\circ}\text{C}$ for 15 min, 90 $^{\circ}\text{C}$ for 20 min, and 85 $^{\circ}\text{C}$ for 15 min.

4.2.3 Bonding Strength Test

Lap shear test was conducted to evaluate the bonding strength of PMMA samples at a rate of 1 mm/min using a Shimadzu Autograph universal testing machine as shown in Fig. 4.2.

Fig. 4.2 Specimen setup during lap shear test



4.2.4 *Fabrication of Microfluidics Device*

The microfluidics device consists of a serpentine microchannel as illustrated in Fig. 4.1c. The fabrication involves machining of two parts of PMMA substrates. The first part of PMMA substrate was patterned with a serpentine microchannel using 0.2 mm end mill bit through CNC machining. The second part of PMMA was cut to form a blank substrate. Both PMMA substrates were later thermally bonded using the best bonding parameter setting obtained in the bonding evaluation experiment.

4.3 Results and Discussion

4.3.1 *Bonding Result*

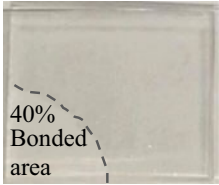
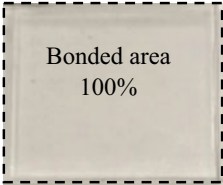
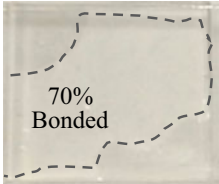
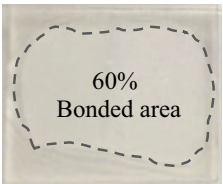
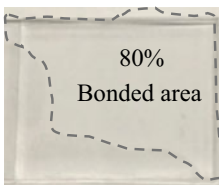
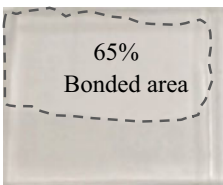
Results for PMMA–PMMA bonding are summarized in Table 4.1. According to visual inspection, the PMMA surface treated with ethanol and curing in the oven at 85 °C for 15 min showed perfect bonding. However, at this curing parameter setting, PMMA treated with isopropanol can best obtain bonding covering only 40% of the area. Overall, there is no direct correlation between increasing curing temperature and time with the bonding quality. However, it can be seen that surface treatment with ethanol produced better results compared to isopropanol.

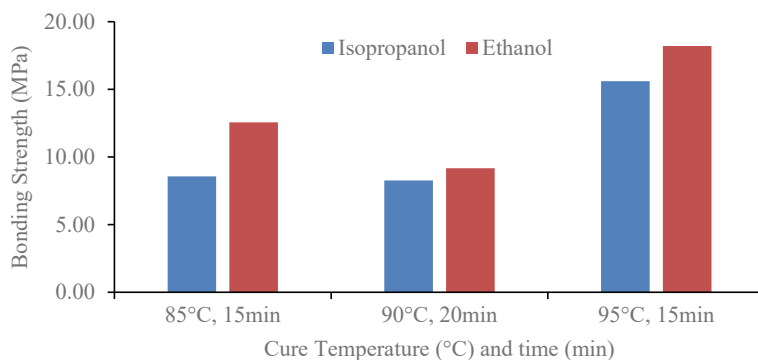
Bonding strength results based on lap shear test are shown in Fig. 4.3. The PMMA sample cured at 95 °C for 15 min has shown higher bonding strength with 18 MPa for the sample treated with ethanol and 15 MPa for the sample treated with isopropanol. Although the highest bonding strength was obtained at this curing condition setting, however, the bonded area was not fully covered. Moderate bonding strength can be seen when samples were cured at a temperature of 85 °C for 15 min. The sample treated with ethanol has a bonding strength of 13 MPa and produced 100% covered area, while the sample treated with isopropanol has bonding strength of 9 MPa, but only 40% of the bonded area was covered. Based on this condition, the sample treated with ethanol and cured at a temperature of 95 °C for 15 min can be assumed as the best parameter setting for PMMA–PMMA bonding.

4.3.2 *Sealing of a Microfluidics Device*

The structured microchannel on PMMA substrates fabricated using CNC micro-milling before bonding is shown in Fig. 4.4a, while a complete microfluidic device after bonding is shown in Fig. 4.4b. The bonding process was performed using ethanol to treat the PMMA surface and cured in the oven at 85 °C for 15 min. Visual inspection showed a perfect bonding with 100% area covered. A leak test was conducted by pipetting red ink (water based) into the inlet. A capillary flow was

Table 4.1 Bonding results for samples treated with isopropanol and ethanol

| Temperature (°C) | Cure time (min) | Isopropanol | Ethanol |
|------------------|-----------------|---|---|
| 85 | 15 |  |  |
| 90 | 20 |  |  |
| 95 | 15 |  |  |

**Fig. 4.3** Bonding strength results from lap shear test

observed which indicates that the channel surface is hydrophilic. No leakages were observed even after the device was left for 4 h (Fig. 4.4b). A liquid flow test was conducted by injecting DI water using a syringe pump and successfully delivered at flow rate 0.3 ml/min.

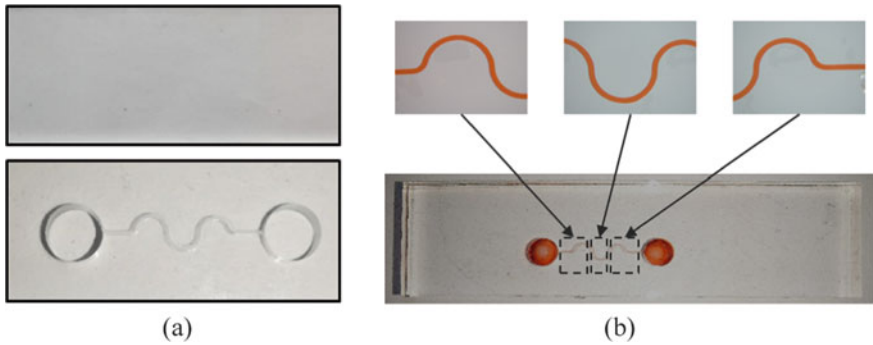


Fig. 4.4 **a** Structured microchannel on PMMA substrate before bonding and **b** microfluidic device after bonding. Section view of channel during leak test

4.4 Conclusion

PMMA is one of the most often utilized polymers in the fabrication of microdevices, owing to its low fabrication cost and wide availability. This work develops a simple method to seal the microchannel for fabrication of microfluidics devices by treating PMMA surface with solvents and applying low pressure during direct thermal bonding. Unlike using isopropanol, applying ethanol onto PMMA surface and subsequently curing in oven at a temperature of 85 °C for 15 min produces excellent bonding with 100% area coverage. The bond strength through lap shear test was obtained at 13 MPa. Additionally, a microfluidic device comprising a serpentine microchannel was fabricated using this parameter setting. Excellent microchannel sealing was achieved with leak proof and capable to deliver fluid at 0.3 ml/min.

Acknowledgements This work was supported by the Fundamental Research Grant Scheme (FRGS), the Ministry of Higher Education Malaysia (Grant No.: FRGS/1/2019/TK03/UITM/02/16).

References

- Chiang CC, Immanuel PN, Chiu YH, Huang SJ (2021) Heterogeneous bonding of pmma and double-sided polished silicon wafers through H₂O plasma treatment for microfluidic devices. *Coatings* 11(5)
- Faghih MM, Sharp MK (2019) Solvent-based bonding of PMMA–PMMA for microfluidic applications. *Microsyst Technol* 25(9):3547–3558
- Giri K, Tsao C (2022) Recent advances in thermoplastic microfluidic bonding. *Micromachines (basel)* 13(3):486
- Song IH, Park T (2017) PMMA solution assisted room temperature bonding for PMMA–PC hybrid devices. *Micromachines* 8(9):284

- Toossi A, Moghadas H, Daneshmand M, Sameoto D (2015) Bonding PMMA microfluidics using commercial microwave ovens. *J Micromech Microeng* 25(8):5008
- Trinh KTL, Thai DA, Chae WR, Lee NY (2020) Rapid fabrication of poly(methyl methacrylate) devices for lab-on a-chip applications using acetic acid and UV treatment. *ACS Omega* 5(28):17396–17404
- Trinh KTL, Chae WR, Lee NY (2021) Pressure-free assembling of poly(Methyl methacrylate) microdevices via microwave-assisted solvent bonding and its biomedical applications. *Biosensors* 11(12)
- Tsao C, Chang C, Tian Y (n.d.) Water-assisted bonding of thermoplastic microfluidic device for biological applications. SSRN. <https://dx.doi.org/10.2139/ssrn.4020640>. Accessed 15 Feb 2022
- Wan AMD, Moore TA, Young EWK (2017) Solvent bonding for fabrication of PMMA and COP microfluidic devices. *J vis Exp* 119:1–9

Chapter 5

Temperature Distribution Analysis of an Insulated Turbocharger Manifold



Khairul Shahril, Shahril Nizam, Muhammad Najib, and Ishak Azid

Abstract In the past years, many research efforts have been made on the temperature distribution of the turbocharger. In this study, the effect of thermal heat management on manifold surfaces at turbocharged engine performance is experimentally investigated. In this test, the insulation of the manifold on the turbocharger is aimed at reducing the heat losses and thus increasing the indicated efficiency. Thermal heat management was used to simulate the engines. The insulation of the exhaust manifold with the coating, which is silicone resin based, and the thermal wrap influences the heat transfer process and hence the performance and exhaust emissions characteristics of the engines. The purpose of this paper is to analyse the temperature distribution of the turbocharger's manifold and consider the engine performance by using a thermal imaging camera and dynamometer. The experimental research was conducted on one-cylinder, two-stroke with Lifan engine 160 cc equipped with the turbocharger. The turbocharger used is the non-standard Turbo RHB31 VZ21 for this engine as it is usually used for car engine applications.

Keywords Thermal heat management · Heat loss · Insulated manifold · Turbocharger · Temperature distribution

K. Shahril (✉) · S. Nizam · M. Najib · I. Azid
Mechanical Section, Universiti Kuala Lumpur Malaysian Spanish Institute, Kulim Hi-Tech Park,
09000 Kulim, Kedah, Malaysia
e-mail: khairuls@unikl.edu.my

S. Nizam
e-mail: shahrilnizam@unikl.edu.my

M. Najib
e-mail: mnajib@unikl.edu.my

I. Azid
e-mail: ishak.abdulazid@unikl.edu.my

5.1 Introduction

In the automotive industry, several research programmes are underway to minimise engine fuel consumption. Because of the rapid rise in fuel costs, the decline in high-quality fuel production, and environmental concerns, the need for engine designs with lower heat rejection through the use of thermal heat management (THM) is increasing. By using THM at exhaust system, the heat loss can be reduced, and thermal efficiency improved. Durability of engine components can also be enhanced. A major breakthrough in engine technology was achieved through Kamo and Bryzik's pioneering work as the first people to introduce TBC engine systems from 1978 to 1989. A great number of studies have been carried out employing a thermal barrier coating (TBC) to create diesel engines with decreased heat rejection (LHR). Many of them are theoretical investigations, while others are experimental. In the case of the LHR engine, nearly all theoretical analyses forecast greater performance and fuel economy, while certain experimental studies indicate a different picture. In general, diesel engines consume less fuel than their gasoline counterparts (Domakonda and Puli 2012).

According to the first law of thermodynamics, thermal energy is conserved by minimising heat transfer to the cooling and exhaust systems. Theoretically, if the thermal efficiency is lowered, just one-third of the energy is transformed into usable work. The TBC application inhibits heat transmission to the cooling and exhaust systems, resulting in high-temperature gas and combustion chamber walls, which reduces smoke and hydrocarbon (HC) emissions (Ekström et al. 2015).

5.2 Literature

5.2.1 *Heat Transfer in Exhaust System*

The engine's exhaust gases have a very high velocity and temperature. An integral aspect of the exhaust system is an automotive exhaust system that transfers exhaust fumes from the combustion chamber through a silencer (Chinchole et al. 2008). For a one-cylinder two-stroke motorcycle, the manifold temperature and pressure were measured. The test considered three series of measurements. The temperatures were measured along the length of the planned exhaust pipes in the first step, and the optimum length was established using the charging efficiency as a criterion. In the second test, the optimum length of the exhaust pipe was employed, while in the third test, the original equipment manufacturer's exhaust system was used. The modified exhaust system had a positive impact on specific gasoline usage, which was decreased by 12%, according to the researchers. The major hydrocarbon and carbon monoxide emission engine was reduced by at least 27.8% and 10.7%, respectively (Vasava and Jotaniya 2015).

5.2.2 *The Exhaust Manifold of the Turbocharger*

Yamagata (2005) in his Automotive Handbook had explained that the exhaust manifold collects and expels the exhaust gas through the exhaust pipe. Currently, the exhaust manifold must tolerate continuous running temperatures of up to 900 °C. However, higher exhaust gas temperatures will be required to meet environmental and economic standards; thus, the exhaust manifold's thermal reliability must be improved further (Yamagata). In their study, Chen et al. (2017) show that increasing the Nb concentration from 0 to 0.15% improves corrosion resistance and increases fatigue life in a low-cost ferritic stainless steel with an 11% Cr content. For a low-cost strategy, the recently produced 11% Cr–0.11 per cent Ti–0.15% Nb ferritic stainless steel could be used in vehicle exhaust systems to replace higher Cr ones (Chen et al. 2017).

5.2.3 *Development of Thermal Barrier Coating*

The effect of thermal barrier-coated piston top and combustion chamber surfaces on turbocharged diesel engine performance was studied by Ciniviz on 2008. TBC1 (with coated cylinder head and valves) and TBC2 both delivered satisfactory results (with coated cylinder head, piston top, and valves). Engine power was raised by 2%, engine torque was improved by 1.5–2.5%, and brake specific fuel consumption (b.s.f.c.) was reduced by 4.5–9% when compared to a normal diesel engine. TBC has been observed to reduce smoke emissions by up to 18% in experimental trials (Ciniviz et al. 2008).

5.3 Methodology

This experimental investigation is designed to analyse the temperature distribution and engine performance of an insulated exhaust manifold of a turbocharger. Two types of insulators are used, i.e. thermal wrap and thermal coating. The temperature distribution is measured by using a thermal imaging camera (TIG). A direct current-type dynamometer is used in this experiment to analyse the engine performance. It is equipped with a controller data acquisition system and fuel scale. The engine Lifan 160 cc with a micro-turbocharger RHB VZ21 is set up in series with the dynamometer. Figure 5.1 shows the schematic diagram of the set-up. The engine specification is presented in Table 5.1. In order to study the temperature distribution on the exhaust manifold, which is working on the engine, the investigation required measurements by taking the image by using the TIG at least 2 m from the engine.

The thermal resistance diagram of the system for the insulated manifold is shown in Fig. 5.2. The thermal energy acquired by exhaust gases, T_{exh} , is transferred to the

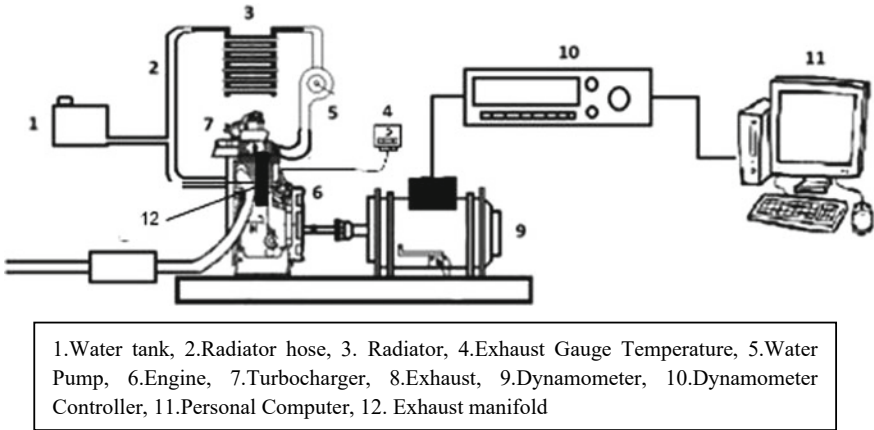


Fig. 5.1 Schematic diagram of the experimental set-up

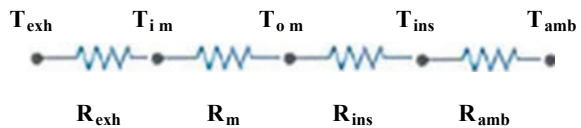
Table 5.1 Specifications of the Lifan 160 cc engine

| Specification | Parameter |
|--------------------------------|--|
| Type | Single-cylinder; four-stroke; oil-cooled |
| Bore × stroke | 60 mm × 57 mm |
| Engine displacement | 161.2 ml |
| Compression ratio | 9.5:1 |
| Primary reduction ratio | 3.722 |
| Ignition system | Magneto to CDI |
| Max. power and rotating speed | 10.3 kW/9500 r/min |
| Max. torque and rotating speed | 11.5 N.m/7000 r/min |
| Idling speed | 1500 r/min |

inner surface of the manifold, T_{im} , via convective heat transfer. Energy is transferred at the manifold by conduction across the manifold's resistance, R_m . The energy transfers to the insulation method (thermal wrap/thermal coating) at the outer manifold surface, T_{om} , is by conduction, R_{ins} . Finally, convection is used to transport heat to the surrounding environment, according to R_{amb} .

The thermal resistances are calculated using following equations:

Fig. 5.2 Thermal resistance of insulated manifold



$$R_{\text{exh}} = \frac{1}{h_{\text{exh}} A_1} \quad (5.1)$$

$$R_{\text{m}} = \frac{\ln\left(\frac{R_2}{R_1}\right)}{2\pi k_{\text{m}} L} \quad (5.2)$$

$$R_{\text{coating}} = \frac{\ln\left(\frac{R_3}{R_2}\right)}{2\pi k_{\text{coating}} L} \quad (5.3)$$

$$R_{\text{wrap}} = \frac{\ln\left(\frac{R_3}{R_2}\right)}{2\pi k_{\text{wrap}} L} \quad (5.4)$$

$$R_{\text{amb}} = \frac{1}{h_{\text{amb}} A_3} \quad (5.5)$$

where h_{exh} and h_{amb} are the convection heat coefficients of exhaust gas and air, respectively. k_{m} , k_{coating} , and k_{wrap} are the thermal conductivities of the manifold, thermal coating, and thermal wrap, respectively. R_1 and R_2 are the inner and outer radii of the manifold surface, while R_3 is the outer surface radius of the insulator. A_1 , A_3 , and L are the area of the inner manifold, area of the manifold with insulator, and length of the manifold, respectively.

After knowing the R_{Total} of each system, the rate of heat loss could be found by using the following formula:

$$\dot{Q} = \frac{T_{\infty 1} - T_{\infty 2}}{R_{\text{Total}}} \quad (5.6)$$

where $T_{\infty 1}$ and $T_{\infty 2}$ are the exhaust temperature and the ambient temperature, respectively.

5.4 Result and Discussion

5.4.1 Temperature Distribution Analysis

For the temperature distribution of the exhaust manifold, a thermal imaging camera (TIC) was used by taking the image of the manifold. From the images taken, the result analysis can be generated by the Wahl software as shown in Fig. 5.3. During the experiment at 4000 rpm of engine speed, it is noted that the non-insulated manifold had the highest surface temperature at point where the exhaust gas is wasted from the engine with a value above 350 °C. At point 01 where the thermocouple was coupled, the temperature shown by the thermal imaging camera (TIC) is 210 °C,

while the exhaust gauge temperature reading is 426 °C. The average temperature at the manifold is 134.3 °C. Then, the ambient temperature was 30.8 °C (Fig. 5.4).

The temperature distribution analysis at the thermal-coated manifold is shown in Fig. 5.5 at 4000 rpm. The highest temperature is also shown at the white colour region above 350 °C. At point 01, the temperature reading is 181.7 °C and the ambient temperature is 30.6 °C. The average temperature across the manifold is 112.5 °C.

For the temperature distribution analysis at the thermal wrap manifold at 4000 rpm, the highest temperature shown at the white colour region is 281.2 °C. At point 01, the temperature reading is 142.3 °C and the ambient temperature is 30.6 °C. The average temperature across the manifold is 108.5 °C (Fig. 5.6).

Based on the experimental result, it is obvious that the thermal heat management gave better thermal performance than the non-insulated manifold. By looking at the colour of the temperature distribution on the manifold, darker the colour means, cooler the surface of the manifold. The image of thermal wrap manifold had a darker distribution which is under 120 °C compared to non-insulated that had more light red to white colour region which means that the temperature is above 200 °C. The reason is that the thermal wrap material has a low thermal conductivity of 0.045 W/m.K, compared to silicone coating (0.32 W/m.K) and the manifold that is made from stainless steel (16.2 W/m.K).

Figure 5.7 presents the temperature of the exhaust gas as a function of engine speed. When comparing the insulated and non-insulated manifolds, the insulated manifold has a greater exhaust temperature.

Fig. 5.3 Cross section of insulated manifold

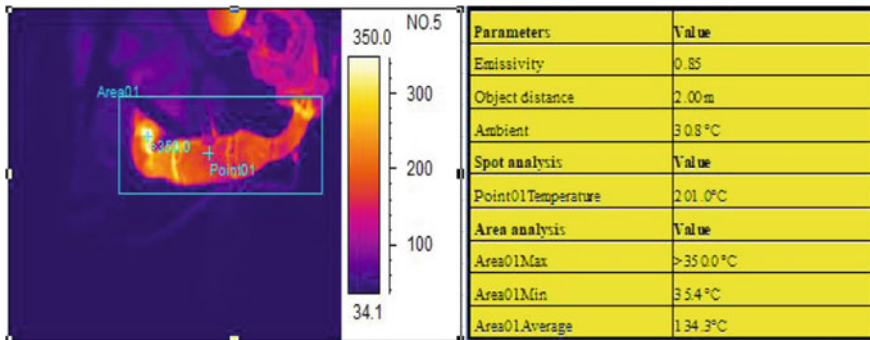
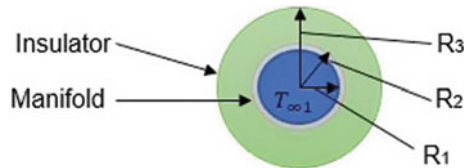


Fig. 5.4 Temperature distribution on the non-insulated manifold

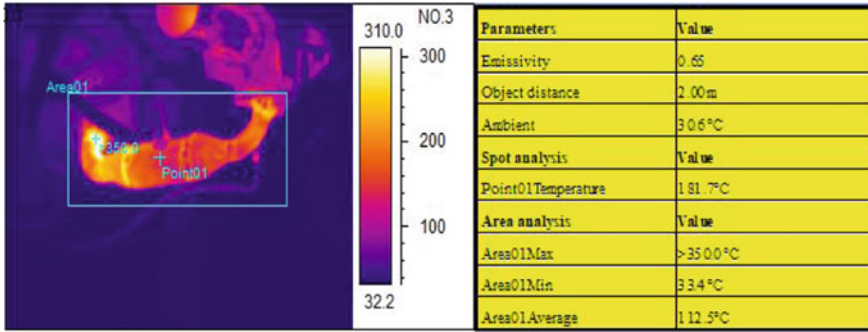


Fig. 5.5 Temperature distribution on the thermal-coated manifold

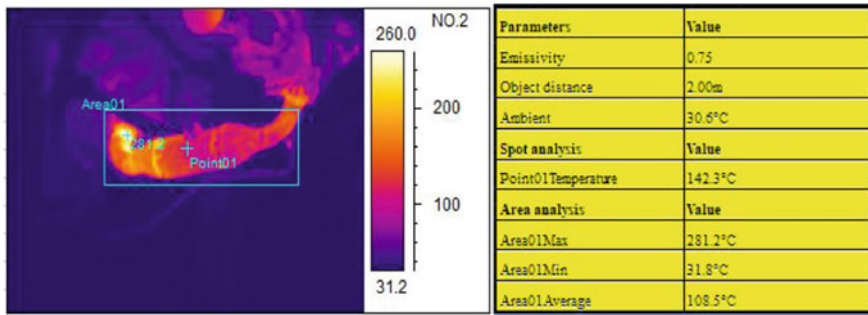
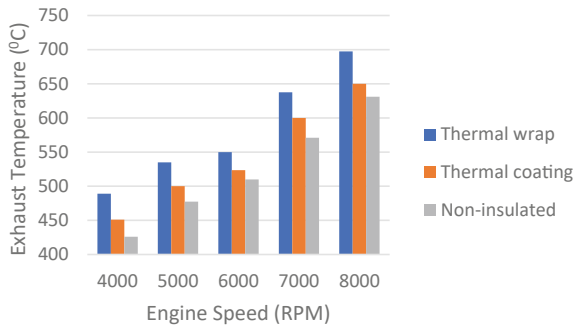


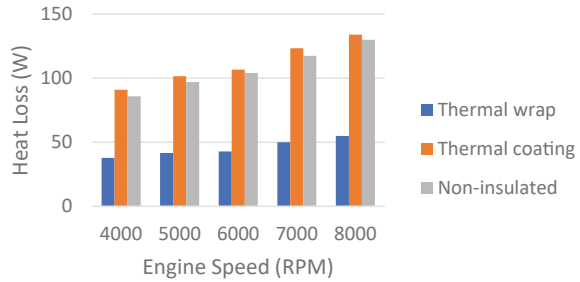
Fig. 5.6 Temperature distribution on the thermal wrap manifold

Fig. 5.7 Variation on exhaust gas temperature



Next, Fig. 5.8 shows that the heat loss values measured at the thermal-coated and non-insulated manifold are slightly similar and higher compared to the thermal wrap manifold. One of the reasons of this huge range is the thickness used by the thermal wrap to insulate it is 3 mm thicker than the thermal-coated which makes the thermal resistance value of the thermal wrap manifold higher. Thermal wrap can only reach the thickness of 100 μm due to the spray characteristics, but it has a higher thermal

Fig. 5.8 Variation of heat loss



conductivity of 0.32 W/m.K compared to the thermal conductivity of thermal wrap (0.045 W/m.K).

5.5 Conclusion

From the images taken by thermal imaging camera, the thermal wrap manifold has a better temperature distribution with the maximum temperature surface 70 °C lower. The heat loss from the thermal wrap manifold decreased by 48 to 76 W from the non-insulated manifold that makes the exhaust gas temperature inside the manifold higher.

Acknowledgements This paper has been financially supported by UniKL-STRG Grant (str17042) provided by Universiti Kuala Lumpur and Fundamental Research Grant Scheme (FRGS), the Ministry of Science, Technology, and Innovation (MOSTI), Malaysia, with reference number FRGS/1/2019/TK03/UNIKL/01/2. Appreciation is also extended to anonymous reviewers for the comments given which led to the significantly improved manuscript quality.

References

- Chen H et al (2017) Increasing the formability of ferritic stainless steel tube by granular medium-based hot forming. *J Phys Conf Ser* 896:12009. <https://doi.org/10.1088/1742-6596/896/1/012009>
- Chinchole SP, Borse RR, Patil RY, Patil G (2008) Review on an innovative approach to study the thermal performance of muffler heat shield for Hero Xtreme 200R bike. *Int Res J Eng Technol*. 5(12):556–559
- Ciniviz M et al (2008) Impact of thermal barrier coating application on the performance and emissions of a turbocharged diesel engine. *P I Mech Eng D-J Aut* 222(12):2447–2455
- Ekström M et al (2015) Evaluation of internal thermal barrier coatings for exhaust manifolds. *Surf Coat Technol* 272:198–212

- Domakonda VK, and Puli RK (2012) Application of thermal barrier coatings in diesel engines: a review. *Energy Power* 2(1):9–17
- Vasava MS, Jotaniya PV (2015) A review on heat transfer analysis in automotive exhaust system. *Int J Innov Res Sci Eng Technol* 4(2):558–561
- Yamagata H (2005) 11 - The turbocharger and the exhaust manifold. In: Yamagata H (ed) *The science and technology of materials in automotive engines*. Woodhead Publishing, pp 248–260

Chapter 6

Experimental Analysis of Carburetor System on Turbocharger Performance



Khairul Shahril, Mohd Nurhidayat Zahmelem, Shahril Nizam Soid, Muhammad Najib Abdul Hamid, and Ishak Abduls Azid

Abstract This thesis deals with the experimental study of a micro-turbocharger test rig for engine performance with a racing carburetor and a standard carburetor. In order to achieve higher performance, bigger engine is needed. But with the turbocharger, the performance can be increased without the need of bigger engine. Therefore, the objective of this thesis is to observe the flow rate and fuel efficiency of the carburetor and evaluate the engine performance with the racing and standard carburetors. The project uses the turbo IHi RHF3, Lifan 160 cc, Taikom 28 mm carburetor, and Deni 18 mm carburetor and was selected according to the specification that needed to investigate the flow rate and fuel efficiency. All the data of the engine performance are collected, and some calculations are made to obtain the result.

Keywords Turbocharger · Carburetor · Experiment

6.1 Introduction

Most of the vehicles on the road nowadays are powered by an internal combustion engine or also known as (ICE). Most of the internal combustion engines use fossil fuel such as gasoline or diesel to make it run (Kalghatgi 2014). The internal combustion

K. Shahril (✉) · M. N. Zahmelem · S. N. Soid · M. N. A. Hamid · I. A. Azid
Mechanical Section, Universiti Kuala Lumpur Malaysian Spanish Institute, Kulim Hi-Tech Park,
09000 Kulim, Kedah, Malaysia
e-mail: khairuls@unikl.edu.my

M. N. Zahmelem
e-mail: mnurhidayat@unikl.edu.my

S. N. Soid
e-mail: shahrilnizam@unikl.edu.my

M. N. A. Hamid
e-mail: mnajib@unikl.edu.my

I. A. Azid
e-mail: ishak.abdulazid@unikl.edu.my

engine mainly consists of four cycles, that is, intake, compression, combustion, and exhaust strokes. During the intake stroke, the engine will induce the air outside the engine to mix with the fuel. After that, it will continue in the compression stroke; that is, the air–fuel mixture inside the engine will be compressed by the piston inside the combustion chamber. The engine power is directly proportional to the air–fuel mixture inside the combustion chamber. In this experimental study, a four-stroke horizontal motorcycle engine that has a cubic centimeter of 160 will be used in order to analyze the performance and potentially make more power by adjusting or replacing the main jet and pilot jet of the carburetor. The power of the engine greatly depends on the amount of air that can be delivered through the intake (Abdullah et al. 2014).

6.2 Literature Review

6.2.1 Carburetor

A comparison study done by Suthisripok et al. (2011) stated that, a vcf x Honda Nice 100S motorcycle whose carburetor was purposely designed for the use of gasoline could achieve the optimum performance condition. The study was conducted by using two different types of fuel, that is, the Gasoline 91 and the E85. The engine was tuned up on the dynamometer at a relatively fuel-rich mixture of 0.85 which in theory would give the best power output. The test conducted was done on the road, that is, a long riding test and a city riding test. The result of the experiment shows that the types of fuel used influence the fuel consumption of the vehicle as agreed by Mothilal et al. (2017). In Fig. 6.1, it shows the comparison from a performance perspective of the vehicle.

There is also a study by Lin and Liu (2008) which focuses on the exhaust gas emissions by using gasoline and ethanol-blended fuels. Figure 6.2 shows the comparison between the fuel blends. The study uses a single-cylinder engine 125 cc four-stroke Taiwan motorcycle that uses a GY6 carburetor fuel system. The result of the study concludes that by blending ethanol with gasoline by several ethanol concentration-blended fuels. The air–fuel ratio also decreased as engine inlet vacuum pressure increased. Air–fuel ratio decreased as the auxiliary nozzle diameter increased under the same main nozzle diameter. Also, air–fuel ratio decreased as the main nozzle diameter increased under the same auxiliary nozzle diameter.

In contrast, Alimin et al. (2009) stated that in two-stroke engine, carburetors are less efficient. This is because of the engine's operation that is two-stroke. In its typical operation, for two-stroke engine, the carburetion involves entrainment of fuel in the intake air stream before intake air begins to enter the engine crankcase. The underside of the piston will compress the charged mixture and enters the cylinder when the piston uncovers the transfer ports. Continuous presence of combustion products from the previously completed combustion power stroke is forced out from the cylinder

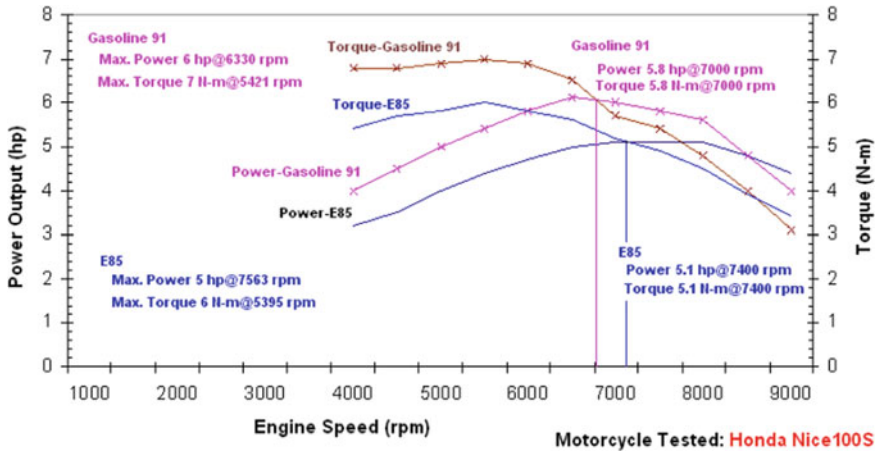
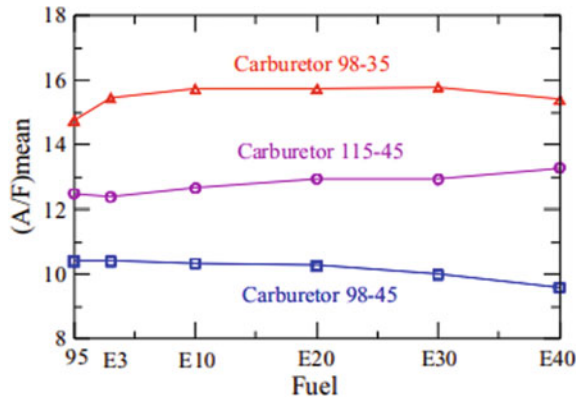


Fig. 6.1 Torque and power output of the used four-stroke motorcycle on dynamometer—Gasoline 91 and E85

Fig. 6.2 Air–fuel ratio comparison



by this new air–fuel mixture. Unfortunately, the exhaust ports are also open at this time, allowing 30–40% of the fuel to be lost directly into the exhaust stream (Radzak et al., 2019); at idle conditions, the losses can be as high as 70%. The process is illustrated in Fig. 6.3.

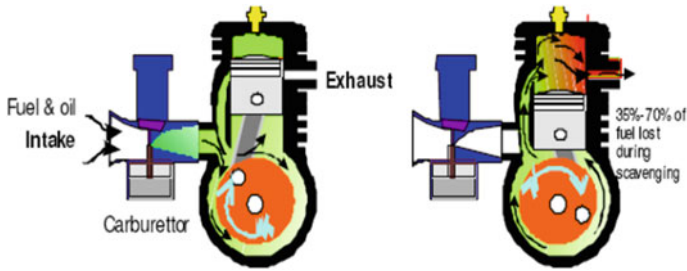


Fig. 6.3 Two-stroke engine cycle with carburetor

6.3 Methodology

6.3.1 Methodology Process

First and foremost, this idea is generated according to the problem statement, which is the existing test rig is not efficient as it supposes to be. In order to achieve higher efficiency and performance, the carburetor needed to be configured to the proper air–fuel mixture. A carburetor is a component that mixes air and fuel before sending the mixture into the combustion chamber. If the mixture is too rich or too lean, it may cause an incomplete combustion process, thus effecting the efficiency and performance. The main jets and the pilot jets of the carburetor are important to be tuned correctly. The function of the pilot jet is to supply the fuel when the engine is on idle or about 15%–20% of the throttle. The main jet functions when the throttle is above 20% or wide open. By selecting the proper size of both jets, the engine will have a more stable idling RPM and more power during wide open throttle.

6.3.2 Parameter Study

There are two important parameter studies about the engine performance before and after the improvement which are:

1. Fuel consumption (mf)
2. Flow rate (Q).

The data for fuel consumption (mf) will be collected from the anemometer with some derivation calculations in order to get the result to be analyzed for the engine performance before and after the improvement. The fuel consumption of the engine will be measured by using RON 95-type fuel.

Fuel consumption (mf)

$$\dot{m}f = \frac{W_1 - W_2}{T} \quad (6.1)$$

Flow rate (Q)

$$Q = vA \tag{6.2}$$

6.4 Results and Discussion

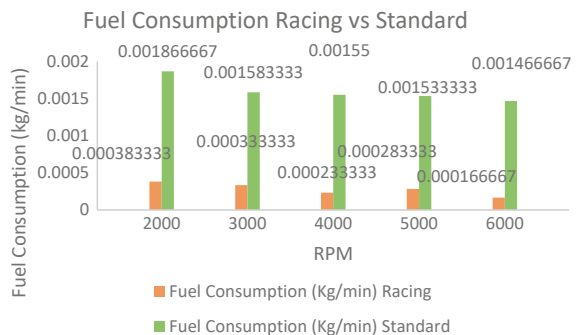
The flow rate and fuel consumption are set from the same revolution per minute in order to compare the performance. It starts from 2000 until 6000 RPM.

6.4.1 Fuel Consumption

The four-stroke motorcycle engine was operated by under different speed by using the same type of petrol which is RON 95 but different carburetors. The graph has shown different fuel consumptions between the racing and standard carburetors at which the most and less fuel consumption takes place when the engine is operated.

The overall fuel consumption is done by investigating the comparison graph in Fig. 6.4, and the standard carburetor uses more fuel than the racing carburetor. This is due to the standard carburetor that tends to vibrate more than the racing carburetor due to the structure of the test rig. Furthermore, upon investigation, the standard carburetor’s air flow area is not as big as the racing carburetor that could take air more efficiently to be used in the combustion chamber and tends to fuel overflow due to the float of the carburetor that vibrates vigorously inside. The maximum efficiency obtained is at 6000 RPM with 88%.

Fig. 6.4 Overall fuel consumption



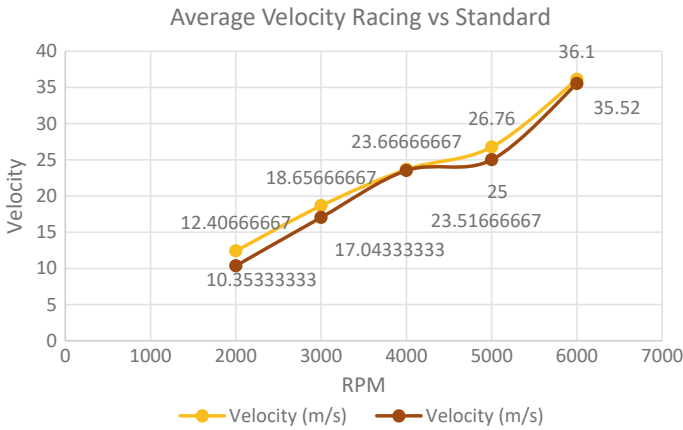


Fig. 6.5 Average velocity between racing and standard carburetors

6.4.2 Velocity

The velocity of the test rig is taken from the exhaust pipe, after the exhaust turbine. The velocity is taken to determine the amount of exhaust gas flow that comes out from the test rig. The velocity is taken three times to get the average velocity of the test rig before and after modification.

Figure 6.5 shows the average velocity of the exhaust gas from the exhaust pipe between both types of carburetors. The average velocity of the racing carburetor starts higher than the standard carburetor that is around 19% higher than the standard carburetor and more linear. But the standard carburetor almost matched the velocity of the racing carburetor at 4000 RPM, and the difference is around 0.64%. After that, for the standard carburetor, there is a stagnant of value in the graph, while the racing carburetor experiences a little drop but still an increase of 7%. Furthermore, the standard carburetor tends to rev itself, and the throttle is unresponsive.

6.4.3 Flow Rate

After the average velocity has been determined, the flow rate of both carburetors can be calculated. The flow rate of the test rig and the amount of exhaust gas are being discharged from the turbocharger.

The flow rate of the test rig can be observed in the comparison graph in Fig. 6.6. The flow rate of both types of carburetor is relatively similar. The flow rate of the racing carburetor is more linear and a bit higher than the standard carburetor, but at 4000 RPM, both have an almost similar value. The stagnation of the graph on the standard carburetor may be due to the inconsistency of the fuel and air mixture being

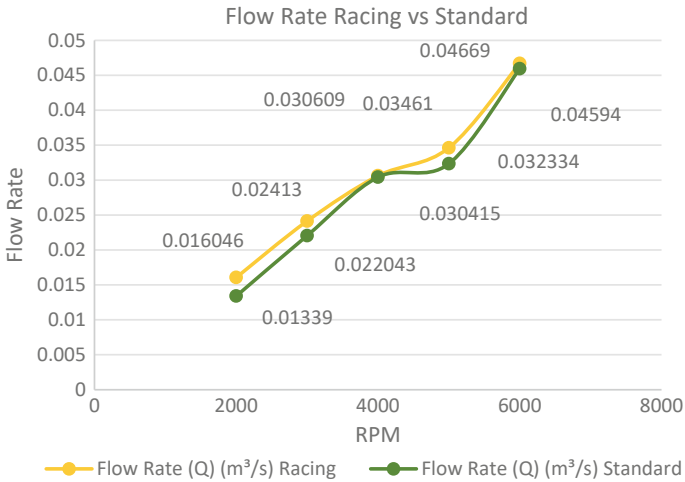


Fig. 6.6 Comparison between racing and standard

supplied due to the structure vibration that causes the carburetor float to shake. As for the racing carburetor, the structure is modified, the exhaust pipe has been extended, and there is less vibration overall on the test rig.

6.5 Conclusion

In this project, an experiment has been conducted to investigate the parameter that influences the micro-turbocharger system mainly on the types of carburetors used. This project focuses on the fuel consumption and the flow rate of the discharged exhaust gas that came through the turbine exhaust. The result shows that by using the racing carburetor, the fuel consumption as well as exhaust flow rate increased about 88% for fuel efficiency at 6000 RPM and 19% for flow rate at 2000 RPM compared to when using the standard carburetor. The graph line on the racing carburetor also is linear and does not flat out as the standard carburetor. The racing carburetor is tuned and made for high performance use even though a turbocharger is installed which is not common to be use on a motorcycle compared to the standard carburetor, which is made for daily commute and not suitable for high performance usage, let alone with a turbocharger installed.

Acknowledgements This paper has been financially supported by UniKL-STRG Grant (str17042) provided by Universiti Kuala Lumpur and Fundamental Research Grant Scheme (FRGS), the Ministry of Science, Technology and Innovation (MOSTI), Malaysia, with reference number FRGS/1/2019/TK03/UNIKL/01/2. Appreciation is also extended to anonymous reviewers for the comments given which led to the significantly improved manuscript quality.

References

- Abdullah NR, Shahrudin NS, Mamat R, Mamat AMI, Zulkifli A (2014) Effects of air intake pressure on the engine performance, fuel economy and exhaust emissions of a small gasoline engine. *J Mech Eng Sci* 6:949–958
- Alimin AJ, Ali MF, Ali MM, Batcha MM, Seri SM, Selamat H (2009) Experimental study on the application of fuel injection retrofitment kit for a small gasoline fuelled engine. In: *Environmental science and technology conference (ESTEC2009)*, Kuala Terengganu Malaysia
- Kalghatgi GT (2014) The outlook for fuels for internal combustion engines. *Int J Engine Res* 15(4):383–398
- Lin FK, Liu TC (2008) A study of carbureted motorcycle exhaust emissions using gasoline-ethanol blended fuels (No. 2008-32-0021). SAE Technical Paper
- Mothilal T, Kaliappan S, Kamal MR, Roy V (2017) Design of turbocharger in petrol engine with intercooler and discharger chamber. *Int J Latest Eng Manage Res* 2(12):81–87
- Radzak MYB, Ibrahim MRB, Shaffee KSB (2019) Heat distribution of micro turbocharger cooling system for motorcycle application. *IJRTE* 8(3):308–314
- Suthisripok T, Promjun T, Rangron A (2011) A comparative study of a used 4-stroke motorcycle engine performance using E85 and gasoline 91. *Fuel* 5:2

Chapter 7

Effect of Fuel Injection Pressure to Engine Performance Characteristics of Palm Oil Diesel Blends in a Small Diesel Engine



Muhammad Haziq Bin Azizan, Shahril Nizam Mohamed Soid, Muhammad Najib Abdul Hamid, Mohd Suyerdi Omar, and Tajul Adli bin Abdul Razak

Abstract The abundant palm oil resources have stimulated the rapid development of the potential biofuel industry in Malaysia. It has diversified and creates new market demand, thus setting up the commodity prices. There are many advantages of using palm oil as a biofuel, particularly as a combustion product that produces less carbon dioxide. This study focuses on the combustion characteristics of palm oil diesel blends at various blends ratios (20%, 40%, and 60% identified as P20, P40, and P60, respectively) in a small diesel engine. Experiments are conducted at various fuel injection pressures. The injection pressures were tested at 180 and 220 bar. The engine performance characteristics such as the brake power, thermal efficiency, and brake-specific fuel consumption were studied. The experiments conclude that although the engine performance is degrading, it can be counter-measured using higher fuel injection pressure. The performance of engine that fueled by palm oil diesel blends improved by using a 220 bar of injection pressures.

Keywords Palm oil diesel blends · Palm oil · Fuel injection · Engine performance

M. H. B. Azizan · S. N. M. Soid (✉) · M. N. A. Hamid · M. S. Omar · T. A. A. Razak
Engineering Section, Universiti Kuala Lumpur, Malaysian Spanish Institute, Kulim Hi-Tech Park,
09000 Kulim, Kedah, Malaysia
e-mail: shahrilnizam@unikl.edu.my

M. N. A. Hamid
e-mail: mnajib@unikl.edu.my

M. S. Omar
e-mail: msuyerdi@unikl.edu.my

T. A. A. Razak
e-mail: tajuladli@unikl.edu.my

7.1 Introduction

Various researchers have proposed the idea of using biodiesel fuel for diesel engines. A combination of diesel and other substances has been experimented with, from powdered coal to peanut oil. The development of today's diesel engine has reached the level as close to a petrol engine. However, the rising cost of diesel and its environmental effects are driving researchers in finding alternative fuels for diesel engines.

Biodiesel is a diesel engine alternative fuel that can help to minimize greenhouse gas emissions. It is very significant to environmental benefits. It is a sulfur-free, oxygenate, and biodegradable fuel that adds oxygen which helps to improve its combustion efficiency. Biodiesel also gained much attention in recent years due to increasing environmental awareness. The trees that produce the oil concurrently absorb the carbon dioxide during the photosynthesis process, thus improving environmental conditions. There are many types of biodiesel produced from straight vegetable oils, animal oil/fats, tallow, and waste oil. Most of them are produced using the base-catalyzed transesterification process.

In Malaysia, the development of biodiesel started in 2006 under the National Biofuel Policy. As one of the largest producers of palm oil products, this policy aimed to capitalize on the emerging biofuel market by pushing palm oil-based biodiesel. Malaysia plays a critical role in meeting the growing worldwide demand for environmentally friendly alternative fuel supplies. Malaysia is now using B10 biodiesel, which contains 10% palm methyl ester and 90% diesel, and is planning for the deployment of B20 biodiesel in the future.

The engine performance parameters are explored in this study at a variety of engine speeds, loads, and injection pressures. The palm oil and diesel fuel are directly blended without the catalyzed transesterification process. Engine performance characteristics are analyzed in terms of brake power (BP), brake torque (BT), thermal efficiency, and brake-specific fuel consumption (BSFC).

7.2 Palm Oil Diesel Blends-Fueled Engine

Malaysia is a major producer and exporter of palm oil in the world. Palm oil may be fractionated using crystallization and separation techniques, allowing it to be used in a wide range of foods and non-food products. In addition to the large supply of palm oil in Malaysia, there is a huge opportunity for renewable energy resources to be investigated, which offers comparable efficiency and benefits to a diesel-fueled engine. Manufacturers in the automotive industry have begun creating energy-efficient vehicles by incorporating new technology and promoting existing technical capabilities in order to achieve environmentally friendly engines. Furthermore, internal combustion engine combustion technologies continue to play an important role in energy conversion in the automotive industry (Alagumalai 2014; Nalgundwar et al. 2016).

There are numbers of research on discovering palm oil usage for internal combustion engine (ICE), which emphasize in three following areas:

- (1) palm oil and its derived properties,
- (2) injection and combustion characteristics,
- (3) engine performance itself.

Palm oil diesel blends (PODBs) have been proven as an alternative fuel in a specific portion without or limited modification on the diesel engine, such as 10% biodiesel (palm oil) with 90% petroleum diesel. The cabinet of Malaysia has approved B10 biodiesel, and its usage is implemented starting from December 1, 2018. There was also an agreement with the Federation of Malaysian Manufacturers to use the B7 biodiesel for the industrial sector. The transport sector uses the B10 biodiesel and other subsidized sectors mandatorily starting from February 2019.

The usage of palm oil-based biodiesel can be extended more. Ensuring that palm oil blends perform at equivalence to the diesel (petroleum) engine, the fuel needs to have required characteristics and burnt in a specific condition, allowing efficient combustion performance on the engine (Lahane and Subramanian 2015; Mosarof et al. 2015). Despite palm oil diesel blend (PODB) promises as alternative fuels, current problems of this POBD fuel are affected by poor spray performance due to its high viscosity. This occurrence led to slow fuel spray development and a poor mixing process between the fuel and air, contributing to a non-homogenous mixture of fuel and air (Emberger et al. 2015).

Understanding the fundamentals of engine performance is essential for achieving energy efficiency goals and embracing alternative fuels. The engine performance depends on the fuel properties. It is significantly essential to enhance palm oil usage as biodiesel in the internal combustion engine. Furthermore, the combustion environment of the diesel engine also needs to be understood, such as pressure and temperature inside the combustion chamber for POBD to burn, air–fuel mixture percentage, as well as injection strategies (Bohl et al. 2017; Eagle et al. 2014; Dharma et al. 2016).

7.3 Methodology

The diesel engine's performance fueled by palm oil diesel blends is investigated by using the engine dynamometer. At various engine speeds and loads, the parameters that influence combustion performance, such as blend ratios and injection pressures, will be examined. Palm oil is blended with diesel according to a volumetric fraction, and the blended fuel is thoroughly mixed before being use in the experiment.

The experimental setup for the investigation is shown in Fig. 7.1. The engine is a single-cylinder 178F direct injection air-cooled diesel with a rated power of 4.0 kW @3600 rev/min. It is coupled with a Kama AC synchronous generator. The dynamometer consists of a shaft connected to the rotor for energy conversion from mechanical energy to electrical energy. The load on the engine is varied by applying

electrical load to the generator by using bulbs and electrical heaters. Each single bulb and heater consumed 100 and 1000 W of electrical power, respectively. Table 7.1 shows the details of engine specifications that are used in the experiment.

The engine is tested using various palm oil diesel blends at different loads from 1000 to 3000 Watts and engine speeds from 1000 to 3000 rpm. The throttle is opened at the beginning of each test with 1000 rpm at the engine's minimum speed. The experiment began with diesel fuel and then progressed to palm oil diesel blends. The palm oil diesel blends ratio is 20, 40, and 60%. In the end, the engine was running

Fig. 7.1 Engine dynamometer setup



Table 7.1 178F Diesel engine specifications

| Parameter | Characteristics |
|---------------|--------------------------|
| Fuel | Diesel |
| Model | 178F |
| Type | Air-cooled diesel engine |
| Combustion | Direct injection |
| Bore × stroke | 78 × 62 mm |
| Max. output | 4.0 kW |
| Cont. output | 3.7 kW |
| Engine speed | 3000–3600 rpm |
| Displacement | 0.296 L |

using ordinary fuel for about 1 min for flushing the fueling system from any palm oil diesel blends. Diesel is often used during the experiments as the fuel for starting up and shutting down the engine, which means that palm oil diesel blends did not remain in the fuel lines and injection system.

In the experiment, parameters are collected, such as fuel flow rate, engine torque, and speed. Engine performance results such as brake power (BP), brake-specific fuel consumption (BSFC), and brake thermal efficiency are calculated using data from the experiment.

7.4 Results and Discussion

Figure 7.2 shows the brake power comparison between diesel and palm oil diesel blends at different injection pressures and engine speeds. It shows that the increased engine load will increase the value of brake power for both engine speeds. Higher injection pressure also will produce better brake power for both engine speeds. P20 provided the highest engine brake power compared to the other blends. The calorific value of the palm oil diesel blends is the main reason of this finding. The calorific value of the fuel will be reduced if there is a higher percentage of palm oil in the fuel blend.

The thermal efficiency represents the engine's overall efficiency. Figure 7.3 compares the thermal efficiency between diesel and palm oil diesel blends at different injection pressures and engine speeds. It shows that the increased engine load will increase the value of thermal efficiency for both engine speeds. Once again, higher injection pressure also produces better thermal efficiency for both engine speeds. P20 also produced the highest engine brake power compared to other blends due to its better performance on brake torque. However, the overall thermal efficiency for all blends is still lower when compared to diesel fuel. However, increasing the injection pressure can close the gap between P20 and diesel fuel at standard injection pressure.

The value of BSFC is used to demonstrate how effective the engine is to turn the fuel supplied into useful work. Figure 7.4 compares the BSFC of diesel and palm oil diesel blends at various injection pressures and engine speeds. The figure shows that the higher blend ratio produces the highest value of BSFC, meaning that the engine consumed a high amount of fuel for P60. P20 achieved the lowest value of BSFC among blends. Once again, higher injection pressure produces lower BSFC for all blends. In summary, lower palm oil percentages in blends and higher injection pressure enhance brake power, thermal efficiency, and BSFC.

7.5 Conclusion

The addition of palm oil to diesel might reduce the dependence on conventional petroleum-based fuel. Palm oil diesel blends can be used in diesel engines without

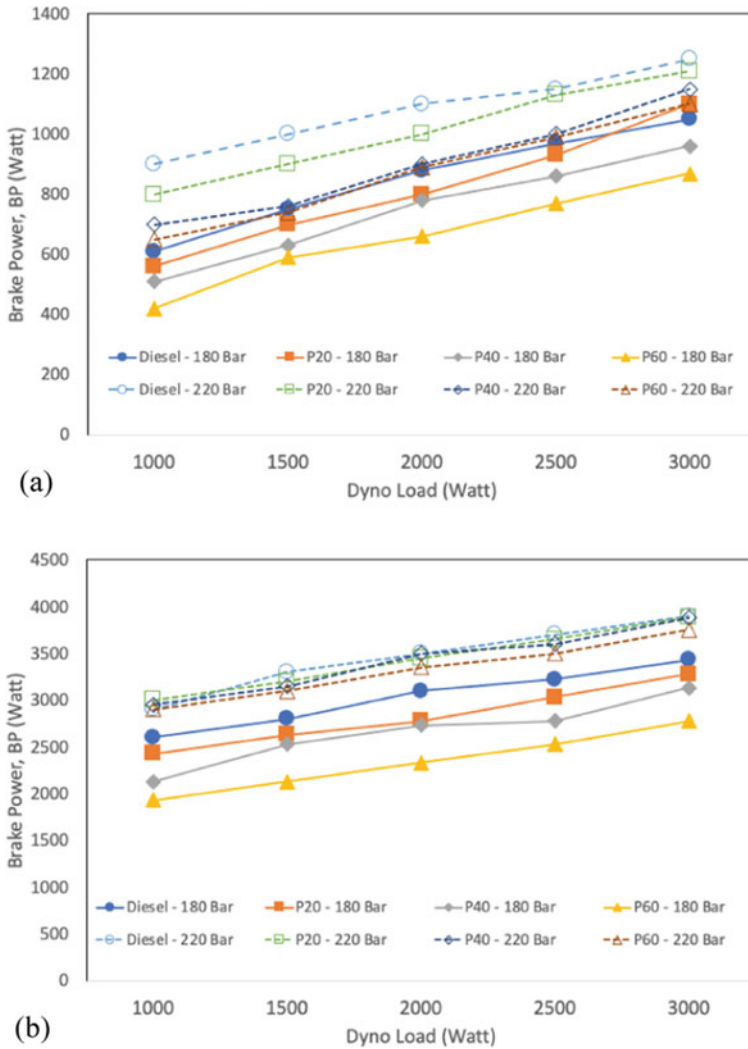


Fig. 7.2 Comparison of engine brake power of palm oil diesel blends to diesel at 180 bar and 220 bar of injection pressure at **a** 2000 rpm and **b** 3000 rpm

causing significant engine system modifications. Although the engine has a slight reduction in brake power and thermal efficiency when compared to diesel, this can be compensated for by adjusting the injection pressure. The results analysis found that P20 had produced the closest to diesel engine performances compared to other blends. Considering injection pressure, increasing the injection pressure could bridge the gap between palm oil blends and diesel. Higher injection pressure can be used to increase engine performance characteristics such as brake power, thermal efficiency, and BSFC.

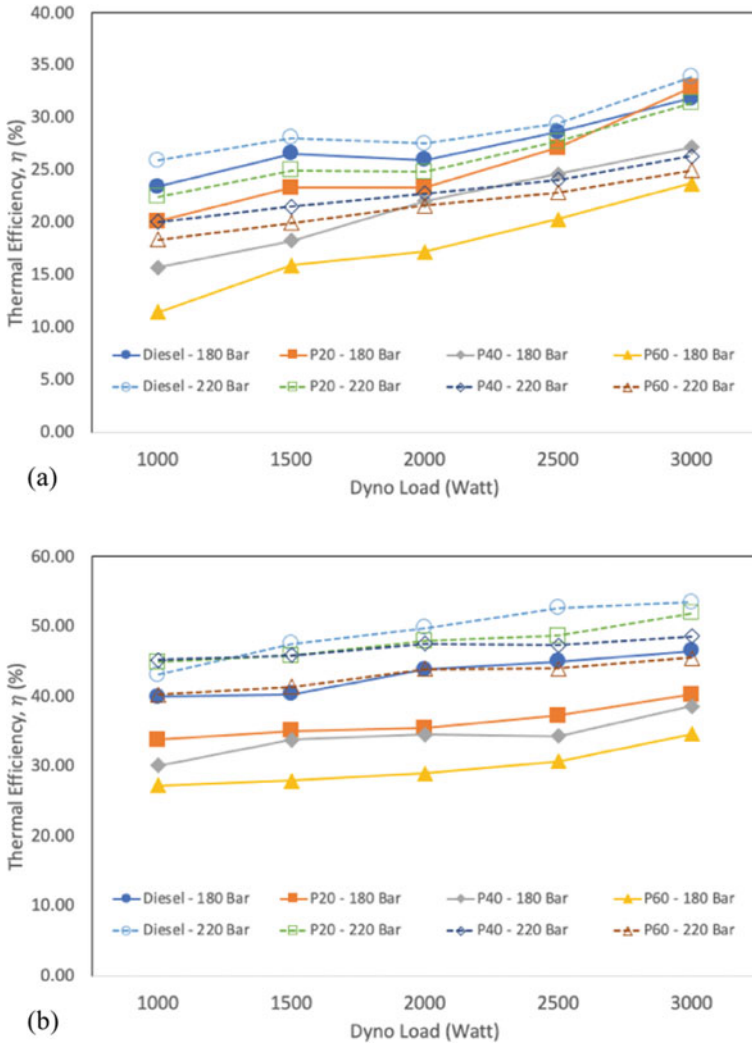


Fig. 7.3 Comparison of brake thermal efficiency of palm oil diesel blends to diesel at 180 bar and 220 bar of injection pressure at **a** 2000 rpm and **b** 3000 rpm

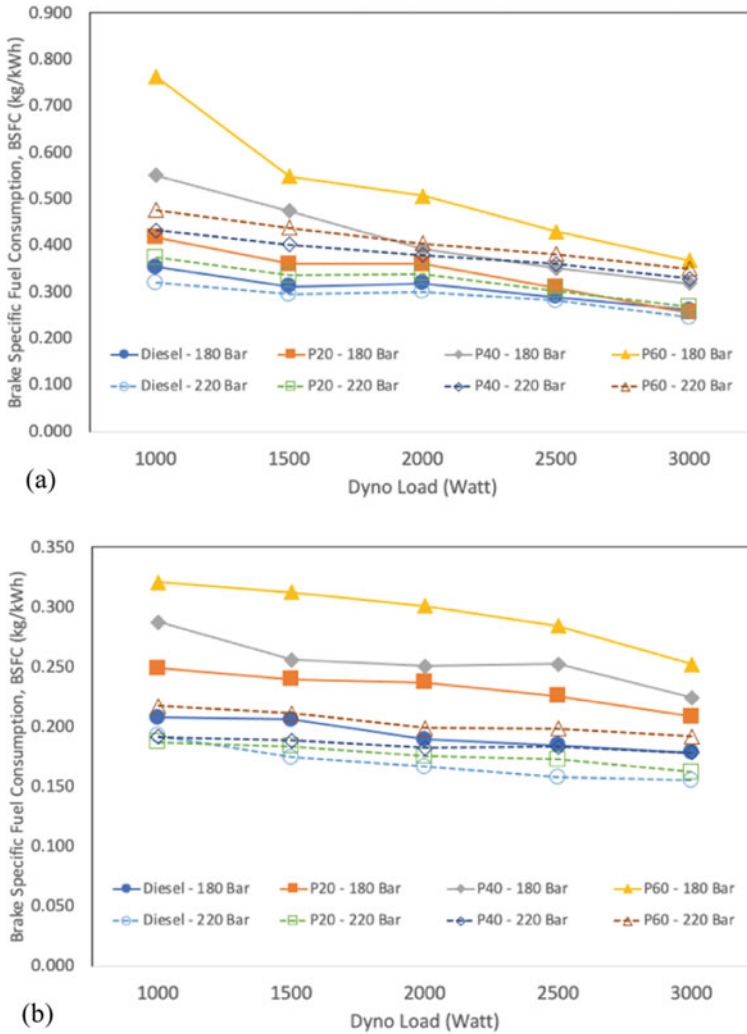


Fig. 7.4 Comparison of brake-specific fuel consumption of palm oil diesel blends to diesel at 180 bar and 220 bar of injection pressure at a 2000 rpm and b 3000 rpm

References

Alagumalai A (2014) Internal combustion engines: progress and prospects. *Renew Sust Ener Rev* 38:561–571

Bohl T, Tian G, Smallbone A et al (2017) Macroscopic spray characteristics of nextgeneration bio-derived diesel fuels in comparison to mineral diesel. *Appl Energy* 186:562–573

Dharma S, Ong HC, Masjuki HH et al (2016) An overview of engine durability and compatibility using biodiesel–bioethanol–diesel blends in compression-ignition engines. *Energy Convers Manage* 128:66–81

- Eagle WE, Morris SB, Wooldridge MS (2014) High-speed imaging of transient diesel spray behavior during high pressure injection of a multi-hole fuel injector. *Fuel* 116:299–309
- Emberger P, Hebecker D, Pickel P et al (2015) Ignition and combustion behaviour of vegetable oils after injection in a constant volume combustion chamber. *Biomass Bioenerg* 78:48–61
- Lahane S, Subramanian KA (2015) Effect of different percentages of biodiesel–diesel blends on injection, spray, combustion, performance, and emission characteristics of a diesel engine. *Fuel* 139:537–545
- Mosarof MH, Kalam MA, Masjuki HH et al (2015) Implementation of palm biodiesel based on economic aspects, performance, emission, and wear characteristics. *Energ Convers Manage* 105:617–629
- Nalgundwar A, Paul B, Sharma SK (2016) Comparison of performance and emissions characteristics of DI CI engine fueled with dual biodiesel blends of palm and jatropha. *Fuel* 173:172–179

Chapter 8

Development of an Optical Measurement Test Rig for Fuel Spray Characteristics Study of a Diesel Direct Injection System—An Experimental Approach



Megat Mohd Amzari Megat Mohd Aris, Shahril Nizam Mohamed Soid, and Ishak Abdul Azid

Abstract Optical measurement techniques have been proven by many researchers in obtaining fundamental spray and combustion characteristics either in a real engine combustion chamber or in a constant volume combustion chamber (CVCC). This technique can be used to observe the spray development and flame behaviour during the combustion process. Few renewable energy resources were extensively studied by various researchers. However, the measurement of its performance is not focusing to their fundamental characteristics especially on the spray characteristics such as tip penetration and cone angle. In this work, an experimental setup was designed to investigate the spray and combustion characteristics at various injection pressures. To examine the effect of different injection configurations, an optical measurement technique in a CVCC was used. The experimental setup consisted of a constant volume combustion chamber, sensors, and high-speed camera. The results were compared at various injection pressures in terms of spray development. The experimental setup was successfully developed to obtain the spray characteristics such as tip penetration and cone angle.

Keywords Diesel · Spray · Injection · Tip penetration · Cone angle

M. M. A. M. M. Aris · S. N. M. Soid (✉) · I. A. Azid
Engineering Section, Universiti Kuala Lumpur Malaysian Spanish Institute, Kulim Hi-Tech Park,
09000 Kulim, Kedah, Malaysia
e-mail: shahrilnizam@unikl.edu.my

M. M. A. M. M. Aris
e-mail: megatamzari@unikl.edu.my

I. A. Azid
e-mail: ishak.abdulazid@unikl.edu.my

8.1 Introduction

Various researchers have employed optical measurement techniques in engine fuel injection and combustion studies (Ghiji et al. 2017; Munsin et al. 2013; Soid and Zainal 2014). As the fundamental combustion characteristics are very important in ensuring better engine performance and emissions, various attempts have been made to understand the combustion process in the internal combustion engine. In some of the optical measurement techniques, few modifications have been carried out to obtain further details of the process, for example by using particle image velocimetry (PIV), laser-induced fluorescence (LIF), and phase Doppler particle anemometry (PDPA) techniques (Soid et al. 2012).

The research related to fuels and engine performance in internal combustion engine (ICE) can be generally classified into three broad areas: fuel and its preparation, engine geometries and features, and engine performance and emissions. To narrow down the studies, scopes of improvement are made by customizing certain existing engine components with different strategies and configurations such as introducing various types of fuels and blends to analyse characteristics and factors affecting engine performance and emission (Alagumalai 2014; Martins and Brito 2020).

Furthermore, phenomenon behavioural interaction between fuel and air towards combustion has also been studied by replicating the engine cylinder to visualize spray and combustion development. There are numbers of researchers that are involved in the development of optical measurement test rigs for fuel spray, whereby the design is made according to their different scope of studies. Optical measurement is usually focusing on two categories: macroscopic and microscopic parameters. The macroscopic parameters such as spray tip length and cone angle can be obtained through direct visualization methods. Meanwhile, microscopic parameters such as velocity, droplet size, and scalar field can be obtained by using PIV or PDPA techniques (Algayyim et al. 2018; Bohl et al. 2017; Tan et al. 2017).

Understanding the fundamentals knowledge of fuel spray development is essential towards achieving the optimum performance for the internal combustion engine. The engine's performance is influenced by the characteristics of the fuel and the quality of the air–fuel mixture; thus, it is critical to ensure that the injection process is as efficient as possible. As a result, it is crucial to analyse the fuel injection characteristics, as they will reveal solutions to improve the process.

In this paper, the development of an experimental setup used is presented based on the objective to measure the fuel spray characteristics. The optical measurement techniques were used to investigate the fundamental diesel fuel spray characteristics in a CVCC. Several experiments were carried out to see how diesel performs when the injection pressure is altered. A CVCC was developed with an optical window in order to accommodate a space for a camera to capture the fuel injection process. The optical window was made of fused silica, which could withstand high temperatures and pressures during combustion. A high-speed camera was used to record the

spray development process. At various injection configurations, the spray tip penetration and cone angle were observed. This setup could also be used to determine the combustion performance of various fuels.

8.2 Methodology

The quality of the air–fuel mixture, which is dependent on the fuel injection into the combustion chamber, has a significant impact to the combustion performance. As a preliminary study, diesel fuel spray characteristics were studied at different fuel injection pressures. The experimental setup for measuring spray characteristics is shown in Fig. 8.1. This experimental setup has been prepared to analyse significant parameters that contribute towards effective condition for spray and combustion development. With regards to the spray development, the setup can be segmented into three stages of experimental processes which are (1) fuel preparation; (2) fuel injection; and (3) image capturing. This setup consists of A: fuel tank with filter, B: controller, C: electric motor, D: fuel pump, E: optical cylinder, F: injector, G: high-speed camera, and H: backlight source.

Focusing on the spray development, the experiments were carried out by supplying fuel from the tank into the fuel pump through a filter to ensure that unintentional particles would not pass through the fuel system. An electric motor was coupled to a fuel pump to pressurize the fuel to the required injection pressure. As pressure built up in the pump section, a signal was sent to the motor driver to give input on further rotation to keep a sustainable pressure within the fuel line. A pressure regulator controlled the required fuel pressure needed to supply the injector where the close/open valve was regulated by a switch box. This switch box was also linked

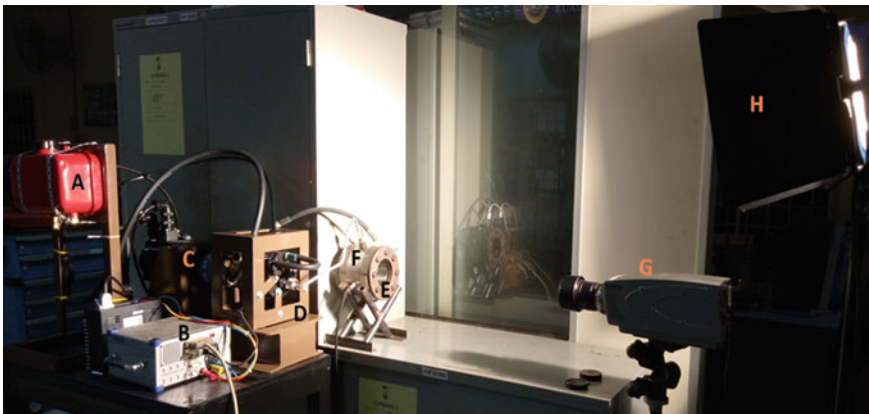


Fig. 8.1 General layout for experimental setup

to the high-speed camera which was put in a ready mode as the valve opened a required pressure for injection stage.

If the pressure regulator valve was kept closed, the fuel would keep circulating within the pressure pump. Once the pressure built up in the fuel line was at the required pressure, the pressure regulator would release a certain amount of fuel to an injector where a needle inside it would push backwards to allow the pressurized fuel to burst through the nozzles of holes from the injector which was attached to an optical cylinder. Figure 8.2 shows the schematic of experimental layout that consists of the fuel injection system, optical cylinder, and high-speed camera.

Meanwhile, the five holes injector (Delphi EJBR04601Z) was used to spread spray inside the cylinder. The holes approximate diameter of 0.19 mm was evenly positioned at angle 72° , and the injection-enclosed angle was 156° . Figure 8.3 shows the close-up view of the injector tip. To open the injection tip nozzles, the injector required approximately 120 bar of pressurized fuel to allow the needle push backwards by a spring effectively. The pressure built up within the fuel line indicated by a pressure gauge ensured the required fuels pressure before being released to the injector. An optical cylinder was prepared to visualize the spray characteristics at certain variables conditions. This cylinder having an inner diameter of 70 mm was made of stainless steel grade 304 and end closed with sight glasses at both ends. The optical cylinder had also an inlet valve port to supply pressurized air at 2 bar inside the cylinder. For this study, injection pressures chosen were 30 MPa, 40 MPa, and 50 MPa, respectively.

A high-speed camera (Olympus i-SPEED TR) was deployed and positioned perpendicular to the plane of the sight glass to capture the image of fuels' spray spreads. The focus length between the camera lens and injection sprays was set up towards plane of optimum images sharpness. As the image captured perpendicular to the tip of the injector but slanting 78° (injection-enclosed angle 156°), the true length of the spray had to be calculated with respect to centre axis of the injector

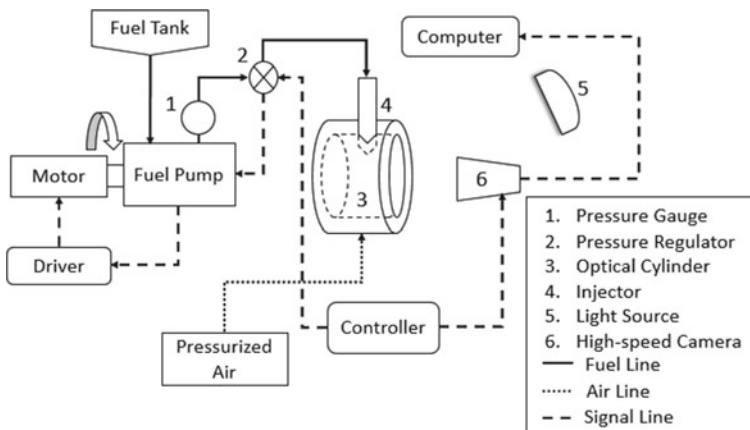
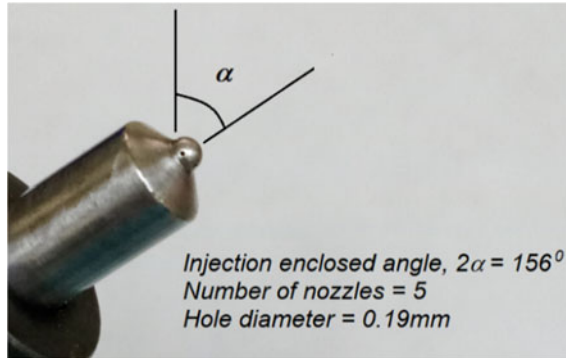


Fig. 8.2 Schematic of experimental layout

Fig. 8.3 Close-up view of injector tip



tip. After start of injection (SOI), the fuel spray was observed for a duration of up to 5 ms as further time would result the spray to reach to the wall of the cylinder. After that, the images were transferred to the i-SPEED Viewer software, and the spray measurements were performed using the SolidWorks CAD software. This technique was also described in the previous study in determining the spray characteristics by visualization (Soid and Zainal 2014).

8.3 Results and Discussion

The development of test rig has enabled fuel characteristics investigation for replication of a diesel direct injection system. Figure 8.4 shows macroscopic views of the injection spread recorded by a high-speed camera setting at certain image focus length over period of milliseconds. Instead of having visual results, these views enabled further investigation on spray characteristics which integrate to properties and condition of injection fuel such as fluid density and viscosity, effects of temperature and pressure, performance of injector, as well as in different types and blends of fuel.

To determine the performance of the fuel spray, there are three indicators that exhibit characteristics of the tested fuel: (1) tip penetration (unit: mm length), (2) cone angle (unit: degree angle), and (3) spray velocity (unit: metre per second). In the current study, these parameters were obtained by processing the image of the spray using the CAD software to measure the length and angle of sprays. Meanwhile, spray speeds were calculated from data of the tip penetration length over time. Figures 5a and b show the plotted data of the standard diesel tested at different injection pressures. In general, a good characteristic of a spray was obtained as indicated by the large cone angle size and speed of penetration, whereby the fuel dispersed widely into the ambient to atomize with air within shorter duration. Conversely, a bad characteristic of spray was happened when a narrow cone angle was produced and not able to disperse into the air but impingement to the cylinder side wall.

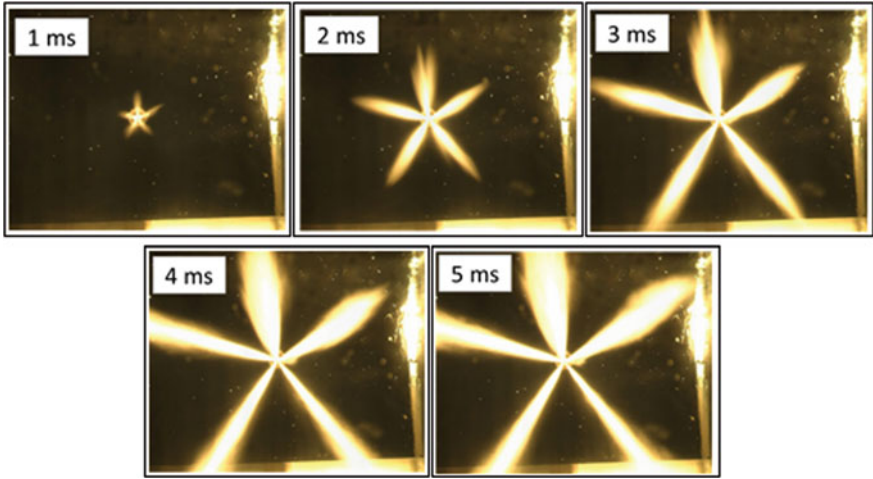
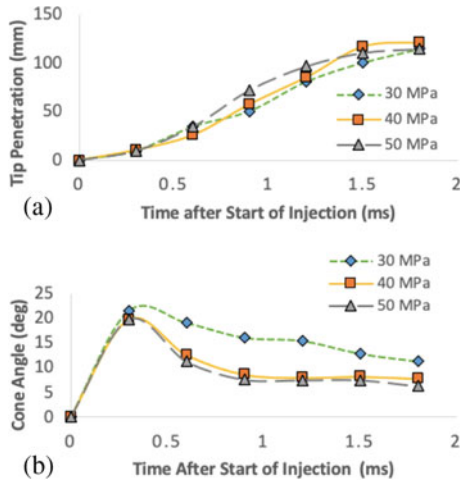


Fig. 8.4 Typical views of the spray patterns from the multi-hole’s injector for 30 MPa bar diesel fuel injection pressure at ambient pressure

Fig. 8.5 Diesel fuel **a** tip penetration and **b** cone angle at various injection pressures



8.4 Conclusion

The optical measurement test rig was successfully developed for the measurement of the fuel spray development process in a CVCC. This technique can be used to model the actual fuel spray process in an internal combustion engine. Various injection parameters can be changed, and their effect to the spray development can be observed. This setup can be used to study various alternative fuels such as biodiesel and plant oil. The results from the analysis can be compared to conventional diesel fuel. Increasing

the injection pressure might also close the gap between the high-viscosity fuels when compared to diesel at standard injection pressure. It can be concluded that this optical technique can help in understanding the fundamental of fuel spray development in terms of tip penetration and cone angle.

References

- Alagumalai A (2014) Internal combustion engines: progress and prospects. *Renew Sust Ener Rev* 38:561–571
- Algayyim SJM, Wandel AP, Yusaf T (2018) The impact of injector hole diameter on spray behaviour for butanol-diesel blends. *Energies* 11(5):1298
- Bohl T, Tian G, Smallbone A et al (2017) Macroscopic spray characteristics of next generation bio-derived diesel fuels in comparison to mineral diesel. *Appl Energ* 186(3):562–573
- Ghiji M, Goldsworthy L, Brandner PA et al (2017) Analysis of diesel spray dynamics using a compressible Eulerian/VOF/LES model and microscopic shadowgraphy. *Fuel* 188:352–366
- Martins J, Brito FP (2020) Alternative fuels for internal combustion engines. *Energies* 13(16):4086
- Munsin R, Chung B, Shing L, Phunpheeranurak K, Phongphankasem T, Laonual Y, Jugjai S, Chanchaona S (2013) Design of constant volume combustion chamber (CVCC) with pre-combustion technique for simulation of CI engine conditions. In: *The 4th TSME international conference on mechanical engineering*, vol 16
- Soid SN, Zainal ZA (2014) Combustion characteristics and optimization of CPG (compressed producer gas) in a constant volume combustion chamber. *Energy* 73:59–69
- Soid SN, Zainal ZA, Iqbal MA et al (2012) Macroscopic spray characteristics of palm oil-diesel blends in a constant volume combustion chamber. *J Sci Ind Res India* 71:740–747
- Tan YH, Abdullah MO, Nolasco-Hipolito C et al (2017) Engine performance and emissions characteristics of a diesel engine fueled with diesel-biodiesel-bioethanol emulsions. *Energ Convers Manage* 132:54–64

Chapter 9

Effect of Rectangular Fins on the Heat Transfer Performance of an Automotive Radiator



Faiza M. Nasir

Abstract The automotive radiator is a type of a compact heat exchanger with the main role to reduce the temperature of the coolant from the engine. The radiator is fitted with many types of fins with the purpose to enhance the heat transfer while reducing the overall size of the radiator. In this simulation study, the effect of using rectangular fins on the radiator heat transfer performance is investigated. Two radiator models were created, one without fins and the other one with rectangular fins. The effect of varying the convection heat transfer coefficient and the coolant's flowrate on the radiator's performance were also studied. It is observed that by adding fins, the coolant's temperature drop increases by 560% and the heat transfer rate increases by 283%. The results also show that as the convection heat transfer coefficient increases, the thermal performance of the radiator improves but remains constant as the coolant flowrate increases.

Keywords Automotive radiator · Compact heat exchanger · Thermal simulation · Thermal resistance

9.1 Introduction

In order to meet the increased demand for more powerful engines, there is a need for automotive radiators with enhanced thermal transport capacity. Many researches have been conducted to improve the radiator's thermal transport by manipulating its design or its coolant (Tran and Wang 2020; Kumar et al. 2020; Shariff et al. 2018; Sahoo et al. 2017; Mohamed et al. 2019). Oliet et al. (2007) conducted parametric studies on automotive radiator and discovered that air and coolant flowrate have a substantial impact on the radiator's heat transfer performance. Experimental parametric study of the fin geometry was also performed by Ismael et al. (2016). They fabricated five

F. M. Nasir (✉)
Universiti Kuala Lumpur, Malaysian Spanish Institute, Kulim Hi-Tech Park, 09000 Kulim,
Kedah, Malaysia
e-mail: faiza@unikl.edu.my

different radiators with different fin pitch wave distance and tested their performance under a wind tunnel.

In an experimental numerical study conducted by Yadav and Singh (2015), the effect of different radiator operating parameters such as coolant mass flowrate, inlet coolant temperature, and the addition of antifreeze on the radiator's thermal performance was investigated. They found a direct relationship between the cooling capacity and the coolant's flowrate and its inlet temperature. A numerical study by Shariff et al. (2018) that focused on the thermal performance of car radiator in Kano State of Nigeria demonstrated that by adding fins, a 25% decrease in the outlet temperature and 33.2% increase in heat removal capacity can be attained. Sakthivel et al. (2021) numerically investigated the effect of using different fin materials (copper and aluminum) and shape of fins (rectangular and curved edge) on the thermal performance of the radiator.

Several studies have been conducted to compare the thermal performance of various shapes of fins for fin and tube heat exchanger. In a study by Wen and Ho (2009), it was shown that compounded fins have the highest effectiveness than plain and wavy fins. Comparing performance of heat exchangers with plain, wavy, and louvered fins under constant fan power, Yan and Sheen (2000) proved that louvered fins have the greatest impact on the heat transfer coefficient of the heat exchanger. Similar superior performance of louvered fins was also found in studies by Carija et al. (2014) and Okbaz et al. (2018).

The main goal of this study is to use SolidWorks to investigate the influence of rectangular-shaped fins on the thermal performance of an automotive radiator. The temperature decrease of the coolant, the total heat transfer rate, and the thermal resistance all contribute to the overall performance.

9.2 Simulation Setup

9.2.1 Simulation Models

The specification for the radiator with the rectangular fins is shown in Table 9.1. The material for the radiator is the aluminum alloy 6061, and the coolant used is water. There are two models simulated in this study: the base model and the fin model. The base model is basically the radiator tube without any fins attached to it, whereas for the fin model, the radiator is fitted with rectangular-shaped fins. The models were created using SolidWorks (see Fig. 9.1).

Table 9.1 Specification of the base model A

| | |
|----------------|----------------------------------|
| Tube depth | 21.58 mm |
| Tube thickness | 0.3 mm |
| Core width | 635 mm |
| Fin pitch | 2.5 mm |
| Fin length | 8.59 mm |
| Tube height | 2.4 mm |
| Core height | 382 mm (actual) 50 mm (model) |
| Fin thickness | 0.1 mm |

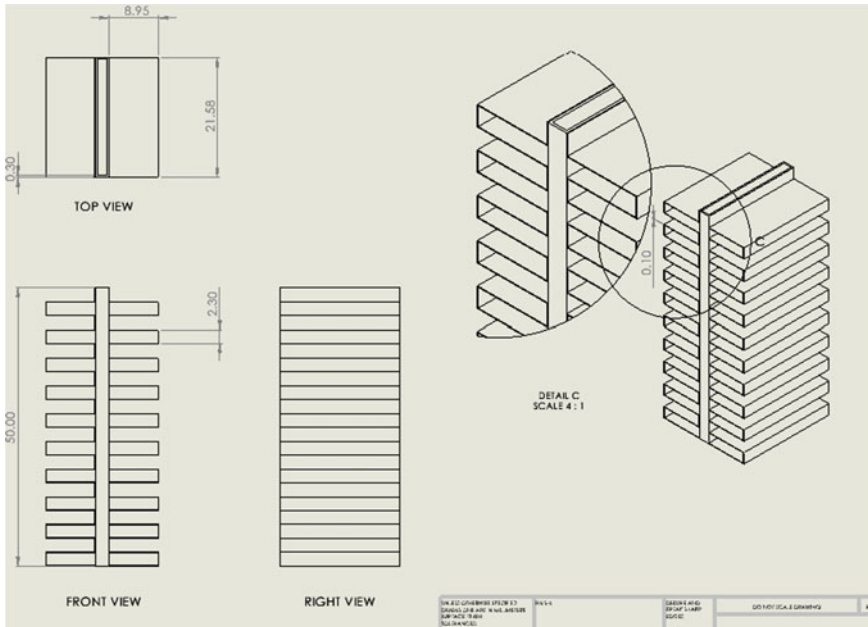


Fig. 9.1 Detailed drawings of the fin model

9.2.2 Boundary Conditions

The thermal simulation for the models was conducted by using the steady thermal-external flow simulation in SolidWorks. The coolant’s inlet temperature is 85 °C, and the temperature of the inlet air is 28 °C. The external convection heat transfer coefficient is varied between 10 and 200 W/m²·K, implying different speeds of the car. The coolant’s inlet flowrate is varied between 5 and 60 LPM, with higher flowrate indicating higher pumping power requirement.

9.2.3 Data Analysis

The heat transfer performance of the radiator is measured by the coolant's temperature drop across the tube, the thermal resistance, and the total heat transfer rate. The temperature drop is defined by Eq. (9.1), and the thermal resistance is defined by Eq. (9.2).

$$\Delta T = T_{w,in} - T_{w,out} \quad (9.1)$$

$$R_t = \frac{T_{w,in} - T_{s,min}}{Q} \quad (9.2)$$

where T_w is the coolant's temperature, $T_{s,min}$ is the minimum temperature of the solid wall of the radiator, and Q is the total heat transfer rate of the radiator.

9.3 Results and Discussion

9.3.1 Effect of Fins

The addition of fins to the radiator will adversely affect its performance. The simulation results for the base model and the fin model are shown in Table 9.2.

As mentioned earlier, the base model is the radiator tube without any fins and the fin model is the radiator with fins. From the results, the total heat transfer rate for the fin model is 282.95% higher than that for the base model. The result shows that the heat transfer rate of the fin model is 38.51 W greater than the base model. The greater heat transfer is attributed to the greater surface area for heat exchange of the fin model that is fitted with the rectangular fins.

The addition of fins to the radiator tube has resulted in a significant rise in the temperature decrease of the coolant flowing through the tube. Without any fins, the radiator is only able to reduce the coolant's temperature by 0.52 °C for 50 mm length of the radiator tube. By adding the rectangular fins, the coolant's temperature reduces by 3.43 °C for 50 mm length of the radiator tube, indicating the significant contribution of the fins in dissipating excess heat from the coolant. The temperature

Table 9.2 Simulation results for base model and the fin model

| Model | Temperature drop | Heat transfer rate (W) | Total surface area |
|--|------------------|------------------------|--------------------|
| Base model | 0.52 | 13.61 | 0.0024 |
| Fin model | 3.43 | 52.12 | 0.0209 |
| Absolute difference of fin model from base model (%) | 559.62 | 282.95 | 770.83 |

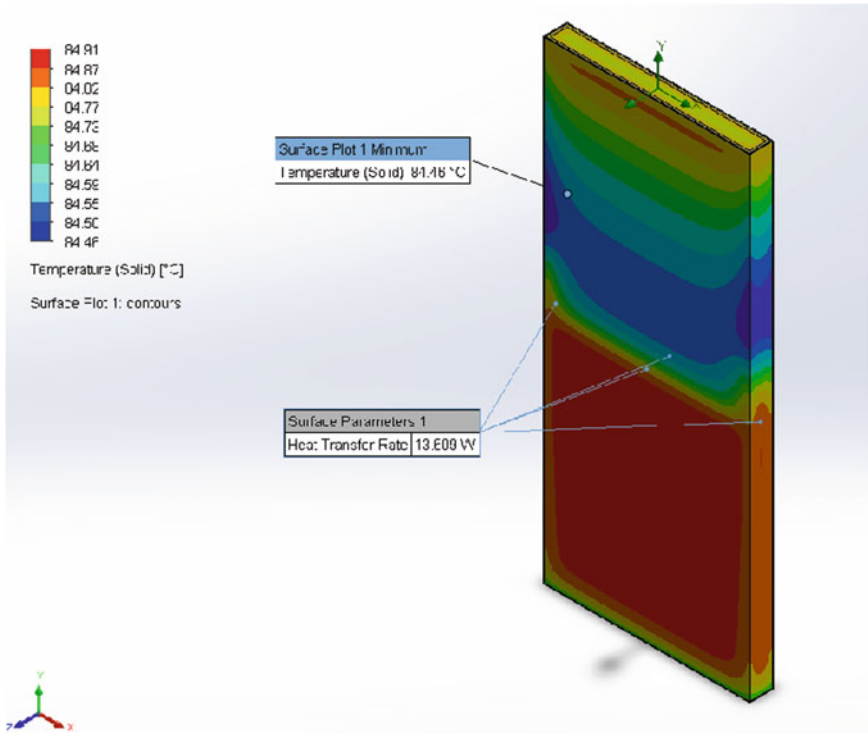


Fig. 9.2 Temperature contour plot for the base model

contour plot for both the base model and the fin model are shown in Figs. 9.2 and 9.3.

9.3.2 Effect of Convection Heat Transfer Coefficient

Oliet et al (2007) investigated a few factors that influence the performance of a radiator, including air and coolant flow, fin density, and air temperature. It has been demonstrated that the mass flow rates of the air and coolant have a significant impact on the heat transfer and performance of the radiator. The convection heat transfer coefficient is inextricably linked to the velocity of the air; the higher the velocity, the greater the value of the coefficient. Figure 9.4 shows the effect of the heat transfer coefficient, h on the thermal resistance and the temperature drop of the radiator with rectangular fins.

Figure 9.4 shows the positive relationship between h and the coolant’s temperature drop. As the heat transfer coefficient increases, the coolant’s temperature drop increases. When $h = 200 \text{ W/m}^2\cdot\text{K}$, the temperature drop of the coolant is $3.43 \text{ }^\circ\text{C}$,

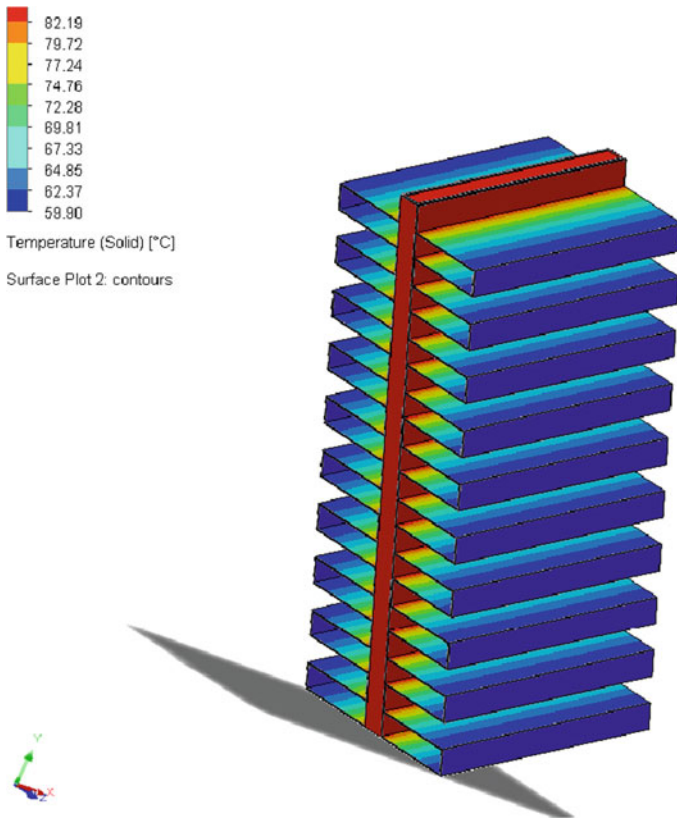


Fig. 9.3 Temperature contour plot for the fin model

and when $h = 50 \text{ W/m}^2\cdot\text{K}$, the drop reduces to $1.23 \text{ }^\circ\text{C}$ for 50 mm length of radiator's tube. The higher value of h indicates higher convection heat transfer occurring on the external surface of the radiator, thus promoting enhanced heat removal from the radiator to the surroundings. This is proven by Fig. 9.5 that shows the greater heat transfer rate produced when the convection heat transfer coefficient is the highest at $200 \text{ W/m}^2\cdot\text{K}$.

There is a negative relationship between heat transfer coefficient and the thermal resistance (Fig. 9.4). The thermal resistance indicates the radiator's resistance to heat transfer, the lower the better, as lower resistance allows a greater amount of heat to be transferred rather than stored. At the highest heat transfer coefficient of $200 \text{ W/m}^2\cdot\text{K}$, the radiator's thermal resistance is $0.571 \text{ }^\circ\text{C/W}$, while when $h = 50 \text{ W/m}^2\cdot\text{K}$, the thermal resistance is $0.701 \text{ }^\circ\text{C/W}$. This is translated to a reduction of 18.54% in thermal resistance when h increases by thrice.

Figure 9.5 shows the total of heat transfer of the radiator increasing from the minimum value of 5.03 W to the maximum value of 63.802 W as the heat transfer

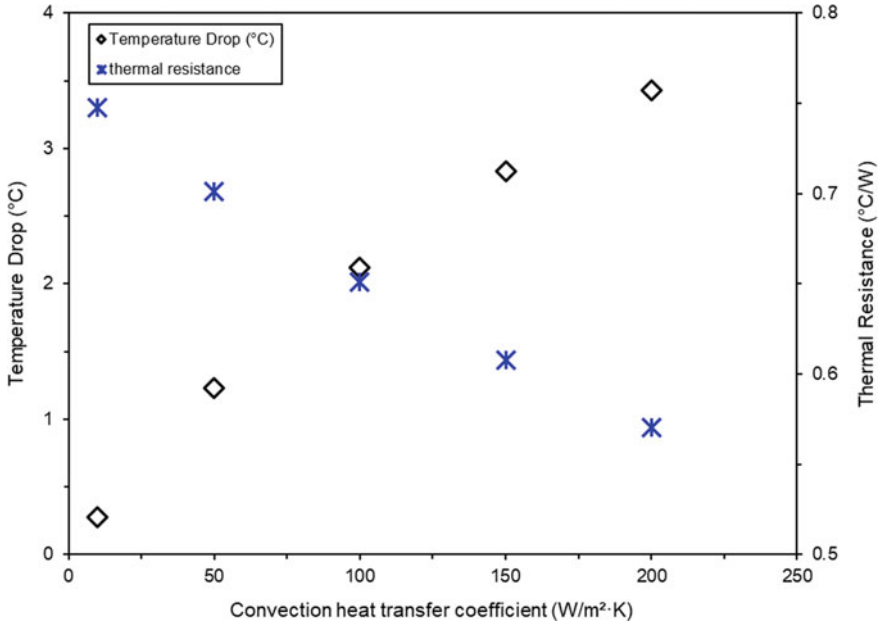


Fig. 9.4 The effect of h on the temperature drop and the thermal resistance

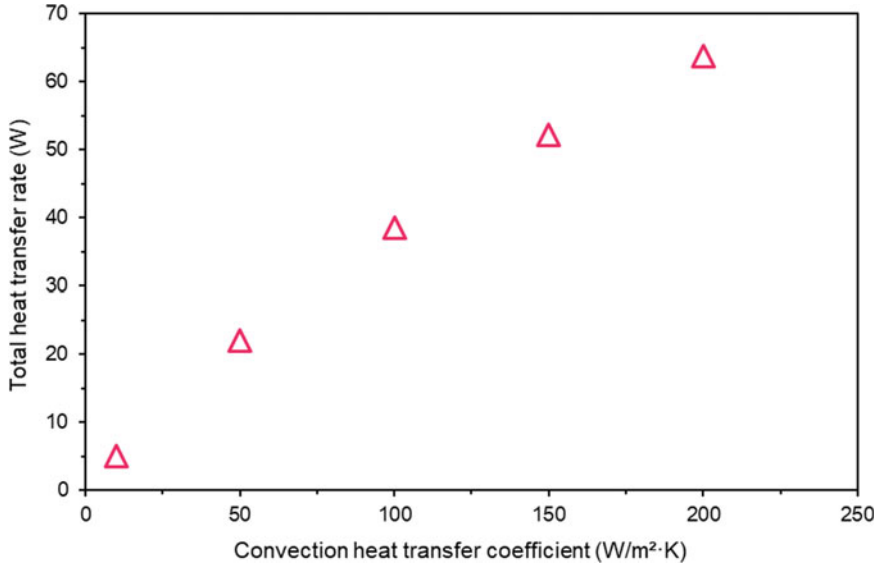


Fig. 9.5 The effect of h on the total heat transfer

increases from 3 to 200 W/m²·K. The higher value of h indicates higher convection heat transfer occurring on the external surface of the radiator, thus promoting enhanced heat removal from the radiator to the surroundings.

9.3.3 Effect of Coolants' Flow Rate

Studies showed that one of the factors that strongly affect the radiator's performance is the coolant flow rate. In this work, the coolant flow rate is varied between 5 and 60 LPM. Figure 9.6 shows the effect of the coolant's flow rate on the temperature drop and the thermal resistance. At the lowest flowrate of 3 LPM, the temperature of the coolant reduces by 6.18 °C while at the highest flowrate of 60 LPM, the temperature reduces by 1.21 °C. The results indicate that as the flowrate increases, the temperature reduction of the coolant reduces, implying that for an effective operation of the radiator, it is better to control the coolant flowrate to the lowest possible. Similar relationship between the coolant's flowrate and the thermal resistance was also observed (Fig. 9.6). As the flowrate increases, the thermal resistance reduces to at least 0.031 °C/W when the coolant's flowrate is 60 LPM.

The effect on the coolant's flowrate on the total heat transfer is considered to be insignificant as the heat transfer varies between 36.23 and 38.98 W when the flowrate

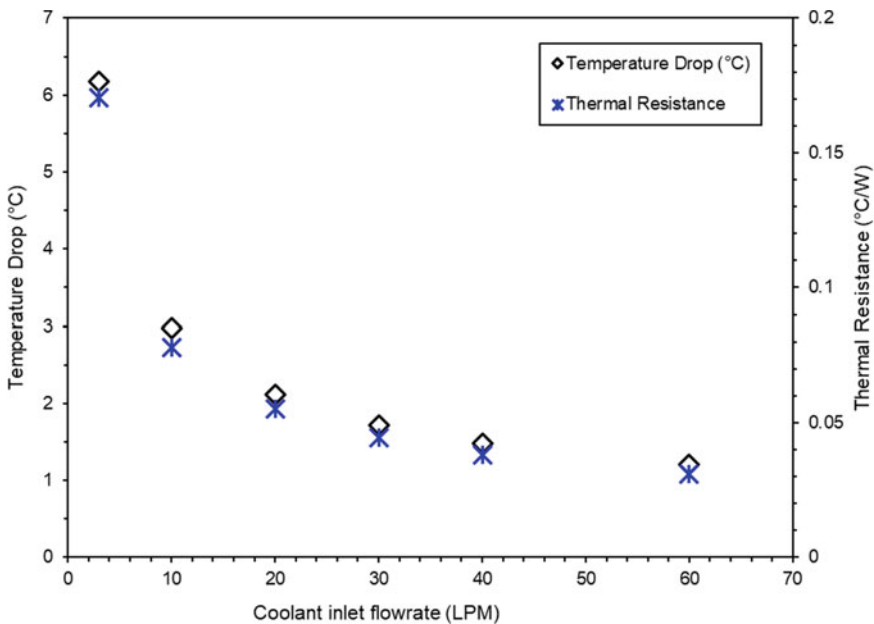


Fig. 9.6 The effect of coolant inlet flowrate on the temperature drop and the thermal resistance

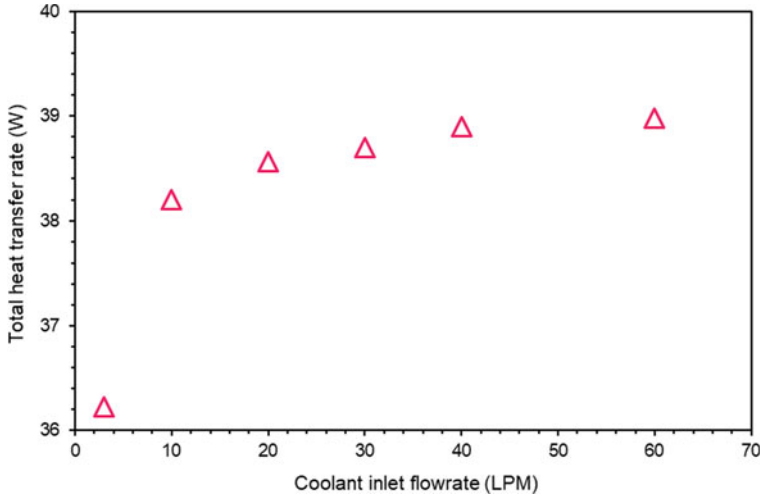


Fig. 9.7 The effect of coolant inlet flowrate on the total heat transfer rate of the radiator

changes from 3 to 60 LPM (Fig. 9.7). It can be observed that the effect is almost negligible when the coolant’s flowrate is greater than 10 LPM.

The simulation results indicate that at low coolant’s flowrate of 3 LPM, the temperature of the coolant can be reduced by at most 6.18 °C albeit at a higher thermal resistance of 0.17 °C/W. The resulted thermal resistance is considered to be within favorable value indicating low radiator’s resistance to heat transfer. There is also an insignificant effect of the flowrate on the total heat transfer. Therefore, based on the results, it is best to operate the radiator with coolant’s flowrate of 3 LPM, instead of a higher value.

9.4 Conclusion

The influence of rectangular fins on the heat transfer performance of an automobile radiator was the focus of this research. There were two types made: one without fins and one with rectangular fins. The effect of changing the convective heat transfer coefficient and the flowrate of the coolant on the coolant’s temperature drop, thermal resistance, and overall heat transfer rate was studied. The results showed that the convection heat transfer coefficient must be as high as feasible to improve the radiator’s performance in dissipating heat from the engine’s coolant. The flowrate of the coolant has no effect on the radiator’s thermal performance, suggesting that the coolant can flow with the lowest flowrate while still delivering comparable thermal performance with the greater flowrate.

References

- Čarija Z, Franković B, Perčić M, Čavrak M (2014) Heat transfer analysis of fin-and-tube heat exchangers with flat and louvered fin geometries. *J Int Acad Refrig* 45:160–167
- Ismael T, Yun SB, Ulugbek F (2016) Radiator heat dissipation performance. *J Electron Cool Therm Control* 6:88–96
- Kumar A, Hassan MA, Chand P (2020) Heat transport in nanofluid coolant car radiator with louvered fins. *Powder Technol* 376:631–642
- Mohamed KA, Younis O, Hussein AK (2019) Numerical investigation of possibility of using shape memory alloy in louvered fins radiators. *CFD Lett* 11:103–116
- Okbaz A, Pınarbaşı A, Olcay AB, Hilmi Aksoy M (2018) An experimental, computational and flow visualization study on the air-side thermal and hydraulic performance of louvered fin and round tube heat exchangers. *Int Int J Heat Mass Transf* 121:153–169
- Oliet C, Oliva A, Castro J, Pérez-Segarra CD (2007) Parametric studies on automotive radiators. *Appl Therm Eng* 27(11–2):2033–2043
- Sahoo RR, Ghosh P, Sarkar J (2017) Performance comparison of various coolants for louvered fin tube automotive radiator. *Therm Sci* 21:2871–2881
- Sakthivel TG, Abishek KM, Yadav RA et al (2021) Design and analysis of radiator fins. *Int J Eng Res Technol*:386–395
- Shariff KB, Abdullahi B, Abubakar SB (2018) Modelling and simulation of car radiator: effects of fins under the atmospheric condition of Kano, Nigeria. *J Adv Res Fluid Mech Therm Sci* 48(1):1–16
- Tran N, Wang CC (2020) Optimization of the airside thermal performance of mini-channel-flat-tube radiators by using composite straight-and-louvered fins. *Int J Heat Mass Transf* 160:120163
- Wen MY, Ho CY (2009) Heat-transfer enhancement in fin-and-tube heat exchanger with improved fin design. *Appl Therm Eng* 29:1050–1057
- Yadav JP, Singh BR (2015) Study on performance evaluation of automotive radiator. *SAMRIDDHI. Eng Sci Technol Int* 2
- Yan WM, Sheen PJ (2000) Heat transfer and friction characteristics of fin-and-tube heat exchangers. *Int J Heat Mass Transf* 43:1651–1659

Chapter 10

Effect of Geometrical Dimension of Fins on the Cooling Performance of an Air-Cooled Engine Cylinder Block



Faiza M. Nasir

Abstract One of the key components vulnerable to significant thermal loads and temperature changes is the internal combustion engine cylinder and thus requires an effective method to dissipate the high amount of heat energy. In order to enhance the heat removal from the engine cylinder, it is fitted with fins or extended surfaces, with different materials, shapes, and sizes. A simulation study was carried out in this work to explore the influence of varying fin sizes on the engine cylinder block. The effect of the geometrical dimensions of fins, such as length and thickness, on the cooling performance of the engine block is investigated in this study. Using the steady-state thermal analysis of the engine block, results of the temperature drop, the heat transfer rate, and the thermal resistance were obtained. Results showed that the performance of the engine block is improved when the fin thickness is between 4 and 5 mm, the length is 30 mm and the number of fins is 7. It can be concluded that fin thickness and fin length have substantial impact on the thermal performance of the engine block.

Keywords Engine block · Compact heat exchanger · Thermal simulation · Thermal resistance

10.1 Introduction

The internal combustion engine cylinder is subjected to extreme temperature and pressure variations during operation. Heat is generated in the engine mainly due to the fuel combustion and partly due to the friction between the moving parts. The engine cylinder is usually made of material with lower melting temperature than the combustion temperature. Therefore, the moving parts in the engine cylinder are prone to melting if its temperature is not properly managed. Engine performance would be compromised by excessive engine temperature since it would diminish the

F. M. Nasir (✉)

Mechanical Section, Universiti Kuala Lumpur Malaysian Spanish Institute, Kulim Hi-Tech Park, 09000 Kulim, Kedah, Malaysia
e-mail: faiza@unikl.edu.my

volumetric efficiency, promote pre-ignition and detonation (Sahoo et al. 2021), and reduce the overall efficiency. Thus, to avoid thermal damage of cylinder parts and materials as well as to minimize engine performance degradation, the engines are purposefully engineered to lose around 70% of their heat through cooling systems with the remainder of the heat being transformed to useable mechanical energy (Thornhill and May 1999; Thornhill et al. 2003).

Cooling systems for an engine cylinder can be in the forms of water cooling, oil cooling, or air cooling depending on the amount of heat generated by the engine. The air-cooling method is primarily employed in small capacity motorcycle engines as they have minimal space requirements and they have a sufficient amount of air flow movement to facilitate the heat dissipation process. Fins or extended surfaces are attached to the engine cylinders have been proven to enhance the amount of heat dissipated significantly. The fins increase the surface area of the cylinder and thus provide far greater heat transfer. The fins, generally thin strips of highly conducting metals, are used on a surface where the convective heat transfer coefficient, h , is very low.

The design of the fins is very important as it can adversely affect the engine performance and longevity. Several design factors that are considered in evaluating the fins' heat transfer performance are fin shape or fin type, fin pitch, fin thickness, fin length, and fin material.

Comparison between wavy fins and annular fins was conducted by Ranjan and Das in terms of heat transfer and effectiveness indicating superior performance by wavy fins (Ranjan and Das 2014). Comparing elliptical fins and cylindrical fins experimentally, the former was found to have higher fin efficiency (Nagarani and Mayilsamy 2010). Heat transfer and pressure drop are both improved by the use of wavy fins in fin-and-tube heat exchangers, according to CFD analysis of fin-and-tube heat exchangers with plain and wavy fins (Bhuiyan et al. 2010). Louver fin surfaces have been proven to enhance the heat transfer compared to other fin types. Heat transfer enhancement of 58% was observed for louvered fins compared to flat fins in a study by Carija et al. (2014). They also suggested that caution should be exercised when choosing the optimal for louvered fins. Experimental comparative study was conducted by Okbaz et al. (2020) to study the impact of using louvered fins and wavy fins for heat exchangers. According to studies, louvered fin surfaces outperform un-interrupted fin surfaces such as plain fin and wavy fin surfaces in terms of heat transfer enhancement (Lozza and Merlo 2001; Wang et al. 2015; Tang et al. 2009).

Fin spacing or fin pitch is a measure of the gap or distance between one fin and the next fin. The relationship between fin spacing and heat transfer performance is still uncertain, as evidenced by the fact that results might be inconsistent (Awais and Bhuiyan 2018). Having higher fin pitch indicates lesser quantity of fins requirement, that consequently lowers the weight and the cost of the heat exchanger (Memon et al. 2005).

In a simulation study by Durgam et al. (2021), comparing the thermal performance of an engine cylinder block fitted with fins of different materials, it was found that aluminium alloy gives the greatest performance. In this study, they considered fin

materials such as gray cast iron, aluminum alloy, and copper alloy. Aluminum alloy was also found to be the best material for fins of an engine cylinder block in a numerical study conducted by Reddy Kummitha and Reddy (2017). Other research looking into the effect of fin materials on heat transfer came to the same conclusion: Aluminum alloy had superior heat transfer performance (Memon et al. 2005; Karthik 2018; Chaitanya et al. 2014; Madhu et al. 2015).

It is the primary objective of this study to investigate numerically the effect of the geometrical dimensions of the fins, such as length and thickness, on the thermal performance on an engine block. The impact of the number of fins on the performance is also considered in this study.

10.2 Simulation Study

10.2.1 Simulation Base Model

The schematic diagram for the engine cylinder considered for this work is shown in Fig. 10.1. The engine cylinder was fitted with 5 annular fins with uniform thickness of 6 mm. Aluminum TS-6061 was used as the material for the engine cylinder and the fins, having a thermal conductivity 180 W/m·K, specific heat 896 J/kg·K, and density 2700 kg/m³. The length of the engine cylinder is 150 mm, and the outer and inner radius of the cylinder are 25 mm and 20 mm, respectively. The length of the fins was 20 mm, and the distance between the fins are equal with each other.

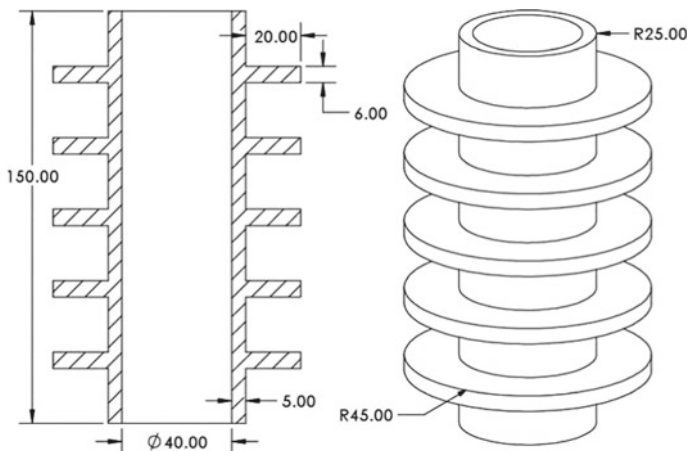


Fig. 10.1 Design of engine cylinder and fins

10.2.2 Assumptions and Boundary Conditions

A few assumptions have been made in order to conduct the thermal analysis of the engine cylinders with annular fins.

- The temperature of the inside wall of the engine cylinder is 500 K or 226.85 °C.
- The radiation heat transfer effect on the engine block is negligible.
- The thermal model of the engine block is a steady-state conduction model with a specified value of convection heat transfer coefficient, h .
- The temperature in the surrounding environment is assumed to be 300 K.

The boundary conditions for this study are inner surface temperature, ambient temperature, and coefficient of convection, h . The inner surface temperature of 500 K is assumed as this value reflects the temperature experienced by the engine cylinder during operation. The outer surface of the engine cylinder that includes the surface of the fins was subjected to convection boundary conditions, where convection heat transfer coefficient, h , is defined. Using the empirical correlation for the coefficient (Incropera et al. 2007), h is determined to be 50 W/m²·°C.

10.2.3 Independent Variables

The focus of this study is to assess the influence of different geometrical properties of the fins on the cooling performance of the engine block. Three geometrical characteristics of the fins are the focus of this study, which are the fin length, fin thickness, and the number of fins attached to the engine block. The length of the fin is varied between 5 and 30 mm, and the fin thickness varies between 2 and 10 mm. The number of fins attached to the engine block is varied between 2 and 7.

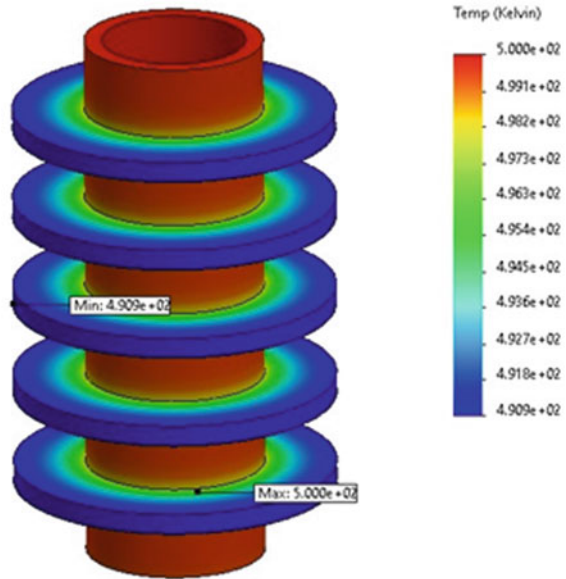
10.2.4 Response Variables

The cooling performance of the engine block is measured by the minimum temperature experienced by the engine block, the amount of heat dissipated, and the total thermal resistance. The first two parameters can easily be obtained from the simulation, while the thermal resistance, R_t , can be found by using Eq. (10.1).

$$R_t = \frac{T_{\max} - T_{\min}}{Q} \quad (10.1)$$

where T_{\max} is the maximum temperature of the engine, T_{\min} is the minimum temperature of the solid wall of the engine block, and Q is the total heat transfer rate.

Fig. 10.2 Temperature contour plot for the base model



10.3 Results and Discussion

10.3.1 Temperature Distribution of the Fin

The temperature distribution of the engine block fitted with 5 annular fins of 5 mm thickness and length of 20 mm is shown by the contour plot in Fig. 10.2. As can be seen in the figure, the wall surface of the engine block is constant at 500 K, whereas the fin experiences reduction in temperature from the inside to the fin tip. The minimum temperature of the engine block is denoted as the temperature at the fin tip, which is 490.9 °C (a reduction of 9.1 °C from the solid wall of the engine block).

10.3.2 The Effect of Fin Thickness

In this study, the fin thickness is varied from 2 to 10 mm. The effect of this variation on the temperature drop and the amount of heat transfer is shown in Fig. 10.3. The results indicate that the temperature drop reduces with the increase in the fin thickness. It is also found that the heat dissipated increases with the fin thickness. At fin thickness of 2 mm, the temperature drop is the highest at 17.7 °C but the heat transfer rate is the lowest at 665.19 W. For an engine block with fin thickness of 10 mm, the temperature drop is the lowest at 6.1 °C and the heat transfer rate is 719.75 W (similar with fin thickness of 8 mm). These results indicate that by increasing the fin thickness up to 5

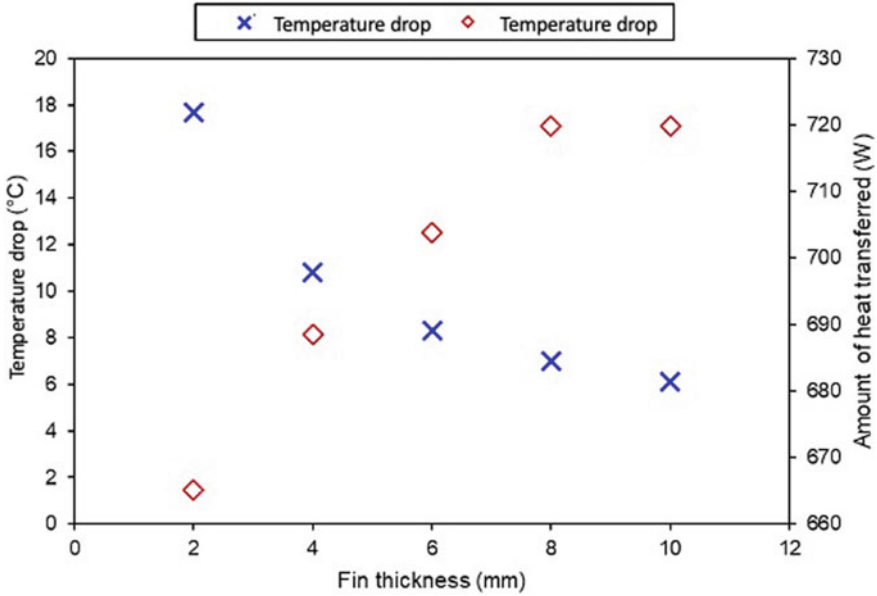


Fig. 10.3 The effect of fin thickness on the temperature drop and the amount of heat transferred from the engine block

times the original size, the heat transfer can be enhanced by 8.2% and the temperature drop reduces by 190%. By increasing the fin thickness, the available surface area for heat transfer increases, thus enhancing the amount of heat dissipation.

From Fig. 10.3, it can be observed that there is an optimum point where the amount of heat transferred and the temperature drop are desirable (both are at the highest possible values), which is occurring when the fin thickness is between 4 and 5 mm. It can also be seen that fin thickness that exceeds 8 mm does not produce significant change in the amount of heat transfer.

Figure 10.4 shows the effect of the variation in the fin thickness on the thermal resistance of the engine block. As the fin thickness increases from 2 to 10 mm, the thermal resistance decreases from 0.00266 to 0.00848 °C/W (reduction of 214%). As the main objective of fins that are attached to the engine block is to reduce the amount of heat and the temperature as much as possible, it is implied from the results that the fin thickness should be between 4 and 5 mm.

10.3.3 The Effect of Fin's Length

Studies showed that the length of fin or the radius of the annular fin produces significant effects on the thermal performance of a heat exchanger. In this study, the length of the fin is varied from 5 to 30 mm. The simulation results of the temperature drop

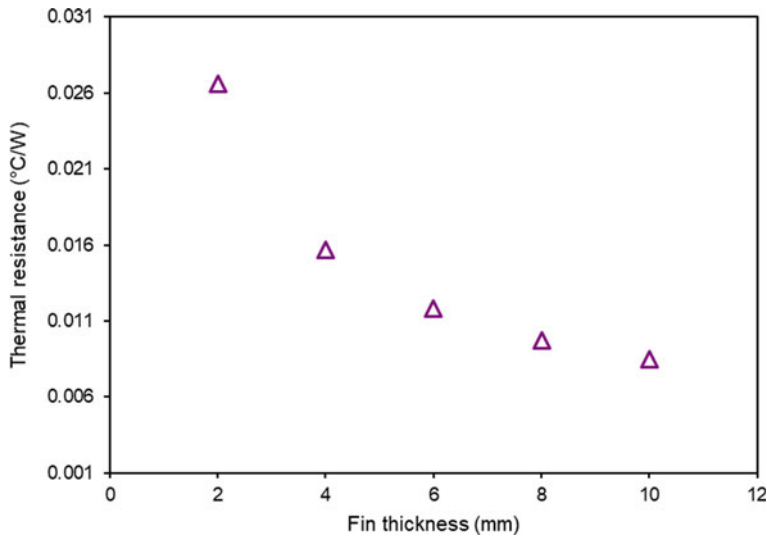


Fig. 10.4 The effect of fin thickness on the thermal resistance

and the amount of heat transferred from the engine block are shown in Fig. 10.5. It can be clearly seen that there are positive relationships between the fin's length and the temperature drop and the heat transfer rate. As the fin's length increases, the temperature drop and the heat transfer increase.

When the length is 5 mm, the temperature drop experienced by the engine block is 1.3 °C compared to 16.4 °C when the length is 30 mm, an improvement of 1162%. With the same variation in fin's length, there is an improvement of 190% in the heat transfer rate from the engine block. By increasing the fin's length, the surface area that is available for heat exchange process between the solid wall and the surrounding's air increases. Simulation results also demonstrated that the thermal resistance of the engine block increases with the fin's length of up to 214% from the lowest thermal resistance of 0.0038 °C/W (Fig. 10.6).

The results clearly showed that in order to dissipate heat and reduce the temperature of the engine block as much as possible, the length of the fins should be as large as possible, in this case, 30 mm.

10.3.4 The Effect of Number of Fins

For an engine block with annular fins with the same length and thickness, but different numbers of fins, the simulated minimum temperature of the engine block is maintained the same. Hence, only the results of heat transfer rate and thermal resistance for different number of fins are discussed (Fig. 10.7).

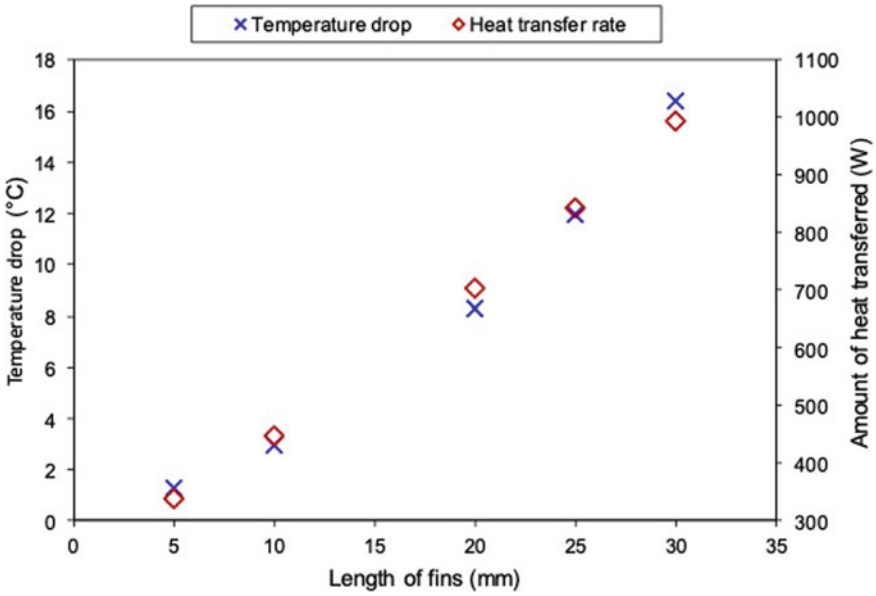


Fig. 10.5 The effect of fin's length on the temperature drop and the heat transfer rate

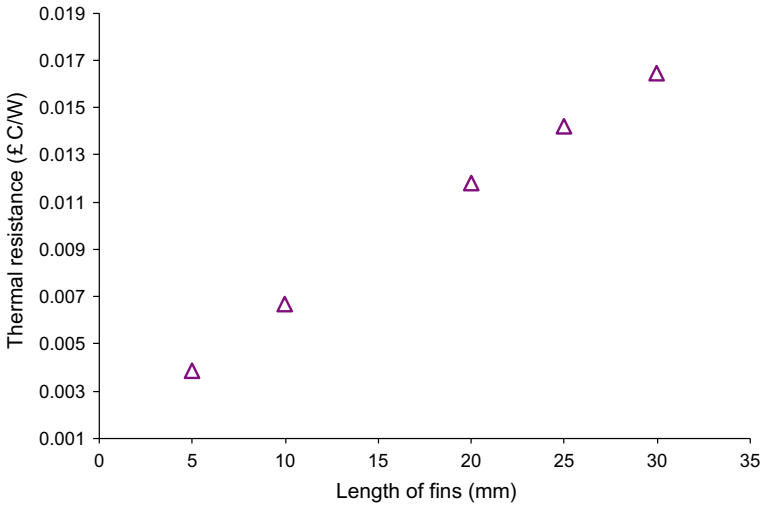


Fig. 10.6 The effect of fin's length on the thermal resistance

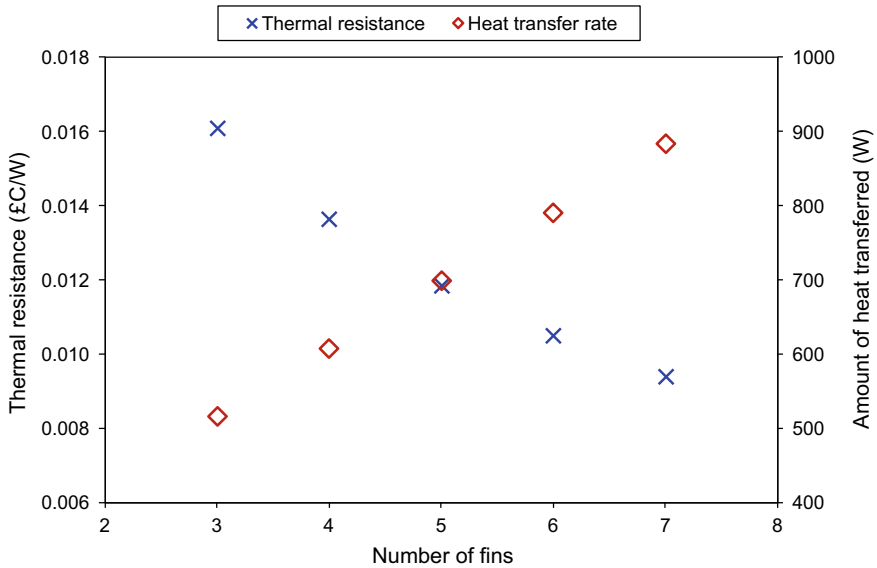


Fig. 10.7 The effect of the number of fins on the thermal resistance and the heat transfer rate

As the number of fins increases from 3 to 7 for the engine block, the amount of heat dissipated increases from 515.83 to 883.45 W (an increase of 71.3%). The thermal resistance also improved by 71.3% as well, as it is only affected by the heat transfer rate at the same minimum temperature of the block. The greater number of fins would produce greater surface area for the heat transfer process, thereby increasing the amount of heat energy that could be dissipated from the surface. Thus, the greater the number of fins attached to the engine block, the better the heat transferred.

10.4 Conclusion

This study focused on the effect of the geometrical dimensions of annular fins, such as length and thickness, on the heat transfer performance of an engine block. The effect of the number of fins on the performance is also investigated. The heat transfer performance of the engine block is characterized by the temperature drop from the inner wall of the block to the tip of the fin, the thermal resistance, and the amount of heat transferred by the block. From the study, it can be concluded that:

- The fin thickness does not significantly affect the amount of heat transfer, but the increase in thickness improves the thermal resistance tremendously.
- There exists an optimum thickness at which the heat transfer rate and the temperature drop are desirable.

- The length of the fins should be as high as possible, in this study, 30 mm as it produces the greatest enhancement in heat transfer rate, temperature drop, and the thermal resistance.
- The higher the number of fins attached to the engine block, the higher the improvement in the thermal performance of the block.

References

- Awais M, Bhuiyan AA (2018) Heat and mass transfer for compact heat exchanger (CHXs) design: a state-of-the-art review. *Int J Heat Mass Transf* 127:359–380
- Bhuiyan AA, Islam AKMS, Sadrul Islam AKM (2010) CFD analysis of different fin and tube heat exchangers. In: *Proceedings 13th annual paper meeting*, pp 1–8
- Čarija Z, Franković B, Perčić M, Čavrak M (2014) Heat transfer analysis of fin-and-tube heat exchangers with flat and louvered fin geometries. *Energy Econ* 45:160–167
- Chaitanya P, Rani B, Kumar K (2014) Thermal analysis and optimization of engine cylinder fins by varying geometry and material. *IOSR J Mech Civ Eng* 11:37–44
- Durgam S, Kale A, Kene N et al (2021) Thermal analysis of fin materials for engine cylinder heat transfer enhancement. *IOP Conf Ser Mater Sci Eng* 1126:1–8
- Incropera FP, DeWitt DP, Bergman TL, Lavine AS (2007) *Fundamentals of heat and mass transfer*. John Wiley & Sons, Hoboken New York
- Karthik S (2018) Material selection for fin based on thermal analysis using Ansys and ANN. *Int J Mech Eng Technol* 9:560–567
- Lozza G, Merlo U (2001) An experimental investigation of heat transfer and friction losses of interrupted and wavy fins for fin-and-tube heat exchangers. *Int J Refrig* 24:409–416
- Madhu P, Sateesh N, Neela Praveen KS (2015) Modeling and simulation of fins for 150cc engine. *Indian J Appl Res* 5:24–28
- Memon ZK, Sundararajan T, Lakshminarasimhan V et al (2005) Parametric study on fin heat transfer for air cooled motorcycle engine. *SAE Technical Papers*, 2005-26-361
- Nagarani N, Mayilsamy K (2010) Experimental heat transfer analysis on annular circular and elliptical fins. *Int J Eng Sci Technol* 2:2839–2845
- Okbaz A, Pınarbaşı A, Olcay AB (2020) Experimental investigation of effect of different tube row-numbers, fin pitches and operating conditions on thermal and hydraulic performances of louvered and wavy finned heat exchangers. *Int J Therm Sci* 151:106256
- Ranjan A, Das DH (2014) Heat transfer analysis of motorcycle engine cylinder using CFD under various fin geometries and speed condition. *Appl Mech Mater* 592–594:1612–1616
- Reddy Kummitha O, Reddy BVR (2017) Thermal analysis of cylinder block with fins for different materials using ANSYS. *Mater Today Proc* 4:8142–8148
- Sahoo BB, Nayak C, Shrivastava M (2021) Numerical investigation on air-cooling enhancement of a motor cycle engine by varying fins geometry. *IOP Conf Ser Mater Sci Eng* 1123(1):012045
- Tang LH, Min Z, Xie GN, Wang QW (2009) Fin pattern effects on air-side heat transfer and friction characteristics of fin-and-tube heat exchangers with large number of large-diameter tube rows. *Heat Transf Eng* 30:171–180
- Thornhill D, May A (1999) An experimental investigation into the cooling of finned metal cylinders, in a free air stream. *SAE Tech Pap*, 1999-01-3307
- Thornhill D, Graham A, Cunningham G et al (2003) Experimental investigation into the free air-cooling of air-cooled cylinders. *SAE Tech Pap*, 2003-32-0034
- Wang CC, Chen KY, Liaw JS, Tseng CY (2015) An experimental study of the air-side performance of fin-and-tube heat exchangers having plain, louver, and semi-dimple vortex generator configuration. *Int J Heat Mass Transf* 80:281–287

Chapter 11

Analysis of Hydraulic Arm Using Hydraulic Jack for Motorcycle Hydraulic Lift



Khairul Shahril, Muhammad Afif Asnawi, Mior Firdaus Mior Abdul Majid, S. Nurashikin, and Ahmad Kamal

Abstract Motorcycle hydraulic lift is widely used for lifting vehicles like a motorcycle at the required height to do maintenance safely and efficiently. The area of application includes vehicle loading, work positioning, etc. Motorcycle hydraulic lift comes in varied forms which can be built to facilitate specialized industrial activities and tasks. The hydraulic lift can be driven by a hydraulic cylinder, pneumatic sources, push chains, or a hydraulic foot pumps in case of light load. This paper deals with the critical part analysis: the hydraulic arm. There will be one part that will run a simulation analysis. SolidWork is used for designing the motorcycle hydraulic lift and used simulation for meshing and analysis work to check stress, strain, and deformation that are induced in the system. The main aim is to determine the stress, strain, and deformation for the hydraulic arm.

Keywords Motorcycle hydraulic lift · Hydraulic lift · Hydraulic · SolidWork · Equivalent stress · Total deformation

11.1 Introduction

Rising mechanic awareness of motorcycle lift issues has generated demand for an improvement in motorcycle lift. This, in turn, has made vehicle workshop an issue for workers. People will think and try to find a way to overcome these problems.

K. Shahril (✉) · M. A. Asnawi · M. F. M. A. Majid · S. Nurashikin · A. Kamal
Universiti Kuala Lumpur, Malaysian Spanish Institute, Kulim Hi-Tech Park, 09000 Kulim,
Kedah, Malaysia
e-mail: khairuls@unikl.edu.my

M. F. M. A. Majid
e-mail: miorfirdaus@unikl.edu.my

S. Nurashikin
e-mail: nurashikins@unikl.edu.my

A. Kamal
e-mail: ahmadkamal@unikl.edu.my



Fig. 11.1 Motorcycle hydraulic lift

A motorcycle hydraulic lift is a lift table that is designed to handle motorcycles specifically, as shown in Fig. 11.1. Most repair shops use motorcycle hydraulic lift to bring the bike off from the ground and level up so that the mechanic does not need to feel any strain on his or her back or lay on the ground to perform any work maintenance for the motorcycle. Also, a motorcyclist has put these table lifts into their home garages so that they can perform simple maintenance such as changing the oil and cleaning the bike without having to get down on the ground. The target weight vehicle motor for this motorcycle hydraulic lift is 100 kg plus.

11.2 Classification Based on Type of Energy Used

11.2.1 Hydraulic Lift

The hydraulic lift is operated using the fluid pressure that raises the platform via power through the use of pressurized hydraulic oil. Slight speed variation is possible owing to temperature fluctuations that can alter the viscosity of the hydraulic oil (Thorat et al. 2017).

11.2.2 Pneumatic Lifts

The pneumatic lifts are operated by utilizing the air pressure, and they are very efficient because the power supply is supported by compressing the atmospheric air. Most of the units do not require electricity and thus can be used at any place where the air is available (Rani et al. 2015).

11.2.3 Mechanical Lifts

The mechanical lifts are extended through a power screw or rack and pinion system, both of which can convert rotational motion. All the electric lifts are mechanical. The benefit of mechanical lift is that the teeth of its gear system prevent from slippage essentially (Momin et al. 2015).

11.2.4 Application of Hydraulic Lift

Hydraulic lift table has many useful purposes. The applications of a hydraulic lift table include a variety of things like using it as a trolley to carry material and lift and raise heavier object, but the platform is ultimately designed to lift motorbike. The lift is most often seen behind the scenes of retail establishments and warehouses, although manufacturing engineers are always redesigning the lift for various uses like lifting heavy loads (Manoharrao and Jamgekar 2016a). The hydraulic lift table can raise a motorbike or superbike so that maintenance does need to go underneath to perform maintenance. By employing hydraulic lift tables in a warehouse, and workshop all heavy items can be lifted with ease and no effort. It can be used to stack pallet, boxes, and other heavy materials like sheet metal or any metal. The metal is usually very heavy to try and lift for the stacking process. This is where a hydraulic lift table can help. In major cities, the hydraulic lift tables are used as platforms for maintenance and construction. Hydraulic lift tables can be designed to operate in many different ways. They must be all lowered and raised, but their main purpose will always be to lift and unload (Manoharrao and Jamgekar 2016b).

11.3 Problem Statement

As shown in Fig. 11.2, it is found some problems regarding motorcycle hydraulic lift like the job to be lifted is more massive, which causes more deformations in hydraulic lift frame and may cause failure at critical points. As loading and unloading or the



Fig. 11.2 Failure at hydraulic arm

usage of the motorcycle hydraulic lift is repeated, there may be chances of fatigue failure.

11.4 Literature

The hydraulic lift has various varieties and designs. The most common type of hydraulic lift is a scissor lift or jack used for lifting a motorbike to change a tire to gain access to go to the underside of the bike to raise the body to an appreciable height. Many other applications such as lifts can be used for various purposes like maintenance and use as a trolley for material handling. The lift can be in pneumatic, hydraulic, or mechanical type. Most of the lift is designed to be portable and work without consuming any electric power to power the hydraulic pump or cylinder. This type of lift can make it more compact and much suitable for people who do medium-scale work (Momin et al. 2015).

As shown in Fig. 11.3, most of the lift is a simple mechanical device used to raise objects or elements from ground level to upward to perform maintenance or specific work with maximum load and minimum effort. Their project described the design and analysis of a mechanical scissor lift that works on the principle of screw jack. The system was developed, keeping in mind that the table lift can be operated by mechanical. So that the overall cost of the hydraulic lift is reduced, their design can also make the table lift more compact and much suitable for medium-scale work (Shinde et al. 2016).

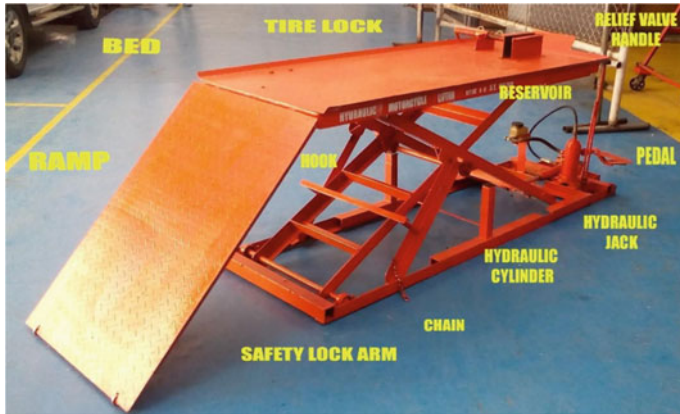


Fig. 11.3 Motorcycle hydraulic lift

11.4.1 Material Selection

The hydraulic lift is made primarily of regular steel profiles. Other parts needed to build motorcycle lift are two springs to hold motorcycle stuck on the lift, four strong swivel wheels so it can be easily moved around, oil catch pan made from sheet metal to make oil change easier, a magnetic bar for tools, a hydraulic cylinder, fasteners, and paint (Timothy Foley et al. 2017). Brass material was used for making bush having low co-efficient of friction (Dhanawade et al. 2017). Top platform is subjected to weight of workman and equipment so it should possess strength. Thus, mild steel is used as shown in Table 11.1 (Wankhede et al. 2018). It is the same properties as in the paper of Manoharrao and Jamgekar (2016a, b).

11.5 Methodology

Figure 11.4 shows the model of motorcycle hydraulic lift. This design used the hydraulic jack that is locked onto the legs of motorcycle hydraulic lift. So when the

Table 11.1 Material properties of mild steel (SAE 1020) (Wankhede et al. 2018)

| | |
|-----------------------|------------------------|
| Young's modulus E | 210 MPa |
| Poisson's ratio ν | 0.29 |
| Mass density | 7860 kg/m ³ |
| Damping co-efficient | 0.008 |
| Yield stress | 350 MPa |
| Ultimate stress | 420 MPa |

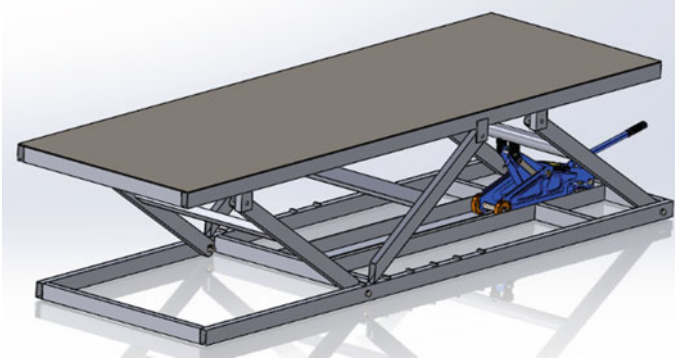


Fig. 11.4 Motorcycle hydraulic lift

hydraulic jack is being pumped, the jack will push the back leg of hydraulic lift to move the platform or main frame upward.

11.5.1 Analytical Analysis

Since the estimated vehicle motor is 100 kg plus with the upper platform, weight is 50 kg. Add both of the weight, and the total is 150 kg, equal to 1471.5 N. Next is to find the required force (F_x) to lift up the platform of motorcycle hydraulic lift. Based on the calculation below, the required force to lift up the platform is 21 kN. All dimensions are in mm (Fig. 11.5).

$$\sum M_A = 0$$

$$-1471.5(0.17065) + F_x(0.06181) = 0$$

$$F_x(0.06181) = 1471.5(0.17065)$$

$$F_x = \frac{251.111475}{0.06181} = 4062.635$$

11.5.2 Simulation Setup

Forces always act in pairs and always act in opposite directions (Action and Reaction Forces: Law Examples—Video Lesson Transcript), and since the force calculated

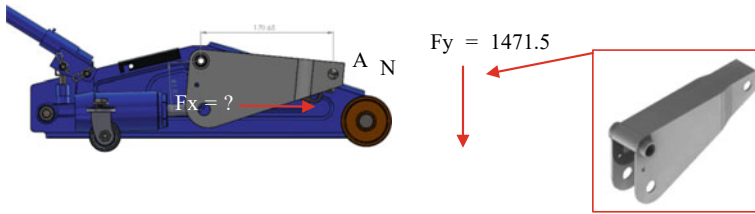
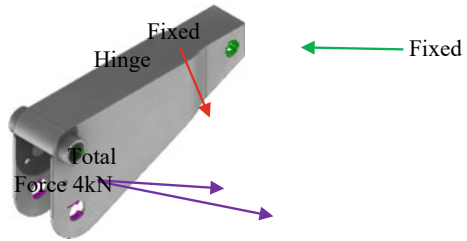


Fig. 11.5 Hydraulic arm from the hydraulic jack

Fig. 11.6 Hydraulic arm



using the moment equation was from the 1471.5 N, it does need to assign force in that area but set fixed support. It will give better accurate results (Fig. 11.6).

11.6 Result and Discussion

There were few considerations while designing the critical part for the motorcycle hydraulic lift configuration was restricted to a few limitations such as:

- i. Focus on a critical part that is the hydraulic arm.
- ii. The hydro arm should be able to carry the upper platform at least 150 kg.
- iii. The safety factor must be in 2, meaning the actual load that the hydraulic arm can carry is 300 kg.

11.6.1 Hydraulic Arm

See Figs. 11.7, 11.8 and 11.9.

11.6.2 Analysis of the Result

See Table 11.2.

Fig. 11.7 Equivalent stress of hydraulic arm

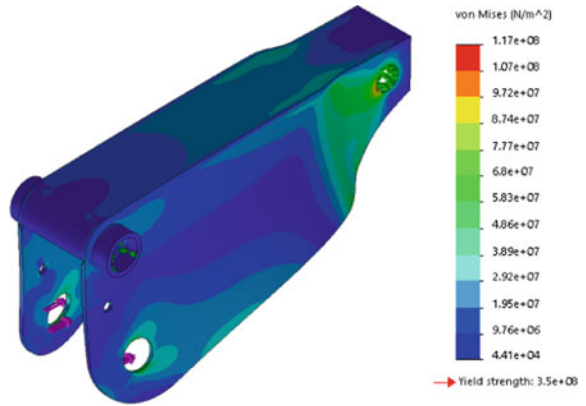


Fig. 11.8 Strain of hydraulic arm

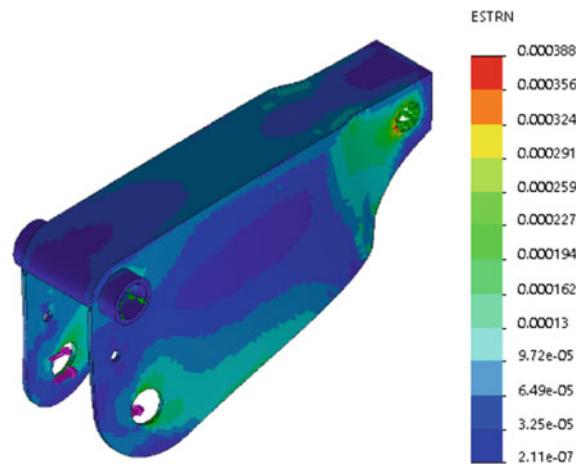


Fig. 11.9 Deformation of hydraulic arm

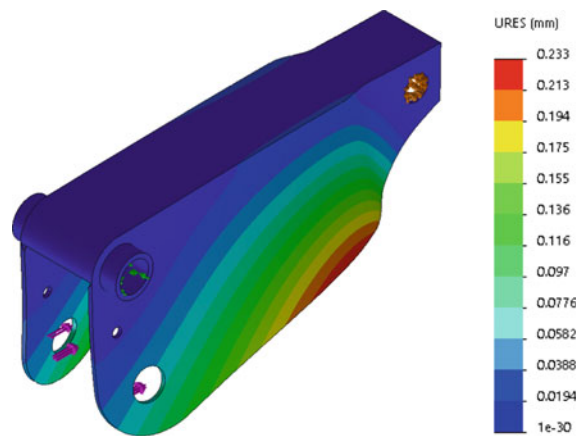


Table 11.2 Result of simulation

| Part | Stress (MPa) | Strain | Deformation (mm) | Safety factor |
|---------------|--------------|---------|------------------|---------------|
| Hydraulic arm | 117 | 0.00038 | 0.238 | 3 |

11.7 Conclusion

In conclusion, based on the objectives of this paper is to find the stress, strain, and deformation for the hydraulic arm from the hydraulic jack using SolidWork simulation. Based on the result shown, the hydraulic arm stress that is induced in the hydraulic jack is below the allowable stress (350 MPa). The hydraulic jack is suitable to use for the motorcycle hydraulic lift.

References

- Action and reaction forces: law & examples—video & lesson transcript. Study.com. [Online]. Available: <https://study.com/academy/lesson/action-and-reaction-forces-law-examples-quiz.html>. Accessed 14 Apr 2021
- Dhanawade SB, Bhujbal SS, Dhane RR, Narkar RR, Bhosale SS (2017) Design, analysis and development of hydraulic scissor lift material loading and unloading. *Int J Adv Eng Res Dev* 4(3):214–221
- Manoharrao SA, Jamegar RS (2016a) Analysis and optimization of hydraulic scissor lift. *Int J Eng Dev Res* 4(4):2321–9939
- Manoharrao SA, Jamegar RS (2016b) Design and analysis of hydraulic scissor lift by FEA. 1277–1292
- Momin GG, Hatti R, Dalvi K, Bargi F, Devare R (2015) Design, manufacturing and analysis of hydraulic scissor lift. *Int J Eng Res Gen Sci* 3(2):733–740
- Rani D, Agarwal N, Tirth V (2015) Design and fabrication of hydraulic scissor lift. *MIT Int J Mech Eng* 5(2):81–87
- Shinde AB, Daphal PB, Nilange PS, Dongre VH, Assistant RKN (2016) Design and fabrication of mechanical lift for transportation. *GRD J Glob Res Dev J Eng* 2(1):30–34
- Thorat SG, Chiddarwar AR, Prasana S (2017) Design and construction of hydraulic scissor lift. *Mitpublications.Org* 7(7):92–95
- Timothy Foley J, Tórir Sigursson G, Gunnarsson JS, Gautason J, Ólafsson OJ (2017) Mobile motorcycle lift for the common man. *MATEC Web Conf* 127:1–6
- Wankhede SD, Joshi SS, Bagwan LJ, Wadmare AV (2018) Analysis and optimization of hydraulic scissor lift. 4(4):1–8

Chapter 12

FMEA Approach to Extend the Engine Oil Drain Interval of a 100-t Truck: A Case Study



Surya Atmadyaya, Mohamad Sazali Said, Azmi Hassan, Fauzan Rahman, Iwan Susanto, Tumianto, and Yusri Yamin

Abstract Since its inception, the engine has undergone many technological advances, from external combustion to internal combustion types. Major components of the engine include the crankshaft, piston, connecting rod, cylinder, cylinder head, etc. Maintenance is highly complex process and may be related to thermal power plant, cement plants, and oil refining plants and including the truck which is operated in mining area. The main purpose of the maintenance recommendation is to eliminate the risk of sudden shutdown of the equipment with an uncontrollable system. This paper is based on the FMEA process which analyzes the potential problems of the extended engine oil drain interval process on 100-t truck. This research was carried out in a coal mine in Indonesia. The FMEA method is to help the maintenance department to make decisions about managing spare parts and can focus more on critical components.

S. Atmadyaya (✉) · M. S. Said
Manufacturing Section, Universiti Kuala Lumpur, Malaysian Spanish Institute Kulim Hi-Tech Park, 09000 Kulim, Kedah, Malaysia
e-mail: atmadyaya.surya@s.unikl.edu.my

M. S. Said
e-mail: msazali@unikl.edu.my

A. Hassan · F. Rahman · I. Susanto · Tumianto · Y. Yamin
Electrical, Electronics and Automation Section, Universiti Kuala Lumpur, Malaysian Spanish Institute Kulim Hi-Tech Park, 09000 Kulim, Kedah, Malaysia
e-mail: azmi.hassan@s.unikl.edu.my

F. Rahman
e-mail: fauzan.rahman@s.unikl.edu.my

I. Susanto
e-mail: iwan.susanto@s.unikl.edu.my

Tumianto
e-mail: tumianto@s.unikl.edu.my

Y. Yamin
e-mail: yamin.yusri@s.unikl.edu.my

Keywords FMEA · Engine · Diesel · Mining · Wear · RPN · Truck · Drain interval

12.1 Introduction

Since its inception, the engine has undergone many technological advances, from external combustion to internal combustion types. Major components of the engine include the crankshaft, piston, connecting rod, cylinder, cylinder head, etc. Depending on the functional requirements, these components are also given intricate shapes that include relatively complex manufacturing processes and procedures. Failure of engine components includes cylinder block breakage, crank pin or crankshaft failure, noise from the engine, mixing of oil and water, engine overheating, squirt, and scratching (Deulgaonkar et al. 2020). Maintenance of a truck which operates in mining operations is highly complex. It is very important to have a good maintenance strategy and propose ongoing recommendation for improvement. The main purpose of the maintenance recommendation is to eliminate the risk of sudden shutdown of the equipment with an uncontrollable system, time-based maintenance, breakdown maintenance, etc. Depending on the maintenance policy, attention should be paid to many equipment in each factory unit. Maintenance is extremely important to ensure operational stability and that all equipment is supposed to be in good conditioning (Dulendra et al. 2019).

12.2 Case Study

This paper is based on the FMEA process which analyzes the potential problems (Ben-Daya et al. 2009) of extended engine oil drain interval process on 100-t truck. This research was carried out in a coal mine. This method is to help the maintenance department make decisions about managing spare parts and that they can focus more on critical components. In a mining operation, the main objective is to produce resources using the minimum possible cost and in selected tools (Samatamba et al. 2019). Lubrication on a machine is a technique or process of reducing the wear rate of one or two surface components (Akpınar Borazan et al. 2013).

Most common causes of damage to 100-t truck engines and their components are shown in Tables 12.1 and 12.2 (Fig. 12.1).

12.2.1 Methodology

Failure mode effect analysis (FMEA) is a systematic method to prevent and understand the problem of a product or process before it occurs or it makes an impact that

Table 12.1 Number of engine failures 2010–2014

| Type engine failed | Number | Cost impact |
|-----------------------------|--------|-------------|
| Water contamination failure | 10 | 357k |
| Fatigue | 14 | 376k |
| Erosive wear | 13 | 412k |
| Air-related failure | 9 | 442k |
| Adhesive wear | 13 | 655k |
| Abrasive wear | 17 | 550k |

Table 12.2 Number of engine failure 2015–2019

| Type engine failed | Number | Cost impact |
|-----------------------------|--------|-------------|
| Water contamination failure | 14 | 366k |
| Fatigue | 14 | 413k |
| Erosive wear | 9 | 460k |
| Air-related failure | 6 | 406k |
| Adhesive wear | 8 | 701k |
| Abrasive wear | 11 | 645k |

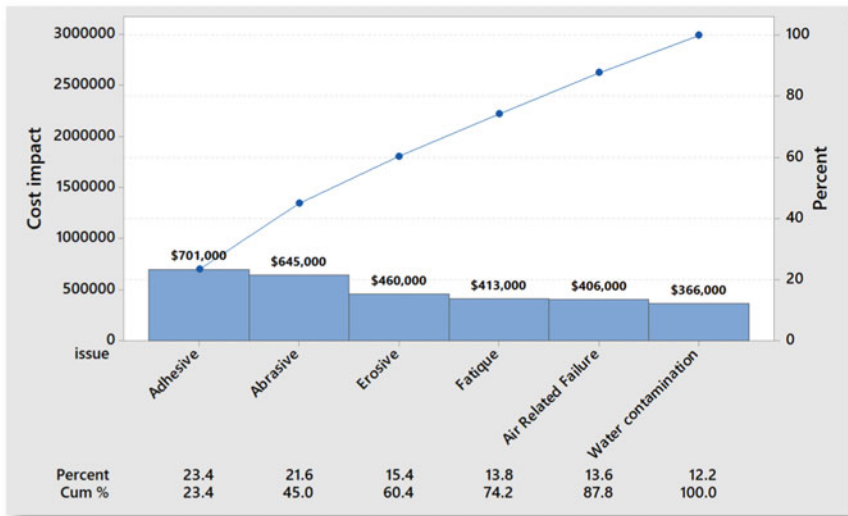


Fig. 12.1 Pareto cost impact engine failed due to engine oil 2015–2019

can have an impact on finances or customers (Muzakkir et al. 2015). The following lists some benefits of the FMEA approach:

- FMEA can drive proactive improvement.
- FMEA can identify events where a process could fail.

- FMEA can assess the severity of failure.
- FMEA helps consider possible failures.
- FMEA can help evaluate existing controls and focus on developing process control plans.
- FMEA helps prioritize actions to reduce or eliminate risks. In the process of compiling the FMEA, the author uses the MINITAB WORKSPACE software which makes it easy to input and accelerate the process of brainstorming and developing FMEA.

Figure 12.2 shows the flow process of FMEA in analyzing issues which commonly occurred on truck 100 t operates in mining operations.

Step 1 Determine process steps

The paper, the engine used, and the second oil engine are listed in Tables 12.3 and 12.4.

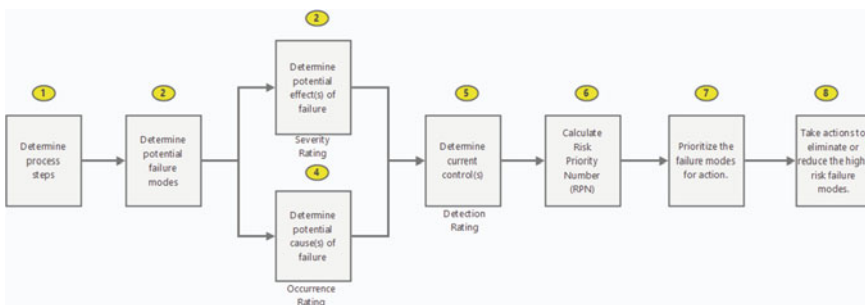


Fig. 12.2 FMEA flow process

Table 12.3 Engine 100-t truck specification

| | | |
|-----------------------|---------|-----------------------|
| Gross power—SAE J1995 | 746 kW | 1000 hp |
| Net power—SAE J1349 | 699 kW | 938 hp |
| Net power—Cat | 699 kW | 938 hp |
| Flywheel power | 699 kW | 938 hp |
| Net power—ISO 9249 | 699 kW | 938 hp |
| Net power—80/1269/EEC | 699 kW | 938 hp |
| Peak torque | 4713 Nm | 3476 lb ft |
| Torque rise | 23 % | |
| Bore | 170 mm | 6.7 in. |
| Stroke | 190 mm | 7.5 in. |
| Displacement | 34.5 L | 2105 in. ³ |

Table 12.4 Engine oil specification 15W40

| Properties | | | Method | Value |
|---------------------|------------|--------------------|------------|-------|
| Kinematic viscosity | at 40 °C | mm ² /s | ASTM D445 | 111 |
| Kinematic viscosity | at 100 °C | mm ² /s | ASTM D445 | 14.63 |
| Dynamic viscosity | at – 20 °C | mPa s | ASTM D5293 | 6343 |
| Viscosity index | | | ASTM D2270 | 136 |
| Flash point (COC) | | °C | ASTM D92 | 230 |
| Pour point | | °C | ASTM D97 | – 39 |
| Density | at 15 °C | kg/l | ASTM D4052 | 0.886 |

Step 2 Determine potential failure modes

When carrying out the FMEA process, the focus is on potential damage related to the quality of lubricants that can occur in lubrication systems such as abrasive wear and adhesive wear.

When announcing failure modes:

- Collect feedback and potential complaints from internal and external customers and suppliers.
- Do brainstorm in regard to potential failure modes.
- Combine and examine failure modes found with the latest scientific literature.

Some of catastrophic failures occurred on major engine components of 100-t truck are shown in Figs. 12.3, 12.4, and 12.5.

Damage to lubricants can also be caused by contamination, moisture, oxidation, and viscosity thinning (Muzakkir et al. 2015).

The duration of engine oil utilization hour on truck 100 t is also having significant impact on quality of oil itself. The analysis review shown in Figs. 12.6, 12.7, 12.8, and 12.9 indicates decreasing of engine oil quality used in 100-t truck after 500 h of operation.

Fig. 12.3 Sample—upper bearing as road sign of adhesive wear



Fig. 12.4 Sample—road sign of adhesive wear at rod journal

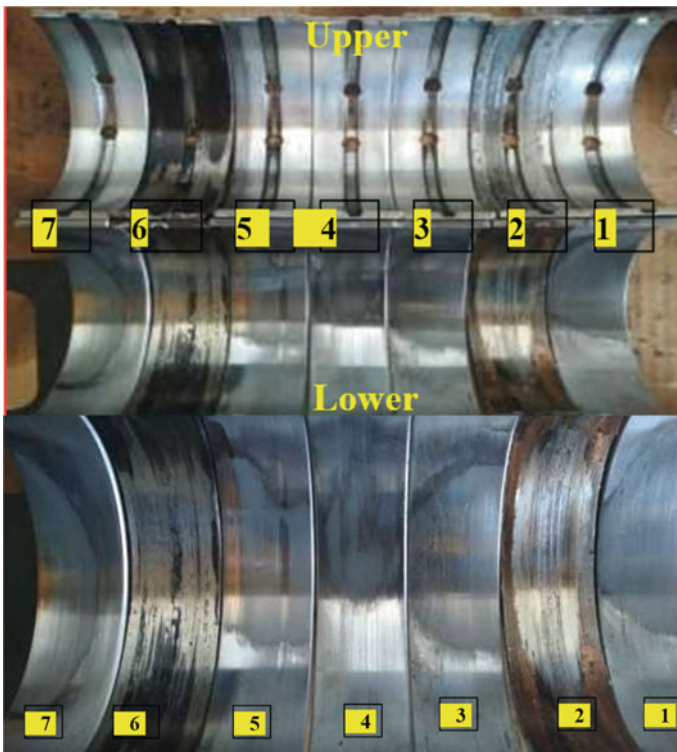


Fig. 12.5 Sample—Main bearing no 2 and 6 with adhesive wear

Step 3 Determine potential effect(s) of failure

For each step of failure mode, all the potential effects of damage are collected, followed by making a severity ranking to measure the frequency and how serious the effect is generated as shown in Table 12.5.

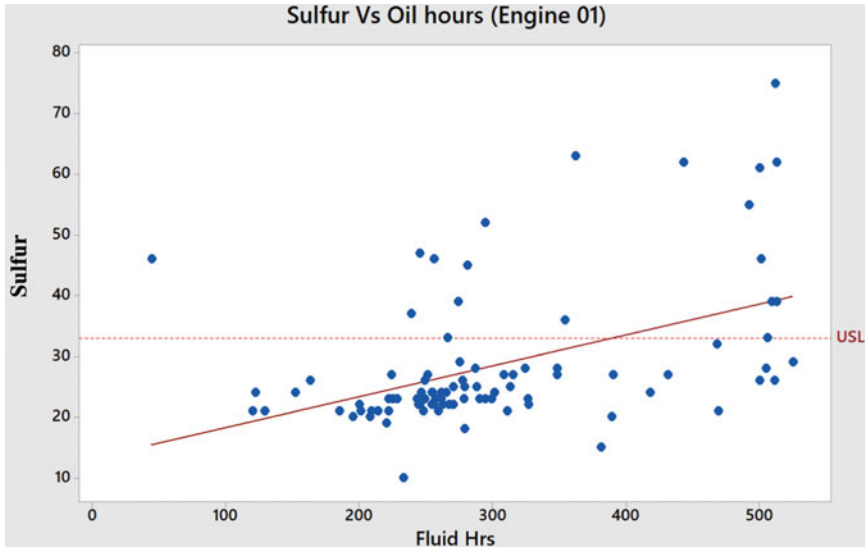


Fig. 12.6 Sulfur trend increase

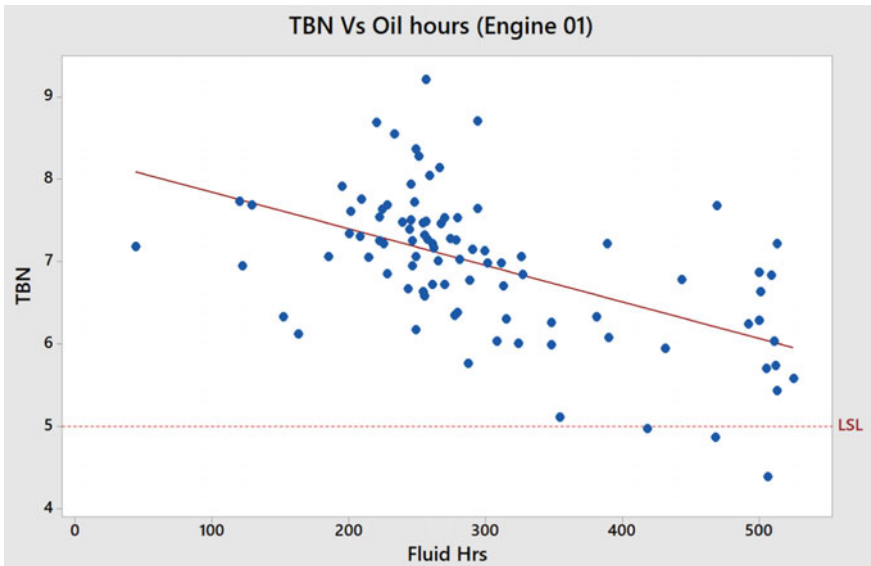


Fig. 12.7 TBN trend decrease

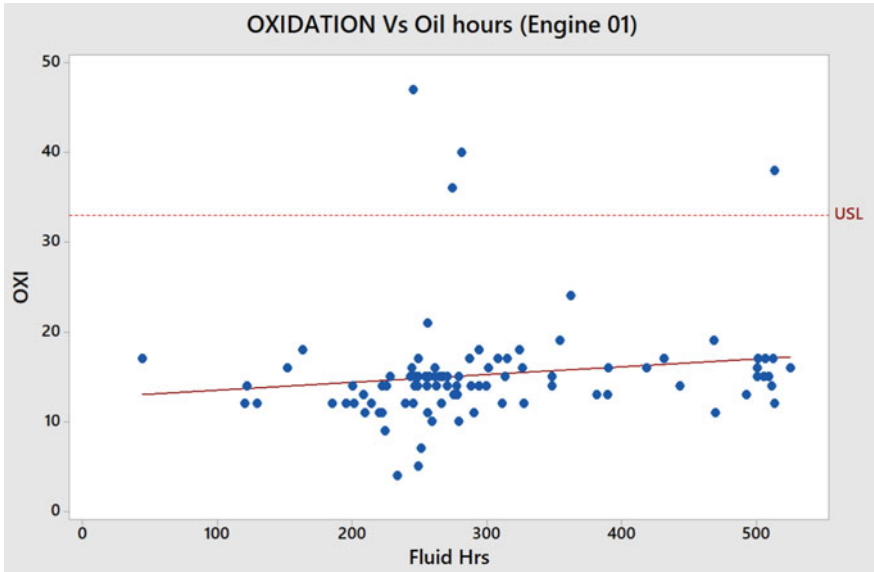


Fig. 12.8 Oxidation trend increase

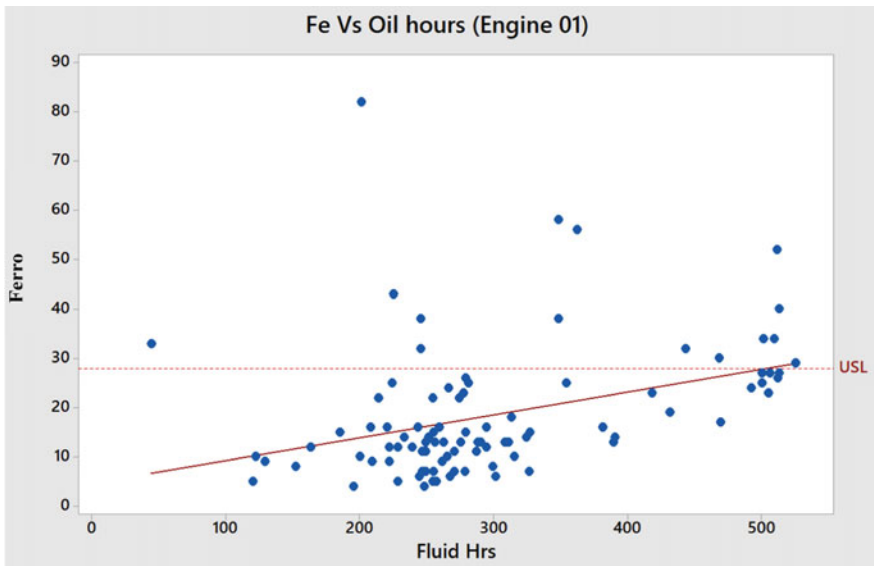


Fig. 12.9 Fe (Ferro) trend increase

Table 12.5 Severity matrix related to the lubricant

| Effect | Rank | Criteria |
|--------------------|------|--|
| No | 1 | No effect on bearing performance |
| Very slight | 2 | Very slight increase in friction only |
| Slight | 3 | Slight increase in friction only |
| Minor | 4 | Minor increase in friction only |
| Moderate | 5 | Moderate increase in friction only |
| Significant | 6 | Increase in friction and slight wear occurrence |
| Major | 7 | Significant increase in friction and moderate wear occurrence |
| Extreme | 8 | Significant increase in friction and wear |
| Serious | 9 | Complete failure of lubrication with maximum increase in friction and wear |
| Hazardous | 10 | Catastrophic failure |

Step 4 Determine potential cause(s) of failure

List potential causes of a potential failure mode, because there may be more than one potential cause as shown in Table 12.6. The brainstorming method can be used for this process with the help of the fishbone tool.

Step 5 Determine current control(s)

The best method for determining or detecting control is to use the history of the previous events data and count how often the failure mode occurred.

Prevent failures before they occur:

- Must be able to detect before an incident occurs.
- If possible, use the mistake-proof process / system method.

Table 12.6 Occurrence matrix related to the lubricant

| Effect | Rank | Criteria |
|-----------------|------|---|
| Almost never | 1 | Failure unlikely history shows no failure |
| Remote | 2 | Rare number of failures likely |
| Very slight | 3 | Very few failures likely |
| Slight | 4 | Few failures likely |
| Low | 5 | Occasional number of failures likely |
| Medium | 6 | Medium number of failures likely |
| Moderately high | 7 | Moderately high number of failures likely |
| High | 8 | High number of failures likely |
| Very high | 9 | Very high number of failures likely |
| Almost certain | 10 | Failure almost certain |

Table 12.7 Detection matrix-related engine oil system

| Effect | Rank | Criteria |
|-------------------|------|--|
| Almost certain | 1 | Proven detection methods available in concept stage |
| Very high | 2 | Proven computer analysis available in early design stage |
| High | 3 | Simulation and/or modeling early stage |
| Moderately high | 4 | Tests on early prototype system elements |
| Medium | 5 | Tests on preproduction system components |
| Low | 6 | Tests on similar system component |
| Slight | 7 | Tests on product with prototype and system components installed |
| Very slight | 8 | Proving durability tests on product with system components installed |
| Remote | 9 | Only unproven or unreliable technique(s) available |
| Almost impossible | 10 | No known techniques available |

Detect failures if they occur:

- Ideally, it is found or detected on the component concerned or until the trending wear element reaches a critical base on OEM recommendation.
- If this is not possible, it can be during 2 PM (periodical maintenance) events.

Table 12.7 shows the detection matrix list and rank approach used in the case study.

Step 6 Calculate Risk Priority Number (RPN)

The (risk priority number) RPN must be calculated on each row

$$\text{Risk Priority Number} = \text{Severity} \times \text{Occurrence} \times \text{Detection formula}$$

The spreadsheet on *MINITAB Workspace* FMEA helps to calculate automatically this number. The total risk priority number is calculated by adding all of the risk priority numbers.

Step 7 Prioritize the failure modes for action

The next step is to make the priority from the highest risk to the lowest risk.

Step 8 Take actions to eliminate or reduce the high-risk failure modes

Creating actions to eliminate or reduce high-risk failure mode by creating a process flow to become a guideline for improvement as shown in Figs. 12.10 and 12.11.

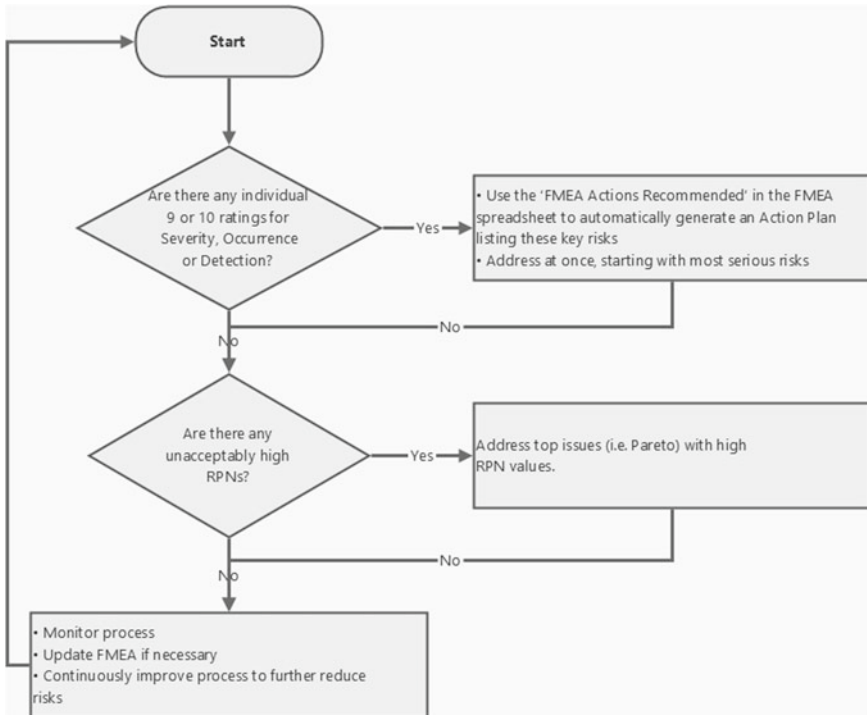


Fig. 12.10 FMEA corrective action—flow chart

12.3 Result and Discussion

Based on the FMEA sheet (see Fig. 12.11) for the journal bearing, it is observed that wear is the predominant mode of failure of the bearing. The most feature of a failure is its detectability. Since it is difficult to require preventive measures for failures that are difficult to detect, therefore, it increases the probability of failure. The journal failure and lubrication system failure mode seriously threaten the bearing performance as they are easily detectable and preventive measures are also taken accordingly. This is essentially true because the bearing is intended to be a sacrificial element of the bearing system. The wear and tear of the bearing may be prevented by using suitable anti-wear lubricant additives, by providing grooving arrangement, etc.

12.4 Conclusions

In this paper, FMEA correction action and its benefits are discussed and the failure part and the basic reason of failure and the factors of failure are discussed. By using

FMEA

| Step # | Item/Component | Potential Failure Mode | Potential Failure Effects | Potential Causes | SEV | OCC | DET | RPN | Recommend | Responsibly |
|--------|----------------|--|---------------------------------|--|-----|-----|-----|-----|---|-------------|
| 1 | OXIDATION | Adhesive wear | Oxidation Number increase | Cooling system fails, Glycol contamination | 8 | 8 | 4 | 256 | > Check cooling system for blocked radiator/faulty water pump | PM crew |
| 2 | SULFATION | Abrasive wear | Sulfation Number increase | Abnormal working temperature | 8 | 8 | 4 | 256 | Resample on next 100 hrs | PM crew |
| 3 | TBN | Fails to supply any lubricant to the bearing | Bearing seizure | Oil alkalinity reserve remaining | 10 | 5 | 1 | 50 | Drain, flush and replace with fresh oil | PM crew |
| 4 | NITRATION | Adhesive wear | NITRATION number increase | Extended oil change. | 4 | 4 | 1 | 16 | Replace with new oil | Field crew |
| 5 | FE (Iron) | Abrasive wear | Fe (Iron) wear trend increase | Oil alkalinity reserve remaining | 4 | 3 | 1 | 12 | Check for unusual noise, Check valve mechanism | Field crew |
| 6 | ALUMINIUM (Al) | Abrasive wear | Aluminum wear trend increase | Extended oil change. | 4 | 3 | 4 | 48 | Check for unusual noise, Check valve mechanism | Field crew |
| 7 | LEAD (Pb) | Abrasive wear | Lead (Pb) wear trend increase | Oil alkalinity reserve remaining | 5 | 2 | 4 | 40 | Inspect filter, change oil | PM crew |
| 8 | COPPER (Cu) | Abrasive wear | Copper number Trend increase | Extended oil change. | 9 | 8 | 5 | 360 | Check for Fuel/Coolant contamination | PM crew |
| 9 | TIN (Sn) | Abrasive wear | TIN (Sn) number Trend increase | Extended oil change. | 8 | 5 | 3 | 120 | Check for unusual noise, change oil | PM crew |
| 10 | NICKEL (Ni) | Abrasive wear | NICKEL (Ni) wear trend increase | Extended oil change. | 8 | 4 | 4 | 128 | Check for unusual noise, change oil | Field crew |

Fig. 12.11 FMEA—engine oil quality issue (Muzakkir et al. 2015)

this FMEA tool, the potential for damage can be identified from the start and their effects are discussed, and severity rank, occurrence of failure, detection rank, and risk priority number are calculated. After calculating all forms of RPN risk that is more than 100, it is a serious problem to be able to provide suggestions for corrective actions and anticipate the part as well as the whole engine and increase the reliability of the component. This study found that to extended engine oil interval should not only consider the benefit reduce quantity but also risk effect of oil properties and preventive maintenance activities on cooling system which is critical to improve. The sample of list FMEA results on the assist company deciding the better action when investigations on extended oil drain intervals are performed.

References

- Akpınar Borazan A, Acikgoz C, Andoglu EM (2013) A case study of effective factors on the right industrial lubricating oil choosing. *J Eng Appl Sci* 2(2):161–166
- Ben-Daya M, Duffua SO, Raouf A, Knezevic J, Ait-Kadi D (2009) *Handbook of maintenance management and engineering*. Springer, London
- Deulgaonkar VR et al (2020) Failure analysis of diesel engine piston in transport utility vehicles. *Eng Fail Anal* 120:10–12
- Dulendra KP, Manish KM, Krishna KM (2019) Risks prioritization using FMEA method case study. *Int J Eng Res* 6(7):355–359
- Muzakkir SM, Ligeshe KP, Hirani H (2015) Failure mode and effect analysis of journal bearing. *Int J Appl Eng* 10(16):36843–36850
- Samatamba B, Zhang L, Besa B (2019) Evaluating and optimizing the effectiveness of mining equipment; the case of Chibuluma south underground mine *J Clean Prod* 252

Chapter 13

Design and Fabrication of a Dip Immersion Probe for Melting and Pouring Practice in Casting Technology



Yap Tek Hong, Nadzri Che Kamis, and Choong Chee Guan

Abstract The accuracy of the molten aluminum temperature is essential to produce a good casting product. The solubility of hydrogen gas in molten aluminum is higher when the melting temperature increases. Over-exposure of hydrogen gas on molten aluminum immediately forms a skin of aluminum oxide, Al_2O_3 that causes drawbacks of mechanical properties in the final casting such as shrinkage, gas porosity, and oxide inclusions. Therefore, the melting temperature of aluminum should be kept as low as possible to minimize the hydrogen pick-up. Dip immersion probe (DIP) is designed to control the hydrogen gas solubility in aluminum by optimizing its melting temperature before the casting process. DIP consists of a couple of nickel chromium (NiCr) and nickel aluminum (NiAl) wires that are attached to a pyrometer and calibrated with a sensor of $-270\text{ }^{\circ}\text{C}$ to $1260\text{ }^{\circ}\text{C}$ range and in a L-shape with 135° to ensure the ergonomic and safety of the user. Inconel 600 sheath material is used as an outer metal to provide good high-temperature strength, resists chloride-ion stress corrosion cracking, and minimizes oxidation at high temperatures. DIP is cost-effective, reliable, safe, and ergonomic especially for the teaching and learning process of small-scale casting activity in the foundry workshop, as well as technical and vocational education and training (TVET) in polytechnics in Malaysia.

Keywords Melting · Pouring · Casting · Temperature · Dip immersion probe

Y. T. Hong (✉) · C. C. Guan
Mechanical Engineering Department, Politeknik Tuanku Syed Sirajuddin, Pauh Putra, 02600
Arau, Perlis, Malaysia
e-mail: yap@ptss.edu.my

C. C. Guan
e-mail: dr.choong@ptss.edu.my

N. C. Kamis
Mathematics, Science and Computer Department, Politeknik Sultan Mizan Zainal Abiddin, 23000
Kuala Dungun, Terengganu, Malaysia
e-mail: nadzri@psmza.edu.my

13.1 Introduction

A foundry workshop is a compulsory practical task to be completed by the students of the Mechanical Engineering Department, Polytechnic Malaysia. There are few activities to be carried out in the casting processes including pattern making, sand molding, melting, and pouring process. Casting revolved as one of the earliest metal shaping methods and is implemented by pouring the molten metal into a refractory mold containing the cavity of the shape, hence allowing the molten metal to solidify into the desired shape. In the end process, the object is taken out from the mold by breaking the mold apart (Rao 2001). In the breaking process, the molds are destroyed if sand molds are used, meanwhile, the molds are separated to remove the casting if a permanent mold is used (Sylvia 1999).

Aluminum is one of a large number of casting alloys in use worldwide in major industrial countries. It is notable as a ductile and low-density metal and has good corrosion resistance, and its melting point is about 660 °C. Generally, solubility of hydrogen in solid aluminum is very low, compared to liquid aluminum. However, the overheating of molten aluminum could cause high solubility of harmful hydrogen gas and consequently leads to the formation of the oxide layer (Khanna 2006). This may potentially cause defects such as shrinkage, gas porosity, and oxide inclusions which eventually contribute to drawbacks of mechanical properties in castings (Brown 2002).

Traditionally, the temperature of molten metal in the furnace is exhibited by its indicator device. However, it cannot be assumed as the exact temperature of the molten metal. Hence, the temperature is commonly measured by a probe known as the laser gun. The ability of the gun is limited, and the temperature of molten metal is inaccurate and always misinterpreted. This is caused by the difference between the temperature of the molten metal at immersion and surface of the furnace. As the alternative, an immersion-type probe was chosen to obtain an accurate molten metal temperature in the furnace. Figure 13.1 shows the constraints and comparatives of current measurement devices at the casting process which (a) laser gun thermometer, (b) built-in type ceramic sheath thermocouple, (c) iron chrome sheath thermocouple, and (d) un-sheath glass fiber-insulated thermocouple.

To reduce this problem, an exact temperature of the molten metal must be assumed to avoiding the potentially of casting defects such as gas porosity. Therefore, the objective of this work is to design and fabricate an immersion-type probe to meet the durability, user-friendly, and ergonomic factors, as well as to measure the temperature of molten aluminum accurately for the best quality of casting products. It is fabricated into L-shape (instead of a conventional probe with I-shape) to ensure the comfort of the user with a longer length for a safety factor, which is vital in the teaching and learning process.

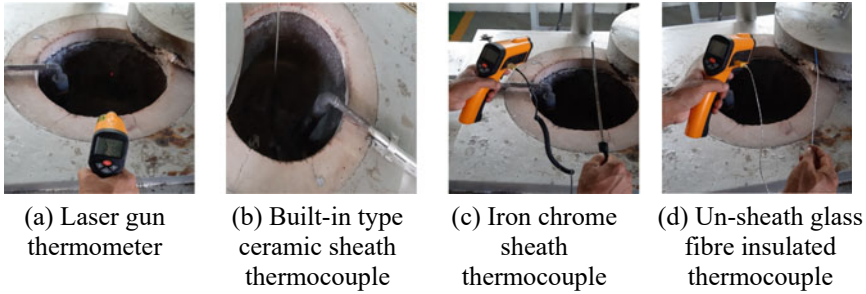


Fig. 13.1 Image of constraints and comparatives of current measurement devices at the casting process which **a** always misinterpreted and suitable for solid medium but not the liquid medium, **b** not durable at high temperature, easy crack, and unportable, **c** easy damage and not durable such as corrode, and **d** undurable, unsafe, not ergonomic and tend to melt at high temperature

13.2 Literature Review

In the twenty-first century, developments of new materials focused toward finding more importance for various engineering applications especially the lighter material namely aluminum (Karuppasamy et al. 2020). Aluminum and aluminum alloys are examples of non-ferrous metals used in engineering and construction fields. They are gaining huge industrial interest and are the most important of all non-ferrous alloys because of their excellent properties (Klemens et al. 2019). This is due to the significant combination of mechanical, physical, and tribological properties over the base alloys which have high strength, high wear, superior malleability, high stiffness, better high-temperature strength, good thermal and electrical conductivity, ease of machining, and improved damping capacity properties (Rana et al. 2012).

Aluminum alloys are used in sand casting work due to their strength-to-weight ratio, good corrosion resistance, and high ductility. These properties contain aluminum and trace amounts of metals such as copper, magnesium, silicon, and zinc (Zhang et al. 2019). One of the commonly used aluminum alloys is LM6 (Al-Si12) which contained strengthening elements and sufficient amounts of eutectic-forming elements (usually fluidity silicon) to make the metal flow through the cavities (Santhi et al. 2012). LM6 stays in the molten state longer than LM25 due to its greater fluidity, therefore helping the metal to reach the extremities of the mold cavities. This can also reduce the risk of defects such as misruns. However, LM6 is difficult to machine due to its high silicon content. LM6 can be used to add simple features (such as drilled holes); however, it is not suitable for intricate features (such as close tolerance holes). LM6 is also one of the most malleable aluminum alloys. This is an important characteristic for many marine applications, such as boat propellers, which must operate efficiently and have some malleability, without breaking, in harsh environments. Table 13.1 shows the chemical content composition of LM6 referring to BS 1490:1998 (Brown 2002).

Table 13.1 Chemical composition (weight percent) of LM6

| Alloy | Cu | Mg | Si | Fe | Mn | Ni | Zn | Pb | Sn | Ti | Al |
|----------------|-----|------|-------------|-----|-----|-----|-----|-----|------|-----|-----------|
| Weight percent | 0.1 | 0.10 | 10.0 – 13.0 | 0.6 | 0.5 | 0.1 | 0.1 | 0.1 | 0.05 | 0.2 | Remainder |

The cast temperature is one of the important variables for the casting process. If the pouring temperature is too low, then the cavity in the mold will not be filled. Hence, this causes the inlet of the mold to freeze, where else if the pouring temperature is too high, it can cause shrinkage and loss of accuracy in the dimensions of the castings. Cast temperatures in aluminum alloys are usually found in between 675 °C and 790 °C and must be maintained at a pouring temperature at ± 800 °C (Klemens et al. 2019).

A thermocouple is a device for temperature measurement invented by Seebeck in 1822. In a thermocouple, small amount of electric currents flow in a closed circuit which consists of two different conductors. The flow is caused by a temperature difference between the junctions of the different conductors. The generated open-circuit voltages (electromotive force, e.m.f.) are the relative Seebeck voltages composed from the pair of conductors or thermoelements of the thermoelectric circuit. Therefore, a thermocouple is used to convert thermal energy into electrical energy due to the resultant of the temperature difference. Hence, it can be used as a source of electrical energy or for the means of temperature measurement (Pollock 1991).

Thermocouples operate according to the Seebeck principle. As mentioned earlier, a thermocouple can produce an electromotive force (e.m.f.) by converting thermal energy into electrical energy. The e.m.f. is measured as electric potential (voltage) produced by the temperature difference and is known as the Seebeck effect. The constant is proportionate to the Seebeck coefficient (S) and is also known as thermopower in Eq. (13.1):

$$\Delta V = -S\Delta T \quad (13.1)$$

where ΔV and ΔT are the voltage and temperature differences, respectively. The temperature at the junctions of a thermocouple is the function of voltage produced (Hadi et al. 2021).

Thermocouples are widely used in tribological studies for temperature data collections. The applications of thermocouples (in data collections) are (i) to measure the bulk temperature of lubricant or process fluid, (ii) to determine air or atmospheric temperature during tests, and (iii) to measure the temperature rise in specimens tested (Starchowiak et al. 2004). At present, thermocouples are being used in industrial, scientific, and OEM applications (original equipment manufacturer).

There are multiple types of thermocouples, with its own unique characteristics in terms of temperature range, durability, vibration resistance, chemical resistance, and application compatibility. However, types J, K, T, and E are the base metal thermocouples and are commonly used. As for type R, S, and B thermocouples which

Table 13.2 Specifications of the dip immersion probe

| No | Parameter | Specification |
|----|-------------------|-----------------|
| a | Temperature range | 0–1260 °C |
| b | Accuracy | ± 1.1 °C |
| c | Probe diameter | 8 mm |
| d | Probe length | L-Shape: 915 mm |
| e | Sheath material | Inconel 600 |

are noble metal thermocouples used in high-temperature applications. Thermocouples are also widely used in research and development to characterize the material properties (Hadi et al. 2021; Yordanov et al. 2018).

13.3 Methodology

In this project, a K-type thermocouple was used in the measurement of the molten temperature and the preparation of aluminum casting alloy (LM6) samples under different temperature conditions.

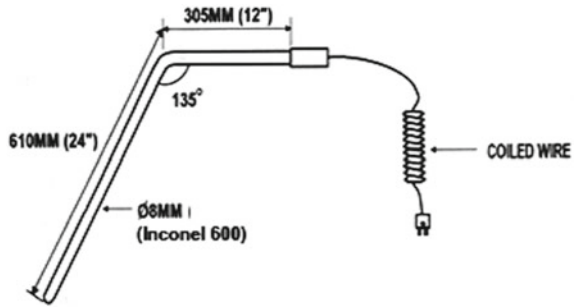
13.3.1 *Specification of DIP Immersion Probe for a Measurement Probe of Casting Process*

The dip immersion probe must be designed according to the cast temperatures in aluminum alloys in the range of 675–800 °C with the following specification as shown in Table 13.2.

13.3.2 *Conceptual, Design, and Fabrication of the Dip Immersion Probe*

The main function of a dip immersion probe is to provide the intended temperature of the 675–800 °C range to the molten aluminum alloy (LM6) in order to obtain the molten metal casting. Sand mold is used in the pouring process, where a higher molten temperature is estimated in the corresponding pouring temperature at the range between 50 and 100 °C higher than the melting temperature of 660 °C. The ergonomics of the user in their casting environment is the main consideration for the design concept. More specifically, the probe was designed or modifies to 135 degrees over the working area to fit the user, not which to eliminate discomfort and

Fig. 13.2 The schematic diagram for DIP immersion probe



risk of injury due to casting work, besides to ensure a certain safety of the user at the measuring process in Fig. 13.2.

The material used in this project was LM6 with the chemical compositions of alloys as shown in Table 13.1. LM6 alloys ingot were being melted at the melting temperature using the crucible furnace. The molten metal is then melted at the silicon carbide crucible at different pouring temperatures. The melting temperatures selected for this project were 650, 700, 750, and 800 °C.

13.3.3 Pouring Temperature Measurement

The pouring temperature was measured by (a) built-in type ceramic sheath thermocouple (CST), (b) laser gun thermometer (LG), and (c) dip immersion probe (DIP). The built-in type of ceramic thermocouple that was attached to the crucible furnace and the pouring temperatures were read at the temperature panel meter gauge. For the laser gun thermometer, the laser beam that was focused on the molten metal was to be measured, and the reading was displayed on the laser infrared thermometer screen. For DIP, the thermocouple tip was inserted into the molten metal, and the reading will display on the thermometer screen (see Fig. 13.3).

13.4 Results and Discussion

The temperatures of molten metal (LM6) were measured by (a) built-in type ceramic sheath thermocouple (CST), (b) laser gun thermometer (LG), and (c) dip immersion probe (DIP) and recorded as shown in Table 13.3.

The results in Table 13.3 can be used to conduct the melting and pouring practice of a typical aluminum alloy, especially for LM6 (Al-Si12) in the casting process. It can be observed that for the measurements by equipment (a) and (b), the reading obtained becomes different with the testing temperature as per set through the reading by the built-in type of ceramic sheath thermocouple at the furnace. The results showed a

Fig. 13.3 Temperature measurement by DIP



Table 13.3 Temperature measurement by (a) built-in type ceramic sheath thermocouple, (b) laser gun thermometer, and (c) DIP immersion probe (DIP)

| Testing temperature, (°C) by equipment | | Reading 1 (°C) | Reading 2 (°C) | Reading 3 (°C) | Average reading (°C) | Different reading (°C) | |
|--|---|----------------|----------------|----------------|----------------------|------------------------|--------|
| 650 | a | CST | 650 | 651 | 652 | 651.0 | |
| | b | LG | 645 | 645 | 646 | 645.5 | - 5.7 |
| | c | DIP | 653 | 653 | 654 | 655.3 | + 4.3 |
| 700 | a | CST | 700 | 700 | 701 | 700.0 | |
| | b | LG | 688 | 690 | 692 | 690.0 | - 10.0 |
| | c | DIP | 702 | 704 | 703 | 703.0 | + 3.0 |
| 750 | a | CST | 750 | 751 | 751 | 750.6 | |
| | b | LG | 745 | 745 | 746 | 745.5 | - 5.3 |
| | c | DIP | 752 | 752 | 753 | 752.3 | + 1.7 |
| 800 | a | CST | 800 | 800 | 801 | 800.5 | |
| | b | LG | 785 | 789 | 790 | 788.0 | - 12.5 |
| | c | DIP | 802 | 803 | 805 | 803.5 | + 2.8 |

series of different readings of temperature with molten aluminum alloys at different temperatures of 650, 700, 750, and 800 °C between (a) built-in type ceramic sheath thermocouple, (b) laser gun thermometer, and (c) dip immersion probe (DIP).

In the measuring using the built-in type ceramic sheath thermocouple and DIP, which shows the differences temperatures of 4.3 °C for 650 °C, 3 °C for 700 °C, 1.7 °C for 750 °C, and 2.8 °C for 800 °C, respectively. This signified that the different methods of temperature between these two measuring methods were not much affected by the value of the molten aluminum temperatures. The differences between are varying but narrow and in between 0.2 and 0.7%. This different value is still under the accuracy of the accuracy (typical values) for the thermocouple sensor. This value does not affect the accuracy of the molten aluminum alloy temperature

within the limits for pouring purposes. This indicated that the value measured by the current probe and DIP is acceptable and has no effect on the pouring temperatures of the molten aluminum alloy.

For the measuring by built-in type ceramic sheath thermocouple and laser gun thermometer, the differences in temperature are 5.7 °C for 650 °C, 10 °C for 700 °C, 5.3 °C for 750 °C, and 12.5 °C for 800 °C, respectively. This indicated that the different method of temperature between these two measurement methods has higher values and affected the value of the molten aluminum temperatures. The differences between are varying and quite large and in between 0.7 and 1.6%. This value affected the accuracy of the molten aluminum alloy temperature within the limits for the pouring purposes. This signified that the value measured by the laser gun thermometer is not acceptable and influences the pouring temperatures of molten aluminum alloy. The large difference in the molten temperatures caused overheating of the molten aluminum which can lead to entrapped gas in the molten metal during the melting and pouring process (Brown 2002). These gases can form trapped air and hydrogen in molten aluminum which may lead to gas porosity. Hence, high melting temperatures can initiate the formation of hot cracks in the mold and form porosity defects in the casting (Sylvia 1999; Khanna 2006; Rana et al. 2012).

13.5 Conclusion

Dip immersion probe (DIP) was successfully designed and fabricated as a device to measure the melting temperature of metals and to ensure the quality of the casting. DIP was provided with the temperature of the molten metal especially aluminum alloys when placed on the furnace. This information can be useful in the melting and pouring process. By using this probe, the temperature can be obtained easily, and the temperature of the molten metal can reduce the overheating of molten metal. DIP is practical and can be used by moving the probe into or out of the process from time to time, with minimal adjustments. It is able to display any apparent change of indicated temperatures. The probe shows a wider temperature range, more prone to drift, more sensitive, and relatively cost-effective with a longer lifespan. It is also more ergonomic designated and safer to handle as compared to conventional probes for small-scale casting activity in foundry workshop.

Acknowledgements The authors would like to thank members from the Foundry Workshop, Mechanical Engineering Department of Politeknik Tuanku Syed Sirajuddin for providing the facilities, support, and assistance for this project and experimental studies.

References

- Brown JR (2002) *Foseco non-ferrous Foundryman's handbook*. Butterworth-Heinemann, Woburn, Massachusetts
- Hadi AS, Hill BE, Issahaq MN (2021) Performance characteristics of custom thermocouples for specialized applications. *Curr Comput-Aided Drug Des* 11(4):1–10
- Karuppasamy R, Barik D, Dennison MS (2020) Production of open-cell metallic foam made of LM6 aluminum alloy through sand casting technique. *Test Engineering and Management* 83:15136–15141
- Khanna OP (2006) *Foundry technology*, 10th Reprint: Dhanpat Rai Publications (P) Ltd, New Delhi
- Klemens A, Rahangmetan, Sariman CF, Syahid M (2019) Study on effect of temperature smelting and pouring to mechanical properties Aluminum 7075. *IOP Conf Ser Earth Environ Sci* 343(1):1–5
- Pollock DD (1991) *Thermocouples: theory and properties*. CRS Press Inc, Florida
- Rana RS, Purohit R, Das S (2012) Reviews on the influences of alloying elements on the microstructure and mechanical properties of aluminum alloys and aluminum alloy composites. *Int J Sci Res Publ* 2(6):1–7
- Rao PN (2001) *Manufacturing technology (foundry, forming & welding)*, 2nd edn. McGraw-Hill, Singapore
- Santhi S, Sakri SB, Rao HD, Sundarrajan S (2012) Mould filling ability characterisation of cast aluminium alloys using design of experiments. *J Metall*. <https://doi.org/10.1155/2012/624650>
- Starchowiak GW, Batchelor AW, Stachowiak GB (2004) *Experimental methods in tribology*, vol 44. Elsevier Ltd, Netherland
- Sylvia JG (1999) *Cast metals technology*. American Foundrymen's Society, Inc, Des Plaines, Illinois, USA
- Yordanov K, Zlateva P, Hadzhidimov I, Stoyanova A (2018) Testing and clearing the high temperature module error from 0 to 1250°C for measurement with 16 K-type thermocouples. In: 20th international symposium on electrical apparatus and technologies. SIELA. <https://doi.org/10.1109/SIELA.2018.8447096>
- Zhang J, Song B, Wei Q, Bourell D, Shi Y (2019) A review of selective laser melting of aluminum alloys: processing, microstructure, property and developing trends. *J Mater Sci Technol* 35(2):270–284

Chapter 14

Heat Transfer Coefficient for Synthetic Jet Cooling at Various Distance



Sh Mohd Firdaus, Nawal Radiah, Ahmad Faiz, Rohidatun Mahmud, Mohd Zulkifli Abdullah, Muhammad Khalil Abdullah, and Khairul Anuar Abd Wahid

Abstract Electronic cooling is constrained by space, which makes it difficult to remove heat that might cause the device to overheat. A synthetic jet is a type of air-based cooling technology that works without the usage of fans. Synthetic jets have zero-net-mass flux as it takes in and discharge high-velocity working fluid from a single outlet. This research analyzed the effect of a volume chamber at various distances between the nozzle and the heated surface. During the investigation, three experiments were carried out: heater characteristic, heated surface temperature, and fluid air velocity for the fabricated synthetic jet. The experiment used a heater with a voltage of 24 V and a power of 100 W. The constant heater surface temperature of 343.15 K was determined using the power input. In this research, five different volumes were tested. Each volume was tested at a distance from 10 to 50 mm between the nozzle and the heated surface. Results show that at 50 mm distance, the maximum temperature decrease was recorded for 1 mm volume. The maximum air velocity for all synthetic jet models was found at a distance of 10 mm, while the minimum air

S. M. Firdaus (✉) · N. Radiah · A. Faiz · R. Mahmud
Advanced Mechanics Research Group, Centre of Mechanical Engineering Studies, College of Engineering, Universiti Teknologi MARA Cawangan Pulau Pinang, 13500 Permatang Pauh, Penang, Malaysia
e-mail: sh.firdaus@uitm.edu.my

R. Mahmud
e-mail: rohidatun@uitm.edu.my

M. Z. Abdullah · M. K. Abdullah
School of Mechanical Engineering, School of Materials and Mineral Resources Engineering, Universiti Sains Malaysia, Engineering Campus, 14300 Nibong Tebal, Penang, Malaysia
e-mail: mezul@usm.my

M. K. Abdullah
e-mail: mkhalil@usm.my

K. A. A. Wahid
Mechanical Engineering Section, Universiti Kuala Lumpur (Malaysia France Institute), Bandar Baru Bangi, Malaysia
e-mail: hhairulanuarabdwahid@unikl.edu.my

Manufacturing Section, Universiti Kuala Lumpur Malaysian Spanish Institute, Kulim Hi-Tech Park, 09000 Kulim, Kedah, Malaysia

velocity was found at a distance of 70 mm. The maximum air velocity is produced by lower volume of synthetic jet 1.29 m/s.

Keywords Electronic cooling · Synthetic jet · Various distance · HTC

14.1 Introduction

Synthetic jet consists of three main parts such as orifice, chamber, and oscillating driver. The important role of the synthetic jet is the oscillating driver, as it controls the jet strength and frequency (Bijarchi et al. 2019). According to Lee et al. (2016), the movement of fluid in and out of the Chamber through the orifice is generated by the membrane oscillation. Under certain operating conditions, when the diaphragm reverses direction and no jet is formed, the ejected fluid is immediately drawn back into the Chamber. However, under the proper combination of amplitude and frequency of oscillation, separation of the ejected fluid occurs on the outer edges of the orifice. Synthetic jet required high frequency ranging from 300 to 700 Hz to oscillate the diaphragm actuator. An optimal driven frequency is required in order to obtain the highest velocity and maximum heat transfer coefficient of a synthetic jet.

The working principle of synthetic jet is due to the intake and eject for high-velocity working fluid from a single opening through the orifice. The intake and eject for high-velocity working fluid from a single opening make synthetic jets zero-net-mass flux (Firdaus et al. 2018). A zero-net-mass-flux jet is a fluid stream with nonzero mean stream-wise momentum formed by the interaction of vortices. Therefore, a synthetic jet is known as zero-net-mass-flux device capable of inducing nonzero momentum along the jet direction (Lee et al. 2016). Synthetic jet advantages compare to other existing methods for cooling electronic device are suited for cooling application at the package and heat sink level due to their ability to direct airflow along the heated surfaces in confined environments and to induce small-scale mixing (Jabbar and Naguib 2019). While the synthetic jet has also lower noise, lower power consumption, flexible form factor, higher reliability, easier miniaturization, and less fouling problem are compared to conventional fans.

14.2 Methodology

Three experiments have been conducted such as experiment of heater characteristic, experiment of various distance between the nozzle to heated surface temperature, and experiment fluid air velocity with various frequency applied to synthetic jet. In the experiment of heater characteristic, it is used to find relationship between the power and temperature of the heater (24 V: 100 W). The design of synthetic jet will have 5 different values of depth of volume for synthetic jet models. There were 1, 2, 3, 4, and 5 mm depth of volume (H) used for all synthetic jet. The diameter of

Table 14.1 Configuration of design synthetic jet

| Model | Depth of chamber (H) (mm) | Diameter of orifice (D_o) (mm) |
|-------|-------------------------------|------------------------------------|
| 1 | 1 | 2 |
| 2 | 2 | 2 |
| 3 | 3 | 2 |
| 4 | 4 | 2 |
| 5 | 5 | 2 |

center orifice (D_o) for synthetic jet is 2 mm for all designs. Table 14.1 shows the configuration design of synthetic jet.

All fabricated synthetic jets were used for heat transfer experiment as shown in Fig. 14.1 to characterize the effect of temperature on the various distance between the nozzle and heated surface temperature. The synthetic jet heat transfer coefficient (HTC) was determined as follows.

$$h = \frac{q_{\text{conv}}}{T_s - T_\infty} \left(\frac{\text{W}}{\text{m}^2\text{K}} \right) \quad (14.1)$$

The surface temperature of heater is the ambient temperature for the experiment. According to Mangate et al. (2019), the net heat flux is supplied. The net heat flux supplied is the difference in the supplied heat flux supplied.

14.3 Results and Discussions

14.3.1 Heater Characteristic

The value of temperature increases proportionally to power. At 0-W power, the heater temperature was 295.54 K which is the same as the room temperature. The heater 24 V: 100W achieved a temperature of 343.15 K when the voltage was at 6.80 V and the current was 2.10 A. The highest temperature that the heater can achieve is 353.81 K as shown in Fig. 14.2. The power has a proportional relationship to the voltage and current. According to Palumbo et al. (2018), the Joule power increases with increasing the voltage amplitude following a power of law.

14.3.2 Fluid Velocity at Various Distance

The highest velocity of synthetic jet was obtained at lowest distance between nozzle and the heated surface. Figure 14.3 shows the velocity, v (m/s), for all synthetic jet

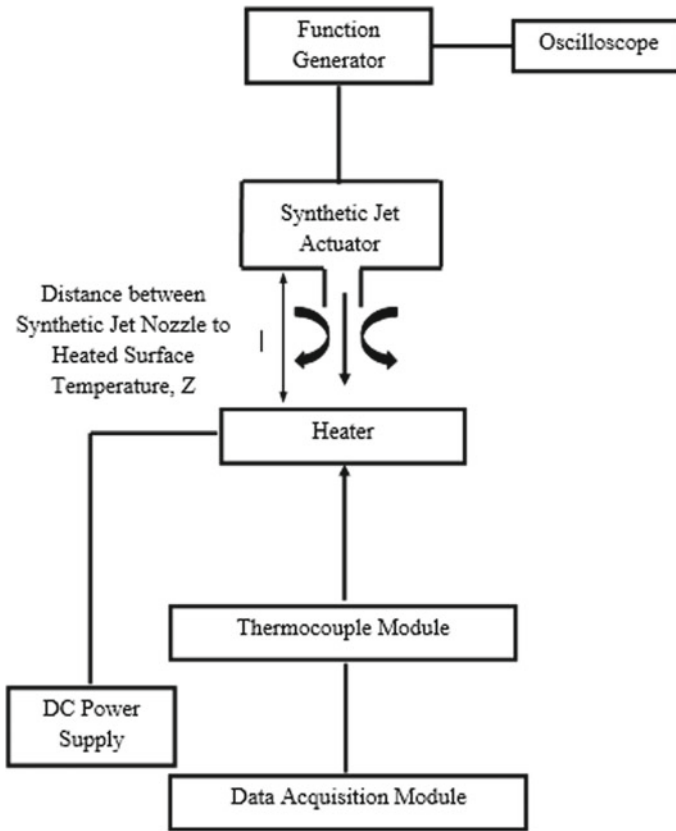


Fig. 14.1 Heat transfer experiment diagram

model, at various distance. Maximum velocity for all models of synthetic jet can be achieved at 10 mm distance while minimum velocity at 70 mm. Model 1 produces the highest velocity is 1.29 m/s. Similar trend or result was obtained by Liu et al. (2015) which shows that maximum velocity occurred at low distance and the velocity decrease as the distance increases. This justifies the experiment for fluid velocity of synthetic jet study.

14.3.3 *HTC Value at Various Distance*

The HTC value decreases as the volume increases. Maximum value of HTC produces by all volume at z distance of 50 mm. Model 1 is given the highest value for the heat transfer coefficient, h , at all distances, and model 5 is given the lowest value at all distances. Thus, maximum value of heat transfer coefficient, h , was 431.75 (W/m² K)

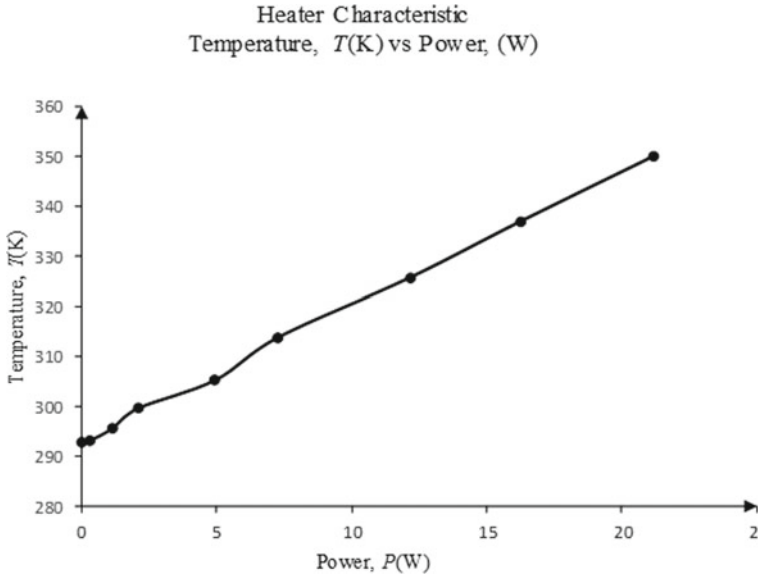


Fig. 14.2 Temperature (K) versus power (W)

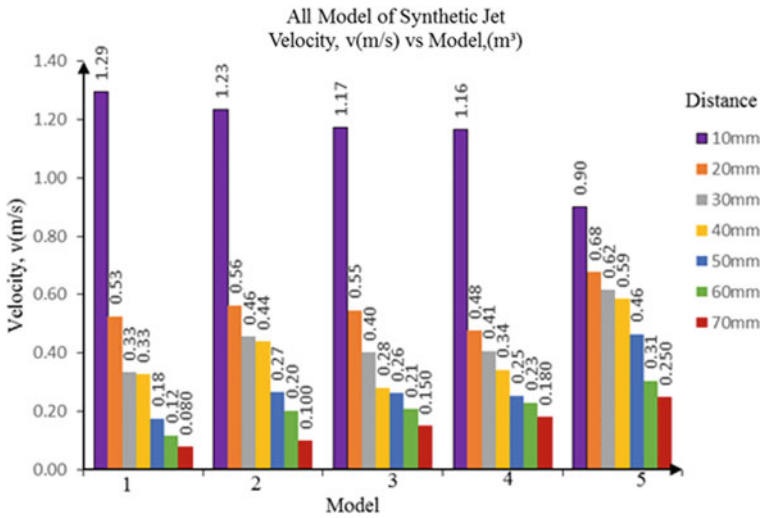


Fig. 14.3 Velocity, v (m/s), for overall model of synthetic jet

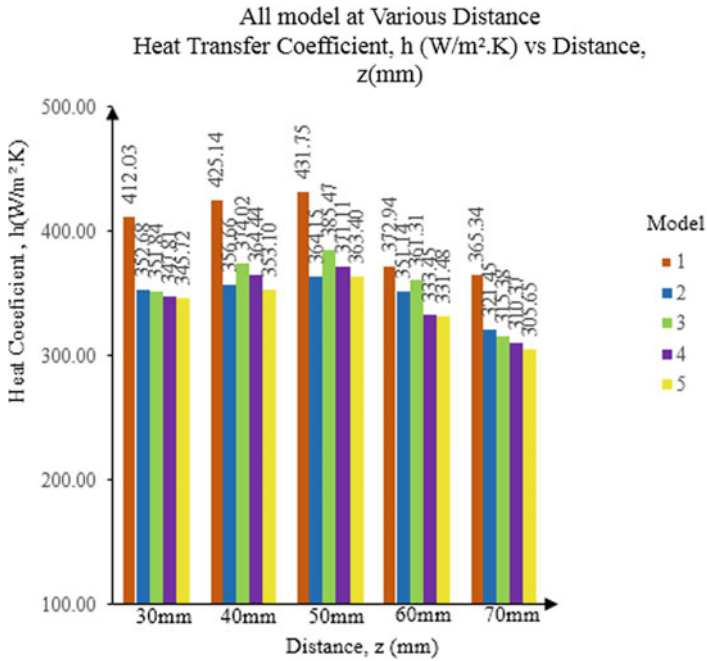


Fig. 14.4 Heat transfer coefficient, h (W/m² K) versus distance, z (mm) for all models at various distance

at 50 mm and minimum was 305.65 (W/m² K) at 70 mm. Figure 14.4 shows for all model at various distances for heat transfer coefficient, h (W/m² K). Mangate et al. (2019) stated that heat transfer coefficient, h , increases rapidly up to some axial distance and then decreases gradually with an increase in axial distance which has a similar pattern for this research output.

14.4 Conclusions

Synthetic jet cooling study at various distances has been successfully carried out. The nozzle to heated surface affects the HTC value and air velocity reached the heated surface. Lower volume produces higher air velocity compared to larger volume of synthetic jet. Higher HTC value at optimizes z distance.

References

- Bijarchi MA, Eghtesad A, Afshin H, Shafii MB (2019) Obtaining uniform cooling on a hot surface by a novel swinging slot impinging jet. *Appl Therm Eng* 150(01):781–790
- Firdaus SM, Abdullah MZ, Khalil MK, Amri W (2018) Synthetic jet cooling diaphragm equation of motion characteristic and verification for computational fluid dynamic modelling. *AIP Conf Proc* 1974(1)
- Jabbar HH, Naguib AM (2019) A computational study of vortex rings interacting with a constant-temperature heated wall. *Int J Heat Fluid Fl* 76:197–214
- Lee CYY, Woyciekoski ML, Copetti JB (2016) Experimental study of synthetic jets with rectangular orifice for electronic cooling. *Exp Therm and Fluid Sci* 78:242–248
- Liu YH, Tsai SY, Wang CC (2015) Effect of driven frequency on flow and heat transfer of an impinging synthetic air jet. *Appl Therm Eng* 75:289–297
- Mangate L, Yadav H, Agrawal A, Chaudhari M (2019) Experimental investigation on thermal and flow characteristics of synthetic jet with multiple-orifice of different shapes. *Int J Therm Sci* 140:344–357
- Palumbo A, Chiatto M, de Luca L (2018) Measurements versus numerical simulations for slotted synthetic jet actuator. *Actuators* 7(3):59

Chapter 15

Thermoelectric Conversion of Engine Cylinder Heat into Electric Energy



Mohamad Shukri bin Mohd Zain, Ahmad Kamal bin Ismail, Khairul Shahril bin Shaffee, Khairul Akmal bin Shamsuddin, Tajul Adli bin Abdul Razak, and Sharzali bin Che Mat

Abstract In an automobile, the internal combustion engine (ICE) does not efficiently convert heat into useful energy. A majority of this heat is expelled out as waste heat. This paper focuses on the recovery and utilization of waste heat into useful electrical energy by converting heat from the engine cylinder head surface directly into electrical energy by using thermoelectric generator (TEG). TEG has two distinct sides, referred to as the hot and cool sides, respectively. When the hot side of the TEG is heated while the cold side is chilled, the TEG is able to generate voltage as a result of the temperature difference. The boost converter boosts the electric potential produced by the TEG thereby increasing the magnitude of voltage required to supply energy to the load. The circuit is connected to the LED light as a load. The results were concluded that temperature difference is the most important factor in obtaining the appropriate voltage.

Keywords Engine cylinder head · Thermoelectric generator · Peltier plate · Seebeck effect · Heat energy

M. S. M. Zain (✉) · A. K. Ismail · K. S. Shaffee · K. A. Shamsuddin · T. A. A. Razak
Universiti Kuala Lumpur, Malaysian Spanish Institute Kulim Hi-Tech Park, 09000 Kulim, Kedah, Malaysia
e-mail: mshukrimz@unikl.edu.my

A. K. Ismail
e-mail: ahmadkamal@unikl.edu.my

K. S. Shaffee
e-mail: khairuls@unikl.edu.my

K. A. Shamsuddin
e-mail: khairulakmal@unikl.edu.my

T. A. A. Razak
e-mail: tajuladli@unikl.edu.my

S. C. Mat
School of Mechanical Engineering, College of Engineering, Cawangan Pulau Pinang, Universiti Teknologi MARA, Kampus Permatang Pauh, 13500 Permatang Pauh, Pulau Pinang, Malaysia
e-mail: sharzali.chemat@uitm.edu.my

15.1 Introduction

The need toward energy is growing by the day, yet there are only few sources available to produce energy as our fuel reserves deplete. Waste heat energy must be utilized in some way. Waste heat can be collected and recycled into useful work using several devices that execute waste heat recycling. Most of the waste heat recovery systems are built in the form of thermal energy, which is then transformed into electricity. The thermoelectric generator (TEG) module is used to efficiently produce energy from waste heat by direct conversion of temperature difference to electric voltage (Gajabe et al. 2018). This study aimed to obtain the heat produced from engine and investigate the effect of the temperature difference between cylinder head and cold region toward performance of voltage by doing an experiment on the cylinder head. The engine cylinder head was the upper part of engine and closes of combustion chamber. The result between voltage and current as a function of temperature difference was obtained in the study. The reading was taken by measuring the temperature at hot region from cylinder head and cold region cooling plate.

15.2 Literature Review

This section focused on the other study reviews that were useful to assist in identifying and considering the method to measure and record the data that were obtained from experiment to improve the performance of the TEG.

15.2.1 Heat Energy

The heat is the form of energy that is widely used in our daily life. The example of heat energy can be found in compressors, internal combustion engine, and other various equipment. In the heat energy, the heat flows between two materials of different temperatures which from the hot surface to the cold surface. The heat can transfer via conduction and radiation or in convection. The heat quantity is measured in terms of Joules (J) in SI units. The magnitude of heat generated at various sources is different; thereby, the temperature of these operating equipment is not the same and hence produces power of different ratings (Venkatesh et al. 2019). All devices under the heat energy follow the laws of thermodynamics including heat engine and heat pump.

15.2.2 Thermoelectric Generator

Thermoelectric power is created when heat energy is converted to electrical energy. This temperature difference causes carrier spread and generates electric current, when the temperature difference between two conductors is large enough, the electrons flow from the hot junction area to the cold junction region (Venkatesh et al. 2019). As a result, electromotive force exists. This process is referred as the Seebeck effect, and the potential difference that occurs during this time period is referred to as the Seebeck voltage (Shu et al. 2012).

The Seebeck Effect and Thermoelectric Module are shown in Figs. 15.1 and 15.2, respectively. Thermoelectric generators are solid-state devices which primary purpose is to convert heat directly to electricity or to convert electrical energy to thermal energy for heating and cooling. This defines that the thermal electron moves from hot junction region to cold junction region. Thus, the electromotive force (emf) is produced in the thermoelectric module directly proportional to the temperature difference (Sunawar et al. 2017). Temperature difference can be stated as Eq. 15.1 below.

$$\Delta T = T_h - T_c \quad (15.1)$$

TEG is often composed of many thermopiles linked in series to maximize the output power (Kamal et al. 2013). Each Peltier plate is composed of several thermocouples (TC) linked in series electrically and thermally. The thermocouple is constructed from two materials with diametrically opposed Seebeck coefficients. Due to Seebeck effect, the appearance of a temperature gradient, ΔT (Eq. 15.1), and

Fig. 15.1 The Seebeck effect

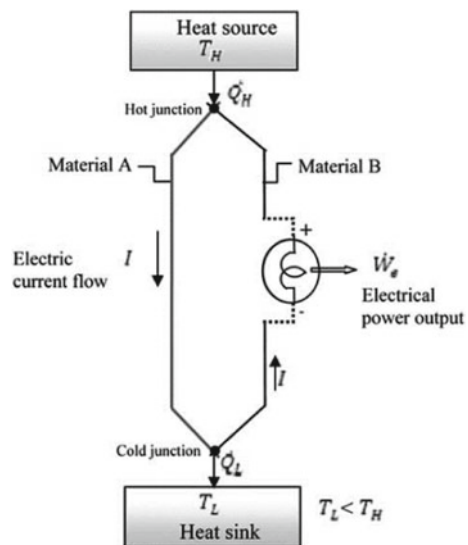
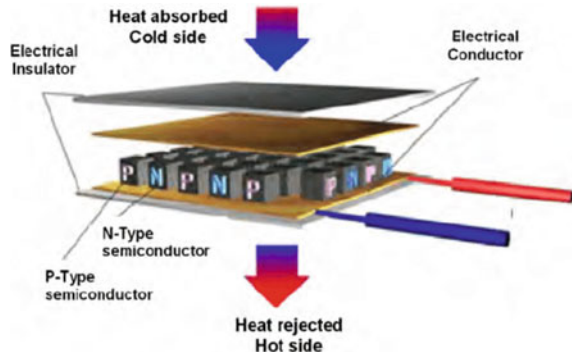


Fig. 15.2 The thermoelectric module



then the voltage can be stated in Eq. 15.2 below.

$$V_{\text{out}} = N\alpha_{\text{AB}}\Delta T \quad (15.2)$$

The TEG is composed of thermocouple pairs of n-type and p-type semiconductor materials. These are electrically coupled to produce a thermopile array consisting of several thermocouples placed between thin ceramic wafers. TEG equipped with liquid on the cold side outperforms all other cooling methods and generate much more net extra power.

15.3 Methodology/Experimental Setup

15.3.1 Experimental Setup

The experiment was conducted on the actual running motorcycle engine (Fig. 15.3) and also laboratory setup. The motorcycle temperature data were observed based on three riding modes such as idle, heavy traffic, and highway ride. The motorcycle operating temperature data were recorded in Table 15.1 as a reference of control temperature for laboratory setup.

The schematic diagram in Fig. 15.4 is designed for the laboratory setup in order to convert heat energy into electric energy. The laboratory design is separated into two parts, the first part is the heat source using IKA hot plate and the second part is the circuit system which consist of a switch, step-up boost converter, and LED light with different power, 1 W and 3 W, respectively.

Figures 15.5 and 15.6 show the photograph of the experimental setup. In the laboratory experiment, the IKA hot plate was heated up with the cylinder head cap and circuit connected to Peltier plate using thermal conductive paste. The standard performance Peltier plate TEC1-12705 has been used as the main part in power

Fig. 15.3 Measurement of engine cylinder head temperature



Table 15.1 Engine cylinder head operating temperature

| Riding mode | Average speed (km/h) | Running temperature (°C) | Surrounding temperature (°C) | Difference temperature (°C) |
|---------------|----------------------|--------------------------|------------------------------|-----------------------------|
| Idle | 0 | 61 | 32 | 29 |
| Highway | 110 | 104 | 37 | 67 |
| Heavy traffic | 15 | 133 | 38 | 95 |

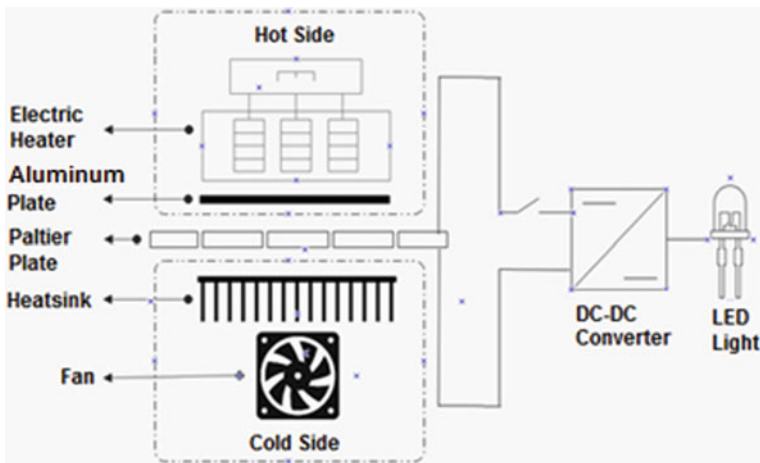


Fig. 15.4 Schematic diagram for laboratory setup

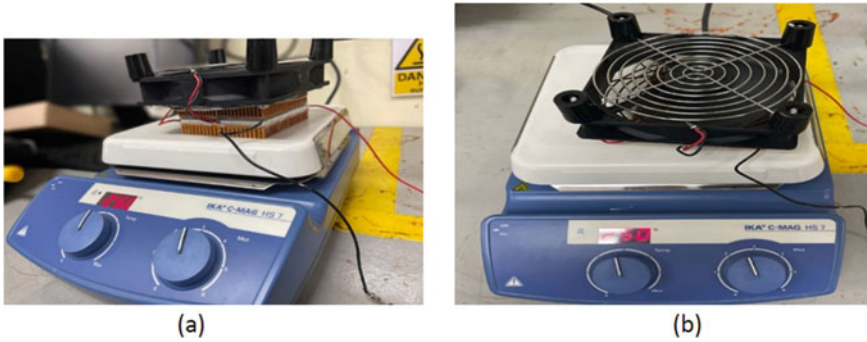
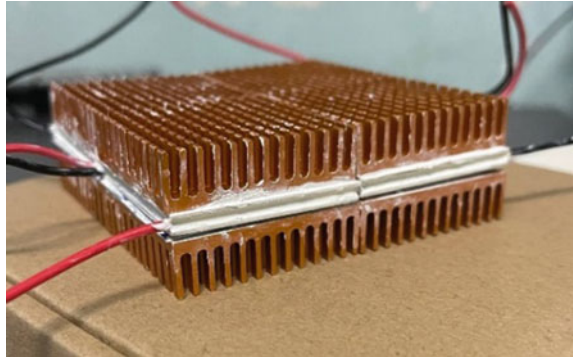


Fig. 15.5 Experimental setup **a** Front view. **b** Top view

Fig. 15.6 Bottom view of experimental setup



generation system. The physical dimensions of the Peltier plate are $40 \text{ mm} \times 40 \text{ mm} \times 3.8 \text{ mm}$ for the width, length, and thickness, respectively.

The Peltier plate then converts the heat energy into electrical energy according to different temperatures set by experiment. After the temperature rises, these electrical energies are then being stored in step-up boost converter. The boost converter works like a battery to store energy and release them at a certain period with the desired amount of current needed. The boost converter is a fast-charging and slower-discharging capacitor than other types of capacitors. The super-capacitor output is given to the boost converter. The boost converter is a type of DC-to-DC converter. The function of boost converter is to convert the output voltage higher than the input voltage. The boost converter output is given to the LED light acting as the load as well as the indicator toward current flow as shown in Fig. 15.7. In this project, the signal of the input and output power to maintain the constant output power is achieved with the help of boost converter.

The TEG device is directly connected to the booster converter. The voltage flow from TEG to booster converter and the wires are related to TEG, switch, and boost converter. An ON/OFF switch is fixed and directly connected to the load. When the switch is ON, the voltage directly passes to the load. In the boost converter, there is a

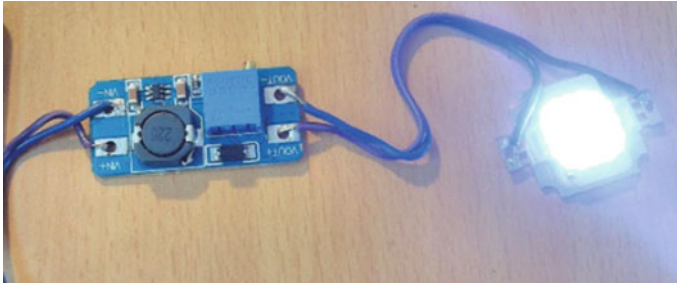


Fig. 15.7 Circuit system

resistor that minimizes the voltage and is directed to LED light. LED light emits that indicates the current is passing. The voltage flow capacity of the load is recorded. Four TEG were electrically connected in series, and thermally conductive silicone was used to adhere them to the aluminum surface as the hot side.

As a result, the energy from the engine cylinder head waste heat can be transferred to TEG and then transferred to the boost converter which controlling the terminal voltage. TEG would help to improve efficiency of engine cylinder head by absorbing and flow it to the electric circuit to produce useful energy. After the heat was supplied to the load, the input and output voltage is taken by using digital multimeter. The data collected is transferred to the table to plot the graph.

15.4 Result and Discussion

The experimental results are shown in Figs. 15.8 and 15.9. Figure 15.8 shows the data of output voltage and current from TEG system. Based on the graph, the higher value of the voltage and current was Voltage2-1W LED load and Current2-1W LED load, respectively. It was found that the output voltage and current increased with the temperature difference regardless of the amount of load. Besides, the output voltage and current were found to decrease by increasing the load.

Figure 15.9 describes that the output power increased with the temperature difference increased. Based on the graph, the higher value of the power was Power2-1W LED. The temperature difference increased due to the high amount of temperature that was supplied to the system. In addition, the output power was found to increase by reducing the load.

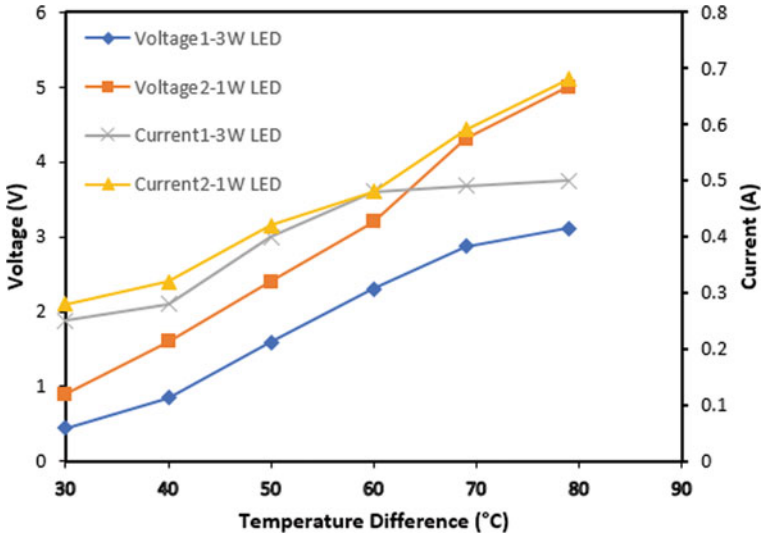


Fig. 15.8 Graph of output voltage and current with 1 and 3 W LED light versus temperature difference

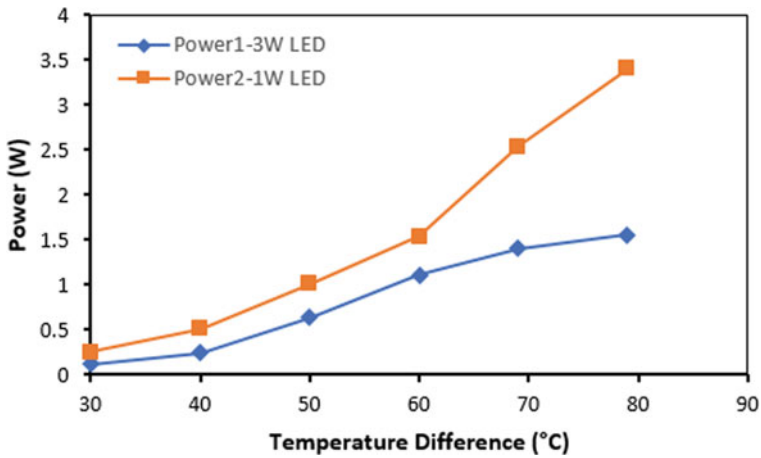


Fig. 15.9 Graph of output power with 1 and 3 W LED light versus temperature difference

15.5 Conclusion

In this paper, the power generation system of a cylinder head waste heat has been studied using TEGs. The output voltage and current have been examined as a function of temperature difference with two different load settings which are 1 and 3 W LED light. It is clear that the output voltage and current increased with the temperature

difference regardless of the amount of load. In addition, the power output was found to decrease by increasing the load. The waste heat of cylinder head that was harvested from TEGs and then converted to electricity can be utilized for low-power unit applications.

References

- Gajabe MKA, Dhanke MKP, Tikhe SJ (2018) A review on utilization of waste heat from automobile based on thermoelectric generator. *International Research Journal of Engineering and Technology (IRJET)* 5(2):469–471
- Kamal A, Zulki M, Zubair M, Ari Z (2013) Application of porous medium burner with micro cogeneration system. *Application of porous medium burner with micro cogeneration system. Energy* 131–142
- Shu G, Zhao J, Tian H, Liang X, Wei H (2012) Parametric and exergetic analysis of waste heat recovery system based on thermoelectric generator and organic Rankine cycle utilizing R123. *Energy* 45(1):806–816
- Sunawar A, Garniwa I, Hudaya C, Generator AT (2017) The design of alternative electric energy utilizes solar heat in the vehicle cabin with thermoelectric module. *International Conference on High Voltage Engineering and Power Systems (ICHVEPS)*. <https://doi.org/10.1109/ICHVEPS.2017.8225928>
- Venkatesh A, Nazar Ali A, Jaiganesh R, Indragandhi V (2019) Extraction and conversion of exhaust heat from automobile engine in to electrical energy. *IOP Conference Series: Materials Science and Engineering* 623(1):52–57

Chapter 16

Ergonomic Analysis of Hand Machine Vibration Based on ISO Standard 5439 (2001)



Mohd Fahmi bin Mohd Husni, Tajul Adli bin Abdul Razak, Nadya binti Abdullah, Mohd Riduan bin Ibrahim, and Shahril Nizam Mohamed Soid

Abstract In the woodcutting process, an ergonomic factor is one of the biggest concerns to produce an efficient work product with less risk of injuries. In this experiment, a jigsaw exerted hand-arm vibration that potentially caused an ergonomic injury to the operator. Different types of blades are used in this experiment to understand the relationship between blade characteristics and vibration during the wood cutting process. In addition, too much exposure to hand-arm vibration decreases job performance as the operator would experience carpal syndrome related to musculoskeletal disorders. This experiment examines the vibrations caused by the jigsaw on the operator's hand when using various blade types. The vibration is measured using a tri-axial accelerometer. The accelerometer is installed on the operator's hand at the position and orientation specified by ISO 5349 standard. The machine vibration is reduced by selecting the fine blade for the woodworking process over the coarse blade. Few blade types are used in this experiment to produce various measurements on the accelerometer. The measured data are compared. The results indicate that different samples produce different vibration magnitudes. The machine's vibration varies, and the highest vibration magnitude is produced by the coarse blade, designed for faster wood cutting operation. It is concluded that the hand-arm vibration (HAV) can be reduced with the proper selection of blades during the cutting operation.

M. F. M. Husni
Top Glove Sdn. Bhd, 41050 Shah Alam, Selangor, Malaysia

T. A. A. Razak (✉) · M. R. Ibrahim · S. N. M. Soid
Universiti Kuala Lumpur, Malaysian Spanish Institute Kulim Hi-Tech Park, 09000 Kulim, Kedah, Malaysia
e-mail: tajuladli@unikl.edu.my

M. R. Ibrahim
e-mail: mohdriduan@unikl.edu.my

S. N. M. Soid
e-mail: shahrilnizam@unikl.edu.my

N. Abdullah
Universiti Selangor, 40000 Shah Alam, Selangor, Malaysia
e-mail: nadya@unisel.edu.my

Keywords Machine process · Hand-held machine · Occupational safety and health · Vibration dampening

16.1 Introduction

Musculoskeletal disorder (MSD) is a common illness related to prolonged exposure and accounted for 31% of all injury and illness cases in 2015 (Bureau of Labor Statistics 2016). Apart from psychosocial work characteristics that produce adverse effect to human (Taibi et al. 2021), machinery also contributed significantly to the issue. The operation of the machinery itself mainly generates vibrations (rotating or reciprocating masses, gas pulsation, aerodynamic phenomena) by the impact of hand-held machinery on hard materials or by the interaction between the machinery and its environment. For example, vibration can be caused by the movement of mobile machinery over rough ground. Machine tools used by construction workers, industry, and agriculture are the most affected by vibration (Eurofound 2017).

Vibration exposure has been linked to various symptoms and long-term vibration exposure in the hand-arm and whole-body systems (Griffin 1990). In several European nations, machine manufacturers are required by the country to decrease the risk of vibrations, encouraging the machine manufacturers to explore suitable technical solutions in reducing vibration emission. It also stipulates that information on vibrational emissions be reported in the instructions for specific machinery categories. The information helps in decreasing the lost days and permanent incapacity to work due to MSD-related ill (Bevan 2015). Prolonged exposure to vibration may not be felt during short duration but can have an effect to spine as human body reacts to counterbalance the inertia caused by the machine. This will damage the low back tissue in a long run (Kia et al. 2020).

Exposures would increase musculoskeletal stress around the spine to counterbalance the inertia of the torso and potentially result in the overuse and damage to the soft tissues in the low back regions.

16.2 ISO 5349

Generally, each standard supports its benefits. However, the following benefits are common to all certifications: increased market potential, compliance with procurement tenders, improved efficiency and cost savings, improved customer service and thus satisfaction, and increased staff morale and motivation.

The ISO 5349-2001, which refers to Mechanical Vibration Measurement and Evaluation of Human Exposure to Hand Transmitted Vibration standard, evaluates hand-arm vibration in the jigsaw wood cutting process. This ISO standard is divided into two parts: ISO 5349-1, which refers to generic requirements, and ISO 5349-2, which relates to special requirements such as practical guidance for the measurement

at the workplace. The ISO 5349 standard is developed as a result of research into the method for collecting data on the human body and categorizing vibration effects in terms of sensitivity to the development of Vibration White Finger (VWF), also known as Raynaud's illness. The vibration response can be classified in general based on the frequency, amplitude, direction, exposure time, and grip force (Joshi et al. 2012). It establishes the general requirement for measuring and evaluating human exposure to hand-transmitted vibration in ISO 5349-1. The material in ISO 5349-2, which provides practical recommendations for implementing appropriate measurement and evaluation methodologies in the workplace, complements it (ISO 2631-1, 1997).

According to its definition, ISO 5341-1 provides the main requirements for measuring and reporting hand-transmitted vibration exposure in three orthogonal axes. Apart from that, for general consideration, ISO 5349-1 is the approach that considers a few factors that are known to cause the effect of human exposure to hand-transmitted vibration in working settings. Among the factors that cause the effect to the human arm are the frequency spectrum of the vibration, the magnitude of the vibration, and the time of exposure each working day (Vas et al, 2021).

In accordance with ISO 5349-1, the ISO 5349-2 provides guidelines for measuring and evaluating hand-transmitted vibration at work. The procedures for taking representative vibration measurements and determining the daily exposure time for each operation were detailed in the guidelines. The purpose of the guided activities is to standardize the experiment so that an 8 J energy equivalent vibration total value can be calculated, representing everyday vibration exposure in real life. This section of ISO 5349-2 applies to all scenarios in which vibration is delivered to the hand-arm system via hand-held or hand-guided machinery, vibrating workpieces, or controls of mobile or permanent machinery.

16.3 Experimental Setup

The experiment uses a jigsaw power tool for wood cutting process. The vibration is measured in three orthogonal directions: x , y , and z by using a tri-axial accelerometer, as shown in Fig. 16.1. The position of the sensor is referred to the standard guideline from ISO Standard 5349-1 (2001).

The experiment is performed using three different blades used: basic for wood T111C, wood T144D, and wood and metal T345XF. The T111C basic for wood blades are reasonable for cutting wood and wood products made of high carbon steel construction for long-life performance. The T144D is relatively good for fast cutting activities. The blade is made of high carbon steel material with a T-shank design for maximum grip and stability during the wood cutting process. The blade of T345XF for wood and metal is an outstanding product with a Bi-metal construction for durability and long life. Figure 16.2 shows the mentioned blades.

Fig. 16.1 Actual experiment setup

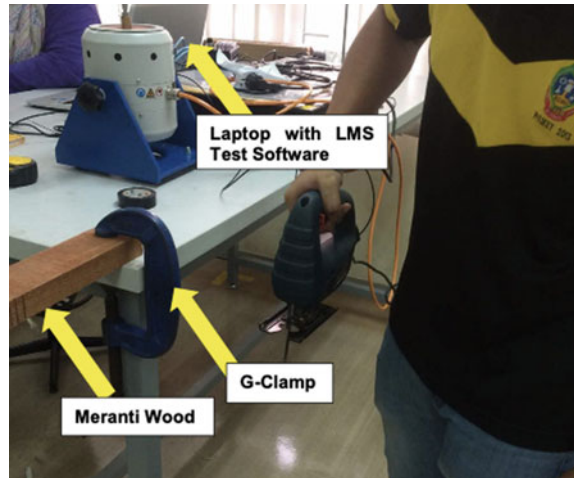


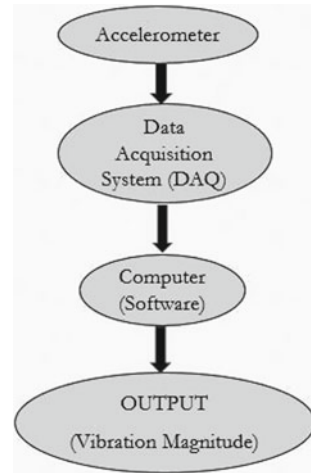
Fig. 16.2 Different blades for the same machine tool

16.4 Data Collection

Referring to the flow chart shown in Fig. 16.3, the data are acquired from the tri-axial accelerometer through connection to the data acquisition system (DAQ) via the PCB tri-axial accelerometer cable with three distinguished pins labeled X , Y , and Z , respectively. Following the acquired data from DAQ, the system converted the analog signal to digital data and transferred the data to the computer PC for meaningful information. The DAQ is performed using the LMS Test Express Software known as spectral analysis to measure the vibration signal.

X , Y , and Z are the representations of acceleration in unit g amplitude. Hence, all the three values must be converted to m/s^2 by multiplying the values with $9.81 m/s^2$ in order to get in a_{RMS} value. The final output was represented in form of the Root Mean Square (RMS) acceleration value in terms of vibration magnitude in m/s^2 and frequency spectrum in Hz. By following the ISO 5349 standard, the RMS value of

Fig. 16.3 Flowchart of data acquisition process



acceleration is computed for examining the extent of vibration entering the hand-arm system from the jigsaw. The vibrations were measured in the three orthogonal directions of X , Y , and Z . Each sample was combined into a single value by using Eq. 16.1.

$$a_{\text{RMS}} = \sqrt{ax^2 + ay^2 + az^2} \quad (16.1)$$

The result of the average vibration magnitude for each of the three types of blade is used to determine the daily vibration exposure using the exposure point system as shown in Fig. 16.3. The points for daily vibration exposure for each type of blade are compared to investigate the vibration level of those three different sawing blades.

16.5 Result

Laboratory experiments were conducted using the hand machine to obtain the amplitude and frequency values produced by the hand-tool machine when using different saw blades. Table 16.1 shows the result in 3-axis directions.

The vibration magnitude levels are averaged to determine the vibration magnitude, and then, the daily vibration exposures are determined by using the exposure point system as shown in Fig. 16.3. In this experiment, the worker is assumed to be exposed to vibration for 3 h in a day. Table 16.2 shows the compilation of magnitude vibration, exposed duration, exposed point, and specific zone for the activity.

Referring to exposure point system by ready reckoner system (Great Britain. Health and Safety Executive 2005), the daily vibration exposure is determined by using the table as shown in Fig. 16.4. The exposure point system is a guide to measure the suitable daily vibration exposure from the jigsaw to the operator's hand.

Table 16.1 Collected data from for each blade

| Type of blade | X-axis | | Y-axis | | Z-axis | | Vibration magnitude (m/s ²) |
|---------------|---------------|----------------|---------------|----------------|---------------|----------------|---|
| | Amplitude (g) | Frequency (Hz) | Amplitude (g) | Frequency (Hz) | Amplitude (g) | Frequency (Hz) | |
| T111C | 0.4739 | 223 | 0.3898 | 112 | 0.2335 | 332 | 6.44 |
| T144D | 0.1859 | 113 | 0.6818 | 114 | 0.1297 | 332 | 7.05 |
| T345XF | 0.1292 | 226 | 0.55706 | 114 | 0.2426 | 115.5 | 6.21 |

Table 16.2 Referring vibration magnitude to exposure duration

| No. | Type of blades | Magnitude vibration, m/s ² | Exposed duration, hours | Exposed point | Zone |
|-----|-------------------------|---------------------------------------|-------------------------|---------------|-----------------------------|
| 1 | T111C (for wood) | 6.44 | 3 | 215 | Above exposure action value |
| 2 | T144D (speed for wood) | 7.05 | 3 | 295 | Likely to be at limitation |
| 3 | T345XF (wood and metal) | 6.21 | 3 | 215 | Above exposure action value |

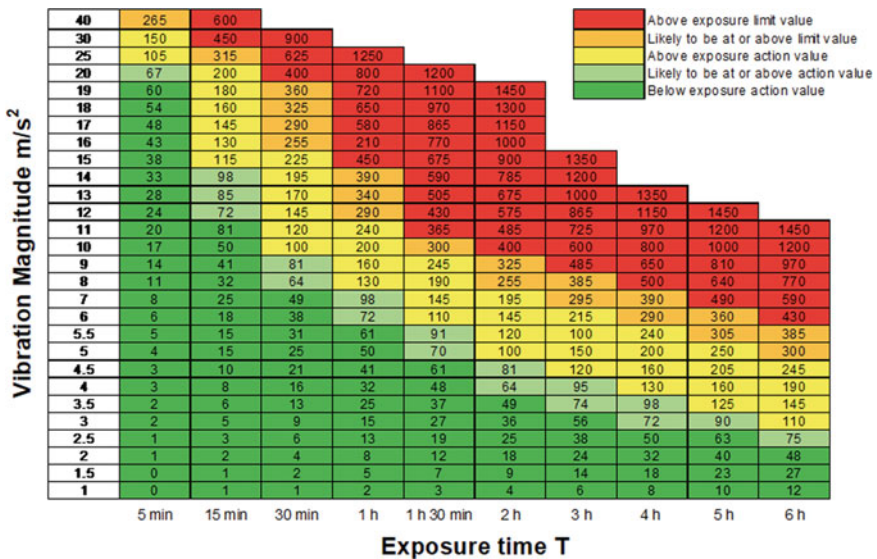


Fig. 16.4 Ready Reckoner table (Great Britain. Health and Safety Executive 2005)

16.6 Discussion

The research shows how a new blade type can reduce machine tool hand-arm vibration while performing a task. The results also revealed that a shorter time spent using the device is required to lower the likelihood of a hand-arm injury.

A ready reckoner is a gadget that calculates the number of exposure points required to initiate vibration action. Only the trigger point that the hands are actually exposed to is included in the exposure length. According to a study, long-term exposure to vibration was only a poor predictor of increasing hand injury severity. The study also discovered that using blades for speedier cutting operations raises the likelihood of developing this disease.

Vibration symptoms in the hands and arms are the effects of excessive vibration caused by the blade's teeth design. Although vibration magnitudes will not reach the directive's exposure action value or limit value, hazards are still present. To minimize the hazards, actions such as reducing exposure times, continuous health surveillance, improved hand grip and other extra accessories equipment, and an improving ergonomics operator position during the cutting process could be the solution. This research hopes in bridging the gaps and brings us closer to those enhanced outcomes for future reference.

16.7 Conclusion

This experiment shows valuable information of hand-arm vibration exposure on a jigsaw machine during operation. Excessive jigsaw machine vibration can cause a disorder known as hand-arm vibration syndrome (HAVS), which has both vascular and neurological components. It is most common in industrial power tools, where the cost of cutting can be reduced simply by using suitable blades for the task. If workers decide to use a coarse blade for faster operation, further research is needed to determine the best approach.

References

- Bevan S (2015) Economic impact of musculoskeletal disorders (MSDs) on work in Europe. *Best Pract Res Clin Rheumatol* 29(3):356–373
- Bureau of Labor Statistics (2016) Nonfatal Occupational Injuries and Illnesses Requiring Days Away from Work. www.bls.gov/iif/oshcdnew.html. Accessed 27 Nov 2021
- Eurofound (2017) Sixth European working conditions survey—overview report (2017 update). Publications Office of the European Union, Luxembourg
- Great Britain. Health and Safety Executive (2005) Hand-arm vibration : the Control of Vibration at Work Regulations 2005. The Stationery Office (TSO)
- Griffin M (1990) Handbook of human vibration, 1st edn. Academic Press
- ISO 2631-1 (1997) International Standard ISO 2631-1. 1997, 1–28

- Joshi A, Leu M, Murray S (2012) Ergonomic analysis of fastening vibration based on ISO Standard 5349 (2001). *Appl Ergon* 43(6):1051–1057
- Kia K, Fitch SM, Newsom SA, Kim JH (2020) Effect of whole-body vibration exposures on physiological stresses: mining heavy equipment applications. *Appl Ergon* 85:103065. <https://doi.org/10.1016/j.apergo.2020.103065>
- Taibi Y, Metzler YA, Bellingrath S, Müller A (2021) A systematic overview on the risk effects of psychosocial work characteristics on musculoskeletal disorders, absenteeism, and workplace accidents. *Appl Ergon* 95:103434. <https://doi.org/10.1016/j.apergo.2021.103434>
- Vas AS, Shubhalakshmi A, Suvarna M (2021) Hand-arm vibration on dentists using ready reckoner: a cross-sectional study. *Int Dent J of Student Res* 8(4):140–144

Chapter 17

Non-symmetrical Force–Deflection Behavior of a NiTi Archwire in Orthodontic Leveling Treatment



Mohd Nizam Ahmad, Abdus Samad Mahmud, Muhammad Hazwan Yusof, and Mohd Suyerdi Omar

Abstract Orthodontics is a branch of dentistry that focuses on dealing with irregularities of teeth such as malocclusion. The orthodontic treatment helps in aligning and straightening teeth which aim to improve the aesthetic appearance and healthy masticatory function. This study was designed to investigate the bending deformation behavior of nickel-titanium (NiTi) archwires in non-symmetrical brackets mounting configuration in orthodontic leveling treatment. A three-bracket bending test was performed in a dry condition at room temperature, 25.5 °C, and testing temperature, 35.5 °C, in compliance with the ISO 15841—Dentistry: wires for use in orthodontics. The NiTi archwires used were 0.016-in. round and 0.016 × 0.022-in. rectangular. The brackets used were made of 0.022-in. stainless steel. For the non-symmetrical loading, the load position is offset by 0.25 mm incremental, up to 1.5 mm from the center. The archwire was deflected to a maximum of 4 mm. Force–deflection curves are plotted from the results of the bending test. The archwire recovered from the greater force magnitude during activation will release at a lower force magnitude at the start of the deactivation stage. An increase in temperature from 25.5 to 35.5 °C increases both activation and deactivation forces. The same behavior was also observed on the rectangular wire, except that the force level on activation and deactivation are higher due to differences. Offsetting the inter-bracket distance requires higher force for the wire deflection, which decreases the internal energy with the leveling treatment process.

M. N. Ahmad (✉)

Engineering Section, Universiti Kuala Lumpur Malaysian Spanish Institute, Kulim Hi-Tech Park, 09000 Kulim, Kedah, Malaysia
e-mail: mohdnizam@unikl.edu.my

A. S. Mahmud · M. H. Yusof

Nanofabrication and Functional Materials Research Group, School of Mechanical Engineering, Universiti Sains Malaysia, Engineering Campus, 14300 Nibong Tebal, Penang, Malaysia
e-mail: abdus@usm.my

M. S. Omar

Mechanical Section, Universiti Kuala Lumpur Malaysian Spanish Institute, Kulim Hi-Tech Park, 09000 Kulim, Kedah, Malaysia
e-mail: msuyerdi@unikl.edu.my

Keywords Shape memory alloy · Activation and deactivation forces · Three-bracket bending

17.1 Introduction

Orthodontic treatment is also known as a method to improve the look and arrangement of teeth by straightening or moving the malpositioned teeth into the desired position. Generally, orthodontic treatment can be fractionated into three stages: the initial stage, the intermediate stage, and the finishing stage (Yoneyama and Miyazaki 2008). In each stage of treatment, the required properties of the wire are considerably different. During the earliest stages of orthodontic therapy, the NiTi archwire is favored above other metal orthodontic wires. One of the reasons is due to less time required to accomplish leveling and less discomfort that patients get with the use of NiTi archwires as indicated by Andreasen and Morrom (Kapila and Sachdeva 1989).

17.2 Literature

NiTi archwires have advantages over others metal orthodontic wires because of shape memory and superelastic properties. In orthodontic treatment, the engagement of archwires occurred in the bracket slots that are attached to the teeth for moving teeth to the desired position which can improve the appearance of the teeth. NiTi archwire is regarded as a good archwire because it can consistently supply enough force for tooth movement, reducing the risk of patient pain, periodontal ligament damage, and resorption undermining (Gurgel et al. 2001). This force should be low and delivered continuously over a suitable period (Nespoli et al. 2015). The goal is to keep a force on the teeth practically continually during treatment, from the very aberrant position for the rest to the almost perfect alignment at the end (Siegener and Ibe 2000).

Force delivery capabilities by the NiTi archwire in orthodontics treatment are the most favorable (Ahmad et al. 2019). Knowing a specific magnitude of force during activation and deactivation is necessary to provide the optimum and predictable treatment results (Youyi et al. 2000). The activation force and deactivation force are two forces that play important roles in orthodontic treatment. The activation force is the force that is required to bend the archwire during engaging it into the orthodontic bracket, while the deactivation force of the orthodontic archwire is formed when it tries to go back to its original formed shape which causes the tooth to move into the desired location. The deactivation force becomes the primary concern in orthodontic treatment.

This research deals to evaluate the force–deflection behavior encountered in non-symmetrical bracket mounting configuration in orthodontic leveling treatment. This condition resembles the variation of tooth size between canine, central incisor, and lateral incisor. The effect of different wire geometry will also be evaluated. Finally,

the force magnitude from the force–deflection curve is discussed to analyze the performance and behavior of NiTi archwire.

17.3 Methodology

The experimental test performed in this study is the three-bracket bending test as shown in Fig. 17.1. The three-bracket bending represents the leveling treatment on the maxillary arch by aligning three brackets that correspond to the lateral incisor, canine, and first premolar. The three-bracket bending test is conducted by using a universal testing machine (Model 3367, Instron) with a 500 N load cell installed. The result from the bending test will be used to plot the force–deflection curve, thus reflecting the behavior exhibited by the archwire.

In the test, 0.022-in. stainless steel bracket sizes are used together with 0.016-in. round NiTi archwire and 0.016 × 0.022-in. rectangular NiTi archwire. The 20 mm NiTi archwire specimen was cut from the archwire’s straight-end segment. A UTM crosshead speed of 1 mm/min deflected the archwires from 2.0 to 4.0 mm. The deflection range was chosen due to the range of possible occasions under clinical conditions.

The canine was represented by the central bracket, which was mounted on the adjustable indenter, and the lateral incisor and first premolar were represented by the adjacent brackets, which were installed on the fixed supports, as shown in Fig. 17.2. Using cyanoacrylate adhesives, the brackets were bonded to the mobile indenter and mounting base. In this wire-bracket design, no ligation tie was added. As a result, there is no friction caused by the ligation tie when it drives the archwire against the bracket slot’s base. The tests were carried out at 25.5 °C ambient temperature and 35.5 °C oral temperature, with the test apparatus being put in a temperature-controlled chamber and the full test being carried out inside the chamber at the chamber’s set temperature. Offsetting the movable indenters by 0.25 mm incrementally, up to 1.5 mm from the center, is used to investigate non-symmetrical force–deflection behavior.

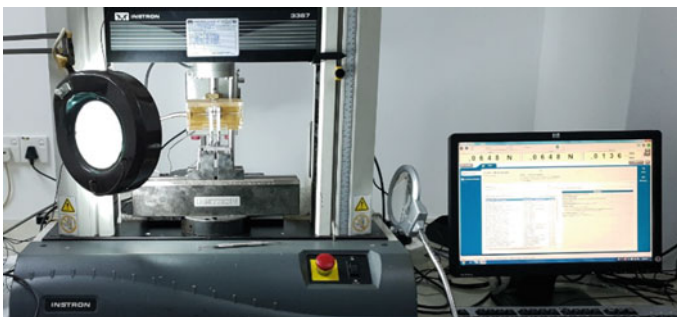
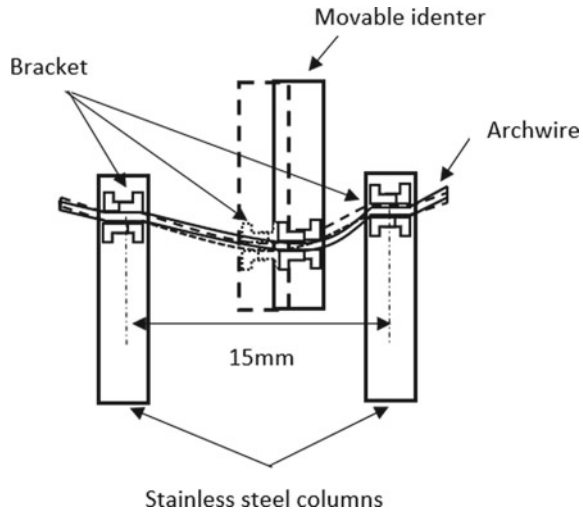


Fig. 17.1 Experimental setup of three-bracket bending test

Fig. 17.2 Schematic of the unsymmetrical three-bracket bending setup



17.4 Result and Discussion

Force–deflection curves on round and rectangular archwires at two different temperatures, under symmetrical bending tests, are shown in Fig. 17.3. The activation cycle starts with a linear slope until 0.8 mm and 1.00 m deflection distance on the round and rectangular archwire, respectively. The plateau shown in the figure transformed into slope a trend and the activation force is high in comparison with the three-point bending which indicated that friction incorporates in this test due to bracket-wire contact. Increases in offset and deflection distance showed to increase in activation and decrease in deactivation force. This indicated that high offset and deflection distance causes more difficulty for the archwire to bend during installation and decreases the internal energy of the archwire during leveling treatment. The activation force is higher on rectangular archwires compared to round archwires following the bending stiffness.

17.4.1 Non-Symmetrical Three-Bracket Bending

Force–deflection curves of round and rectangular NiTi archwires at 4 mm deflection on non-symmetrical bending at room temperature, 25.5 °C, are shown in Fig. 17.4. The linear slope on the activation cycle is nearly identical with symmetrical bending test for offset distance below 0.75 mm and 1.25 mm on the round and rectangular archwire, respectively. However, above that offset distance, the linear slope on both archwires is shown to end at an early deflection distance. This is potentially due to increased offset distance, which the wire contact at the edge of the bracket to occur faster. This subsequently gives enough stress for the archwire to change its

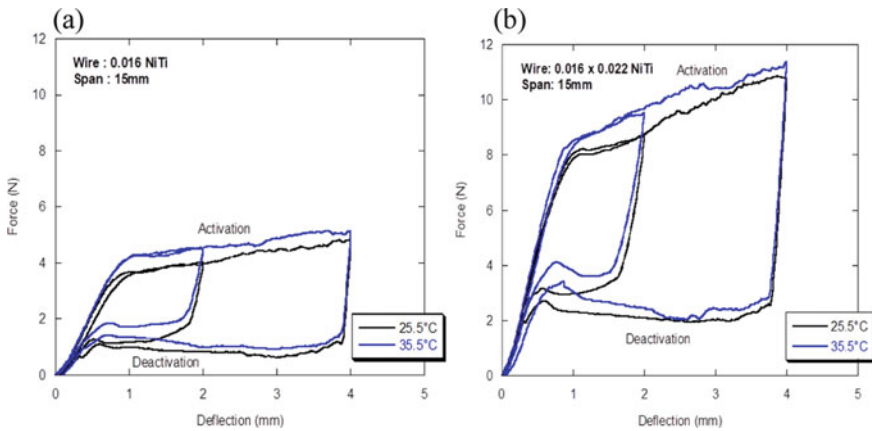


Fig. 17.3 Force–deflection curves on symmetrical bending registered at 2 and 4 mm deflection at two different temperatures on **a** 0.016 round NiTi and **b** 0.016 × 0.022 rectangular NiTi

crystalline structure from austenite to martensite at an earlier deflection distance. Moreover, increases in the offset distance also led to an increase in the activation force and a decrease in the deactivation force. The archwire exhibits the larger magnitude of activation force shown to release at the lower magnitude of deactivation force. Over the reduction of the deflection distance, the deactivation force increases back because of weakened binding intensity as more free play is introduced between the wire bracket. The start of stress-induced martensitic transformation (SIMT) was also shown to it at lower stress with the increase of offset distance above 0.75 mm and 1.25 mm on the round and rectangular wire, respectively.

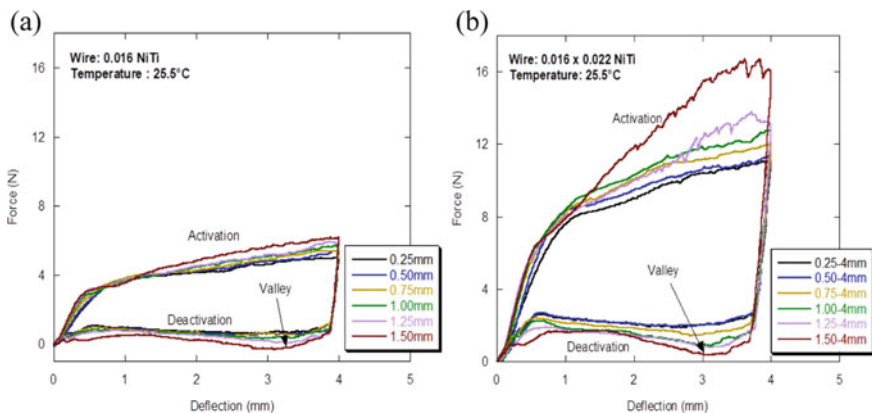


Fig. 17.4 Force–deflection curves on non-symmetrical bending at 25.5 °C on **a** 0.016 NiTi **b** 0.016 × 0.022 NiTi

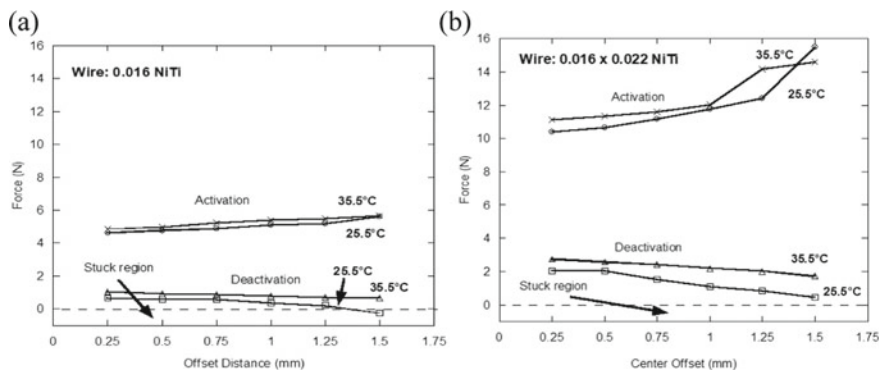


Fig. 17.5 Force magnitude of activation stage and deactivation stage at 3 mm deflection and two different temperatures over various offset distances; **a** 0.016 NiTi round archwire and **b** 0.016 × 0.022 NiTi rectangular archwire

Figure 17.5 summarizes the force magnitude acting between the round and rectangular NiTi wire at two different temperatures over various offset distances. The force magnitude increases when the offset distance decreases at the activation stage. The behavior that occurred behind this is due to the increment in binding friction coefficient with the increase of offset distance. Besides, offsetting the inter-bracket distance decreases the wire length between one side of the bracket edge and this delayed the force to a higher magnitude. However, upon the deactivation stage, the force magnitude decreases as the offset distance increases due to more spring back needed by the wire to overcome the binding friction (Ahmad et al. 2020a, b; Gurgel et al. 2001; Lombardo et al. 2012; Razali and Mahmud 2019; Proffit et al. 2012).

For the case of 1.50 mm offset distance on the round wire during the deactivation stage, the force magnitude entered the stuck region where force is below 0 N. This indicated that the spring-back was fully enrolled by the wire to overcome the binding friction. Therefore, additional force is required to overcome the stuck region. 0.016 NiTi round seems not suitable to be applied by the orthodontist to overcome this situation. This can be replaced by 0.016 × 0.022 NiTi rectangular wire as the force magnitude acting on this situation actions on the desirable force which is around 0. Overall, 0.016 × 0.022 NiTi rectangular wire force magnitude acting on overall is two times higher than for the 0.016 NiTi round wire.

17.4.2 Influence on Clinical Perspectives

“Light continuous force” is a favorable term used in orthodontic to encourage comfort to the patient during treatment. However, until now there is no research found that the ideal force (light) is being applied by the archwire with continuity (Proffit et al.

2012). This term somehow encourages many researchers to evaluate the force being acted by the wire in many cases encountered clinically.

In this present study, the results provide here give some insight to the orthodontist on how the tooth size discrepancies affect the force level during both the activation and deactivation stage. A combination of 0.016×0.022 archwire with 0.022-in. stainless steel bracket is not suitable to be used as most deactivation force is acting above 1.0 N which then provides ineffective tooth movement (Youyi et al. 2000). The usage of the rectangular wire at the end of the leveling treatment should be reconsidered in order to acquire access to the “light continuous force”. In the trend of the archwire to exert a lower force during deactivation with the increase of offset distance, it becomes a necessity for the researcher to study the force system exhibited when introducing a loop into the archwire which might be the answer in facing smaller teeth size. Finally, warm water should be avoided in this scenario to decrease pain because the deactivation force is nearly 1.0 N at oral temperature. Because the NiTi archwire is temperature sensitive, consuming warm water causes the archwire to deliver at a higher force.

17.5 Conclusions

The bending deformation behavior of NiTi archwire under non-symmetrical three-bracket bending was evaluated in this study. The temperature difference and wire sizing toward alteration of force magnitude during both activation and deactivation have been done in a variety of offset distances. The main findings from this work include the following:

1. Due to the obvious friction between the wire and the brackets, the NiTi wires show a plateau transition into a slope.
2. By increasing the offset distance of the deflection load, the force required to bend the wire increased due to the difficulty to bend the wire at a shorter span.
3. By increasing the testing temperature, the force required to induce martensite phase transformation of the NiTi alloy in bending increased because the testing temperature is further higher than the austenite finish temperature.
4. The bigger cross-sectional area on 0.016×0.022 NiTi rectangular archwire compared to 0.016 NiTi round archwire resulted in higher activation and deactivation forces magnitude due to higher friction associated with more contact between bracket slots occurred.

References

- Ahmad MN, Mahmud AS, Razali MF, Mokhtar N (2019) Force-deflection behaviour of NiTi archwires in a polytetrafluoroethylene (Teflon) bracket system. *Mater Sci Eng Technol* 50(3):289–294
- Ahmad MN, Mahmud AS, Razali MF, Mokhtar N (2020a) Binding friction of NiTi archwires at different size and shape in 3-bracket bending configuration. *Adv Struct Mat* 131(2):25–32
- Ahmad MN, Mahmud AS, Razali MF, Mokhtar N (2020b) Force-deflection behavior of NiTi archwire at different configurations of bracket system. *Materwiss Werksttech* 51:10
- Gurgel JA, Kerr S, Powers JM, LeCrone V (2001) Force-deflection properties of superelastic nickel-titanium archwires. *Am J Orthod Dentofacial Orthop: Official Publication of the American Association of Orthodontists, Its Constituent Societies, and the American Board of Orthodontics* 120(4):378–382
- Kapila S, Sachdeva R (1989) Mechanical properties and clinical applications of orthodontic wires. *Am J Orthod Dentofacial Orthop* 96(2):100–109
- Lombardo L, Marafioti M, Stefanoni F, Mollica F, Siciliani G (2012) Load deflection characteristics and force level of nickel titanium initial archwires. *Angle Orthod* 82(3):507–521
- Nespoli A, Villa E, Bergo L, Rizzacasa A, Passaretti F (2015) DSC and three-point bending test for the study of the thermo-mechanical history of NiTi and NiTi-based orthodontic archwires: the material point of view. *J Therm Anal Calorim* 120(2):1129–1138
- Proffit WR, Fields HW, Sarver DM (2012) *Contemporary orthodontics*. Elsevier (Fifth), London
- Razali MF, Mahmud AS (2019) Computational study on the effect of contact friction towards deactivation force of superelastic NiTi arch wire in a bracket system. *Mater Res Express* 6(8):85709. <https://doi.org/10.1088/2053-1591/ab2255>
- Siegner D, Ibe D (2000) Clinical application of shape-memory alloys in orthodontics. In: Yahia L (ed) *Shape memory implants*. Springer, Berlin, pp 210–228
- Yoneyama T, Miyazaki S (2008) Shape memory alloys for biomedical applications. In: *Shape memory alloys for biomedical applications*. Sawston, United Kingdom
- Youyi C, Ming Z, Fengzhi Y (2000) Orthodontic application of NiTi shape-memory alloy in China. In: Yahia L (ed) *Shape memory implants*. Springer, Berlin, pp 229–235

Chapter 18

Evaluation of Bending Deformation Behavior of a NiTi Archwire at Various Orthodontic Bracket Conditions



Mohd Nizam Ahmad, Abdus Samad Mahmud, and Mohd Suyerdi Omar

Abstract NiTi archwires are often used in orthodontic tooth treatment nowadays. The goal of this study is to investigate the bending deformation behavior of NiTi archwires in orthodontic brackets under various bending conditions. Using 0.022-in. bracket size, an experimental test setup was designed to bend three brackets, frictionless three brackets, elastomeric ligated three brackets, and five brackets at room temperatures (27 °C). A 0.016-in. NiTi round wire was used for the bending testing. As a frictionless material, polytetrafluoroethylene (PTFE, Teflon) is used. All bending tests have done three different deflections (2, 3, and 4 mm). The bending deformation of the archwire was used to determine and measure binding friction. Apart from frictions, the stainless-steel bracket configuration caused the wire to release the force in a sloping trend as compared to the Teflon bracket in the test. When constrained (ligated) and with the five brackets, the binding friction increases. These findings highlight that the usage of ligature and numbers of brackets has directly affected the bending deformation behavior during orthodontic leveling treatment.

Keywords NiTi shape memory alloy · Bending deformation behavior · Three-bracket bending · Five-bracket bending · Fabricated Teflon bracket

M. N. Ahmad (✉)
Engineering Section, Universiti Kuala Lumpur Malaysian Spanish Institute, Kulim Hi-Tech Park,
09000 Kulim, Kedah, Malaysia
e-mail: mohdnizam@unikl.edu.my

A. S. Mahmud
Nanofabrication and Functional Materials Research Group, School of Mechanical Engineering,
Universiti Sains Malaysia, Engineering Campus, 14300 Nibong Tebal, Penang, Malaysia
e-mail: abdus@usm.my

M. S. Omar
Mechanical Section, Universiti Kuala Lumpur Malaysian Spanish Institute, Kulim Hi-Tech Park,
09000 Kulim, Kedah, Malaysia
e-mail: msuyerdi@unikl.edu.my

18.1 Introduction

During orthodontic treatment, the tooth is being moved by the recovery of NiTi's bent archwire, when the wire returns back to its original arch shape. The NiTi shape memory alloy has unique superelasticity behavior that can produce constant force up to 8% stretch elongation (Thompson 2000). Constant and continuous force is needed for optimal tooth movement, at the same time, to reduce unwanted clinical side effects due to higher force (Cobourne and DiBiase 2010; Yee et al. 2009). In the actual treatment, the NiTi archwire is slid along the bracket slot during treatment, producing different bending deformation behaviors. As a result, it is essential to consider the NiTi archwire's bending deformation behavior under various orthodontic bracket conditions.

18.2 Literature

Bending methods determine the bending deformation behavior of NiTi archwires. The different bending methods yield various behaviors and characteristics of the force–deflection curve (Wilkinson et al. 2002). In orthodontics, the three-point bending test is a basic method for determining and analyzing the bending deformation behavior of NiTi archwires (Wilkinson et al. 2002). This bending method should follow the American Dental Association's Specification No. 32 for Orthodontic wires and ISO 15841: Wires for use in orthodontic (Standard 2014). However, the usage of three-point bending is not considered sufficient since this approach neglects the function of the bracket in the actual orthodontic treatment. As a result, few researchers have adapted the three-point bending test into the bracket bending test to simulate the real state of forces applied to the archwire (Elayyan et al. 2010; Nucera et al. 2014; Oltjen et al. 1997). The three-bracket bending imitates the actual bending condition during the orthodontic treatment, while the classical three-point bending test only allows the NiTi archwire to slip free during the bending test.

The bending deformation behavior of the archwire is assessed by examining the force produced at the deflection magnitudes and brackets' distance. The interaction between the archwire and bracket slot causes the gradual force–deflection trend, as well as the magnitude of specific displacement (Meling and Ødegaard 2001). The distance between brackets became the span during the archwire bending, thereby affecting the force–deflection behavior of the NiTi archwire (Badawi et al. 2009). The ligation force from the ligation technique also affects the bending deformation behavior of the NiTi archwire. The frictional resistance of self-ligating brackets, elastomeric-ligated brackets, and stainless-steel ligated brackets was studied, and it was discovered that the self-ligating bracket had the lowest frictional resistance (Leite et al. 2014).

A higher friction coefficient at the archwire–bracket interface was found to be influencing the frictions (Clocheret et al. 2004). The coefficient of friction on the

NiTi archwire and stainless-steel bracket interface was measured and found to be in the range of 0.21–0.27 (Alper Oz et al. 2012). Alternative materials with a lower coefficient are Teflon, and recent evidence of its application shows the potential to reduce the frictions with the lower coefficient of friction (Fraunhofer and Jr 1995; Murayama et al. 2013).

The goal of this study is to assess the bending deformation behavior of NiTi archwires when using orthodontic stainless-steel brackets in a various situations. Three brackets, fabricated Teflon five brackets, and ligated bracket were used as an experimental setup to simulate various bending test conditions. The bending tests used friction on brackets to predict the bending deformation behavior of the superelastic NiTi archwire under various wire constraint conditions, whereas a frictionless bending state was achieved using a fabricated Teflon bracket. This *in vitro* investigation was done at room temperature and dry condition (without saliva). Force–deflection curves plotted are very useful since they show forces over deflection at both conditions of installation of the wire in the bracket (activation phase) and wire recovery after installation (deactivation phase).

18.3 Methodology

The three-bracket bending jig setup is shown in Fig. 18.1a. The jig consists of two bars, the jig base, and indenter, which are made from stainless steel. Stainless steel was used as jig because it is easy to clean and glued bracket and has a good cosmetic appearance. The dimensions of the bar are 7 mm × 7 mm × 30 mm to mimic the size of teeth. The bars were bolted to the jig base with screws. The jig base is attached at an adjustable clammer at the universal tensile machine (UTM, Instron 3367) before testing. A UTM load cell with a maximum static load of 500 N is attached to an indenter with dimensions of 3 mm × 10 mm × 50 mm (resolution 0.01 N). During the bending test, a crosshead speed of 1 mm per minute is employed to provide load. For this investigation, a typical stainless-steel bracket (Natural Orthodontics) with a mini MBT prescription and a 0.022-in. (0.559 mm) size was used. Before glueing brackets to stainless-steel bars with cyanoacrylate adhesive (Selleys), proper alignments are determined using a digital caliper, height gauge (Mitutoyo), and mini bubble level protector (Haccury). The arrangement of the bars and indenter is representing the arrangement of the tooth at the maxillary jaw, canine, first premolar, and second premolar as in the phantom model. A bending span of 15.0 mm was used with an average midpoint within the tooth and an indenter was placed in the middle, 7.5 mm on each side. The elastomeric ligatures (commercial unbranded ligature ties O-ring type) are applied at bracket hooks to hold the NiTi archwire in the bracket slot, during the ligated bracket bending condition.

Three-brackets bending setup the extended to frictionless bending condition by using a fabricated Teflon bracket as shown in Fig. 18.1b. The fabricated Teflon brackets are made by machining a Teflon bar into a small insert and then using the press-fit method to attach it to the stainless-steel square housing. The Teflon

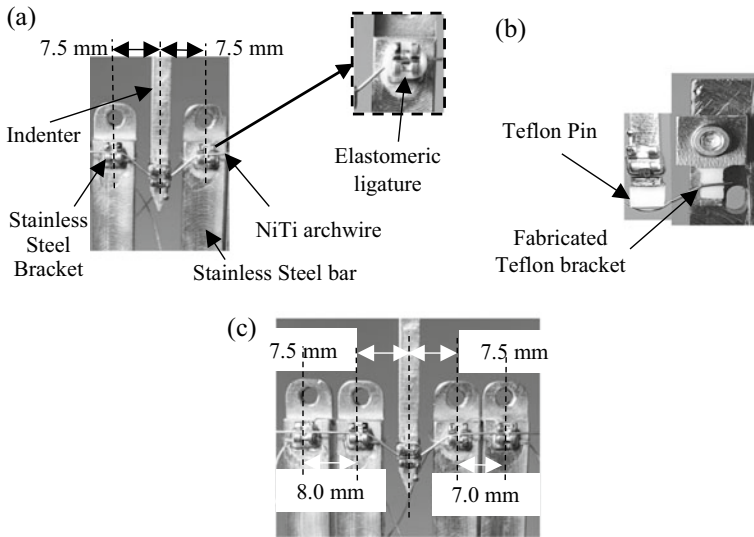


Fig. 18.1 Setup of various condition bending tests; **a** three brackets and extend to elastomeric ligated, **b** fabricated Teflon bracket, **c** five brackets

inserts have the same slot size as the conventional bracket size. The square housing dimension is matching with the new stainless-steel bar of $10 \text{ mm} \times 7 \text{ mm} \times 30 \text{ mm}$, where the fabricated Teflon bracket was bolted. Teflon pins are fabricated by gluing a small Teflon bar, $3.1 \text{ mm} \times 10 \text{ mm} \times 3 \text{ mm}$ on the flat indenter tip. The five-bracket bending setup is shown in Fig. 18.1c. The setup is an extension to the existing three-bracket bending jig. Other bars were installed to the jig with the same brackets was placed, but with a slightly different on tooth line-up. The arrangement of the bars and indenter is representing the arrangement of the tooth at maxillary jaw, lateral incisor, canine, first premolar, second premolar, and first molar, at which the midpoint distance within the tooth is 8.0 mm, 7.5 mm, 7.5 mm, and 7.0 mm to replicate actual tooth conditions.

Alignment activities are performed, to ensure the bending jig which is positioned correctly at the UTM clamped base. A 30-mm NiTi archwire was cut on the straight section and installed on bracket slots as a dummy for alignment. Digital caliper and magnifying glass are used to observe the bending span and that the indenter is in position. The NiTi archwire (G&H Orthodontics) size used is 0.016-in. round. The bending test was performed five times at three deflections of 2, 3, and 4 mm at the beginning to demonstrate the superelasticity behavior of the NiTi wire. After similarities of five times' test results are observed, the tests were performed three times only for every deflection and the best of three results was used for further evaluation.

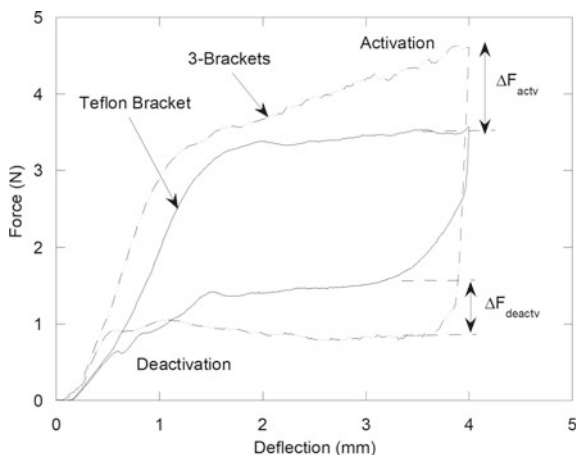
18.4 Result and Discussion

In the three-bracket configuration, Fig. 18.2 depicts the bending deformation behavior of the 0.016-in. NiTi orthodontic wire. The deformation is linear elastic up to 1-mm wire deflection, and the force plateau remains flat, demonstrating stress-induced martensitic transformation (SIMT) behavior. On the constructed Teflon brackets, the archwire deformation behavior generated a flat force plateau, whereas the stainless-steel back produced a gradient slope. Because Teflon brackets are frictionless, deformation can occur without binding friction, resulting in a flat force plateau, whereas the force gradient in stainless-steel brackets indicates the presence of binding friction between the wire and the bracket tip. The force gradient was positive throughout the activation phase but negative during the deactivation phase, with a small valley deformed during the early stages of strain recovery. The increased binding friction between the wire and the upper surfaces of the bracket's tip causes the formation of a valley on the deactivation curve of the wire on stainless steel. This slows down the wire's retraction to a significantly lower force magnitude. The geometry of the wire bending curvature limits the contact of the wire with the top side bracket's tip once the strain recovery reaches a particular strain value, so the deactivation curve returned to a linear gradient.

An interesting finding was found during the bending test performed in the presence of friction due to the archwire bend at the bracket edge. The friction is clearly shown in Fig. 18.2, namely the binding friction. The binding friction is measured by the force difference of the flat force plateau at the Teflon bracket and the force gradient at the orthodontic bracket. The binding friction measured at 4-mm deflection is 1.142 N on the activation curve and 0.974 N on the linear gradient behavior of the deactivation curve. Discussion on the frictions that occurred will be made later.

Figure 18.3 illustrates the bending deformation behavior of the 0.016-in. NiTi orthodontic archwire at 3-mm deflection under all bending conditions. The bending

Fig. 18.2 Bending deformation behavior of 0.016-in. orthodontic NiTi archwire



deformation trend on all force–deflection curves is the same but has a different magnitude of forces. The usage of stainless-steel bracket always shows a force increase in gradient slope compared with the flat force plateau (frictionless) at Teflon bracket. Meanwhile, the ligated three-bracket bending produced the highest bending force, slightly higher than the five-bracket bending conditions, at both the activation and deactivation phases. Table 18.1 shows the binding frictions at bending conditions.

Frictions that occurred during the bending tests are identified into two types: sliding friction and binding friction as clearly shown in Fig. 18.3. The sliding friction occurred when the wire slides in the bracket slot during the bending test, while binding friction occurred when the wire is bent in the bracket slot during incremental deflections. From the force–deflection curve, the binding friction starts after around 0.2-mm deflection at most bending tests but started immediately on the ligated three-bracket bending. At the initial bending test condition, the wire slid at the bracket tip at the beginning and start making contact with the top lateral bracket tip. Once the contact was established, the wire starts to bend to a short load slope as shown

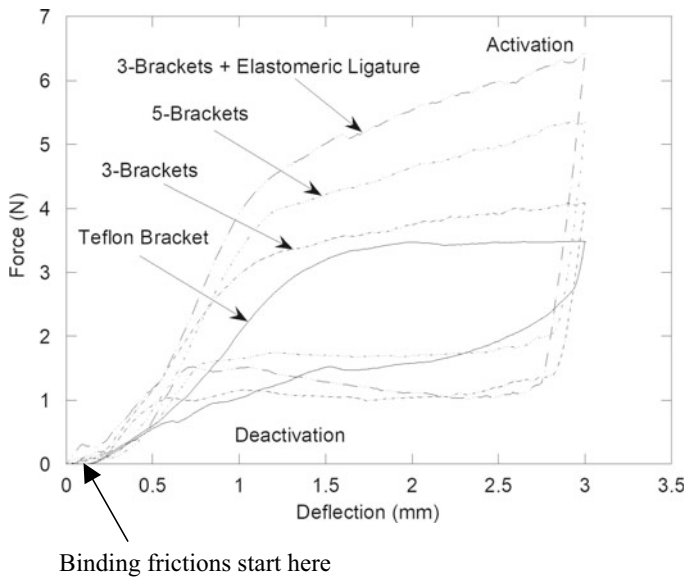


Fig. 18.3 Bending deformation behavior of the 0.016-in. NiTi archwire at all bending conditions

Table 18.1 Binding friction measured at all bending conditions at 3 mm deflection

| Deformation phase | Binding friction (N) at three different brackets' configuration | | |
|-------------------|---|---------------------------|---------------|
| | Three brackets | Three brackets + ligature | Five brackets |
| Activation | 1.142 | 3.577 | 2.671 |
| Deactivation | 0.974 | 1.291 | 0.988 |

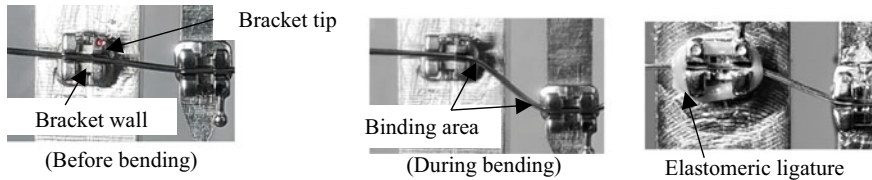


Fig. 18.4 Binding area and wire bent in the bracket

in Fig. 18.4. When the load is continuously applied and the wire deflection angle is more than the critical contact angle, the pure binding friction occurred.

A different condition happens when bending performed with elastomeric ligation is tight at the bracket tip as shown in Fig. 18.4. When applying the elastomeric ligation, the wire is pulled to the bracket wall and slid at the bracket wall and then bracket tip. Sliding on an extra bracket surface produced a slightly higher sliding friction compared to wires without ligation that is very small. The magnitude of binding friction is also the highest compared to the other bending conditions due to the effect that the ligation pulled the wire to the bracket wall. The elastic force from the elastomeric ligation causes both sliding and binding frictions to occur during the bending test.

The bending deformation behavior of the NiTi wire in the bracket application is influenced by binding frictions. Table 18.1 summarizes the binding frictions measured at 4-mm deflection of all bending conditions during the activation and deactivation phases. Ligation effects were increasing the binding friction significantly. Higher binding friction contributes to lengthening the treatment process when only lower forces are used to induce tooth movement. The recovery force generated from the NiTi wire's superelasticity behavior was primarily used to overcome binding friction, with the remainder of the force being used for tooth movement. Referring to Fig. 18.4, if without or minimum magnitude of binding friction, all recovery force from superelasticity behavior can be used to induce tooth movement. When the tooth received enough and a continuous amount of force induced, the tooth movement will be fast and treatment time will be shorter. The clinician needs to do some adjustments due to a lower force will require more clinic visits by patient.

The deactivation phase of the NiTi archwire is the treatment phase on orthodontic treatment because the wire superelasticity behavior was maximally used to the tooth, while during the activation phase, the wire is bent by the clinician when installing the wire into the bracket slot. Referring to Fig. 18.4 and Table 18.1, a higher force is used during the activation phase and produced a higher binding friction due to higher force when using a stainless bracket. However, if using the frictionless bracket, installation and recovery forces are flat plateau over deflections because the force is only used to overcome the internal resistance during phase transformation, not to overcome frictions. This constant load will reduce pain on the patient during the wire installation process and also during treatment.

Although ligation was significantly affecting the performance of the NiTi archwire in the orthodontic treatment and produced higher frictions, it is still being used due to economic cost. Braces cost with elastomeric ligature is the lowest among other braces options. Degradation of the elastomeric force over time in the oral condition is another factor that accepts elastomeric ligature application in orthodontic treatment. Higher frictions only occur at the early stages of treatment and will reduce over time.

Due to binding friction, the NiTi archwire performance is not fully utilized for tooth movement. Superelasticity behavior that produces good recovery force was used to overcome frictions rather than to induce tooth movement. A self-ligating bracket is the best solution to reduce frictions and allow the superelasticity behavior of the NiTi archwire to be fully utilized during the orthodontic treatment. Minimum binding friction at this bracket is due to the fact that the archwire are not a constraint and pulled to slide at the bracket wall. Mostly, the archwire will slide on the bracket tip during the treatment. However, the use of a self-ligating bracket is costly due to the bracket itself which is expensive and requires extra works by the clinician during wire installation.

18.5 Conclusions

In this work, the aim was successfully achieved to evaluate the bending deformation behavior of the NiTi archwire at various bending conditions, in the orthodontic treatment. The following conclusions can be highlighted at the end of this study:

- a. Bending deformation behavior is influenced by frictions generated. Higher friction causes the archwire to deflect less, while lower friction causes the wire to deflect more, at the same magnitude of force applied.
- b. Elastomeric ligature is major in affecting the bending deformation behavior. Higher frictions occurred during the application of this ligature, compared with the five-bracket bending and three-bracket bending.
- c. Superelasticity behavior of NiTi wire is not fully utilized due to frictions that occurred in the orthodontic treatment, as illustrated at various bending conditions.

References

- Alper Oz A, Arici N, Arici S (2012) The clinical and laboratory effects of bracket type during canine distalization with sliding mechanics. *Angle Orthod* 82(2):326–332
- Badawi HM, Toogood RW, Carey JPR, Heo G, Major PW (2009) Three-dimensional orthodontic force measurements. *Am J Orthod Def Facial Orthop* 136(4):518–528
- Clocheret K, Willems G, Carels C, Celis JP (2004) Dynamic frictional behaviour of orthodontic archwires and brackets. *Eur J Orthodont* 26(2):163–170
- Cobourne MT, DiBiase AT (2010) *Handbook of orthodontics*. Mosby Elsevier, London

- Elayyan F, Silikas N, Bearn D (2010) Mechanical properties of coated superelastic archwires in conventional and self-ligating orthodontic brackets. *Am J Orthod Dentofacial Orthop* 137(2):213–217
- Fraunhofer JAV, Jr DJDFRES (1995) Frictional resistances using Teflon-coated ligatures with various bracket-archwire combinations. *Angle Orthod*65(1):63–72
- Leite VV, Lopes MB, Gonini Júnior A, Almeida MRD, Moura SK, Almeida RRD (2014) Comparison of frictional resistance between self-ligating and conventional brackets tied with elastomeric and metal ligature in orthodontic archwires. *Dental Press J Orthod* 19(3):114–119
- Meling TR, Ødegaard J (2001) The effect of short-term temperature changes on superelastic nickel-titanium archwires activated in orthodontic bending. *Am J Orthod Dentofacial Orthop* 119(3):263–273
- Murayama M, Namura Y, Tamura T, Iwai H, Shimizu N (2013) Relationship between friction force and orthodontic force at the leveling stage using a coated wire. *J Appl Oral Sci: Revista FOB* 21(6):554–559
- Nucera R, Gatto E, Borsellino C, Aceto P, Fabiano F, Giancarlo C, Matarese G, Perillo L (2014) Influence of bracket-slot design on the forces released by superelastic nickel-titanium alignment wires in different deflection configurations. *Angle Orthod* 84(3):541–547
- Oltjen JM, Jr MGD, Ghosh J, Nanda RS, Currier GF (1997) Stiffness-deflection behaviour of selected orthodontic wires. *Angle Orthod*67(3):209–218
- Standard I (2014) Dentistry—wires for use in orthodontics. ISO Standard 15841:1–70
- Thompson SA (2000) An overview of nickel-titanium alloys used in dentistry. *Int Endod J* 33(4):297–310
- Wilkinson PD, Dysart PS, Hood JAA, Herbison GP (2002) Load-deflection characteristics of superelastic nickel-titanium orthodontic wires. *Am J Orthod Dentofac Orthop* 121(5):483–495
- Yee JA, Türk T, Elekdağ-Türk S, Cheng LL, Darendeliler MA (2009) Rate of tooth movement under heavy and light continuous orthodontic forces. *Am J Orthod Dentofac Orthop* 136(2):1–9

Chapter 19

Application of Dampening Accessories for Reduction of Hand-Arm Vibration Exposure



Mohd Fahmi bin Mohd Husni, Tajul Adli bin Abdul Razak, Ahmad Khusairy Hakiim bin Abdul Azim, Mohd Nizam Ahmad, and Muhammad Najib Abdul Hamid

Abstract The study on the ergonomics of the wood cutting process can help to minimize risk injuries during a wood cutting operation. It is also expected that prolonged exposure to hand-arm vibration can lead to the development of the carpal syndrome to the operator. This paper focused on experimenting with the vibrations produced by a jigsaw hand-arm and the effect of dampening accessories on the vibration exposure during the wood cutting operation. The vibration of the tool is measured using a triaxial accelerometer connected to data acquisition system. The triaxial sensor is mounted on the operator's hand with reference to ISO 5349 (2001) guidelines. Three different blades are used to identify different vibration effects to the same hand-arm tool. The results indicate that the usage of blades designed for speed cutting produces the most vibration. The machine vibration improves by adding a silicone rubber with different thicknesses embedded to the glove. Silicone rubber acts as a damper and reduces the hand-arm vibration. The thickness is optimized between acceptable vibration exposure and cutting result. It is found that the optimum thickness for rubber dampening is between 2 and 8 mm. The increase of more than 8 mm rubber dampening thickness not only leads to unacceptable cutting result but also will increase the vibration transferred to human's hand.

M. F. M. Husni
Top Glove Sdn. Bhd, 41050 Shah Alam, Selangor, Malaysia

T. A. A. Razak (✉) · M. N. Ahmad · M. N. A. Hamid
Engineering Section, Universiti Kuala Lumpur, Malaysian Spanish Institute Kulim Hi-Tech Park,
09000 Kulim, Kedah, Malaysia
e-mail: tajuladli@unikl.edu.my

M. N. Ahmad
e-mail: mohdnizam@unikl.edu.my

M. N. A. Hamid
e-mail: mnajib@unikl.edu.my

A. K. H. A. Azim
Politeknik Muadzam Shah, 26700 Muadzam Shah, Pahang, Malaysia
e-mail: khusairy@pms.edu.my

Keywords Machine process · Hand-held machine · Occupational safety and health · Vibration dampening

19.1 Introduction

Musculoskeletal disorders (MSDs) are a common illness related to prolonged exposure and accounted for 31% of all injury and illness cases in 2015 by the Bureau of Labor Statistics (CA Incidence 2011). The operation of the machinery itself mainly generates vibrations (rotating or reciprocating masses, gas pulsation, aerodynamic phenomena) by the impact of hand-held machinery on hard materials or by the interaction between the machinery and its environment. For example, vibration can be caused by the movement of mobile machinery over rough ground. Machine tools used by construction workers, industry, and agriculture are the most affected by vibration (Eurofound 2017). Furthermore, increasing the feed force will also have effect on vibration (Xu et al. 2021). The use of dampening, especially, damping measures at high frequency range leads to significant vibration reductions in the resonance cases (Wegener et al. 2021).

Several symptoms and prolonged illness have been identified to be related to vibration exposure, on hand-arm, and whole-body systems (Griffin 1991). Clarifying the key sources of workpiece vibrations, identifying and comprehending their features and contributing factors, and creating and using relevant methods and technologies to successfully limit vibration exposure are all important stages toward the goal of intervention (Xu et al. 2021).

The vibration transmitted from a jigsaw machine tool to the operator's hand is varied based on different cutting blades. High-performance blades for faster cutting operation produce more vibration compared to common blades. The machine vibration can be reduced with the use of a dampener that can absorb the transmitted vibration. However, the optimum dampening thickness is required to provide a faster cutting process without reducing any quality of the finished product.

19.2 ISO 5349

Each standard supports its own benefits within every industry; however, the common benefits across the certifications include: widened market potential, compliance to procurement tenders, improved efficiency and cost savings, higher level of customer service and therefore satisfaction, and heightened staff moral and motivation (HAV exposure points system ready reckoner note—points formulas).

The ISO 5349-2001 (mechanical vibration—measurement and evaluation of human exposure to hand-transmitted vibration) standard is used to detect hand-arm vibration in the jigsaw wood cutting process. This ISO standard is divided into two parts: ISO 5349-1 (generic requirements) and ISO 5349-2 (special requirements)

(practical guidance for the measurement at the workplace). The ISO 5349 standard was developed as a result of research into the technique for collecting data on the human body and categorizing vibration effects in terms of sensitivity to the development of vibration white finger (VWF), also known as Raynaud's illness. In general, the vibration response can be categorized using the frequency, amplitude, direction, time of exposure, and grip force (Joshi et al. 2001). In ISO 5349-1, it specifies the general requirement for the measurement and evaluation of human exposure to hand-transmitted vibration. It is enhanced by the information given in ISO 5439-2, which gives the practical guidance for the implementation of appropriate measurement and evaluation techniques at the work place (ISO 1997).

The scope stated in ISO 5341-1 specifies the general requirements for measuring and reporting hand-transmitted vibration exposure in three orthogonal axes. ISO 5349-1 is also referred as a general requirements for measuring and evaluating human exposure to hand-transmitted vibration which are known to prompt the effect of human expose to hand-transmitted vibration in working conditions. The factors included the frequency spectrum of the vibration, the magnitude of the vibration, and the duration of exposure per working day.

In accordance with ISO 5349-1, the ISO 5349-2 provides guidelines for the measurement and evaluation of hand-transmitted vibration at work. The procedures for taking representative vibration measurements and determining the daily exposure time for each operation were detailed in the guidelines. The purpose of the guided activities are to standardize the experiment so that an 8-j energy equivalent vibration total value can be calculated, which represents everyday vibration exposure in real life. This section of ISO 5349-2 applies to all scenarios in which vibration is delivered to the hand-arm system via hand-held or hand-guided machinery, vibrating workpieces, or controls of mobile or permanent machinery.

19.3 Experimental Setup

The experiment uses a jigsaw power tool for the wood cutting process. The vibration is measured in three orthogonal directions: x , y , and z by using a triaxial accelerometer, as shown in Fig. 19.1. The position of the sensor is referred to the standard guideline from ISO standard 5349-1 (2001).

The experiment is performed for three different blades: basic for wood T111C, wood T144D, and wood and metal T345XF. The T111C basic for wood blades is reasonable for cutting wood and wood products are made up of high carbon steel construction for long life performance. The T144D is relatively fast cutting activities. The blade is made up of high carbon steel material with a T-shank design for maximum grip and stability during the wood cutting process. The blade of T345XF for wood and metal is an outstanding product with bi-metal construction for durability and long life. Figure 19.2 shows the mentioned blades.

Fig. 19.1 Actual experimental setup



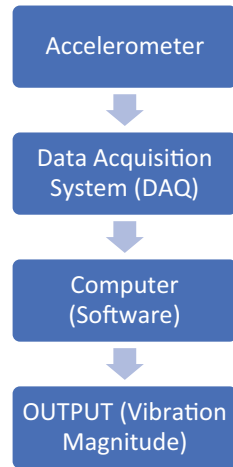
Fig. 19.2 Different blades for the same machine tool

19.4 Data Collection

Referring to the flow chart shown in Fig. 19.3, the data are acquired from the triaxial accelerometer through connection to the data acquisition system (DAQ) via the PCB triaxial accelerometer cable with three distinguished pins labeled X, Y, and Z, respectively. Following the acquired data from the DAQ, the system converted the analog signal to digital data and transferred the data to the personal computer for meaningful information. The DAQ is performed using the LMS Test Express software known as spectral analysis to measure the vibration signal.

X, Y, and Z are the representation of acceleration amplitudes in units of g. Hence, all the three values must be converted to m/s^2 by multiplying the values with $9.81 m/s^2$

Fig. 19.3 Flowchart of data acquisition process



in order to get in a_{RMS} value. The final output was represented in form of the root mean square (RMS) acceleration value in terms of vibration magnitude in m/s^2 and frequency spectrum in Hz. By following the ISO 5349 standard, the RMS value of acceleration is computed for examining the extent of vibration entering the hand-arm system from the jigsaw. The vibrations are measured in the three orthogonal directions of X, Y, and Z. Each samples were combined into a single value by using the following equation:

$$a_{\text{RMS}} = \sqrt{ax^2 + ay^2 + az^2}. \quad (19.1)$$

The result of the average vibration magnitude for each three types of blades is used to determine the daily vibration exposure using the exposure point system as shown in Fig. 19.5. The points for daily vibration exposure for each type of blade are compared to investigate the vibration level of those three different sawing blades.

19.5 Result

Laboratory experiments were conducted using the hand machine to obtain the amplitude and frequency values produced by the hand tool machine when using different saw blades. Table 19.1 shows the result in three-axis condition.

In this experiment, the worker is assumed to be exposed to vibration for 3 h in a day. Figure 19.4 shows the compilation of magnitude vibration with reference to the blade type. The vibration magnitude levels are averaged to determine the total vibration magnitude, and then, the daily vibration exposure is determined by using the exposure point system as shown in Fig. 19.5.

Table 19.1 Collected data from for each blade

| Type of blade | X-axis | | Y-axis | | Z-axis | | Vibration magnitude (m/s ²) |
|---------------|---------------|----------------|---------------|----------------|---------------|----------------|---|
| | Amplitude (g) | Frequency (Hz) | Amplitude (g) | Frequency (Hz) | Amplitude (g) | Frequency (Hz) | |
| T111C | 0.4739 | 223 | 0.3898 | 112 | 0.2335 | 332 | 6.44 |
| T144D | 0.1859 | 113 | 0.6818 | 114 | 0.1297 | 332 | 7.05 |
| T345XF | 0.1292 | 226 | 0.55706 | 114 | 0.2426 | 115.5 | 6.21 |

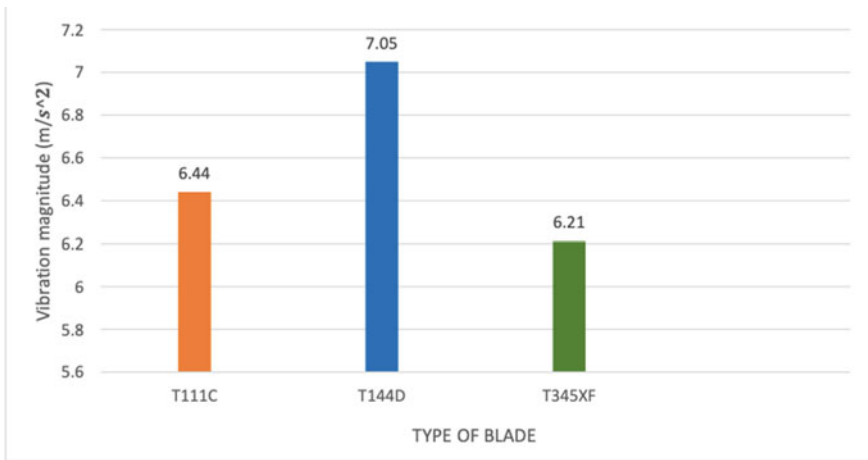


Fig. 19.4 Vibration magnitude based on type of blade

Referring to the exposure point system by the ready reckoner system (HW Community), the daily vibration exposure is determined by using the table as shown in Fig. 19.5. The exposure point system is a guide to measure the suitable daily vibration exposure from the jigsaw to the operator’s hand.

19.6 Discussion

Figure 19.6 shows the vibration pattern for blades T144D and T345XF. The graph indicates that the thickness of the silicone has a direct effect on the vibration pattern. The vibration decreases steadily from 2 to 8 mm thickness but increases significantly during 10 mm thickness. The pattern for blade T111C, however, has marginally fluctuated, but increases slightly at 10 mm thickness.

As shown in Fig. 19.6, the application of silicone rubber as a method to reduce the hand-arm vibration proofs to be a good solution. The vibration value for each

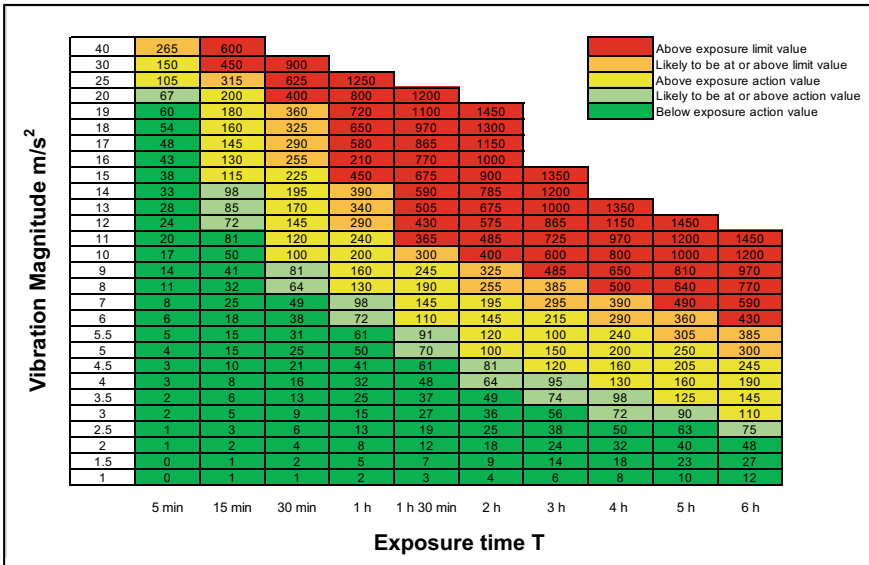


Fig. 19.5 Ready reckoner table (HAV exposure points system ready reckoner note—points formulas)

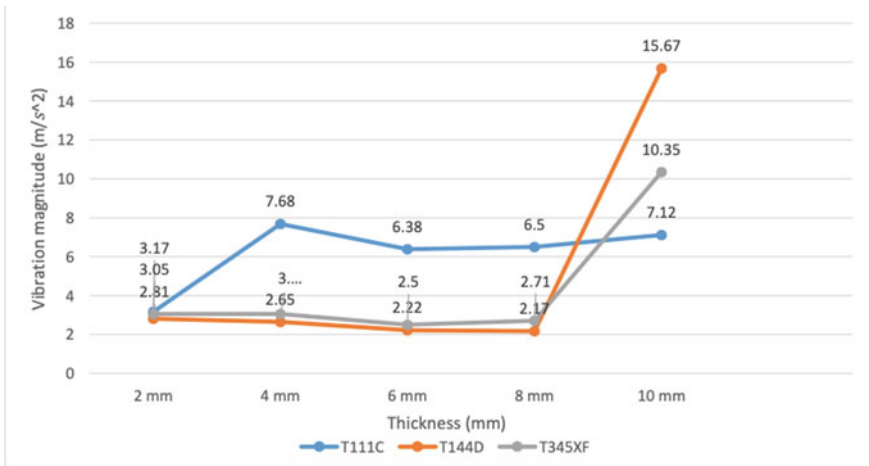


Fig. 19.6 Effects of the dampening thickness toward vibration magnitude

blade decreases as the thickness of the silicone rubber increases. The efficiency of the silicone rubber, however, shows a different result for blade T111C. It shows an inconsistent graph pattern and produces greater vibration compared to the other types of blade.

Fig. 19.7 Inner condition of the dampening glove with silicone rubber



T111C blade understandably provides the best result since it is the official blade as it is the default blade offered by the manufacturer together with the machine. The machine is believed to be optimized according to the T111C blade. The implementation of silicone rubber as a dampener to the machine-blade combination has disrupted the balance resulting to an increase in vibrations in cutting process. Although the vibration decreases after 4 mm, it begins to increase when thickness is approaching 10 mm.

A similar pattern is recorded when the dampener thickness reaches 10 mm. The vibration magnitude increases for all types of blades. This is due to excessive force used by the operator to hold the jigsaw handle to maintain the position during the cutting process as the thickness becomes thicker. In terms of ergonomic, at 10 mm thickness, the operator experiences discomfort due to a thick layer of the silicone rubber used on the glove for dampening purpose. Figure 19.7 shows the position of the silicone dampener in the hand glove.

It can be concluded that the thickness of the silicone rubber between 2 and 8 mm is the optimum thickness of the silicone rubber that can reduce hand-arm vibration exposure. The score point on the exposure point system is mostly falling below than exposure action value (EAV) which is in the green zone and below 4.5 m/s^2 or 120 points, especially for blades T144D and T345XF. Compared to the previous test with no silicone rubber used as vibration dampening, the vibration magnitude produced for all types of blades was higher, and they are above the EAV, which is in the yellow zone. However, these exposures must not be assumed to be safe. There may be a risk of HAVS in some workers, especially after many years of exposure.

19.7 Conclusion

This experiment answers questions about hand-arm vibration exposure on a jigsaw machine during operation. Excessive jigsaw machine vibration can cause a disorder known as hand-arm vibration syndrome (HAVS), which has both vascular and neurological components. It is most common in industrial power tools, where the cost of cutting can be reduced simply by using the right blades for the job. If workers decided to use a coarse blade for faster operation, more research is needed to determine the best approach.

This experiment found that a silicone rubber dampener is only effective between 2 and 8 mm. The dampener's efficiency will be greatly reduced if it is thicker than 8 mm. The operator's unsteady feeling caused by the thicker dampener has resulted in a natural reaction of a firmer hand grip during the cutting process, increasing the vibration exerted by the machine on the hand. Hand-arm vibration syndrome (HAVS), which has both vascular and neurological components, can be caused by excessive jigsaw machine vibration. It is most frequent in industrial power tools, where the vibration of the cutting process can be minimized simply by using a silicone rubber dampener.

References

- CA Incidence (2016) Nonfatal occupational injuries and illnesses requiring days away from work, 2011, no. 202. Available: <http://www.bls.gov/news.release/osh2.nr0.htm>
- Eurofound (2017) Sixth European working conditions survey—overview report (2017 update)
- Griffin M (1991) Handbook of human vibration, 1st edn. Academic Press, pp 27–42
- HAV exposure points system & ready reckoner note—points formulas
- HW Community, Exposure points system and ready-reckoner. HSE book. <https://www.hse.gov.uk/vibration/hav/readyreckoner.htm>
- ISO 2631-1, International standard ISO 2631-1, 1997:1–2. Available: www.iso.org/iso/standards.htm
- Joshi A, Leu M, Murray S (2001) Ergonomic analysis of fastening vibration based on ISO Standard 5349 (2001). *Appl Ergon* 43(6):1051–1057
- Wegener K, Bleicher F, Heisel U, Hoffmeister HW, Möhring HC (2021) Noise and vibrations in machine tools. *CIRP Ann* 70(2):611–633
- Xu XS et al (2021) An investigation of the effectiveness of vibration-reducing gloves for controlling vibration exposures during grinding handheld workpieces. *Appl Ergon* 95:103454

Chapter 20

The Analysis of Automatic Transmission Stands (U-Shaped Holder) for Repair, Maintenance and Educational Purposes Using a Simulation Method



Siti Rohana Binti Ahmad, Nur Nadhirah Binti Abdul Razak,
and Muhammad Zunnurrin Bin Ghazali

Abstract Nowadays, the automatic transmission is commonly used in car production. Automatic transmissions come in a number of different types with a range of weight and size. The automatic transmission is placed on its stand during the repair and maintenance process. However, the stand structure of an automatic transmission mostly becomes a danger and harms to the mechanics due to its heavy weight. Most of the educational trainers for automatic transmission stands cannot be rotated. Thus, it is difficult for operator to access certain parts of the automatic transmission. In this study, the automatic transmission stand structure that is equipped with the U-shaped holder with fixed stand was analyzed out using a simulation method. The idea of this analysis was to provide an improvement toward a better holding of the automatic transmission during the repair, maintenance and educational purposes. The SOLIDWORK 2016 software is used to design and simulate the U-shaped holder with fixed stands. The holder can be rotated up to 90° of adjustable angle to ease the operator during assemble and/or disassemble process of maintenance. Then, the analysis of the strength of the stand structure by using a simulation method was carried out using 100 kg of maximum load of the automatic structure at different angles of rotation consisting of 0°, 45° and 90°. From the analysis, the stress is increased 6% but decreased 3% of strain by increasing the angle of rotation. The increased angle of rotation less affected the stand stress and strain due to the sturdy design to withstand the load. Therefore, this type of stand structure becomes a compatible design that can be used in automotive repair and maintenance industries.

Keywords Automatic transmission · Maintenance · Stand structure

S. R. B. Ahmad (✉) · N. N. B. Abdul Razak
Mechanical Section Universiti Kuala Lumpur, Malaysian Spanish Institute Kulim Hi-Tech Park,
09000 Kulim, Kedah, Malaysia
e-mail: sitirohana@unikl.edu.my

S. R. B. Ahmad · M. Z. B. Ghazali
R&Z Auto, Car Repair and Service Centre, 470, Jalan Kota Kenari 3, 09000 Kulim, Kedah,
Malaysia

20.1 Introduction

An automatic transmission is a gear system in the vehicle at which the gears can change automatically at different speeds without assistance or manually by the driver. It is a type of transmission which does not depend upon the driver to shift gears which means that there are no gear shift and clutch pedal in the automatic transmission car. This is because it operates automatically once the driver put the transmission into drive (Fischer et al. 2015).

In 1921, the first automatic transmission was created by Alfred Horner Munro who was a Canadian steam engineer at Regina, Saskatchewan, Canada. Firstly, he designed his device to utilize compressed air rather than hydraulic fluid, but it lacked in power and was not successfully sold commercially. The American inventor Oscar H. Banker evolved the concept and invented the first practical automatic transmission. Then, the automobile company General Motors established the first modern automatic transmission in 1930s that used hydraulic fluid. Next, in 1940, the model “Hydra-Matic” transmission was proposed. The automatic transmission’s revolution continues to expand as time goes by and the most important changes or improvements made in automatic transmission in design and performance are the number of forward gears’ transmission available now and the switch that are from mechanically (manual) controlled to electronically (automatic) controlled transmission operations (Sheth et al. 2014).

Beforehand, the same basic principles were used and operated by all automatic transmissions. Currently, there are several different types and versions of automatic transmission available in markets at which different types of it have different types, size and weight (Fischer et al. 2015). The different types of the automatic transmission are applied based on the performance and model of the vehicle. The several basic types of automatic transmission that in use nowadays are the traditional automatic transmission/torque converter, dual-clutch transmission (DCT), automated-manual transmission (AMT), direct shift gearbox (DSG), continuously variable transmission (CVT), planetary gear transmission and Tiptronic transmission.

The methods used in placing the automatic transmission during repairing, maintenance and educational purpose will frequently pose a danger. This method has always been causing fatigue and far risk of worker injury, endangering the lives of mechanics. For example, the existing equipment used to place and position the automatic transmission used at the Universiti Kuala Lumpur Malaysian Spanish Institute (UniKL MSI) workshop for educational purpose as shown in Fig. 20.1. This figure shows that the equipment used is fixed attached and placed directly on the workbench table. It is not adjustable in length, height and rotation. This limitation caused limited space and lack of flexibility to handle and operate the automatic transmission.

This project introduces new ideas for automatic transmission stands. This project will focus on the design of a U-shaped holder for automatic transmission stand structure. A strength analysis using a simulation method was performed to provide a secure hold on various types of automatic transmissions during repair, maintenance and educational purposes.



Fig. 20.1 Automatic transmission stand used at the UniKL MSI

20.2 Literature

20.2.1 Automatic Transmission

An automatic transmission or automatic gearbox may be a type of motor vehicle transmission that can automatically change gear ratios as the vehicle moves, which frees the driver from having to shift gears manually. This means that such a car has no foot pedal and requires no gear shift operation by the driver (Adzimah et al. 2013).



In 1921, Alfred Horner Munro, a Canadian steam engineer, invented the automatic transmission. Later on in 1923, the transmission was patented. He designed his device to use compressed air rather than hydraulic fluid, and it then caused a huge lack of power and could not be sold commercially. General Motors then developed the first automatic transmission using hydraulic fluid in the 1930s and introduced the “Hydra-Matic” transmission in 1940 which became much more successful and increased fuel economy (Fischer et al. 2015).

An automatic transmission does not use a clutch but uses a converter. It is a fluid coupling which utilizes a separate pump and turbine spinning in opposite directions within the converter which then allows the engine to spin independently of the transmission. The automatic transmission also made up from several components for the system is being fully functional (Sawasaki et al. 1994).

The driver only needs to release the accelerator pedal or apply the brake to slow and stop the vehicle. When the vehicle stops, the automatic transmission disengages the torque converter clutch and automatically downshifts until the first gear.

The several different characteristics include the performance, size, measurement and weight of the automatic transmission. Table 20.1 shows a few versions for types of automatic transmission in modern vehicles (Jürgens 1994) that can be used for automatic transmission stand structure (U-shaped holder).

Table 20.1 Types of automatic transmission

| Types | Diagram | Details | Length (mm) | Weight (kg) |
|---|---|---|-------------|-------------|
| Torque converter/traditional automatic transmission |  | <ul style="list-style-type: none"> • Uses a hydraulic fluid coupling or also known as a torque converter to do the job of changing gears instead of a clutch • Provides smooth and precise engine control when the engine control unit (ECU) is directly connected to the mechanism • Easiest and most reliable automatic transmission | 620 | 91 |
| Continuously variable transmission (CVT) |  | <ul style="list-style-type: none"> • Using belts or pulleys rather than traditional steel gears • Allows to control the engine speed or RPM for accelerating or decelerating depending on throttle action • Largely used in two-wheelers where acceleration and braking is the main function | 590 | 90 |

20.2.2 Maintenance of Automatic Transmission

There are a few symptoms which show that the automatic transmission has problems. One of it is when the car starts behaving strangely and the gear shift becomes less smooth. Occasionally, the symptoms showed when the accelerator is pressed, but the car does not move forward. At the beginning, these symptoms may not be a problem, but it may get worse after some time and then will lead to serious causes to be concerned. The complications of the transmission often occur because of overheating. It is due to the high temperature that makes it lose its lubricating characteristics and may oxidize. This will leave deposits inside the transmission. When it is exposed to high temperature, the rubber seals and gaskets inside the transmission will harden and cause leaking due to the metal parts warp and lose their strength.

Thus, this will result in transmission breakdown. Automatic transmission repair and maintenance are complicated and may differ significantly for different types of automatic transmissions. There are a few basic steps for repair and maintenance of the automatic transmissions such as the following activities:

1. Identification of faulty automatic transmission components based on shifting and gearbox operation.
2. Removal of the automatic transmission.
3. Disassembly of the automatic transmission (required for the repair).
4. Determination of component wear.
5. Replacement of damaged and non-repairable parts.
6. Assembly of all the components using new gaskets and sealing.
7. Installation of the automatic transmission on the vehicle and filling it with fresh oil.

Other than that, an automatic transmission is practically a machinery that must be carefully installed and repaired. It is important to make the correct steps that are performed based on the right methods. Throughout the years, repair and maintenance techniques of the automatic transmission have been optimized by using the correct tools and equipment to enhance the performance and durability. A successfully repaired automatic transmission demands skill, detailed attention and proper tools and equipment. Dismantling and servicing can also be carried out on equipment which is not operational. The equipment must be isolated from electrical supply and measures must be taken to prevent accidental connection to the mains during the maintenance. Other reasons that lead to the damage of the automatic transmission are due to negligence, poor manufacturer design and repairs done by untrained or inexperienced technicians (Hancock 1961). So, the proper tools and equipment are needed as the holder or stand during the repair and maintenance of the automatic transmission.

20.2.3 Automatic Transmission Stand/Holder

The automatic transmission stands or holder is a product which is used to hold and support the automatic transmission during the repair, maintenance or educational purposes (Hancock 1961). Basically, this product is infrequently used and known in public society due to its uses which is limited for certain types of people based on the needs of their work, study or to do maintenance of the automatic transmission. Currently, there are a few designs with different characteristics (Zanetti et al. 2014) available in market. As the closest example of this product which can be looked up is the product used at the University Kuala Lumpur Malaysian Spanish Institute (UniKL MSI) as shown in Fig. 20.1. The red circle in Fig. 20.1 indicates the stand that was used in the workshop to support the automatic transmission and the type of transmission used was the torque convertor transmission. The product is used for educational purposes as the students in UniKL MSI have a few subjects such

as automotive powertrain which requires them to study and operate the automatic transmission with the monitor and observation from their respective lecturers or technicians. The characteristics of the automatic transmission holder used in UniKL MSI are that it is placed on the workbench and fixed attached with screws. Another characteristic is that it is not adjustable, which means that the automatic transmission has a fixed position. Thus, the flexibility to use this automatic transmission during educational purposes is limited and inconvenient.

20.2.4 Comparison Between Previous Product and Automatic Transmission Stands (U-shaped Holder) Structure

There are two types of literature found for this study which are:

1. Comparison of existing products available in the market (Table 20.2).
2. Comparison of these/journals related to the proposed project (Table 20.3).

Table 20.2 Previous versus new automatic transmission stands


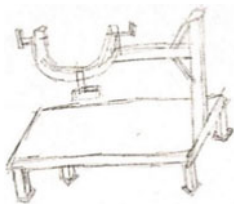
| | Previous products | New products |
|-------------------|--|--|
| 1. Factor | GM-Transmission Holding Fixture/Tool (Streetside Tool, 2015) | Automatic Transmission Stand Structure (U-shaped holder) |
| 2. Design |  |  |
| 3. Stand | No stand | Rubber based |
| 4. Holder | Dual tightening handles | Bracket shaped |
| 5. Maximum load | | 100 kg |
| 6. Flexibility | Not adjustable | Not adjustable |
| 7. Arm's rotation | Full 360° swing | 180° swiveling and locking head |
| 8. Price | 129 USD @ RM 562.12 | RM 300.00 |
| 9. Weight | 7.3 kg | 20 kg |
| 10. Measurement | 200 250 350 700R4 | 130 cm/70 cm |
| 11. Material | Steel | Mild steel |

Table 20.3 Theses/journals related to the project

| | | |
|----------------------|--|---|
| 1. Paper title | Automobile gearbox holding device during maintenance (Adzimah et al. 2013) | Apparatus for mounting a transmission on an engine stand (Davis 1996) |
| 2. Problem statement | <ol style="list-style-type: none"> 1. The method used during repairs on gearboxes of automobile always poses danger 2. Cause fatigue and much risk of worker injury; endanger | <ol style="list-style-type: none"> 1. Transmissions are difficult to repair due to their shape, size and weight 2. Must be stabilized to prevent it from moving |
| 3. Method | <ul style="list-style-type: none"> • Calculation for the efficiency of device and fabrication | <ul style="list-style-type: none"> • Case study |
| 4. Novelty | <ul style="list-style-type: none"> • It includes a support plate on which the gearbox will rest • The links, joined together by pins to the brackets, and therefore, the joints make the up and down movement of the support • It also includes a base within the form of a board with wheels to make easy the drawing and pushing of the device with the gearbox on it | <ul style="list-style-type: none"> • An apparatus for mounting a transmission on an engine stand, including a frame and a mounting plate pivotally carried by said frame and pivoting about an axis of rotation, the transmission defining a centroidal axis |
| 5. Comment | <ul style="list-style-type: none"> • This device will relieve stress and prevent the possibilities of severe injuries on mechanics • It is efficient enough to be used for the purpose, for which it was designed based on the efficiency | <ul style="list-style-type: none"> • The apparatus of the present invention is comprised substantially of a pair of mounting brackets for the attachment of the transmission and the securement to the selected engine stand |

20.3 Methodology

20.3.1 *Design and Morphological Chart for Automatic Transmission Stands (U-Shaped Holder) Structure*

Table 20.4 shows the sketching and morphological of the design.

20.3.2 *Specification*

Table 20.5 shows the specification of the automatic transmission stands with U-shaped holder design.

Table 20.4 Morphological chart

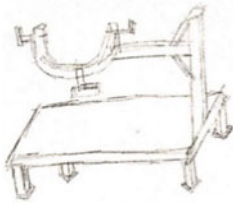
| Concept | Automatic transmission stands (U-shaped holder) |
|---|--|
| (1) Design |  |
| (2) Stand | Rubber-based Has a rubber-based stand to prevent the product to dislocate during the installation of automatic transmission |
| (3) Material | Steel |
| (4) Flexibility | Adjustable rotation |
| (5) Installation/support of AT to the product | Bracket-shaped |
| (6) Spacing | Space consuming—large and bulky |
| (7) Advantages | 1. Easy installation Has a rubber-based stand to prevent the products to dislocate during installation of automatic transmission 2. Save space Smaller in size due to fixed length and height |
| (8) Disadvantages | Not convenient It is not adjustable in terms of length and height |

Table 20.5 Specification of automatic transmission stands (U-shaped holder)

| Characteristic | New design |
|-----------------------------|------------------|
| (1) Length (mm) | Not adjustable |
| (2) Height (mm) | Not adjustable |
| (3) Angle of rotation | 180° |
| (4) Type of base | Rubber-based |
| (5) Types of materials used | Mild Steel |
| (6) Maximum load (kg) | Less than 100 kg |

20.3.3 Detailed Drawing

The isometric view (3D drawing) and orthographic view (2D drawing) of the design are shown in Figs. 20.2 and 20.3, respectively. The stand can be placed on the workbench as well as on the floor. It can be rotated and fixed at a certain rotation angle.

Fig. 20.2 Isometric view of the automatic transmission stand (U-shaped holder)

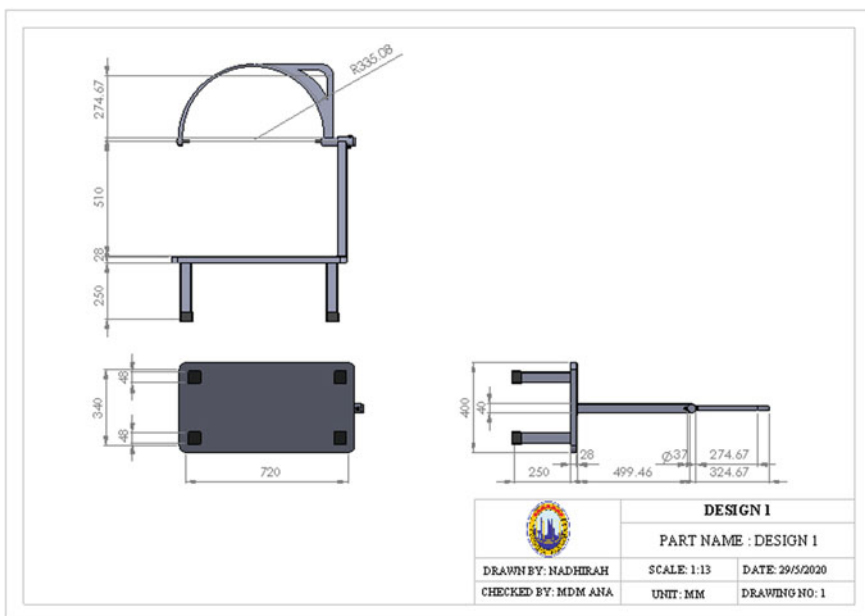
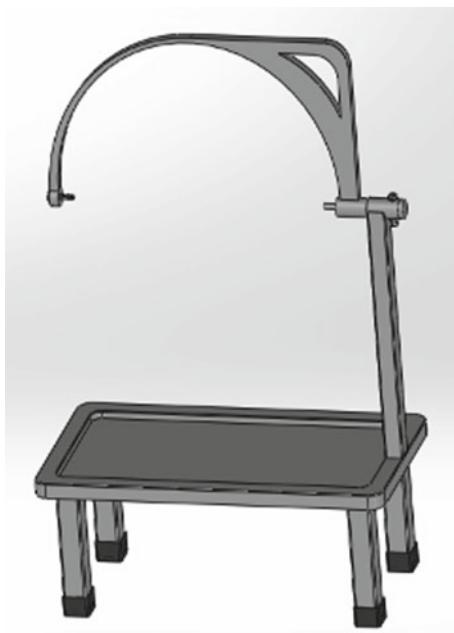


Fig. 20.3 Orthographic view of the automatic transmission stand (U-shaped holder)

20.3.4 Simulation Method

The SOLIDWORK simulation software is used to analyze the design. This software is used to do analyses for the strength of the products in a way which is as follows:

1. It can withstand the maximum load (weight of automatic transmission) which is 100 kg.
2. The stand holder can be adjusted at an angle of rotation (0° , 45° or 90°).

20.4 Results and Discussion

The specific parameters used for the simulation process of the design are shown in Table 20.6.

Figure 20.4 shows an example of stress analysis of the design. The critical high stress concentration is at the holder that is near to the vertical stand. The results for stress when load of 1000 N is applied to the design with a height of 800 mm at angles of 0° , 45° and 90° are shown in Fig. 20.5. From the graph, the value of the minimum stress is 0.0583 MPa, while the maximum stress is 0.0618 MPa. According to the stress results for the design, the minimum and maximum values of stress show a slightly difference of 5.61%. By increasing the rotation angle, the stress is increased in Fig. 20.5. It might be due to the gravitational effect on the load for the increased rotational angle.

Figure 20.6 shows an example of strain analysis of the design. The strain for this design with a height of 800 mm at angles of 0° , 45° and 90° is shown in Fig. 20.7. This graph indicates that the value of the maximum strain is 0.00227% which is at height of 800 mm (90°) and the maximum strain is 0.00234% at height of 800 mm (0°). The difference from the minimum and maximum values of the strain result is 4.11%. In this graph, the strain is decreasing as the angle for this design is rotating from angle 0° to 90° when 1000 N load is applied. Hence, by analyzing the value of strain result, the highest value of strain is at the height of 800 mm (0°), which shows that it has the most changes in deformation compared to the others.

Table 20.7 shows the summary of the stress and strain results at 800 mm height of the design. From the result, the stress is increased while the strain is decreased by increasing the angle of rotational. The design has an adequate strength and deformation to withstand 1000 N load at very changes in angle of rotation. The cantilever

Table 20.6 Setup parameters for simulation process of the automatic transmission stand (U-shaped holder)

| Parameter | Details |
|------------------------------|-----------------|
| Material | Mild steel |
| Maximum load | 100 kg (1000 N) |
| Poisson's ratio (mild steel) | 0.303 |
| Maximum angle | 90° |

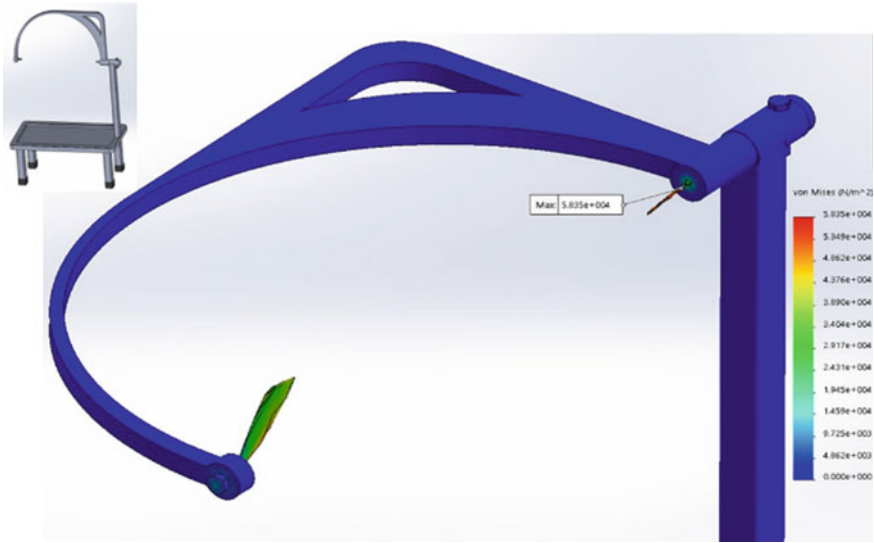
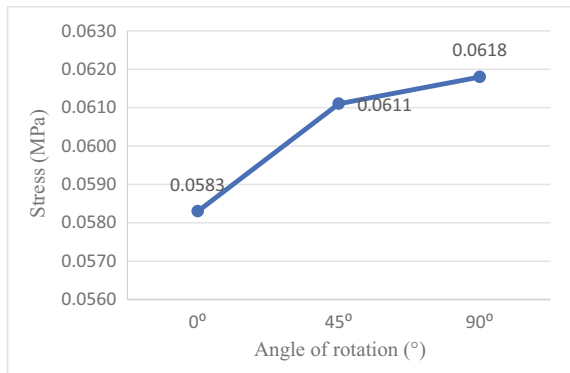


Fig. 20.4 Simulation using SOLIDWORKS: stress analysis

Fig. 20.5 Stress results for the design at 0°, 45° and 90° rotation angles of the design at 800 mm of design height



condition with end clamp at each side is quite unbalanced so when load is acting upon by the cantilever, the other side of the clamp must bear more forces and pressure. This will affect the lifespan of the product due to its elasticity even though its stress value. However, based on this study, this design could support the maximum load of 100 kg and the flexibility which is the angle of rotation can be adjusted up to 90°.

For this adjustable automatic transmission stand structure (U-shaped holder) study, the future recommendations would be as follows: (1) added features or system that can make this product adjustable in terms of height, (2) comfort improvement and reducing the weight of the design by using a lighter material for the product, (3) safer and more presentable products such as better finishing, unique and attractive design.

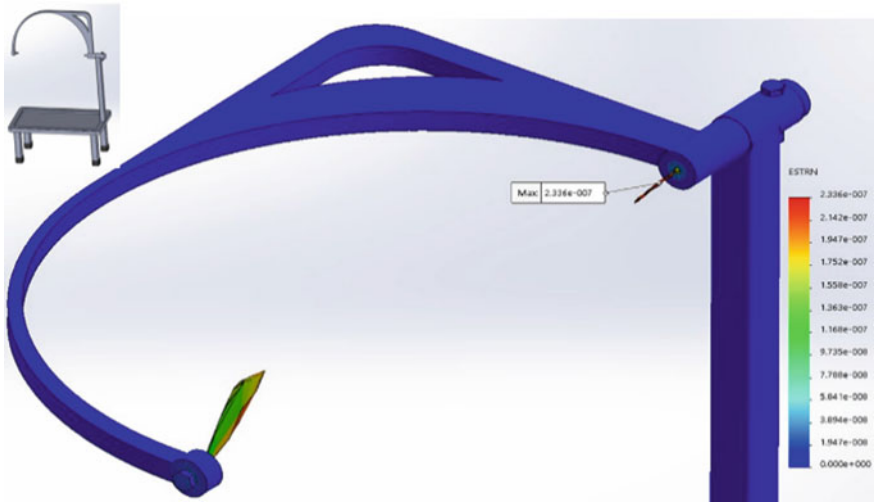


Fig. 20.6 Simulation using SOLIDWORKS: strain analysis

Fig. 20.7 Strain results for the design at 0°, 45° and 90° rotation angles of the design at 800 mm of design height

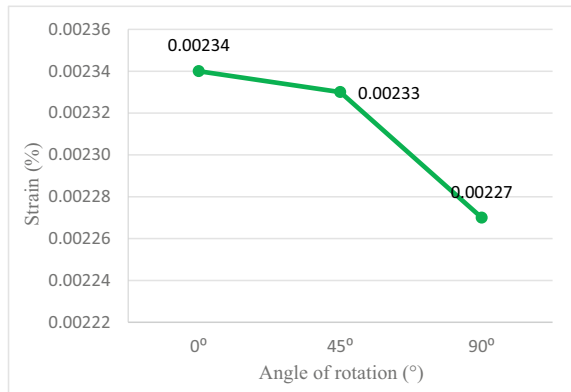


Table 20.7 Summary of the stress and strain results

| Height (mm) | Stress, MPa | | | Strain, % | | |
|-------------|----------------------|-----------------------|-----------------------|----------------------|-----------------------|-----------------------|
| | $\theta_1 = 0^\circ$ | $\theta_2 = 45^\circ$ | $\theta_3 = 90^\circ$ | $\theta_1 = 0^\circ$ | $\theta_2 = 45^\circ$ | $\theta_3 = 90^\circ$ |
| 800 | 0.0583 | 0.0611 | 0.0618 | 0.00234 | 0.00233 | 0.00227 |

20.5 Conclusions

In conclusion, the automatic transmission stand with U-shaped holder was designed. The study is related to the product that will relieve stress and prevent the possibility of severe injuries to mechanics. The maximum stress is 0.0611 MPa at 90°. However,

the minimum strain of 0.00227% was indicated at this angle. The device is efficient enough to be used for the purpose for which it was designed based on the efficiency. It is reliable and safe to withstand 100 kg of automatic transmission that can hold the automatic transmission in any position during its maintenance. The principle of operation of the design is easy and flexible. The U-shaped holder can be adjusted up to 90° angle of rotation. The length and height for this design are fixed and cannot be adjusted. Therefore, it can provide the withstand to the automatic transmission at any angle required and enables secure holding on the stand to the user during repair and maintenance process according to the simulation results. The invention provides a simple and adjustable in many ways, practical, easy assembled and disassembled stand for repairing and maintenance of the automatic transmission.

References

- Adzimah KS, Akinwonmi AS, Oswell P (2013) Automobile gearbox holding device during maintenance. *Inter J Eng Sci* 2(9):10–16
- Davis Jr WM (1996) Apparatus for mounting a transmission of an engine stand. United States Patent US5562271A. <https://patents.google.com/patent/US5562271A>
- Fischer R, Küçükay F, Jürgens G, Najork R, Pollak B (2015) *The automotive transmission book*, vol 1. Springer, Berlin, pp 229–273
- Hancock HE (1961) 15–18. 1499071806676259668-02985448 (storage.googleapis.com). Accessed 22 June 2020
- Jürgens G (1994) Transmission systems: a comparative view. In: 5th LuK symposium. Microsoft Word—6_Transmission_Systems.doc (schaeffler.com) Accessed 19 Feb 2020
- Sawasaki T, Kawamura S, Mori Y, Kagawa M (1994) U.S. Patent No. 5295920. Washington, DC: U.S. Patent and Trademark Office
- Sheth S, Gajjar BR, Chauhan P (2014) A scope and study of automatic transmission system in context of operating parameter and professional requirement. National Conference on Emerging Trends in Engineering, Technology & Management, INDUS Institute of Technology & Engineering, Ahmedabad, India 2:1–5
- Streetside Tools SST-0156-B - GM - Transmission Holding Fixture/Tool with Base (2015) Amazon.com: <https://www.amazon.com/SST-0156-BF-Transmission-Holding-Fixture-without/dp/B018HRLQUK>. Accessed on 7 Feb 2021
- Zanetti EM, Franceschini G, Audenino AL (2014) Dynamic stability of under hoist transmission jacks. *Saf Sci* 68:34–40

Chapter 21

Design Improvement and Fabrication of a Jig for Holding a Workpiece in a Coordinate Measuring Machine



Siti Shareeda Mohd Nasir, Norasikin Hussin, Nor Azirah Mohd Fohimi, Dzulijah Ibrahim, and Rohidatun Mahmud Wahab

Abstract A coordinate measuring machine (CMM) is one of the most common devices in engineering measurement. A CMM is a device to measure the geometry of physical specimen by sensing on the surface of the specimen with the measuring probe. Unfortunately, the measuring probe in the Metrology Laboratory at UiTM Cawangan Pulau Pinang is not able to touch the surface of the workpiece with a thickness less than 40 mm. In order to solve this issue, a special jig needs to be used. The existing jig has some problems where the measurement results are inaccurate and causing damage to the accessories of CMM. Thus, the objective of this study is to improve the design and fabrication of the jig for the CMM in order to replace the existing jig. The jig will be used to hold and clamp the cylindrical and square workpiece and ensure that the measuring probe can touch the workpiece perfectly. The Pugh method is used to identify the best conceptual design. The new design of the jig has been built up using the CATIA software. Hardwood and polylactic acid (PLA) were selected for the jig material. The fabrication of the jig has been done using the 3D printing technology. Comparison has also been done with the new and

S. S. M. Nasir (✉) · N. Hussin · N. A. M. Fohimi · D. Ibrahim · R. M. Wahab
Pusat Pengajian Kejuruteraan Mekanikal, Universiti Teknologi MARA, Cawangan Pulau Pinang,
Kampus Permatang Pauh, 13500 Permatang Pauh, Pulau Pinang, Malaysia
e-mail: shareeda.mn@uitm.edu.my

N. Hussin
e-mail: norasikin245@uitm.edu.my

N. A. M. Fohimi
e-mail: noraz330@uitm.edu.my

D. Ibrahim
e-mail: dzullijah@uitm.edu.my

R. M. Wahab
e-mail: rohidatun@uitm.edu.my

S. S. M. Nasir · N. A. M. Fohimi
Advanced Mechanics Research Group, Pusat Pengajian Kejuruteraan Mekanikal, Universiti
Teknologi MARA, Cawangan Pulau Pinang, Kampus Permatang Pauh, 13500 Permatang Pauh,
Pulau Pinang, Malaysia

existing jig. The results show that the improved jig is more suitable and acceptable to replace the existing jig.

Keywords Jig · Design · Coordinate measuring machine (CMM)

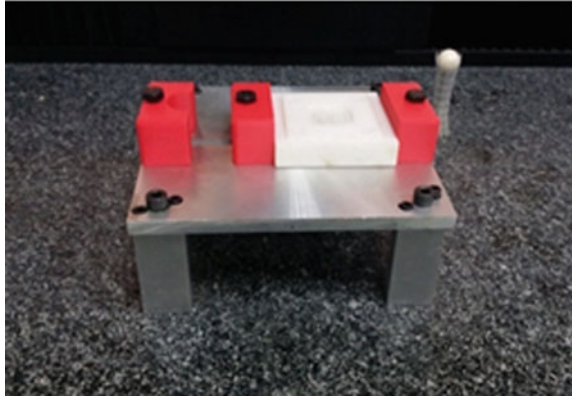
21.1 Introduction

The jig works by holding or clamping devices which are used to fix the workpiece firmly on the working table. The function of the jig is to ensure a high degree of precision, interchangeability and duplication in products' manufacturing, and it is also applied to manipulate the location and movement of other tools (Hussin et al. 2018). Smith Patel et al. stated that jigs are special purpose tools which are used to facilitate the production like machining, assembling and inspection operation (Altalmas et al. 2013). Measuring and inspection are the means by which poor quality is detected and good quality is assured in products that are produced in a production process (Honkala et al. 2007). Inspection by measurement is usually carried out by two techniques which are manually operated devices such as calipers, micrometer and modern technologies such as coordinate measuring machine (CMM). The advantages of using a CMM compared to manual inspection are accuracy, speed and human error reduction. In the CMM, the important component is a measuring probe. The measuring probe is used to touch the surface of the workpiece that needs to be measured. Then, the measurement result for the specific variables will be carried out. The smooth measuring probe movement will give accurate and acceptable measurement results. If the measuring probe cannot touch the workpiece with a thickness of less than 40 mm, the CMM requires an additional device (Mania and Tomczak 2020). A suitable additional device is a jig.

Thus, this study aims to improve the design of a jig for the CMM in the Metrology Laboratory at UiTM Cawangan Pulau Pinang in order to replace the existing jig. The existing jig has a few issues in engineering measurement, and this needs to be solved. In practice, the condition of the jig is not suitable for use because of the imbalance of the jig feet which can affect the movement of measuring probe. To overcome this issues, the new design of the jig is required.

21.2 Problem Statement

Figure 21.1 shows the existing jig used for clamping the square and cylindrical workpiece during the measurement process by CMM (Hussin et al. 2018). However, the existing jig has a few problems during the measurement process. The main problem is about the stand of the jig. This jig has four stands, and one of them is not stable and unbalanced because it is uneven with others. Therefore, this jig is not suitable to be used because it will affect the CMM measuring probe to touch the workpiece. The

Fig. 21.1 Existing jig



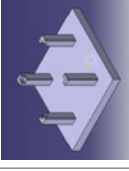
function of the CMM measuring probe is to determine the coordinate of points on a workpiece surface. The clamping components of the jig cannot function properly in order to clamp the workpiece. Other than that, the position of the workpiece after being clamped is not suitable because the position is slightly into the jig. Since the price for a CMM measuring probe is quite expensive, the incident when the probe collides with the clamping components is considered. The jig consists of sharp edges that can cause injury during conducting the measurement. Thus, the improvement of jig design is required to replace the existing jig.

21.3 Methodology

The purpose of a new jig design is to improve the existing jig in order to hold, clamp and support the workpiece with a thickness of less than 40 mm. The conceptual design is used in this study to determine the best design for the jig improvement. The observation and brainstorming on methods or mechanisms that are related with the process fabrication and measurement have been considered. Several factors are considered in designing of jig such as size and geometry, capacity of machine, clamping method, weight, material selection, safety and portable part. Each of design factors is summarized in Table 21.1.

The decision-matrix method, known as Pugh method, is used to identify the best conceptual design. The Pugh method is a qualitative technique to rank the design factors. The Pugh method frequently is used in engineering design to select the best viable and feasible option in making the decision of the best design. The matrix is also known as Pugh matrix. The Pugh matrix is not a mathematical matrix, but it is a simple concept to expressing the significance ideas in visible. Each factor of the design characteristic needs to be evaluated to obtain the score. Thus, the Pugh matrix is performed to assign a relative score for the concept design. The scale for the score

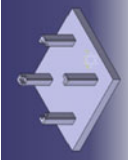
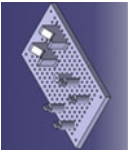
Table 21.1 Pugh chart of conceptual design

| Concept design | |  |  |  |
|--------------------------------------|--------|--|---|---|
| Characteristics | Weight | Design A | Design B | Design C |
| Size and geometry | 3 | + | 0 | - |
| Type and capacity of machine | 1 | + | 0 | - |
| Available clamping arrangement | 2 | + | + | 0 |
| Location with rigidity and vibration | 2 | + | + | 0 |
| Use and ejecting the jig | 1 | 0 | 0 | + |
| Safety | 1 | 0 | 0 | 0 |
| Sum + | | 4 | 2 | 0 |
| Sum 0 | | 2 | 4 | 4 |
| Sum - | | 0 | 0 | 2 |

(continued)

Table 21.1 (continued)

| Concept design | | | | | |
|-----------------|--------|----------|----------|----------|--|
| Characteristics | Weight | Design A | Design B | Design C | |
| Net score | | 8 | 4 | -5 | |
| Rank | | 1 | 2 | 3 | |
| Continue? | | Yes | No | No | |



is divided into three symbols which are ‘-’ as acceptable, ‘0’ as good and ‘+’ as excellent. Table 21.1 shows the score for each factor.

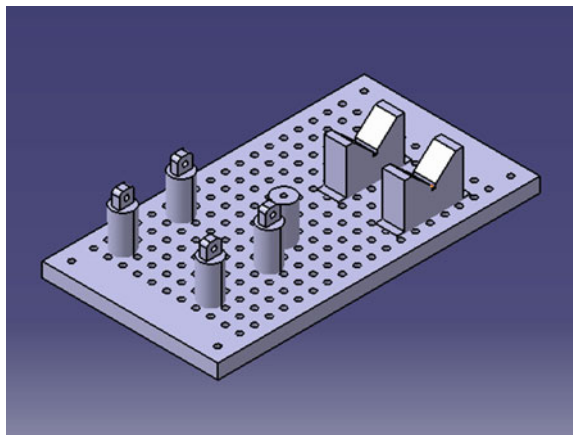
Concept selection is an activity in the product design process, where alternative concepts are compared and a decision is made to select the best alternatives (Honkala et al. 2007). The rank concept is given in order to evaluate the highest score based on the net score. The net score for design A is 8, which is the highest score among the other design. The net score for design B and design C is 4 and - 5, respectively. Hence, design A has been chosen for the final design.

21.4 Results and Discussion

In this study, the conceptual design A is the best design because of the highest net score. The 3D model of the new jig has been build up using the CATIA software as shown in Fig. 21.2. For design A, the base plate consists of holes with 440 mm in length, 240 mm in width and 20 mm of thickness. The function of the holes on the base plate is to locate the standoff according to the shape of the workpiece. The standoff or also known as pin locator is being used to hold the square workpiece. Then, the bolt will be used to clamp the workpiece through the hole on the top of the standoff. The V block is being used to locate the cylindrical workpiece.

The material that is used for the base plate is hardwood which is Oak wood, while the material for the standoff and V block is polylactic acid (PLA). The Oak wood is used for the base plate because it is highly valued for its unique properties, durability, light in weight, good in strength for both tension and compression, provide rigidity and toughness (Mania and Tomczak 2020). The ripping cut and cross-cut process is used to fabricate the base plate. The function of the base plate jig is to grip with the CMM table and avoiding the movement of the jig during process measurement. The base plate consists of 202 holes including each on the edge of the base plate with

Fig. 21.2 Conceptual design A using the CATIA software



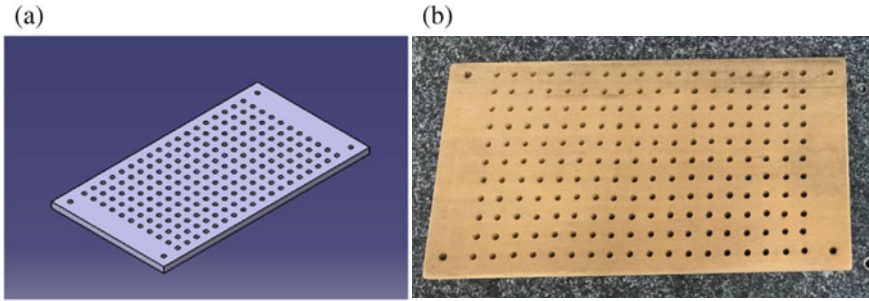


Fig. 21.3 a Three-dimensional design of base plate; b base plate jig

8 mm in diameter as shown in Fig. 21.3. The purpose of the base plate jig is to place the standoffs and V block according to the shape of the workpiece. The function of the holes is to grip the standoff and V block with base plate. Thus, the placement of the standoff and V block on the top of base plate can be adjusted.

The PLA is used to fabricate the standoff and V block. PLA material is widely used in 3D printing technology. The characteristics of PLA with lower printing temperature than other materials which is in range of 180–230 °C cause this material to not misshape easily (Sarhan Othman et al. 2019). The fabrication of the V block and standoff is done using the 3D printing technology. The function of the standoff is used to hold and clamp the square workpiece. The height of the standoff is 80 mm and the diameter is 30 mm. The standoffs are clamped on the base plate jig by using studs. The height of the standoff can be increased with the combination of a feet. The dimension of the feet is 60 mm of height with 30 mm diameter. This design provides the feet to support and adjust the height of the standoff (Figs. 21.4 and 21.5).

The function of the V block is to hold the cylindrical workpiece during the measurement process. The ‘V’ shape acts to provide two points of contact between the surface and the workpiece. It can be clamped on the base plate by using studs. The length of the block is 100, 30 mm in width and 70 mm of height. The dimensional

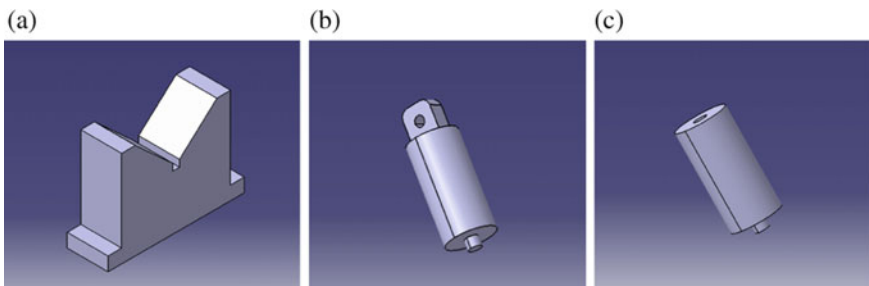


Fig. 21.4 Three-dimensional design of a V block; b standoff; c feet



Fig. 21.5 All the parts after 3D printing and finishing

Table 21.2 Jig components and function

| Item | Part name | Quantity | Function |
|------|------------|----------|--|
| 1 | Base plate | 1 | Flat surface as a base to put V block, standoff and feet |
| 2 | V block | 2 | To clamp cylindrical workpiece |
| 3 | Standoff | 4 | To hold square workpiece |
| 4 | Feet | 4 | To adjust the height of standoff |

tolerance of the V block, standoff and feet is ± 0.03 mm. Table 21.2 shows each of the jig component with their individual function.

The bolt will be used to clamp the square workpiece through the hole on the top of the standoff, while the V block is being used to locate the cylindrical workpiece to avoid movement during the measurement process as shown in Figs. 21.6 and 21.7. By using this new jig, the cylindrical and square workpiece can be easily hold and the measuring probe can touch the surface of the workpiece with a thickness less than 40 mm. The measurement process can also be done smoothly. The importance of this design is to ensure that the measuring probe can touch the workpiece without any disturbance. When the measuring probe accidentally hit other objects, it may cause damage to the equipment and accessories of the CMM. Besides that, the inaccuracy of the measuring probe in touching the workpiece will affect the measurement result (Miguel et al. 2003).

21.5 Conclusion

This paper illustrates the improvement of the design and fabrication of a jig for the CMM in the Metrology Laboratory at UiTM Cawangan Pulau Pinang. The purpose of the jig is to ensure that the measuring probe can touch the workpiece during the measurement process. The functions of the jig are to hold, clamp and support the cylindrical and square workpiece. The jig can be used for a workpiece with thickness

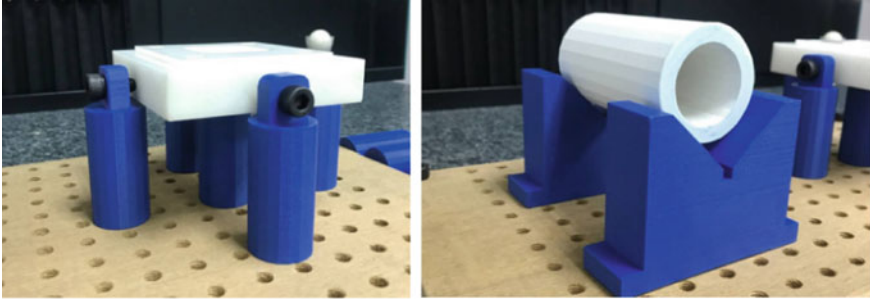
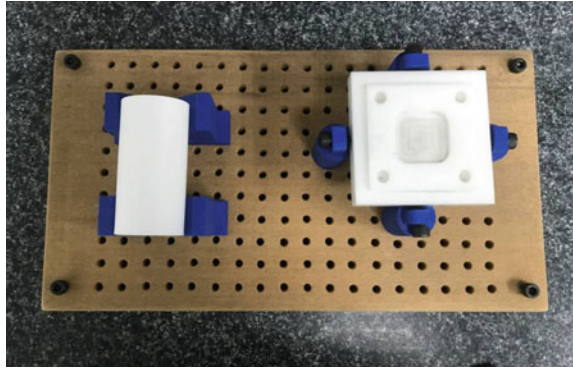


Fig. 21.6 Holding the square and cylindrical workpiece

Fig. 21.7 Complete clamp of the workpiece



less than 40 mm. The problem with the stability of the feet on the existing jig was resolved. The base plate is used to secure the jig from moving, and it is fastened on the granite table. As a result, the use of the standoffs increased the heights of the workpiece. Aside from that, the standoff was clamped to the base plate to improve the clamping stability.

Acknowledgements This research was not funded by any grant. The authors would like to thank the Center for *Mechanical Engineering* Studies as granted us permission to conduct site measurement inside the Metrology Laboratory and express their appreciation to Universiti Teknologi MARA, Cawangan Pulau Pinang, Malaysia, for giving the opportunity and support to do this research study.

References

- Altalmas TM, Ahmad S, Aula A, Akmeliawati R, Sidek SN (2013) Mechanical design and simulation of two-wheeled wheelchair using solidworks. IOP Conf Ser: Mater Sci Eng. 53(1):012042

- Honkala S, Hämäläinen M, Salonen M (2007) Comparison of four existing concept selection methods. In: Proceedings of ICED 2007 16th international conference on engineering design, vol 7, pp 1–11
- Hussin N, Ibrahim D, Yahya NHM, Zulkkhiflee NI (2018) Design of jig for coordinate measuring machine. *J Mech Eng, SI* 5:97–107
- Mania P, Tomczak A (2020) Properties of oak roundwood with and without frost cracks. *For* 11(5):538
- Miguel PA, King T, Abackerli AJ (2003) CMM touch trigger performance verification using a probe test apparatus. *J Braz Soc Mech Sci & Eng* 25(2):147–153
- Sarhan Othman M, Fakhrur Razi Misran M, Helmi Khamisan Z (2019) Study on mechanical properties of Pla printed using 3D printer. *J Adv Res Appl Mech* 59(1):10–18

Chapter 22

Design of a Measurement Method for Surface Roughness Using a Vision System



**Mohd Fauzi Abu Hassan, Muhammad Azhan Abdull Lazit,
Mohd Faizal Abu Talib, Zakiah Ahmad, and Mohd Fadzil Abu Hassan**

Abstract Industrial surface roughness measurement is primarily based on styli. Stylus-based measurement of surface roughness has some limitations since the diameter of the stylus tip is acting as a filter in steep valleys. It is also a time-consuming process and offline. Due to the emergence of powerful cameras and superior image processing techniques, the vision-based surface roughness measurement system has the potential to emerge as a reliable online surface roughness measuring system. The work presented is an attempt to create a surface roughness assessment technique using vision-based image processing. A group of two-dimensional images of turned surfaces was first obtained, and the image pixel intensity distribution parameters for each of these surface images were calculated. Features of statistical parameters were used to characterize the surface roughness using the pixel intensity of the turned surface images. Features were found to correlate better with Ra values of the surface roughness. A regression analysis was used for the further process. Hence, the technique may be preferred for online surface characterization of turned surfaces. A MATLAB GUI is used to display the result.

Keywords Surface · Parameters · Vision-based · Contact · Regression

M. F. A. Hassan (✉) · M. A. A. Lazit · M. F. A. Talib · Z. Ahmad
Universiti Kuala Lumpur, Malaysia Spanish Institute Kulim Hi-Tech Park, 09000 Kulim, Kedah,
Malaysia
e-mail: mohdfauzi@unikl.edu.my

M. F. A. Talib
e-mail: mfaizal@unikl.edu.my

Z. Ahmad
e-mail: zakiah@unikl.edu.my

M. F. A. Hassan
Universiti Kuala Lumpur, Malaysia France Institute, Bangi, Selangor, Malaysia
e-mail: fadzil@unikl.edu.my

22.1 Introduction

Surface roughness measurement is one of the basic measurements that determines the quality and performance of the final product. In recent years, the importance of surface texture has gained attention in many fields, and this is still increasing. In particular, the surface roughness is an important factor in determining the satisfactory performance of a workpiece in areas (Samtas et al. 2014). Techniques for measuring the surface roughness can be split into two general categories. The first category of techniques differentiates the surface roughness by contact techniques. The stylus instrument is an example of the methods in the first category. The tip of the stylus instrument moves vertically up and down, along the surface profile generating the roughness parameters of the specimen under study. The second category techniques estimate the roughness of a surface by non-contact methods such as image processing. Mean image, standard deviation of image, and variation of images are the examples of parameters that can be used to measure the roughness using an image. Fiber optics developments and the advent of large-scale, high-speed computers, and common vision systems have made image processing quick, fast, and versatile. Surface images are used to calculate the roughness for processing in image processing techniques. The lay pattern will decide whether the surface is rough or smooth, obtained from the pictures.

A stylus instrument is reliable to measure the surface roughness, but the stylus tip is prevalent with disadvantage that it could not penetrate in valleys less than the tip diameter. Thus, it gives an overall surface roughness by averaging. When using a malleable surface, damage may be induced to the contact area or the tip. The setup and operation time for surface measurement using a stylus profiler is considerably high. Hence, a reliable non-contact optical technique for surface measurement has good potential to measure based on a powerful CCD camera and fast processing digital computers.

22.2 Literature

The calculation of surface roughness is the calculation of the small-scale variations of a physical surface's height. This contrasts with broader variations in scale such as shape and waviness, which are usually part of the surface geometry (Butler 2014). Nithyanantham and Suresh (2016) proposed to preprocess the surface images of the specimens using the geometric search technique to prevent the effects of inappropriate lighting and noise. Adding the low-pass filter to the image, the effects of salt and pepper are reduced. Mohamed Suhail et al. (2018), Priya and Ali (2015) used 1D signal generation to minimize the effects of lighting by eliminating the edge. The images obtained by the larger resolution are then reduced to smaller pixels for evaluation. The average pixel resolution gives an image signal with 1D.

For surface characterization using the Euclidean distance and Hamming distance metrics, characteristics were extracted and compared. As well as the dissimilarity between two vectors, the spatial difference is the Euclidean distance. The greater the distance between Euclidean's, the greater the difference. The standard deviation of the image signal for the Hamming interval was reached, provided that the functional components were distributed in the Gaussians. By counting the number of errors, the Hamming distance of the image signals and test image signals was achieved. The dissimilarity count between the reference and the test specimen is computed (Priya and Ali 2015).

Songli et al. (2016) said that after the noise has been removed, they used edge detection, which is not directly depending on the image grayscale, but depends on the image gray level change. For surface roughness calculation, speckle strength and contrast may be used. The method of measurement is very straightforward and includes one laser and an imaging device. The effects of surface variance and angle of incidence on speckle statistics are analyzed (Prabhathan et al. 2017).

Some paper proposed the shaded from shading (SFS) method to measure three-dimensional surface roughness. 3D reconstruction of the surface image and 3D of surface roughness extraction (Min et al. 2016). Shivanna et al. (2014) proposed another 3D measurement at which a confocal microscope was used. The microscope was capable of taking high-resolution 3D images. Confocal scanning microscopy is a technique with depth selectivity for obtaining high-resolution optical images. The key feature of confocal microscopy is its ability to acquire selected depths in the focus image, a process known as optical sectional. Samtas et al. (2014) proposed a method by using an artificial neural network. Images were being converted into binary format because this way they are more effective with the statistical property. He created a training network and improved the prediction program.

22.3 Methodology

22.3.1 Data Collection and Experimental Setup

All equipment is setup, and a few specimens are involved in this project. The software is also used in this project for the surface roughness tester and to capture and process the images. The surface roughness tester used the SURFPAK software to carry out the contact measurement, while a microscope camera was used along with the microHD software to capture the images.

In this experiment, 12 different metal surfaces are introduced. All the specimens were milled using dry milling. Figure 22.1 shows the 12 surface metal workpieces' and the references' specimen.

Surface roughness tester used to measure the roughness of the specimen is shown in Fig. 22.2a. It comes with the SURFPAK software to accumulate the machine. This machine is connected to the computer and can run automatically after setting up the

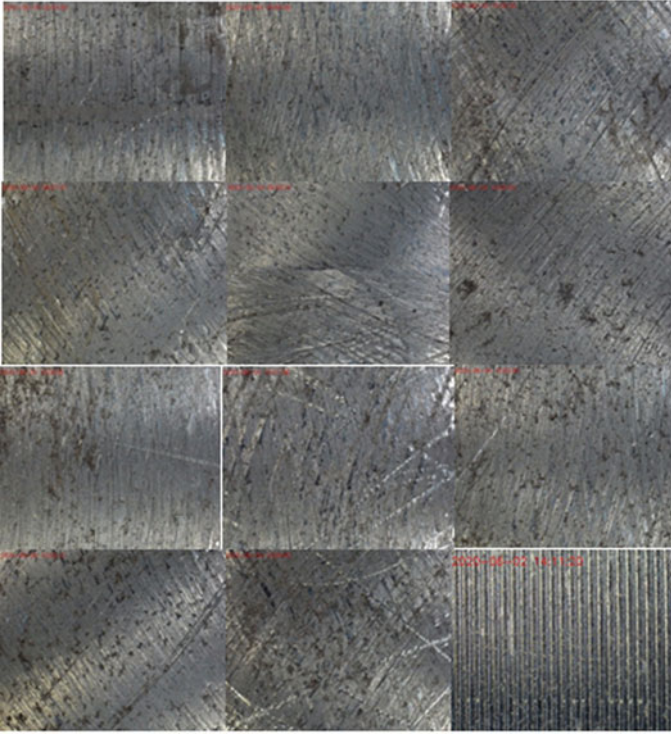


Fig. 22.1 Specimens

origin. The stylus moves upward and downward, along the surface producing the roughness parameters of the specimen, and evaluates the roughness parameter, Ra.

Figure 22.2b shows the 1080p microscope camera which comes with the MicroHD software that is used for modeling the vision method of the surface roughness measurement. Table 22.1 shows the specification of the camera. The camera was placed 90° to the specimen surface. The same camera and lighting conditions were used for capturing the images of all surfaces.

22.3.2 Preprocessing

Then, the images are converted into grayscale. This is one of processing techniques used to effectively extract image data in various areas. Basically, to transform the image to grayscale as a noise-removing preprocessing stage. When a RGB image is converted to grayscale, lots of information that is not needed for processing will be discarded. The entire image processing, including filtering and classification, is done

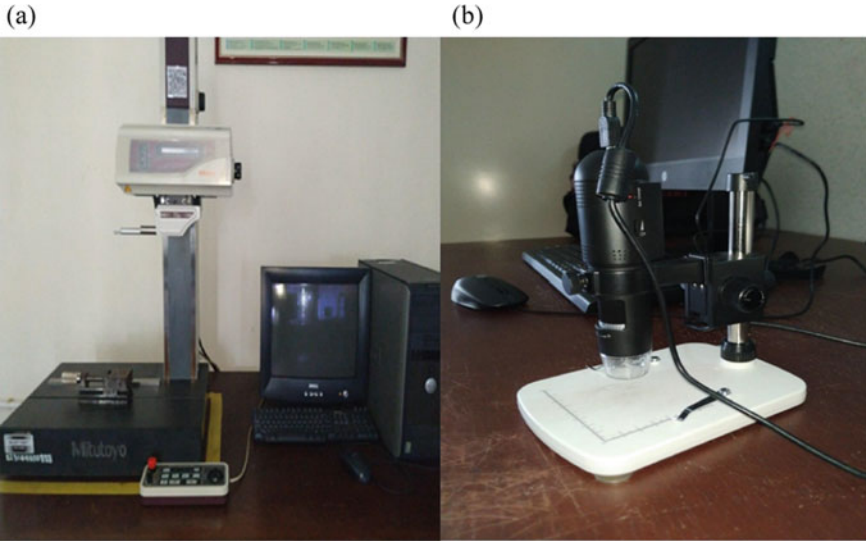


Fig. 22.2 a Surface roughness tester and b microscope camera

Table 22.1 Specification of camera

| Item | Specification |
|-----------------------|--|
| Camera type | High-quality CMOS |
| Focal distance | 0–50 mm |
| Zoom magnified | 10× to 230× |
| Resolution of video | 1080 p (1920 × 1080) |
| Format of video | H.264 |
| Resolution of picture | 3 M/5 M/8 M/12 M |
| Frame rate | Wireless: 1080 p: 15 fps; VGA: 25 fps Wired: VGA: 30 fps |
| Format of picture | JPEG |
| Power supply | DC 5 V/1 A (USB) |
| Battery | 1100 mAh Lithium |
| Battery time | < 100 min |
| Source of light | 6 LEDs (adjustable) |
| System required | iOS 5.1 or latest, Android, Windows-XP (SP2), Windows-7, Windows-8, Windows-10 |

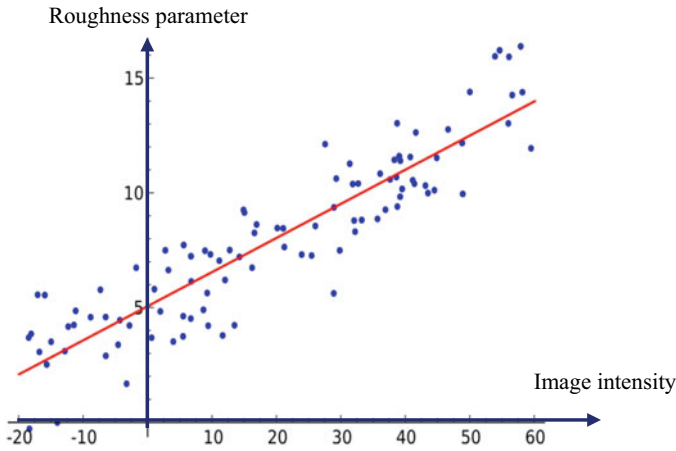


Fig. 22.3 Regression

with the MATLAB software. With the addition of toolboxes, the easily accessible features of the MATLAB program can be extended.

22.3.3 Features' Extraction

Every image has an intensity that can be obtained. As a result of this, numerous texture parameters, such as mean and standard deviations, have been extracted. Thus, it was measured to achieve the medium and standard image deviation.

22.3.4 Regression

Regression analysis is a reliable method of evaluating which factors have effect on a subject of interest. The relationship between predictor and response variables is specifically defined by a data model. By comparing the image intensity with roughness, the correlation of image intensity and roughness parameters, R_a , have been plotted in Fig. 22.3. The determination coefficient or R^2 was calculated.

22.3.5 Implementation

As an implementation, an application had been developed by using a MATLAB GUI which is shown in Fig. 22.4. The main function of this application is to monitor the

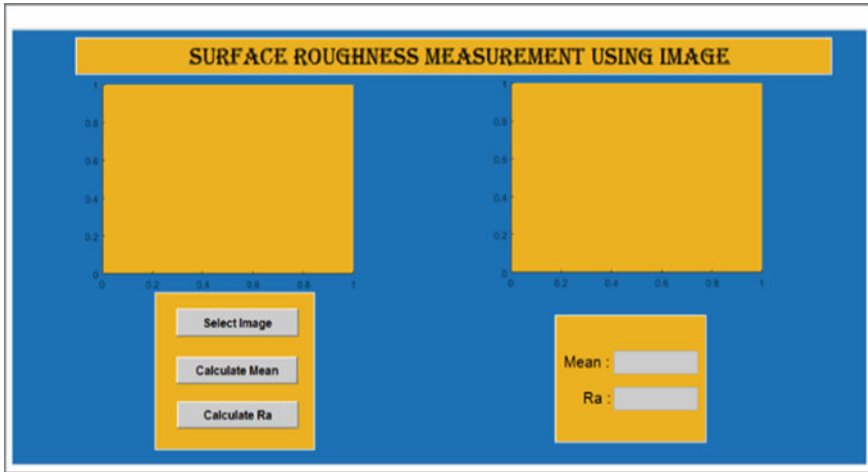


Fig. 22.4 Example of the MATLAB GUI

original image of surface and the pixel value of the image. In this application, the mean of the image and the roughness parameter are calculated and displayed. On behalf of the user, they can select other surface image to calculate the roughness.

22.4 Result and Discussion

Table 22.2 shows the roughness of workpiece measured by the surface roughness tester.

Figure 22.5 shows the profile of specimen 1. The profile shows the pixel values of the image of the specimen. From the pixel value, the mean and standard deviation were calculated for modeling the measurement method of the surface roughness. The mean and standard deviations from the pixel values were determined. The roughness of the test surface can be compared with image parameters. The image intensity parameters are shown in Table 22.3.

The correlation of the mean of the image and Ra are plotted in Fig. 22.6. The standard deviation pixel intensity plotted with Ra is shown in Fig. 22.7. From the patterns, it can be summarized that the image intensity corresponds good with the parameters of roughness Ra.

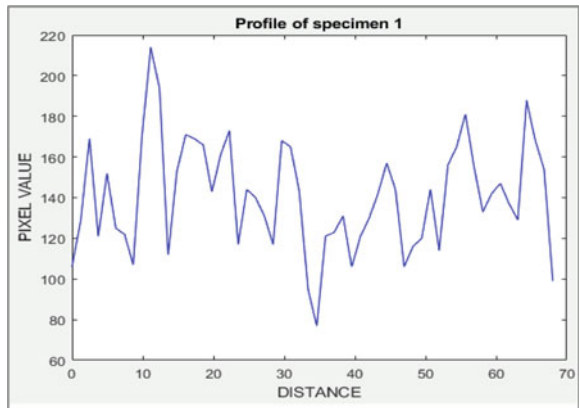
The weak correlation is mainly due to the shadow effect induced on the neighboring areas by the surface peaks. The peaks appear to change the intensity values in the region with the light beam incidence angle. But, studies show that this effect cannot be removed entirely.

The R^2 values showing the correlation effects between the mean and the standard image deviation for Ra values are 0.7815 and 0.1459, respectively. Figures 22.6

Table 22.2 Roughness of workpiece measured by surface roughness tester

| Specimen | Surface roughness, Ra (μm) | | | Average Ra (μm) |
|----------|---|--------|-------|------------------------------|
| | 1 | 2 | 3 | |
| Master | 2.965 | 2.976 | 2.971 | 2.970 |
| 1 | 3.424 | 3.414 | 3.402 | 3.413 |
| 2 | 2.325 | 2.333 | 2.355 | 2.337 |
| 3 | 3.583 | 3.597 | 3.581 | 3.587 |
| 4 | 2.870 | 2.878 | 2.878 | 2.875 |
| 5 | 3.107 | 3.1111 | 3.124 | 3.114 |
| 6 | 2.947 | 2.949 | 2.939 | 2.945 |
| 7 | 2.750 | 2.764 | 2.761 | 2.758 |
| 8 | 3.575 | 3.577 | 3.568 | 3.573 |
| 9 | 3.238 | 3.234 | 3.241 | 3.237 |
| 10 | 3.335 | 3.338 | 3.341 | 3.338 |
| 11 | 2.997 | 2.979 | 2.979 | 2.985 |

Fig. 22.5 Profile of specimen 1



and 22.7 also show that the mean intensity and standard image deviation of the images differ directly with the parameter of surface roughness with Ra. A rough surface allows the monochromatic light source to diffuse more widely, which leads to broader scattering. This helped to increase the value of the standard deviation. By increasing the roughness that results in increased dispersion of light, which leads to greater dispersion of the image (Table 22.4).

Table 22.3 Roughness and image intensity

| Specimen | Ra | Image intensity | |
|----------|-------|-----------------|--------------------|
| | | Mean | Standard deviation |
| 2 | 2.337 | 98.9525 | 28.4294 |
| 7 | 2.758 | 102.4253 | 27.1895 |
| 4 | 2.875 | 108.9299 | 24.1680 |
| 6 | 2.945 | 104.1143 | 25.3090 |
| 11 | 2.985 | 102.7567 | 25.0979 |
| 5 | 3.114 | 105.3545 | 27.2561 |
| 9 | 3.237 | 105.5742 | 27.9358 |
| 10 | 3.338 | 102.4253 | 27.3745 |
| 1 | 3.413 | 110.6252 | 29.6008 |
| 8 | 3.573 | 110.7913 | 30.6314 |
| 3 | 3.587 | 113.2823 | 27.1283 |

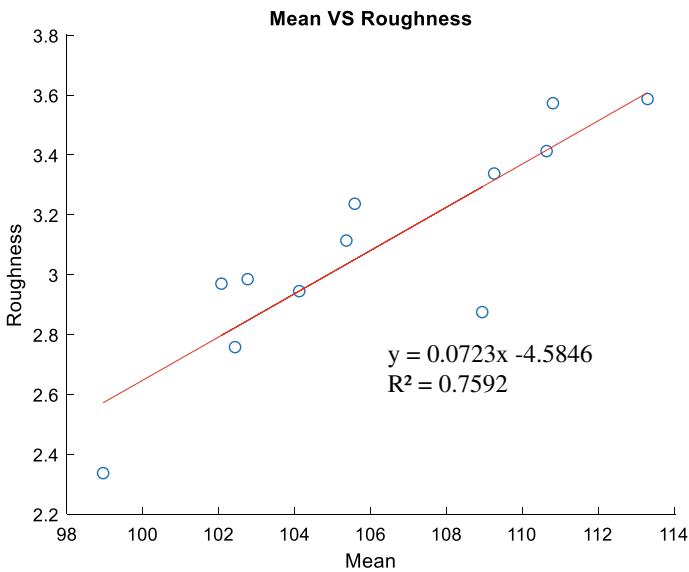


Fig. 22.6 Ra versus mean of intensity image

22.5 Conclusions

First, a set of the roughness, Ra of the workpieces was tabled. Then, a set of 2D images of turned surfaces was obtained. By developing an algorithm, the distribution parameter of image pixel intensity was calculated from each surface image. After correlating the parameters of surface roughness and image pixel intensity, the mean image has been found to be better associated with Ra, the ruggedness parameters.

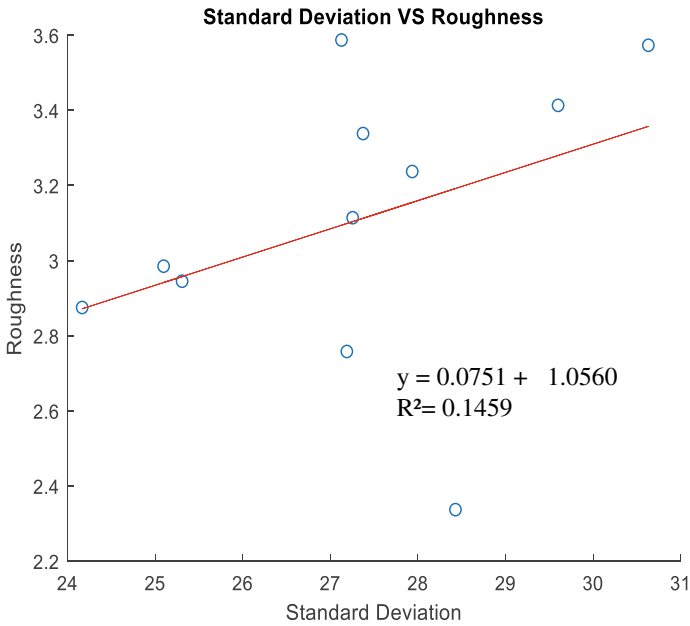


Fig. 22.7 Ra versus standard deviation of intensity image

Table 22.4 Ra from tester and Ra from image

| Specimen | Ra from tester | Ra from image |
|----------|----------------|---------------|
| 2 | 2.337 | 3.312 |
| 7 | 2.758 | 3.417 |
| 4 | 2.875 | 3.287 |
| 6 | 2.945 | 3.620 |
| 11 | 2.985 | 3.015 |
| 5 | 3.114 | 2.816 |
| 9 | 3.237 | 2.791 |
| 10 | 3.338 | 2.526 |
| 1 | 3.413 | 2.919 |
| 8 | 3.573 | 3.430 |
| 3 | 3.587 | 3.031 |

The better link between Ra and the mean of the intensity value is that the picture intensity dispersion level can calculate the surface roughness.

The reliability of the method can be further enhanced by using a laser. This laser will create speckle images of the specimen on the camera. The speckle image is better to evaluate because of the effect of the light source angle of incidence on the surface. Mean and standard deviation are calculated based on the pixel value of the image;

the bigger the image, the more pixel value; and this can be enhanced by upgrading the camera or edit the image itself. The regression also can be further analyzed by nonlinear regression.

References

- Butler D (2014) Surface roughness measurement. In: Dongqing L (ed) Encyclopedia of microfluidics and nanofluidics, vol 2. Springer, US, pp 1945–1949
- Min L, Li D, Dong S (2016) 3D surface roughness measurement based on SFS method. In: Proceedings of 2016 8th international conference on intelligent human-machine systems and cybernetics, IHMSC, vol 2, pp 484–488
- Mohamed Suhail SI, Mahashar Ali J, Siddhi Jailani H, Murugan M (2018) Vision based system for surface roughness characterisation of milled surfaces using speckle line images. IOP Conf Ser Mater Sci Eng 402
- Nithyanantham N, Suresh P (2016) Evaluation of cast iron surface roughness using image processing and machine vision system. ARPN J Eng Appl Sci 11(2):1111–1116
- Prabhathan P, Song C, Haridas A, Prasad G, Chan K (2017) Intensity and contrast based surface roughness measurement approaches for rough and shiny surfaces. Fifth Int Conf Opt Photonics Eng 10449:1044912
- Priya JD, Ali JM (2015) Design of a measurement system for surface roughness using speckle images. Int J Adv Eng Res Dev 2(04):300–305
- Samtas G et al (2014) Measurement and evaluation of surface roughness based on optic system using image processing and artificial neural network. Int J Adv Manuf Technol 73(1–4):353–364
- Shivanna DM, Kiran MB, Kavitha SD (2014) Evaluation of 3D surface roughness parameters of EDM components using vision system. Procedia Mater. Sci. 5:2132–2141
- Songli Y et al (2016) Design of surface roughness measuring system based on machine vision. Int J Innov Res Eng Manag 3(4):307–309